UNIVERSITY OF OKLAHOMA

GRADUATE COLLEGE

FROM SEA TO CITY: OBSERVING THE COMPLEX EVOLUTION OF THE COASTAL-URBAN PLANETARY BOUNDARY LAYER, SEA BREEZE MODIFICATIONS TO THE BOUNDARY LAYER, AND INVESTIGATING MESOSCALE PROCESSES NECESSARY FOR CONVECTION INITIATION IN HOUSTON, TEXAS DURING THE CUBIC FIELD CAMPAIGN

A DISSERTATION

SUBMITTED TO THE GRADUATE FACULTY

in partial fulfillment of the requirements for the

degree of

Doctor of Philosophy

By

MICHELLE ROSE STORM

Norman, Oklahoma

2025

Downloaded from SHAREOK. Persistent Handle URL: https://hdl.handle.net/11244/341766

FROM SEA TO CITY: OBSERVING THE COMPLEX EVOLUTION OF THE COASTAL-URBAN PLANETARY BOUNDARY LAYER, SEA BREEZE MODIFICATIONS TO THE BOUNDARY LAYER, AND INVESTIGATING MESOSCALE PROCESSES NECESSARY FOR CONVECTION INITIATION IN HOUSTON, TEXAS DURING THE CUBIC FIELD CAMPAIGN

A DISSERTATION APPROVED FOR THE
SCHOOL OF METEOROLOGY

BY THE COMMITTEE CONSISTING OF

Dr. Petra Klein (Chair)

Dr. Elizabeth N. Smith

Dr. Otavio Acevedo

Dr. Scott Salesky

Dr. Michael Wimberly

© Copyright by MICHELLE ROSE STORM 2025
All Rights Reserved.

Acknowledgments

I want to thank all of the amazing people who have had a hand in my success in gaining this degree, for which I am incredibly grateful. I have been so fortunate to have numerous amazing mentors in my relatively short career thus far. I first met my advisors, Drs. Smith and Klein, in 2019 during my REU and I am so thankful for their never-ending support of me in all the random things I wanted to dive into while at OU. They encouraged me to expand my experiences beyond my own research, which led to conducting field work in the Southeast US, attending a women's leadership conference, participating in a 5-week research cruise across the Atlantic Ocean, and many other things during my time at OU. I learned so many skills while under their advisorship. Petra and Liz, thank you both for providing so much support and help in my growth as a scientist. It isn't often in our field to be lucky enough to have two female advisors, and I don't take that for granted. I am also endlessly grateful to Dr. Clark Evans, my master's advisor, who continued to provide support and be a sounding board whenever I called upon him. To our CUBIC collaborator, Dr. Tim Wagner, for the continued guidance and wisdom for the last several years, I appreciate your time and expert knowledge so much. To Dr. Tom Galarneau, for taking the leap with me on a random side project that led to a published paper and my first experience at a small specialty conference, and the continued advice you provided throughout the years. Finally, to Drs. Tammy Weckwerth and Bill Brown for their mentorship during my last year of my PhD while I was a visiting student at NCAR. Your leadership and mentorship helped get me past the finish line, thank you.

When I was about to start my senior year of my undergraduate studies, I met with one of my professors, Dr. Sam Ng, to discuss options moving forward. I expressed my desire to work on research, but my self doubt about whether I was smart enough for graduate school. I was an untraditional student, which meant I came in later, worked my way through school, and at the time I had zero research opportunities under my belt. I very clearly remember him telling me it would 'be a shame' if I didn't go forward with graduate school and pursuing research work. That conversation changed my trajectory, and I am so thankful for it. My first leap into anything research related came during the NWC REU in 2019, when I came to OU to work with Dr. Smith as an intern for the summer. I fell in love with all things observational research related that summer, was introduced to field work while volunteering on the TORUS campaign, and gained confidence

in my abilities to pursue research. I also met so many wonderful people that summer, including my now lifelong friend Maddy Diedrichsen, who I know will always be up for a climbing adventure any time I ask.

I never could have foreseen the road I would travel while gaining my upper-level education, but I am so thankful for all the experiences. I have made wonderful friends along the way, all of whom I am eternally grateful for. To Victoria, our daily snapchats and voice memos are one of the few things that kept me sane when things felt impossible. You're an incredible scientist and I'm so happy to have you as my best friend, to continue cheerleading each other, and to share in our science adventures for years to come. To Arianna, you are one of the quirkiest and funniest people I'm lucky to be friends with, and I will miss our AMS trips together (but Germany will be a fun place to come visit). To the BLISS group and all my office mates, it was never a dull moment sharing space with you all. I'm thankful for all the support, laughs, and talks that have been had in the last few years.

Last, but definitely not least, a huge thank you to my family. To my husband, Josh, who stood by my side through all the highs and lows. I wouldn't have finished this degree without your support and love. To my mom, your excitement for my journey, the weather, and all the experiences I've had have helped remind me why I am here when I sometimes couldn't remember. I'm so appreciative of your love, encouragement, and support too. To my brothers and sisters who always encouraged me and told me 'how cool' it was to pursue these degrees, I thank you too. Finally, many others have helped me along the way that I haven't personally called out, but your support, love, kindness, and faith in me all helped get me to the end, thank you!

Table of Contents

Acknowledgments ..... **iv**
List of Tables ..... **viii**
List of Figures ..... **ix**
Abstract ..... **xiv**
Chapter 1 ..... **1**
Introduction **1**
1.1 The Planetary Boundary Layer 1
1.2 Coastal-Urban Environments 4
1.2.1 Coastal Breezes 5
1.2.2 Urban Heat Islands 8
1.3 Research Goals and Science Questions 10
Chapter 2 ..... **11**
Observing the Sea Breeze **11**
2.1 TRACER-CUBIC 11
2.2 CUBIC Case Classification Methods: Synoptic vs. Regional Flow 16
2.3 Sea Breeze Identification 27
2.4 CUBIC Sea Breeze Statistics 30
Chapter 3 ..... **41**
Spatial Variability in Coastal-Urban Planetary Boundary Layer Heights **41**
3.1 Introduction 41
3.2 Data Analysis Methods 43
3.2.1 Planetary Boundary Layer Height Algorithm 43
3.2.2 Composite Techniques 44
3.3 Campaign-Duration Composites 45
3.4 Regional Flow Influences 52
3.5 Sea Breeze vs. Non-Sea Breeze Planetary Boundary Layer Heights 55
3.6 Sea Breeze vs. Non-Sea Breeze Thermodynamic and Kinematic Characteristics 57
3.7 Summary and Conclusions 61
Chapter 4 ..... **64**
Sea Breeze Effects on Planetary Boundary Layer Evolution **64**
4.1 Introduction 64
4.2 Sea Breeze Case Comparison: Onshore vs. Offshore 66
4.3 Kinematic and Thermodynamic Composites 80

4.4 Discussion and Conclusions 92
Chapter 5 ..... **94**
Sea Breeze Forced Convection Initiation: A Case Study on Observations and Ensemble Forecasts from 17 August 2022 ..... **94**
5.1 Introduction 94
5.2 Warn-on Forecast System Overview 96
5.3 PBL Parameterizations 97
5.4 Forecast Evaluation and Coastal Sea Breeze Modifications to the PBL 98
5.5 Mesoscale Process Investigations - Sea Breeze Spatial Evolution and Convection Initiation 112
5.6 Discussion and Conclusions 130
Chapter 6 ..... **133**
Summary and Conclusions **133**
Reference List **138**

List of Tables

2.1 Summary of the 700 hPa SOM subgroup (southerly, northwesterly, northeasterly, and transitional) statistics. Included SOM nodes for each subgroup are listed, as well as the 21-year, CUBIC, and sea breeze percentages of occurrence 21
4.1 Regional flow composite case numbers at each site 82
5.1 WoFS model specifications, including ensemble member specific physics combinations 97

List of Figures

1.1 Schematic illustration of diurnal PBL evolution assuming homogeneous conditions. Figure reprinted from Stull (2012).....2

1.2 Sea breeze schematic depicting low pressure over the land surface and associated rising motion, high pressure over the water surface, creating the pressure gradient force directed onshore. Sea breeze front depicted by blue line and return flow depicted aloft (adapted from Miller et al. 2003).....6

1.3 Urban breeze diagram depicting urban directed near surface flow with divergent flow aloft, from Ada Carpenter, Carbon Brief, based on Yang et al. (2024) and Mestayer and Anquentin (1995).....9

2.1 CUBIC domain, with additional TRACER AMF main site shown in La Porte. Shading on map represents local climate zones (Demuzere et al. 2021: Spicer 2024). Doppler lidar wind roses at 100-m ground level (AGL) indicate predominant daytime (sunrise to sunset) wind direction throughout the campaign. CLAMPS1 was deployed at the urban site, SPARC at the exurban site, and CLAMPS2 at the coastal site 13

2.2 CUBIC Doppler lidar data availability heatmap for the urban (a), coastal (b), and exurban (c) sites. Temporal resolution shown is 10 min, to be consistent with the resolution of the TROPoe datasets. Panel titles include the total number of days with available data at each site. Coastal data was limited due to delayed deployment of Doppler lidar system. 16

2.3 SOM nodes for the 21-year climatology and associated percentage of occurrence (in titles). Shading and black contours depict MSLP (hPa) 18

2.4 SOM nodes for the 21-year climatology and associated percentage of occurrence (in titles). Shading and black contours depict 700 hPa geopotential height (m), black arrows show flow direction over the Houston area, and colored boxes indicate synoptic regime subgroups; southerly (blue), northwesterly (pink), northeasterly (green), and transitional (gold)..... 20

2.5 Composites of ARM radiosondes for northeasterly (a) and northwesterly (b) SOM regimes. Thick lines denote composite mean values and thin lines represent +/- one standard deviation. 22

2.6 SOM node 6 (left), the 9 June 2022 700 hPa geopotential heights at 1500 UTC from the ERA5 dataset (middle), and SOM node 9 (right) are shown as an example case highlighting the sensitivity of individual case placement into SOM nodes.....24

2.7 Regional-based regime radiosonde composites for the onshore (a), offshore (b), southwesterly (c), and northeasterly (d) regimes. Thick lines denote composite mean values and thin lines represent +/- one standard deviation.....26

2.8 Example of an identified SB case using CUBIC observations and KHGX radar reflectivity data at the urban location on 17 July 2022. Wind speed (a), wind direction and wind barbs (b), and vertical velocity (c) are shown in the main plot, with sunrise/sunset (thin black dashed

lines) and SBF (thick black dashed line) times denoted. The smaller subplot shows surface meteorological tower data (d) consisting of temperature (blue), relative humidity (red), and pressure (green) with the SBF denoted by the arrows pointing within the black box. The insert on the lower right shows the associated radar reflectivity data with the estimated SBF location (black dotted line) and urban site (gray star; e) 29
2.9 Number of SB cases per month observed during CUBIC. Black line represents 1700-2100 UTC averaged monthly land-sea temperature differences 31
2.10 Box and whisker plots comparing 1800 UTC land-sea temperature differences between SB (left) and non-SB (right) cases. Dot-dashed lines represent 3°C and 5.5°C temperature differences. 33
2.11 CUBIC observed sea breeze cases divided by regional regime types per month 34
2.12 Box and whisker plots comparing land-sea temperature differences on SB days based on regional regime types 35
2.13 SB passage times binned into 30 min intervals at the coastal (blue), exurban (green), and urban (black) CUBIC observation sites 36
2.14 SB propagation time from coastal location to urban site, colored by regional flow regime 36
2.15 SB passage times in 30 min bins for the Urban site (a, b), Exurban site (c, d), and Coastal site (e, f). Left column (a, c, e) colored by month; June (green) July (blue), August (orange), and September (pink). Right column (b, d, f) colored by regional flow regime; onshore (blue), offshore (pink), northeasterly (green), and southwesterly (gold) 38
2.16 SB propagation time versus land-sea temperature difference scatter plot colored by regional flow regime; onshore (blue), offshore (pink), northeasterly (green), and southwesterly (gold). Dashed lines denote averages 39
3.1 a) Campaign averaged PBLH for the full records at each site (solid lines) and the reduced-record when data were available at all three sites (dashed lines). b) Difference in PBLH estimates between full-record and reduced-record composites. Grey dotted lines indicate campaign average sunrise and sunset times 46
3.2 Composites of 2-m surface temperature for the CUBIC campaign duration derived from the URMA reanalysis dataset. Top panels represent daytime temperatures at 1800 and 2100 UTC and bottom panels depict nighttime temperatures at 0300 and 0600 UTC. The observation locations of the three CUBIC sites and the ARM AMF site are shown along with the location of the central business district (CBD) of Houston 48
3.3 Campaign averaged PBLH violin plots every 3 hours from 1200-0900 UTC. Thick black line indicates value mean, while thin orange line indicates the median 51
3.4 IQR for each site every 3 hours from 1200-0900 UTC. Grey dashed line indicates campaign average sunset time 52

3.5 Campaign averaged PBLH at the urban site (a), exurban site (b), and coastal site (c) for onshore (blue), northeasterly (green), offshore (pink), and southwesterly (gold) regional regimes 55
3.6 PBLH composites for SB (solid lines) and Non-SB (dashed) days. The vertical dotted lines correspond to the campaign average sunrise and sunset times. The table insert lists the average maximum heights for each type of case and the corresponding differences. Additional horizontal dashed lines help denote height differences between cases. 57
3.7 Maximum PBLH time-relative thermodynamic (a) and kinematic (b) 100-200 m layer-averaged time series for 3 hours before and after maximum PBLH time for SB days (Solid lines) and non-SB days (dashed lines). The vertical lines represent the time of maximum PBLH 60
3.8 Vertical velocity variance comparisons at a) 1800 UTC, b) 1900 UTC, c) 2000 UTC, and d) 2100 UTC for each location for SB (solid lines) and non-SB (dashed lines) days 61
4.1 Time-height wind speed and wind barbs (a,b), instantaneous vertical velocity (c,d), vertical velocity variance (e,f), and potential temperature (filled contours) and water vapor mixing ratio (black contours; g,h) at the coastal location from 1000-1000 UTC for the offshore (left) and onshore (right) SB cases. Black dashed lines indicate SB passage times, while gray dashed lines depict sunrise and sunset times 68
4.2 Same as Fig. 4.1, but at the exurban site. Gap in Lidar data due to overheating Lidar 69
4.3 Same as Fig. 4.1, but for the urban location 70
4.4 Horizontal wind speed profiles for the onshore (solid) and offshore (dashed)cases for the urban (black), exurban (green), and coastal (blue) sites. Panels show profiles at 1000 UTC, 1130 UTC, 1300 UTC, and 1530 UTC 71
4.5 Potential temperature (red) and water vapor mixing ratio (blue) profiles for the onshore case for the urban (solid), exurban (dashed), and coastal (dotted) sites. Profiles are at 1000 UTC, 1130 UTC, 1300 UTC, and 1530 UTC 73
4.6 Same as Fig. 4.5, but for the offshore case 74
4.7 Time-height horizontal wind speed and wind barbs (top), vertical velocity (middle), and vertical velocity variance (bottom) at the coastal (left) and urban (right) sites for the offshore (bottom) and onshore (top) cases. The time axes are centered on SB passage time and span 4 hours total. 76
4.8 Averaged wind speed two hours before (dashed lines) and two hours after (solid lines) SB passage for the onshore (left) and offshore (right) cases at the coastal (blue) and urban (gold) locations 77
4.9 Potential temperature 6-hour time series for the onshore (left) and offshore (right) cases at the urban (top), exurban (middle), and coastal (bottom) sites. Time axes are centered on SB passage time 78
4.10 Same as Fig. 4.9 but for water vapor mixing ratio 79

4.11 SB circulation schematic depicting physical explanation of PBL and 700 hPa flow interconnections....81
4.12 Composite SB passage time-centered wind speed observations at the coastal site for the onshore (a), offshore (b), southwesterly (c), and northeasterly (d) SB cases....83
4.13 Composites of wind profiles two hours before (dashed lines) and two hours after (solid lines) SB passage at the coastal site for the onshore (blue), offshore (pink), southwesterly (gold), and northeasterly (green) cases. Black profile denotes total average across all cases, with shading representing +/- 1 standard deviation....84
4.14 Same as Fig. 4.12 but for the urban location....86
4.15 Same as Fig. 4.13 but for the urban location....87
4.16 Vertical velocity variance composites at the coastal site for the southerly (top) and northwesterly (bottom) synoptic regime SB cases. Black dashed line depicts differentiation in turbulence regimes post-SB....88
4.17 Same as Fig. 4.16 but for the urban location....89
4.18 Composite SB passage time-centered temperature observations for the onshore (column 1), offshore (column 2), northeasterly (column 3), and southwesterly (column 4) regional regimes at the urban (top), exurban (middle), and coastal (bottom) sites. Contours correspond to heights from the surface to 2000 m; darker colors = closer to the surface....91
4.19 Same as Fig. 4.18, but water vapor mixing ratio....92
5.1 Observed radar reflectivity on 17 August 2022 at KHGX. Dotted lines indicate the leading edge of the SBF....99
5.2 Observed (purple x-markers) and simulated radar reflectivity >= 35 dBz. Esnemble members colored by PBL scheme: YSU (pink), MYJ (green), and MYNN (blue)....100
5.3 Observed (black) versus modeled (colored) temperature profiles with the 1730 UTC radiosonde. The observed temperature profile was collected with a radiosonde released at the AMF site. Ensemble members colored via PBL scheme: YSU (pink), MYJ (green), and MYNN (blue), and shading in (a) corresponds to profiles shown in (b)....101
5.4 Comparison of observed and WoFS PBL-scheme averaged surface temperatures for the duration of the simulation at the urban (a) and coastal (b) sites....103
5.5 Sea breeze passage times for each ensemble member at the coastal location. Colors correspond to the three different PBL schemes: YSU (pink), MYJ (green), and MYNN (blue). The black dashed line represents the observed SB time....105
5.6 Land-sea temperature differences for each ensemble member, separated by PBL schemes. The horizontal line indicates the observed value while the light grey area corresponds to +/- 0.5°C of the observed value and vertical displacement is done to mitigate overlapping points....105
5.7 Doppler lidar observed (black) and simulated (colored) wind profiles two hours before (dashed lines) and two hours after (solid lines) SB

passage at the coastal site. Thick colored lines denote PBL-scheme averaged profiles and skinny lines represent each individual ensemble member. Colors represent different PBL schemes: YSU (pink), MYJ (green), and MYNN (blue) 107
5.8 Observed (top) and simulated (bottom) potential temperature for the duration of the simulation period (1700-2300 UTC). Solid black lines denote observed SB passage, dashed black lines depict modeled SB passage, and wind barbs are included on simulated subplots. The top row in the bottom half corresponds to YSU ensemble members, the middle row denotes MYJ ensemble members, and the bottom row shows MYNN ensemble ensemble members 109
5.9 Same as Fig. 5.8, but for water vapor mixing ratio 111
5.10 Depiction of vertical cross-section path (dashed line) across Houston CBD showing the start and end points (blue dots) to the southeast of the coastal site and northwest of the urban site, respectively 113
5.11 Observed (left) and simulated (right) vertical velocity through duration of simulation period (1700-2300 UTC). Solid black lines denote observed SB passage, dashed black lines depict modeled SB passage, and wind barbs are included on simulated subplots 114
5.12 Vertical cross section at 1910 UTC depicting wind barbs, updrafts > 0.5 ms^{-1} (red dashed contours), water vapor mixing ratio > 16.0 gkg^{-1} (green contours), horizontal wind speed > 4 ms^{-1} (warm colored filled contours), and radar reflectivity > 10 dBz (filled contours). Black boxes denote updrafts along SBF, while purple boxes show updrafts ahead of SBF but associated with the leading edge of the moist airmass 116
5.13 Same as Fig. 5.12, but at 2010 UTC 117
5.14 Same as Fig. 5.12, but at 2130 UTC 119
5.15 Same as Fig. 5.12, but at 2230 UTC 120
5.16 Fig. 5.16: Vertical cross section at 1910 UTC depicting wind barbs, updrafts > 0.5 ms^{-1} (red daashed contours), horizontal wind speed > 4 ms^{-1} (purple contours) and water vapor mixing ratio > 15 gkg^{-1} (green filled contours) 122
5.17 Same as Fig. 5.16, but at 2010 UTC 123
5.18 Same as Fig. 5.16, but at 2130 UTC 124
5.19 Same as Fig. 5.16, but at 2230 UTC 125
5.20 Vertical cross section at 1910 UTC depicting wind barbs, updrafts > 0.5 ms^{-1} (red dashed contours), and equivalent potential temperature (filled contours). Black boxes denote location of MAHTE behind the SBF 127
5.21 Same as Fig. 5.20, but at 2010 UTC 128
5.22 Same as Fig. 5.20, but at 2130 UTC 129
5.23 Same as Fig. 5.20, but at 2230 UTC 130

Abstract

Coastal-urban environments are characterized by complex interactions between mesoscale processes and abrupt surface characteristic changes that influence the planetary boundary layer (PBL) evolution, convection potential, and air quality conditions. One of the most prevalent and influential mesoscale circulations that affects coastal-urban regions is the sea breeze (SB), driven by daytime thermal contrasts between the land and sea. The SB is responsible for advecting cooler, more moist air from over the water inland, which can result in thermodynamic and kinematic changes to PBL properties, lead to convection initiation (CI), and affect local air quality. The overarching goal of this dissertation is to further our understanding of the complex coastal-urban environment and interactions between mesoscale processes with a particular focus on SB effects on the PBL. The Coastal-Urban Boundary Layer Interactions with Convection (CUBIC) field campaign utilized an array of PBL profiling instruments to gather observations across the coastal-urban region of Houston, Texas, with the objective to characterize Houston's PBL and examine the role of the SB and urban heat island (UHI) effects on the evolution of the PBL. Each of the three sites collected continuous, high-resolution kinematic and thermodynamic data for a four-month period to culminate in a rich dataset suitable for spatial and temporal analyses of the PBL and SB.

First, a classification method for handling the large number of CUBIC cases was developed. Initially, a self-organizing map (SOM) technique was applied to objectively sort each CUBIC day into one of four synoptic regimes based on 700 hPa geopotential heights following the techniques applied by Wang et al. (2022). However, verification of the SOM's ability to represent the regional flow over the Houston area showed an inability for the SOM to capture the local conditions. Thus, a regional flow classification method based on sounding analyses (700 hPa flow) over the Houston area was adapted to ensure connections between the upper-level flow and PBL responses to the SB were local and consisted of four regimes: onshore, offshore, northeasterly, and southwesterly. Next, the SB was identified using a multivariate approach in which 4 out of 5 specified criteria were needed for a case to be flagged as a SB. A total of 52 days, or 41% of CUBIC dates, developed a SB. Of the SB cases, 98.2% occur when land-sea temperature differences are at least 3°C, with signs of seasonal changes to the SB, with later onset times and faster propagation speeds in September SB cases. Investigations in regional flow regime effects

on SB timing show no significant differences amongst regimes, suggesting that onset timing and propagation depend on additional mesoscale and seasonal forcings beyond ΔT or regional regime.

Examination of the PBL height (PBLH), estimated via a fuzzy logic algorithm combining data from multiple instruments, showed substantial spatial heterogeneity across the coastal-urban interface. This spatial heterogeneity was attributed to mesoscale influences, such as the SB and UHI effects. The urban site exhibited PBLH values ~480 m higher than at the coastal location, as well as a two-hour temporal difference in when the maximum PBLH is reached. In the overnight period, the nocturnal PBLH at the urban site remains elevated by up to 250 m, further indicating that sharp contrasts in surface characteristics can lead to meaningful differences in PBL structure. Regional-scale flow regimes revealed limited influence on the maximum PBLH, but some regime-dependent differences during the morning and evening transition periods. A larger role in observed PBLH variability was found to be the SB, with SB events shown to take place on days with deeper PBLs across all sites when compared to non-SB cases.

To better understand the array of PBL responses to the SB and possible effects from regional flow, two detailed case studies, compared with composite analyses, revealed that the depth, structure, and turbulence signatures of the PBL response to the SB evolve as the circulation moves inland. The urban site consistently exhibited stronger and deeper wind profiles, with offshore cases producing greater post-SB wind speeds and a more pronounced jet-like structure. In contrast, thermodynamic responses varied across space but showed no systematic differences between regional flow regimes, suggesting that pre-existing thermodynamic structure is a more important determinant of SB modification than regional flow. These results point to local-scale and surface processes, such as surface fluxes, cloud cover, and spatial heterogeneity in land cover, as key drivers of the observed variability in PBL responses to the SB across Houston.

Finally, a case that was characterized by exceptionally strong thermodynamic and kinematic SB responses and CI along the SB front (SBF), offered an ideal opportunity to integrate high-resolution observations with a numerical weather prediction (NWP) ensemble to explore the processes important to SB-forced CI. The analysis indicated that persistent ascent along or ahead of the inland-propagating SBF, in combination with pre-existing moisture, plays a critical role in successful CI. Ensemble simulations further revealed forced ascent across much of the domain prior to CI, filling gaps between the coastal and urban observations and providing a more complete depiction of the spatial evolution of the SB.

Chapter 1

Introduction

1.1 The Planetary Boundary Layer

The planetary boundary layer (PBL), the dynamic interface between Earth's surface and the atmosphere, is pivotal in driving meteorological processes that influence weather patterns, climate behavior, and pollutant dispersion. It responds to surface forcings on the order of minutes to hours, resulting in a distinct diurnal cycle of PBL height (PBLH), stability, and turbulent mixing (Garratt 1994; Stull 2012). For instance, the nocturnal PBL is typically shallow, on the order of tens to hundreds of meters, and is distinguished by stable stratification and limited turbulent mixing. Conversely, the daytime convective boundary layer (CBL) is well-mixed, with strong turbulence leading to a much deeper PBL, typically reaching 1000 m and extending up to 3000 m in the summer on days with strong insolation. The type and use of Earth's surface, along with solar energy transmitted through the atmosphere, control the diurnal evolution of the PBL and the partitioning of mass and energy fluxes. The CBL forms during the day as a result of the absorption of solar radiation at the surface and the transfer of sensible and latent heat energy from the surface to the atmosphere. This transfer of heat produces convectively driven updrafts and downdrafts that act to vertically mix heat, mass, and momentum from the surface through the PBL. Additionally, the entrainment zone, i.e., the relatively thin layer at the interface between the PBL and free atmosphere, influences the PBL growth and its thermodynamic and turbulence structure. At the entrainment zone, air from the free troposphere mixes with air from the PBL, which can directly affect cloud formation, convection initiation (CI), and pollutant dispersion. In the overnight period, the lack of insolation leads to the formation of a stable boundary layer due to radiative cooling at the surface. In an ideal environment of flat, homogeneous land, the PBL evolves canonically, as depicted by Stull (2012) in Fig. 1.1. However, this idealized view of the diurnal PBL evolution does not capture the impacts of horizontal heterogeneity of soil properties across the Earth's surface, terrain and land-use changes, or large-scale weather patterns (Pinto et al. 2006).

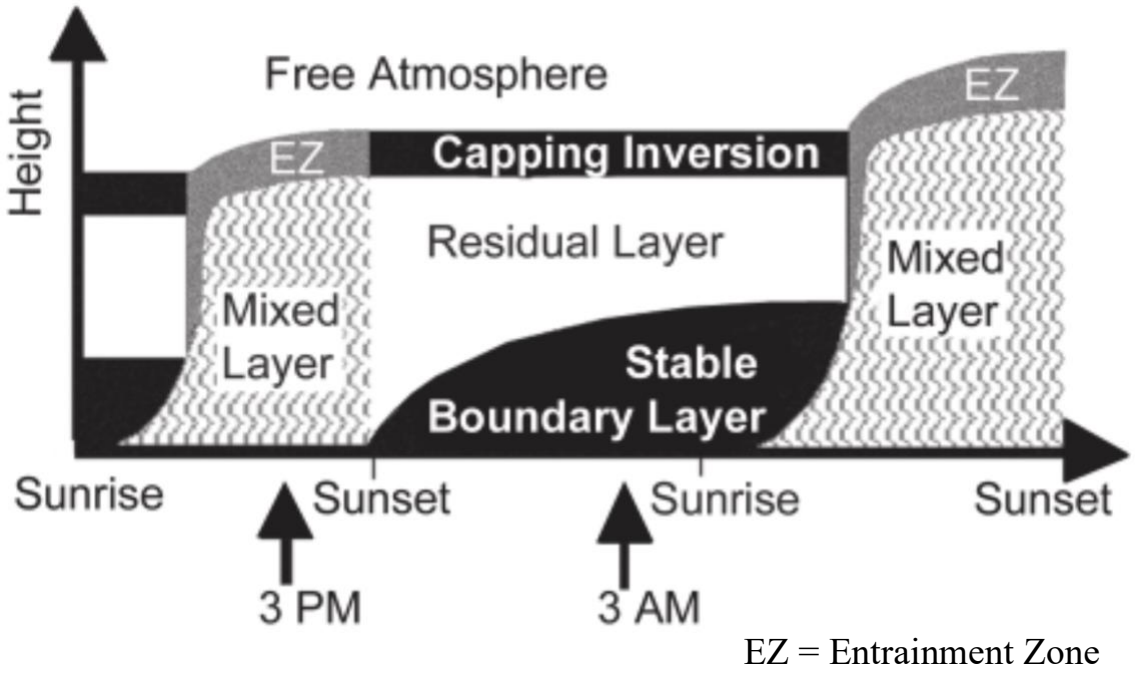


Fig. 1.1: Schematic illustration of diurnal PBL evolution assuming homogeneous conditions. Figure reprinted from Stull (2012).

An important component of studying the PBL is determining the PBL height (PBLH), the height of the boundary between surface-influenced processes and the free atmosphere. It characterizes the vertical extent of turbulent mixing, defines the height at which clouds and convection typically form, and bounds the volume available for the dispersion of air pollutants (Seibert et al. 2000; Haman et al. 2014). Many applications rely on estimations of PBLH, including those used to investigate phenomena like CI (Weckwerth et al. 2019; Xu et al. 2023) and air pollution dispersion (Liu et al. 2011; Miao et al. 2016). The PBLH is dynamic, varying diurnally, seasonally, and spatially due, in part, to the influence of land surface characteristics on surface fluxes that help drive buoyancy. While the PBLH is a key parameter, it is difficult to define and observe. The definition of PBLH for a given study can be dependent on the investigator's application or even the observations, necessitating approaches that combine multiple techniques for a well-rounded estimation of PBLH (Kotthaus et al. 2023). Traditionally, radiosonde data have been used to estimate PBLH with numerous methods, including identifying the height of the maximum potential temperature gradient, the height of surface-based temperature inversions, the height of the minimum relative humidity gradient, or several others. It remains a challenge in PBL

work to find a universal method of estimating PBLH that works well under different stability conditions (Liu and Liang 2010; Seidel et al. 2010; Aryee et al. 2020; Gu et al. 2020).

While the United States has a dense network of operational surface meteorological stations (Automated Surface Observing Systems and mesonets), weather radars, and satellite capabilities, there persists a lack of continuous spatiotemporal observations through the depth of the PBL (NRC 2009; Everett 2018; Geerts et al. 2018; Teixeria et al. 2021). Current operational remote sensing technologies face challenges within this layer: satellites have limited ability to observe the entirety of the PBL, particularly when clouds are present because of attenuating signals and blocked radiation, and operational weather radars offer limited vertical resolution and poor coverage of the PBL, since the radar beams scan above the height of the PBL top as the distance from the radar increases. Radiosondes, launched by the National Weather Service (NWS) twice a day (0000 and 1200 UTC), are the only operational, direct measurements of the PBL and these measurements are often spaced hundreds of kilometers apart, which leads to an undersampling of mesoscale and diurnal variability of the PBL (Pinto et al. 2021). As a result of these limitations in spatial and temporal coverage, the PBL continues to be one of the least observed portions of the atmosphere, and the need to observe a wide range of motions to adequately resolve turbulence, microscale, and mesoscale processes poses additional challenges for PBL observations.

More recently, other methods employing remote sensing instruments like interferometers, lidars, or radar wind profilers have been used to provide more frequent observations through the depth of the PBL, addressing the potential shortcomings of temporally coarse radiosonde observations (Rogers et al. 1993; Turner and Löhnert, 2014; Spuler et al. 2021). In cases where integrated profiling systems are used, such as the University of Oklahoma's Collaborative Lower Atmospheric Mobile Profiling System (CLAMPS; Wagner et al. 2019), observations from collocated instruments can be combined using fuzzy logic algorithms to produce PBLH estimations that combine the strengths of different instruments, while mitigating possible instrument weakness points (Kotthaus et al. 2023; Smith and Carlin 2024). Regardless of the observational method used to estimate PBLH, knowledge of this parameter provides critical context for interpreting PBL processes and insight to boundary layer thermodynamics and kinematics.

As discussed above, the weather and physical processes that take place within the PBL have direct health, economic, and societal impacts, including those regarding air pollution (Miller

et al. 2020; Sohrabi et al. 2020), severe weather (Smiley et al. 2022; Strader et al. 2022), and extreme heat risks (O'lenick et al. 2020; Watkins et al. 2021), making this portion of the atmosphere an important place to study and further our understanding. Integrated profiling systems, such as CLAMPS, provide opportunities to overcome data gaps in the PBL and to gain new insights about the PBLH evolution in complex environments such as coastal-urban environments, where large populations are concentrated and numerous local forcings and interactions strongly influence weather patterns. Important aspects of coastal-urban environments are further detailed in the next section.

1.2 Coastal-Urban Environments

Coastal-urban environments experience unique and complex PBL processes and interactions due to the combination of influences from mesoscale coastal breeze circulations and urban heat island (UHI) effects, as well as abrupt surface characteristic changes between the city and water interface (Haman et al. 2012; Hu and Xue 2016; Wu et al. 2024). The changes in surface characteristics across these regions lead to sharp gradients in temperature and moisture, in addition to drastic changes to surface roughness properties (Arya 2001; Baker et al. 2001; Marshall et al. 2004; Kustas et al. 2005; Varquez et al. 2015; Kristovich et al. 2019). Vertical and horizontal wind, temperature, and moisture gradients can evolve rapidly in these environments, necessitating high-resolution measurements to accurately capture the processes that take place. Furthermore, the development of thermal internal boundary layers (TIBL) has been observed within coastal-urban regions. A TIBL forms in coastal regions due to the horizontal advection of cool marine air over a warm land surface that leads to an unstable shallow layer within the marine layer (Arrillaga et al. 2016; Calmet and Mestayer 2016). The TIBL deepens with inland distance and the depth can be estimated using a number of different equations that take into account factors such as the distance from the coast, wind speed, lapse rates, and other variables. Observational studies have found the height of the TIBL in coastal-urban regions can be anywhere from 150 m at 5 km inland to 400 m at 15 km inland (Batchvarova and Gryning 1998; Yuan et al. 2006). Finally, coastal-urban regions often experience unhealthy air quality levels, especially in port locations where there are increased pollutants from shipping and freight operations (Daum et al. 2003; Williams et al. 2009; Viana et al. 2014). For example, Houston, the fourth most populous city in the United States, has a long

history of bad air quality, with numerous days exceeding unhealthy ozone levels (EPA 2025). Houston also experiences frequent summertime convection, adding another component of complexity to the environment and thereby deeming this city a hot spot for targeted field campaigns in recent years in an effort to better understand the many complexities present in coastal-urban environments.

1.2.1 Coastal Breezes

Coastal breeze circulations, which include sea breezes (SBs), lake breezes, and bay breezes, are a common feature in coastal regions throughout the world, occurring most often during the warm season when daytime heating is at its greatest and synoptic forcing is weak (Miller et al. 2003; Hughes and Vernon 2018). The basic physical mechanisms driving the development and propagation of coastal breezes have been well understood for many years, with extensive literature covering both observational and modeling perspectives, with Miller et al. (2003) and Crosman and Horel (2010) providing excellent overviews of the advances of each. Coastal breezes form due to differential heating of the air over land and water, creating a pressure and density gradient, with near-surface low pressure developing over the warm land and high pressure over the cool water surface (Fig. 1.2). As a result, a baroclinic circulation is induced with an onshore-directed density current and offshore flow aloft. The SB front (SBF) depicted in Fig. 1.2 is the leading edge of the onshore propagation of the marine air mass associated with the SB (or any other coastal breeze circulation). Propagation of the SBF is dependent on many factors, including prevailing flow, land surface characteristics, and the magnitude of the land-sea temperature gradient, with penetration distances reaching up to 400 km (Hu and Xue 2016; Noble et al. 2024). Miller and Keim (2003) refer to the strength of a SB based on the land-sea temperature difference, with stronger SBs (i.e., greater temperature differences) penetrating deeper inland and extending higher vertically.

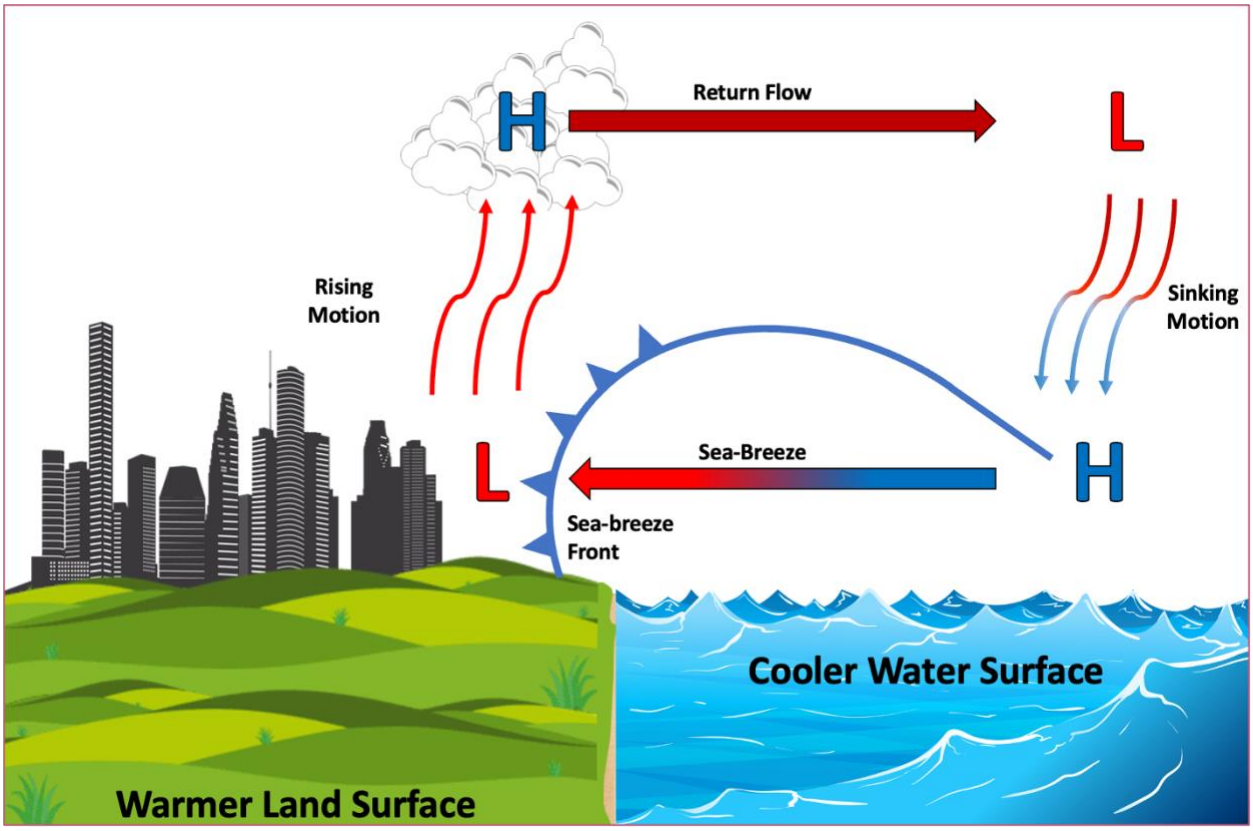


Fig. 1.2: Sea breeze schematic depicting low pressure over the land surface and associated rising motion, high pressure over the water surface, creating the pressure gradient force directed onshore. Sea breeze front depicted by blue line and return flow depicted aloft (adapted from Miller et al. 2003).

While the basic mechanisms are well known, the SB remains a popular area of study because it impacts many atmospheric processes, its effects and manifestations vary in space and time, and because it affects a large percentage of the world's population. Accurate representation of the SB is important for air pollution modeling, convection and precipitation prediction, offshore wind energy production, and heat stress forecasting (Papanastasiou et al. 2010; Meir et al. 2013; Steele et al. 2013; Sharma et al. 2024). For example, if there is the chance for extreme heat, but the possibility of a SB to propagate inland and provide relief, context about the timing and magnitude of surface cooling could help emergency planners prepare temporary cooling stations. In coastal-urban environments (e.g., Houston, TX), knowledge about convergence zones associated with the SBF is key to accurately forecasting air quality and thunderstorm conditions. The SB can both aid in dispersing air pollution and act to trap air pollution depending on the time

of SB onset, the intensity of the SB, and the location of the SB (Banta et al. 2005). When the SB forms late in the afternoon, often under conditions with offshore large-scale flow, the SBF can stall over pollution sources for more than an hour, allowing concentrated emissions to build up when photochemistry is active, leading to degraded air quality over a region. In addition to air quality modifications, SBs can also trigger convection and lead to measurable rainfall. A prior study in India has shown that summertime SBs can contribute to up to 70-80% of seasonal rainfall (Reddy et al. 2021). Enhanced convergence associated with the SBF can force updrafts, lift air parcels past the lifting condensation level (LCL), and lead to the formation of clouds and precipitation if environmental conditions are appropriate. Sharma et al. (2024) found that convection associated with the SBF in Houston's coastal-urban area peaked in the early to mid-afternoon, with the majority of cells having a short time span of 45 mins or less.

In regions around the world, studies have shown that near-surface offshore large-scale flow results in a later SB onset, with diminished inland propagation (Gilliam et al. 2004; Azorin-Molina and Chen 2009; Hughes and Vernon 2018; Reddy et al. 2021). Of particular interest, Gilliam et al. (2004) found that the greatest SBF intensity occurs under surface offshore flow, especially when pre-SB wind conditions are between 4-6 ms^{-1}. Prior studies have also identified increased upward motion within the PBL associated with SBF passage, often with updraft magnitudes of 1-2 ms^{-1} at the SBF, sometimes triggering convection (Arrillaga et al. 2018; Wagner et al. 2022; Wang et al. 2024). After the SB passes, most studies documented cooling surface temperatures, rises in relative humidity, and decreased turbulence. While the general behavior is consistent across the literature, the magnitude of these effects has not been well characterized in all regions where SBs are common. The literature also shows a large spread in the effects of the SB (e.g., magnitude of surface cooling or potential for CI to occur), which necessitates continued exploration of the SB. Hughes and Vernon (2018) noted that the SB can develop slowly, without clear evidence of a frontal passage, prompting their creation of a ‘weak’ sea breeze classification and highlighting one of the challenges of automated SB detection methods. Additionally, many studies focus on findings for specific seasons (e.g., summer vs winter SB cases), with few examining intraseasonal variability. For example, in Delaware, the temperature dropped on average 3-5°C and the dewpoint temperature dropped on average 1-2°C after SB passage during the summer, but the variability for SBs that occur within differing synoptic environments within the same season was not considered (Hughes and Vernon 2018). In Houston, many SB studies focus on air quality effects, convection,

or seasonal changes, leaving the warm-season variability of the post-SB PBL less characterized (Rappenglueck et al. 2008; Banta et al. 2011; Caicedo et al. 2019).

1.2.2 Urban Heat Islands

Another important component of understanding coastal-urban environments is the UHI, or the phenomenon that occurs when air temperatures in urban areas are higher than their surrounding non-urban areas (Oke 1995). UHIs arise when cities, which are heavily comprised of impervious surfaces like concrete and asphalt, absorb and store more solar energy than surrounding rural areas, leading to greater surface and air temperatures (Voogt and Oke 2003). Chen et al. (2011) illustrates the differences in diurnal temperatures between various structures within the urban domain, highlighting variations in thermal conductivities and heat capacities. They show that the urban ground surface has the greatest amplitude, while wall surface temperatures have the smallest diurnal range. Furthermore, studies have shown urban areas can be up to 5-7°C warmer than their circumjacent rural areas, particularly in the overnight period when radiative cooling in rural areas leads to quick reductions in sensible heat (Smith et al. 2011; Heaviside et al. 2015; Hu and Xue 2016). An example of this effect was shown in a model-based study by Marshall et al. (2004) with the diurnal cycle of temperatures being amplified in Florida when natural vegetation was replaced with up-to-date land cover, including man-made surfaces. The greater temperatures lead to increased vertical mixing via buoyancy-driven turbulence. Not only do temperatures rise in the city, but the lack of natural surfaces leads to a reduction in latent heat flux (i.e., drier air in urban areas). In addition to surface flux and resultant vertical mixing changes, urban spaces can also induce a local circulation, the urban breeze, similar in principle to coastal breezes (Oke 2005; Fig. 1.3). As another mesoscale process, the urban breeze circulation develops in response to the horizontal variations in temperature between the urban and surrounding areas (Hidalgo et al. 2008). The urban breeze is characterized by surface flow from rural regions converging on an urban site, with divergent flow above the urban location at the top of the PBL. Altogether, the presence of an urban area can drastically alter the PBL thermodynamic and kinematic structure when compared to the idealized, canonical diurnal PBL cycle.

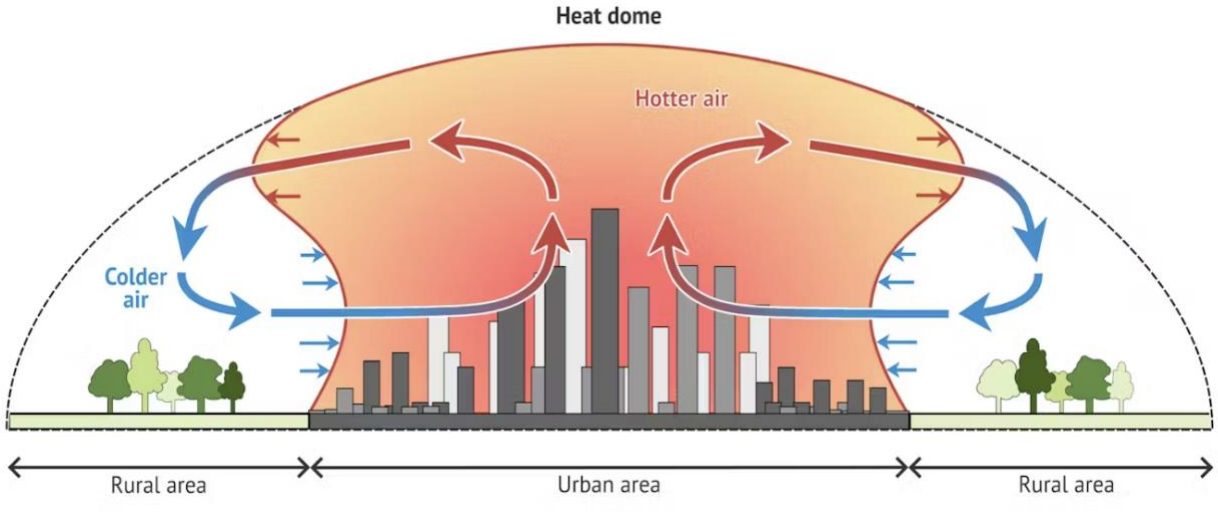


Fig. 1.3: Urban breeze diagram depicting urban directed near surface flow with divergent flow aloft, from Ada Carpenter, Carbon Brief, based on Yang et al. (2024) and Mestayer and Anquentin (1995).

The interaction between the UHI and SB circulation is complex, with both mesoscale processes modifying the coastal-urban thermodynamic and kinematic structures of the PBL. Past modeling and observational studies have found differing atmospheric responses in regards to the interaction between urban centers and inland propagating SBs. For instance, some studies have found that the SB propagation speed is inhibited by the UHI, with a decreased inland propagation distance due to UHI convergence and greater surface friction (Bornstein and Thompson 1981; Yoshikado 1994; Kusaka et al. 2000; Ferdiansyah et al. 2020). Conversely, the UHI has also been shown to contribute to greater land-sea temperature gradients, allowing for a stronger initial SBF, greater heat flux over the city, and a resultant increase in the urban breeze circulation and low-level flow associated with the SB (Sarkar et al. 1998; Ohashi and Kida 2002). Many factors contribute to the interactions between these mesoscale mechanisms, including the background synoptic conditions, size of the urban area, and other meteorological and land surface factors (Ohashi and Kida 2002; Miao et al. 2011). Despite decades of work investigating urban and SB interactions, there is no clear consensus on how these mesoscale features respond and interact with each other, in part due to limited observational studies. Thus, further exploration of the interplay between urban and coastal phenomena utilizing spatially distributed PBL profile observations is

necessary to better understand how the PBL evolves in time and across coastal-urban environments.

1.3 Research Goals and Science Questions

This work aims to expand our knowledge and understanding of the evolution of the PBL and the SB within a coastal-urban environment using an integrated approach utilizing multiple ground-based PBL profiling systems and numerical weather prediction (NWP) simulations. The collection of concurrent, continuous boundary layer profile observations across a coastal-urban domain allows for an extensive investigation into how the boundary layer evolves and interacts with SB and UHI circulations. Through a combination of analyses of observed PBL profiles, data integration from multiple instruments into value-added products, and simulations with a convection allowing ensemble NWP modeling system, this dissertation aims to address the following questions:

1. Is there a critical land-sea temperature difference needed in Houston for a SB to initiate, and how does synoptic versus regional flow affect SB timing?
2. What are the primary influences that affect the spatial PBLH diurnal evolution across the coastal-urban interface?
3. What is the influence of lower tropospheric regional flow in the PBL response to SB passage?
4. What physical mechanisms associated with the SB are important to SB-driven CI and can model ensemble simulations resolve these phenomena?

Chapter 2

Observing the Sea Breeze

2.1 TRACER-CUBIC

The TRacking Aerosol Convection interactions ExpeRiment (TRACER; Jensen et al. 2025) field campaign took place in the greater Houston area from October 2021 through September 2022, with an intensive operation period (IOP) from June 1 through September 30, 2022. TRACER was supported by the Department of Energy's Atmospheric Radiation Measurement (ARM) mobile facility (Jensen et al. 2019) and consisted of numerous instruments and observing platforms, real-time weather forecast briefings, and numerical modeling efforts. The driving science goal of TRACER was to quantify the role that spatially heterogeneous distributions of aerosols play in the development and evolution of convective clouds. Specifically, the study aimed at investigating how the microphysical, dynamic, and radiative properties of deep convective clouds change throughout different parts of the Houston coastal environment and under different aerosol loading regimes. Given the importance of aerosols, the main ARM ground-based instrumentation suite was deployed to La Porte, TX, as it is representative of aerosol loading from multiple local and anthropogenic sources. TRACER consisted of many smaller sub-campaigns with varying scientific objectives, ranging from convective storm morphology to radiation budget studies, leading to a large amount of scientific data collection in the Houston region during the summer of 2022.

The Coastal-Urban Boundary Layer Interactions with Convection (CUBIC) campaign was organized between the University of Oklahoma, the NOAA National Severe Storms Laboratory, and the University of Wisconsin - Madison and took place from 1 June to 25 September 2022 as a subcampaign under the larger, parent TRACER campaign (Jensen et al. 2019; Jensen et al. 2023; Klein et al. 2023). CUBIC was proposed in conjunction with TRACER in order to address the need for high-resolution thermodynamic and kinematic observations through the depth of the PBL throughout Houston, with an objective to characterize Houston's PBL, which encompasses many coastal and urban influences (i.e., SBs and UHI effects) that impact the diurnal evolution of PBL characteristics. It was hypothesized that urban and SB circulations affect the structure of the PBL,

leading to temporal and spatial variability in flow patterns. Additionally, CUBIC aims to further understand the characteristics of the pre-convective environment by evaluating the impacts of environmental modifications, such as enhanced ascent, increased low-level moisture, or wind speed changes, by local circulations.

The CUBIC campaign deployed three mobile boundary layer profiling platforms, two Collaborative Lower Atmospheric Mobile Profiling System (CLAMPS) units, and the Space Science and Engineering Center Portable Atmospheric Research Center (SPARC) unit throughout the Houston-Galveston region to observe distinct PBL environments (Wagner et al. 2019; Fig. 2.1). The configuration of the platforms, which transects through Houston, provides the opportunity to capture and investigate the spatial and temporal thermodynamic and kinematic differences present within varying land cover regions of the city. The shading in Fig. 2.1 represents the local climate zones (LCZ) for the Houston area, which are determined via the land cover for a region. The concept of LCZs was created in 2012 as a standard way to characterize urban landscapes that takes into account microscale land cover and the different physical properties associated with varying land cover types (Stewart and Oke 2012; Demuzere et al. 2021). The LCZ classification system consists of 17 zone types, each with a unique combination of surface cover, human activity, and surface structure, and was originally developed specifically for UHI studies. The universality allows for a systematic comparability of global UHI studies and the maps allow for enhanced understanding of important small-scale land-atmosphere interactions by providing context about land cover heterogeneity. The LCZ map for the Houston area was generated by Spicer (2024) using the most up-to-date data available.

The Houston-Galveston region comprises various land-cover categorizations (i.e. LCZ), with open-to-compact low and high-rise developed land and heavy industry within Houston's city center and surrounding neighborhoods, pastures and cultivated croplands to the west and south of the city, and a mixture of forests and grasslands to the north. The three CUBIC mobile profiling units were strategically sited to investigate the influence of land-cover gradients and to capture the spatial variability of PBL properties across the region. CLAMPS-1 (C1) was deployed 17 km north of downtown Houston in Aldine and situated within open mid-rise developed land. SPARC was deployed in Pearland to observe an exurban environment ~25 km south of downtown and along the outskirts of the developed land to the north and within the sparsely built LZC classification. While SPARC was located in a similar LCZ as C1, the air masses at the two sites are expected to

be distinct, with C1 being downwind of Houston throughout the majority of the campaign (~70% of the time) and SPARC experiencing advected air from the vegetated lands to the south, evidenced via the daytime wind rose analyses included in Fig. 2.1. CLAMPS-2 (C2) was located in La Marque at the University of Houston's Coastal Center (UHCC), ~50 km south-southeast of downtown and 25 km from the Gulf coast, to sample an environment directly influenced by coastal processes. The land cover surrounding C2 is comprised of brush and scattered trees. In addition to the CUBIC observation sites, data collected from the ARM AMF site, the main observation location for the parent TRACER campaign, is used, with the site located near the heavy industry region of Houston in La Porte. The naming convention for the remainder of this work, driven by the sampled air masses at each location and for clarity purposes, is urban (C1), exurban (SPARC), coastal (C2), and industrial (AMF).

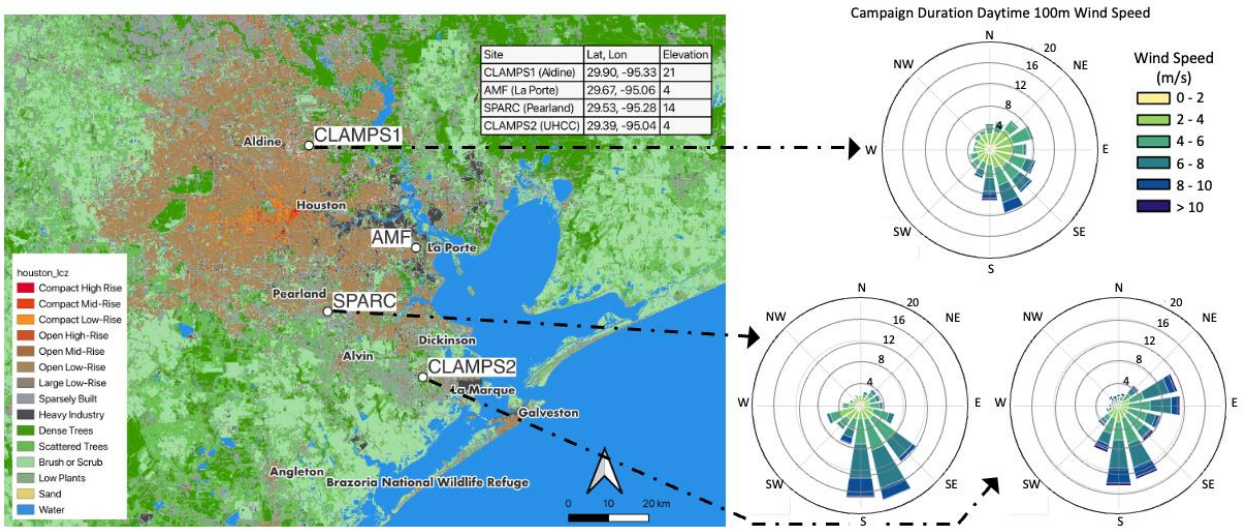


Fig. 2.1: CUBIC domain, with additional TRACER AMF main site shown in La Porte. Shading on map represents local climate zones (Demuzere et al. 2021; Spicer 2024). Doppler lidar wind roses at 100-m above ground level (AGL) indicate predominant daytime (sunrise to sunset) wind direction throughout the campaign. CLAMPS1 was deployed at the urban site, SPARC at the exurban site, and CLAMPS2 at the coastal site.

Each profiling platform is built and equipped similarly to collect temporally high-resolution thermodynamic and kinematic observations through the depth of the PBL that are

complementary to each other. The CLAMPS units are meant to operate as sibling systems, so each system includes a Halo Streamline Doppler wind lidar, an Atmospheric Emitted Radiance Interferometer (AERI), a microwave radiometer (MWR), and a surface meteorological station. The SPARC unit is similar to the CLAMPS platforms but does not include a microwave radiometer. There are also no surface winds from SPARC during CUBIC due to siting issues. The high temporal resolution of the CLAMPS and SPARC instruments permits observations of small-scale processes commonly found in the PBL.

To collect both horizontal and vertical wind data from the Doppler lidars, a scanning strategy consisting of fixed-point vertical stares and planned position indicator (PPI) scans at 60° elevation angle every 15 minutes was employed at all sites. A velocity azimuth display (VAD) technique is applied to the lidar PPI scans to determine the horizontal wind speed and direction every 15 minutes with a vertical grid spacing of approximately 26 m (Browning and Wexler 1968; Paschke et al. 2015). The fixed-point data are at a 1 s (CLAMPS) or 20 s (SPARC) resolution with a simple signal-to-noise ratio filter applied (SNR + 1 < X, where X = Doppler lidar noise threshold; C1=1.006, C2=1.0075, SPARC=1.005). The longer temporal resolution with the SPARC lidar is due to the difference in configuration between the systems, with the SPARC lidar using a greater number of pulses per ray. A single ray (i.e., one line-of-sight measurement) is derived from averaging multiple pulses. SPARC uses a greater number of pulses to form a single ray, which results in a higher SNR, but a lower temporal resolution as more time is spent on each ray. In instances where the vertical velocity variance (σ_w) is calculated, a 15-minute time period is used, corresponding to the temporal span between each PPI scan. The thermodynamic data are retrieved from the raw AERI and/or MWR radiance observations following a retrieval process using the Tropospheric Remotely Observed Profiling via optimal estimation (TROPoe) algorithm. This algorithm is an updated version of the AERIoe algorithm from (Turner and Lohnert 2014; Turner et al. 2018), which uses an a priori nearby sounding dataset (climatological soundings), Rapid Refresh (RAP) analyses, and radiance observations from the AERI and/or MWR from specific spectral bands to retrieve thermodynamic profiles via the optimal estimation technique (Rodgers 2000). The retrieved profiles are produced every ten minutes and the effective vertical resolution varies as a function of observing conditions and height. For further information about the profiling units and optimal estimation methods see (Rodgers 2000; Turner et al. 2018; Wagner et al. 2019; Maahn et al. 2020). The retrievals shown in this study use different instrument combinations due

to instrument availability and quality issues. The retrievals at C1 and SPARC use only the AERI data, as the C1 MWR data quality was suspect and SPARC does not include an MWR. At C2, the AERI was found to have high noise levels, so the retrievals only include MWR data. The lack of AERI data reduces the vertical resolution of the observed radiance measurements and thus leads to decreased capability to observe small vertical scale differences in retrieved profiles.

Throughout the four-month-long deployment, there were a few notable data losses that occurred at different sites and times. The largest data losses took place with the Doppler lidar systems, with only minimal losses to the thermodynamic data provided by the infrared interferometers and/or microwave radiometers due to rainy periods. The Doppler lidar at the exurban site, which was housed outside of the mobile trailer, would often become too hot during the afternoon, causing a shutdown of the lidar. This results in data losses in 50-60% of days during the peak afternoon heating period between 1830-2100 UTC (Local Time = UTC - 5), leaving 44 days in which there is full daytime lidar data availability at all three locations on the same day (Fig. 2.2). During the overnight period at the coastal site, condensation often formed on the inside of the lidar lens, leading to data losses in 50-60% of days between the hours of 0830-1330 UTC. The Doppler lidar at the urban location did not experience instrument issues throughout the campaign, so only minor data losses occurred in conjunction with localized rainfall events in which the lidar is unable to collect usable data.

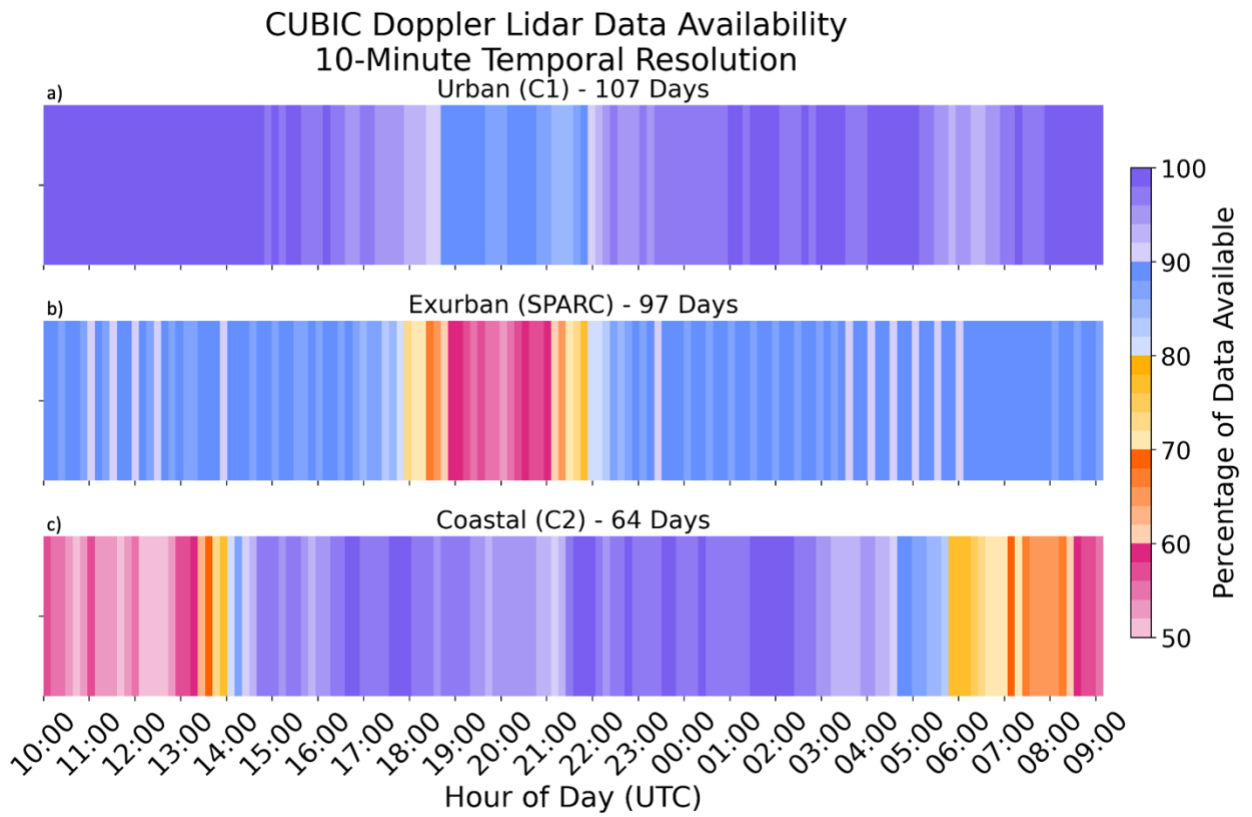


Fig. 2.2: CUBIC Doppler lidar data availability heatmap for the urban (a), coastal (b), and exurban (c) sites. Temporal resolution shown is 10 min, to be consistent with the resolution of the TROPoe datasets. Panel titles include the total number of days with available data at each site. Coastal data was limited due to delayed deployment of Doppler lidar system.

2.2 CUBIC Case Classification Methods: Synoptic vs. Regional Flow

To investigate the contributing factors of PBL and SB variability observed throughout the summer of 2022, the CUBIC dataset was first divided into synoptic flow regimes using a self-organizing map (SOM) technique. The SOM technique is employed to determine distinct synoptic patterns, similar to the method applied by Wang et al. (2022) that links summertime synoptic patterns with cloud properties in Houston. The premise for this method is to categorize the CUBIC dates into synoptic regimes as a way to handle the large number of cases and investigate possible influences of large-scale weather patterns on PBL properties. SOM techniques have been utilized as a clustering and pattern recognition method in many meteorological and oceanographic applications since the late 1990s (Liu and Weisberg 2011; Sheridan et al. 2011; Spassiani et al.

2021). The SOM is an unsupervised neural network based on a competitive machine learning approach that consists of choosing a desired output node (e.g., the synoptic flow patterns) that relates to an input pattern (e.g., the 700-hPa geopotential height input data that contains the pattern) and fine-tuning the output iteratively (Kohonen 2012). While the SOM approach is an objective way to sort synoptic patterns, some subjectivity still exists when selecting parameters that are needed to run the SOM algorithm. In the case of CUBIC, the level of geopotential heights, duration of data, and number of nodes are all examples of subjective decisions driving the objective results.

To produce the SOMs, 21 years of the Fifth-generation European Center for Medium-Range Weather Forecasts (ECMWF) reanalysis data (ERA5) from 2002-2022 of 1500 UTC 700 hPa geopotential heights for June through September are used (Hersbach 2023). To train the SOM algorithm, 700 hPa geopotential heights were chosen to reduce the terrain effects from the Sierra Madres mountains while still capturing the low-level synoptic scale troughs and ridges as well as the dominant pressure systems during the summer. Experiments with levels closer to the surface, including mean sea level pressure (MSLP), were conducted prior to choosing the 700 hPa level, but proved to inaccurately capture the synoptic-scale patterns due to the effects of the topography to the west (Fig. 2.3). Since weather systems generally propagate from the west to the east, knowledge of the height patterns to the west of Houston are crucial for accurate synoptic-based analyses, thus a geopotential height that is elevated enough to mitigate effects from the terrain and to capture the west Texas conditions is necessary. The sensitivity testing, input data, and SOM configurations are consistent with the findings from past works using SOMs for meteorological pattern categorization (Wang et al. 2022; Ford et al. 2015; Mechem et al. 2018).

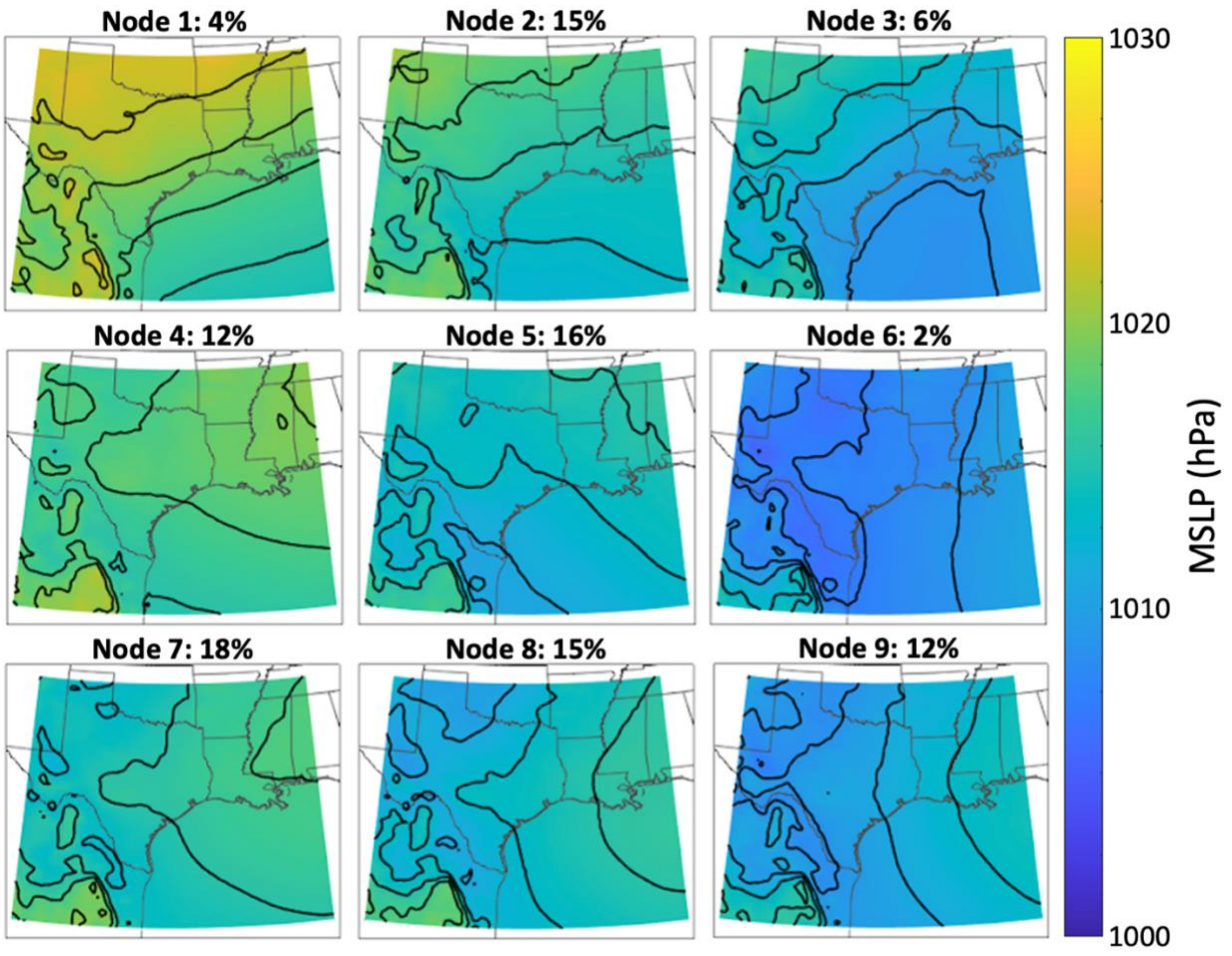


Fig. 2.3: SOM nodes for the 21-year climatology and associated percentage of occurrence (in titles). Shading and black contours depict MSLP (hPa).

The 1500 UTC hour is chosen to ensure that conditions are reflective of same-day daytime weather patterns prior to SB development. Prior to processing the data with the SOM algorithm, the geopotential heights are normalized to mitigate the effects of magnitude variability across the data. A two-step sorting approach is adopted, in which the full 21 years of data are run through the process to produce an 8x8 set of maps consisting of 64 nodes (not shown). This results in a node that consists of only tropical cyclone (TC) days. These dates were subjectively verified against satellite imagery and discarded, as TC conditions and effects of TCs on the PBL are outside the scope of this work. The remaining days (N=2396) are then processed through the algorithm again to produce a 3x3 set of maps (9 distinct nodes) with distinguishable synoptic regimes (Fig. 2.4). The final 3x3 set of maps are further sorted into 4 synoptic flow regimes based on the flow

direction over Houston; southerly (nodes 1-3, 5, 6), northwesterly (nodes 8, 9), northeasterly (node 4), and other/transitional (node 7). Individual days are output to a list during the SOM process, allowing for statistics to be calculated regarding the occurrence of days for certain regimes/nodes. It is important, before any synoptic-based analyses are undertaken, to understand how the CUBIC campaign's conditions compare to the climatology for the region. SOM analyses for the full 21-year period show conditions throughout the CUBIC campaign are representative of a climatologically normal summer season in the Houston-Galveston region. The SOM analyses indicate that the Houston area experiences a southerly synoptic regime in 70.5% of days during the CUBIC campaign. A northwesterly regime is seen in 21.3% of days, while the northeasterly and transitional/other regimes each occur in ~4% of days (Table 2.1). The percentages for the CUBIC campaign are nearly identical to the climatological percentage of occurrences of each synoptic regime, varying by less than 2% for each regime.

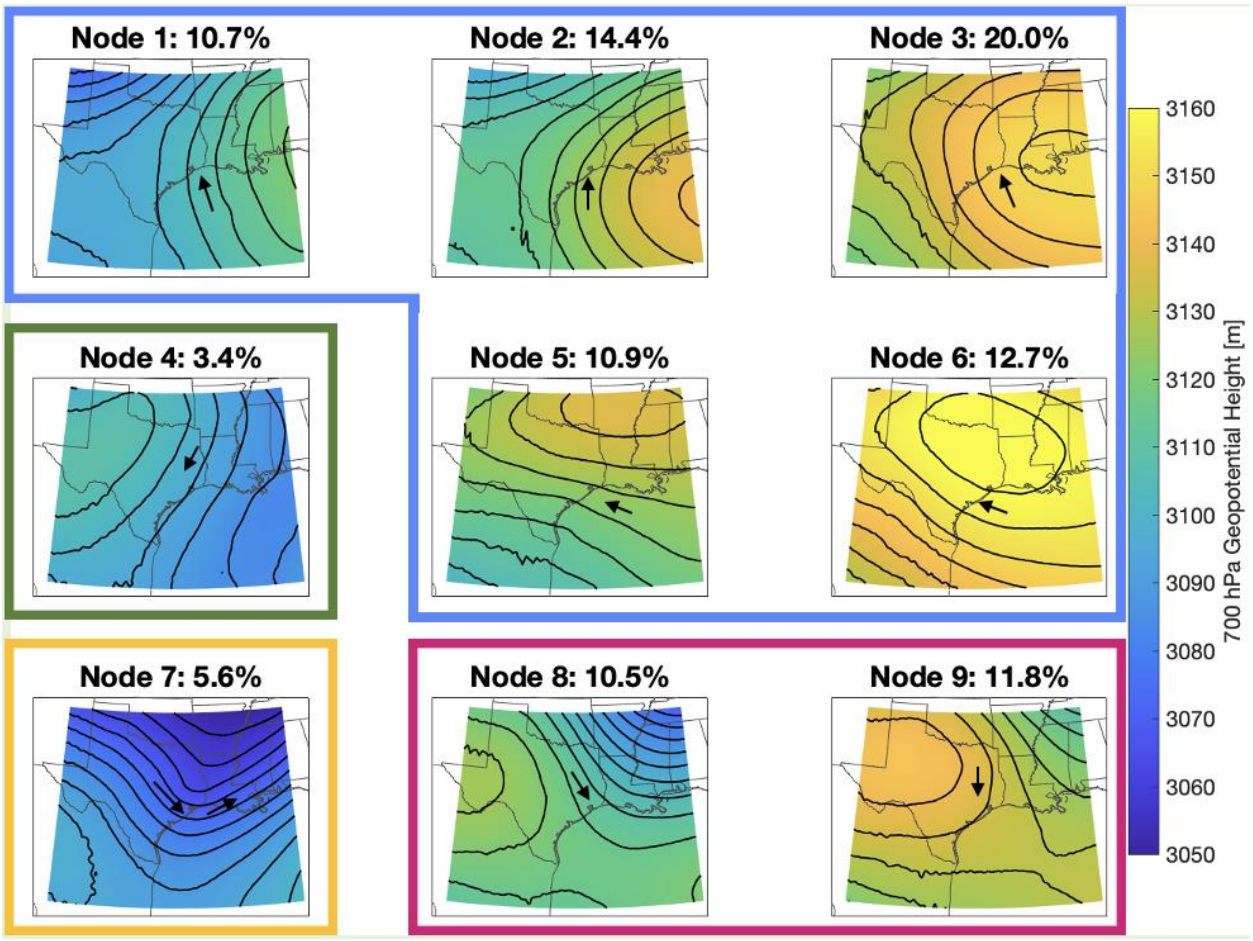


Fig. 2.4: SOM nodes for the 21-year climatology and associated percentage of occurrence (in titles). Shading and black contours depict 700 hPa geopotential height (m), black arrows show flow direction over Houston area, and colored boxes indicate synoptic regime subgroups; southerly (blue), northwesterly (pink), northeasterly (green), and transitional (gold).

Table 2.1: Summary of the 700 hPa SOM subgroup (southerly, northwesterly, northeasterly, and transitional) statistics. Included SOM nodes for each subgroup are listed, as well as the 21-year, CUBIC, and sea breeze percentages of occurrence.

Synoptic Regimes				
Flow	SOM Nodes	% of Occurrence		
		21-year Climo	CUBIC (N=122)	Sea-Breeze Cases (N=49)
Southerly	1, 2, 3, 5, 6	69	71	59
Northwesterly	8, 9	22	21	29
Northeasterly	4	3	4	6
Other/Transitional	7	6	4	6

Upon initial analyses into the two most prominent synoptic regimes, the southerly and northwesterly regimes, individual case studies and composite analyses showed little differences in pre-SB PBL conditions (not shown). The SOM analyses were not intended to capture the PBL conditions, given that 700 hPa is above the PBL, however, such similar conditions prompted questions and further investigation into the representativeness of the SOM clustering. As a part of the TRACER campaign, atmospheric soundings were launched four times daily, at 0530, 1130, 1730, and 2330 UTC from the main ARM site in La Porte, TX (AMF) near Galveston Bay (Fig. 2.1). Unfortunately, observed soundings were not available at 1500 UTC, to be consistent with the SOM framework, but comparing 1130 UTC and 1730 UTC sounding composites show some discrepancies between the expected 700 hPa flow via the SOM and what was observed above the AMF site. Fig. 2.5 shows the 1730 UTC sounding composites for the northwesterly and northeasterly SOM regime cases. The northwesterly composite shows a southwesterly wind direction at 700 hPa. The northeasterly composite does show northeasterly precisely at 700 hPa,

but several levels above and below 700 hPa are northwesterly or northerly in direction. The southerly composite shows southerly winds at 700 hPa and the transitional shows northwesterly winds. All four synoptic regime classifications indicated the same directions based on 1130 UTC composites and the 1730 UTC composites (not shown). The differences between sounding composites and SOM flow definitions motivates further analysis of the SOM patterns.

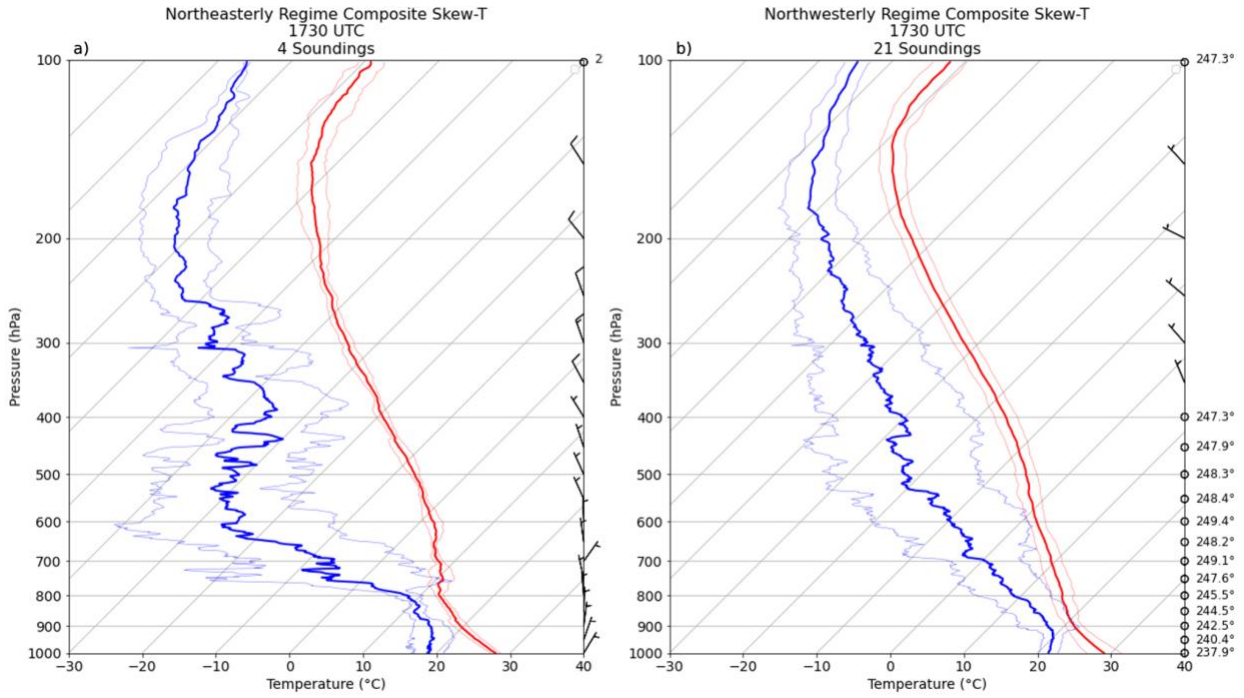


Fig. 2.5: Composites of ARM radiosondes for northeasterly (a) and northwesterly (b) SOM regimes. Thick lines denote composite mean values and thin lines represent +/- one standard deviation.

As a first step in understanding the discrepancies, daily 1500 UTC ERA5 700 hPa geopotential heights (same input data used in the SOM) are subjectively sorted, based on the SOM node patterns. The purpose of this exercise was to compare a human's interpretation of the present pattern (i.e., daily height) to the SOM node patterns in order to identify cases that did not match the SOM-identified nodes (e.g., the SOM puts a day in node 3 while the subjective interpretation puts the day in node 7). While this negates the largest benefit of using a SOM approach (objective vs. subjective), it allows one to assess and better understand how the SOM is applying each day into the resultant nodes. Of 122 cases, 17% (21) of cases were subjectively matched to a different

SOM node than labeled by the algorithm. Of these cases, 62% (13) of cases were placed into an adjacent SOM node, whereas the remaining 38% (8) of cases were allocated into a non-adjacent node.

Adjacent versus non-adjacent node placement is important because the arrangement of SOM patterns is not arbitrary. In a produced SOM, each node is meant to represent a prototypical pattern. The adjacent nodes represent similar patterns, creating a continuous spectrum of variability across the SOM nodes (Kohonen 2001). This property sets SOM techniques apart from other clustering methods, such as k-means clustering, in which clusters are treated independently and discretely; the SOM captures the gradual transition between distinct patterns, preserving topological structures. A Gaussian neighborhood function governs the extent that a surrounding node is adjusted during the training process. In early training stages, large neighborhood radii ensure the SOM nodes adapt in tandem, allowing for global organization of the map. As iterations and training progress, the radius is reduced, which allows for fine-scale adjustments to be made and distinctions between adjacent nodes to be made clearer (Hewitson and Crane 2002). Ultimately, the final resulting SOM node presents local continuity, where adjacent nodes correspond to similar patterns and non-adjacent nodes capture increasingly different patterns.

The local continuity property of SOMs helps explain why the SOM allocations and a subjective placement of cases differ. For example, the difference between nodes 6 and 9 depend on the positioning of the high-pressure center and indications of a trough in the eastern domain, thus a slight change in the location of this center would lead to differing results on which node to place a case into (and therefore changing the flow specifically over Houston; Fig. 2.6). For example, the SOM algorithm placed 9 June into Node 9, but the same case was allocated to Node 6 in the subjective analysis. These nodes reflect differing expected flow over Houston, despite the patterns being quite similar. As Reusch et al. (2005) describe, when a SOM is trained on geopotential height fields, nearby nodes often correspond to variations of a single synoptic regime (e.g., different spatial displacements of a trough), while nodes further apart represent qualitatively different flow patterns. Only 7% of CUBIC cases (8 out of 122) were subjectively placed into non-adjacent nodes, lending confidence to the SOMs ability to capture the qualitative synoptic regime patterns well. Since SOMs use an approach that necessitates each case is placed into a node (even if it does not match well to any node), an error of 7% is not unreasonable.

Still, representing the qualitative regime sufficiently does not address the issue of not capturing the flow over Houston. In the end, the application and use of the SOM analysis to characterize the regional scale flow over Houston is not viable, nor is it what the SOM is meant to do. The SOM characterizes the larger scale, southeastern Texas synoptic patterns, for which the regional scale flow over Houston can be (and is often) different. The SOM is not meant to capture the specific flow over an individual point, which is where the discrepancies between the sounding composites and SOM categorization of cases originate. As a result, it was decided that a new framework for categorizing cases would be necessary, to ensure that analyses reflect the regional flow over Houston and to allow for making more direct inferences about upper-level flow impacts on the PBL.

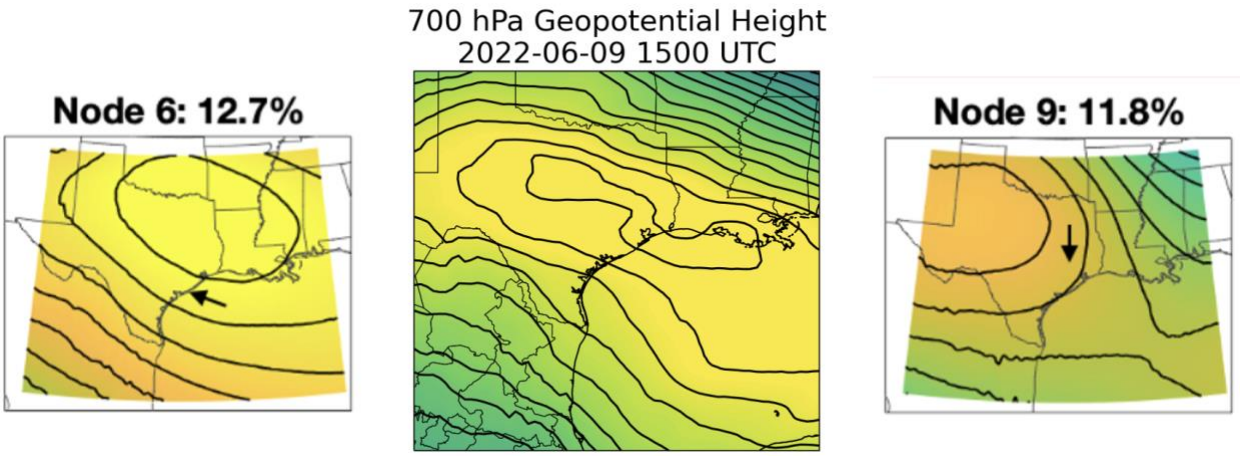


Fig. 2.6: SOM node 6 (left), the 9 June 2022 700 hPa geopotential heights at 1500 UTC from the ERA5 dataset (middle), and SOM node 9 (right) are shown as an example case highlighting the sensitivity of individual case placement into SOM nodes.

To determine a regional classification for the CUBIC campaign, the 1730 UTC observed soundings are used and analyzed with a simple wind thresholding technique. The 700 hPa flow for each day of the campaign (N=116) is classified into a regime defined by wind direction thresholds: northeasterly: 35-55°, onshore: 55-215°, southwesterly: 215-235°, and offshore: 235-35°. The directional thresholds are based on the orientation of the Texas coastline, which is oriented from southwest to northeast, approximately 225° to 45°, with smaller margins for the coast parallel flow regimes. Fig. 2.7 depicts the sounding composites for the regional flow regimes. Each regime

clearly shows expected wind direction at 700 hPa. With the newly developed regime, the distribution of cases across regimes is much more uniform than with the SOM-based synoptic regime classification. The onshore regime is the most prominent, with 56 cases accounting for 48.3% of CUBIC cases. The other regimes have more similar case counts, with 19.8%, 16.4%, and 15.5% of cases for the northeasterly, offshore, and southwesterly regimes respectively.

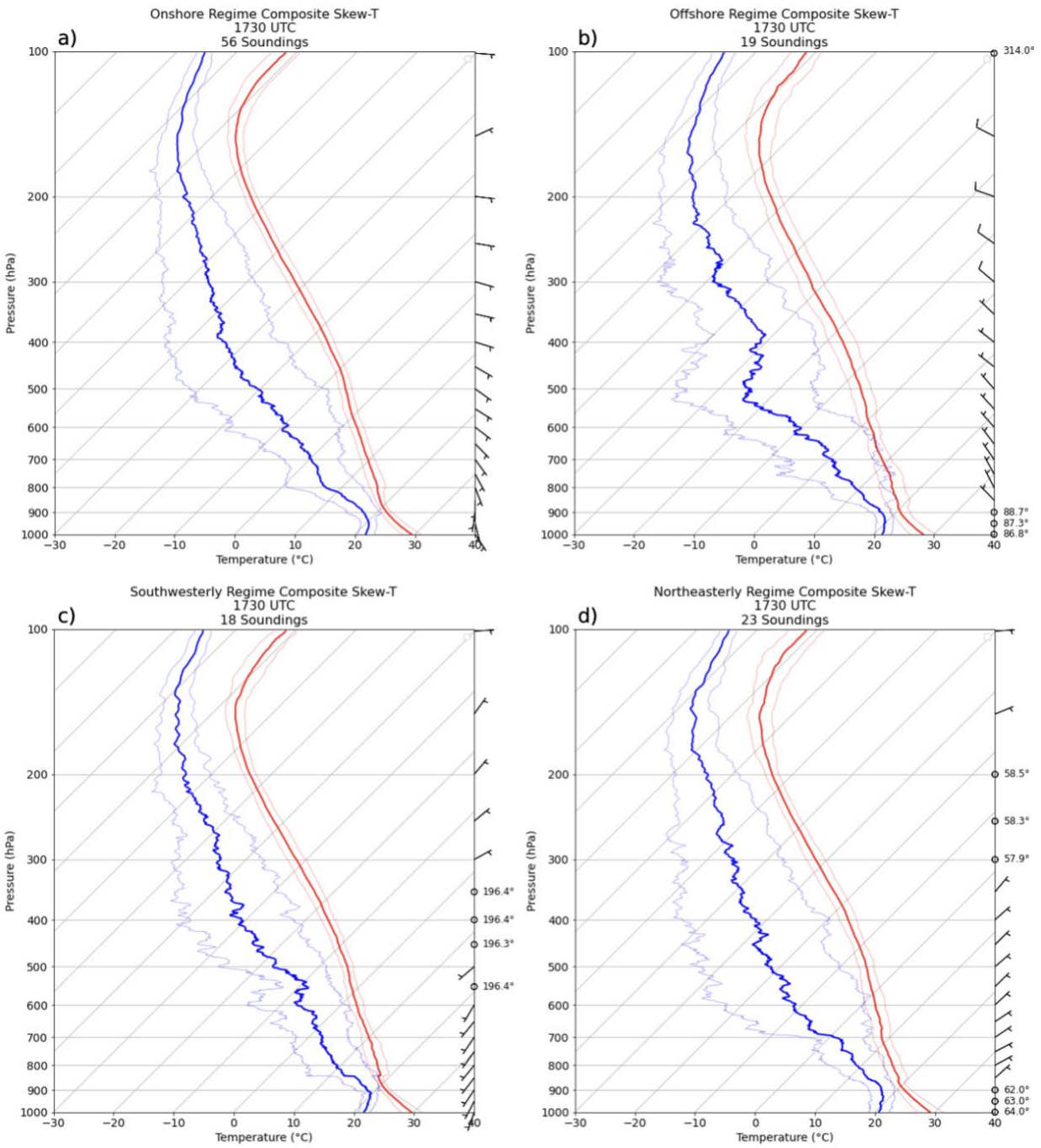


Fig. 2.7: Regional-based regime radiosonde composites for the onshore (a), offshore (b), southwesterly (c), and northeasterly (d) regimes. Thick lines denote composite mean values and thin lines represent +/- one standard deviation.

While the SOMs proved effective at identifying broader, synoptic scale patterns, their limitations in resolving Houston's local flow necessitated a more regionally tailored classification

approach. By shifting to an observed sounding-based approach, the regime definitions are now locally representative, providing a more robust foundation for investigating direct upper-level influences on PBL evolution and SB dynamics.

2.3 Sea Breeze Identification

A driving component of this work involves PBL responses to the SB. Given the varying meteorological conditions around the world and differing shapes of coastlines, a one-size-fits-all approach has not been found for SB identification. Common objective approaches to SB identification typically include finding points in surface time series data where large shifts from the background conditions occur simultaneously (e.g. rise in relative humidity, shift in wind direction, or drops in temperature). In Houston, the predominant wind direction during the summertime is southerly to southeasterly, which aligns with onshore flow. The SB is typically weaker and more difficult to identify when onshore flow conditions exist (Atkins and Wakimoto 1997; Gilliam et al. 2004). As a result, attempts of applying past SB objective identification methods proved to be too restrictive and severely limited the number of actual SB cases, as many thresholds required greater surface responses to the SB than what was observed (for more information on past SB identification methods see Sect. 4.1). For this work, a multistep approach was conducted for each day of the campaign to identify SB events. At each CUBIC location, analyses of the surface and ground-based remote sensing data were completed to identify periods in which at least 4 out of 5 of the following changes in atmospheric conditions occurred simultaneously:

1. Rapid rise in surface relative humidity,
2. Rapid drop in surface temperature,
3. Wind shift to southerly/southeasterly, coast-perpendicular flow,
4. Increase in low-level wind speed,
5. Identification of SB front via radar reflectivity scans.

Since the predominant flow was often southerly, wind shifts at SB passage could be minimal/undetectable using surface station data. Additionally, not all SBs result in fine line radar

reflectivity signatures, so a combination of multiple SB signatures is needed to flag a day as having a SB. Thus, the identification of SB cases used within was completed in a subjective manner, with a mix of qualitative (1, 2, 4) and quantitative (3, 5) metrics, without the application of an objectively driven algorithm. For every suspected SB case, further analysis is completed to ensure the detected changes are associated with a SB and not another mesoscale feature (e.g. not a thunderstorm outflow boundary from a nearby storm). An example of the multiple SB signatures is presented together in Fig. 2.8 for clarity.

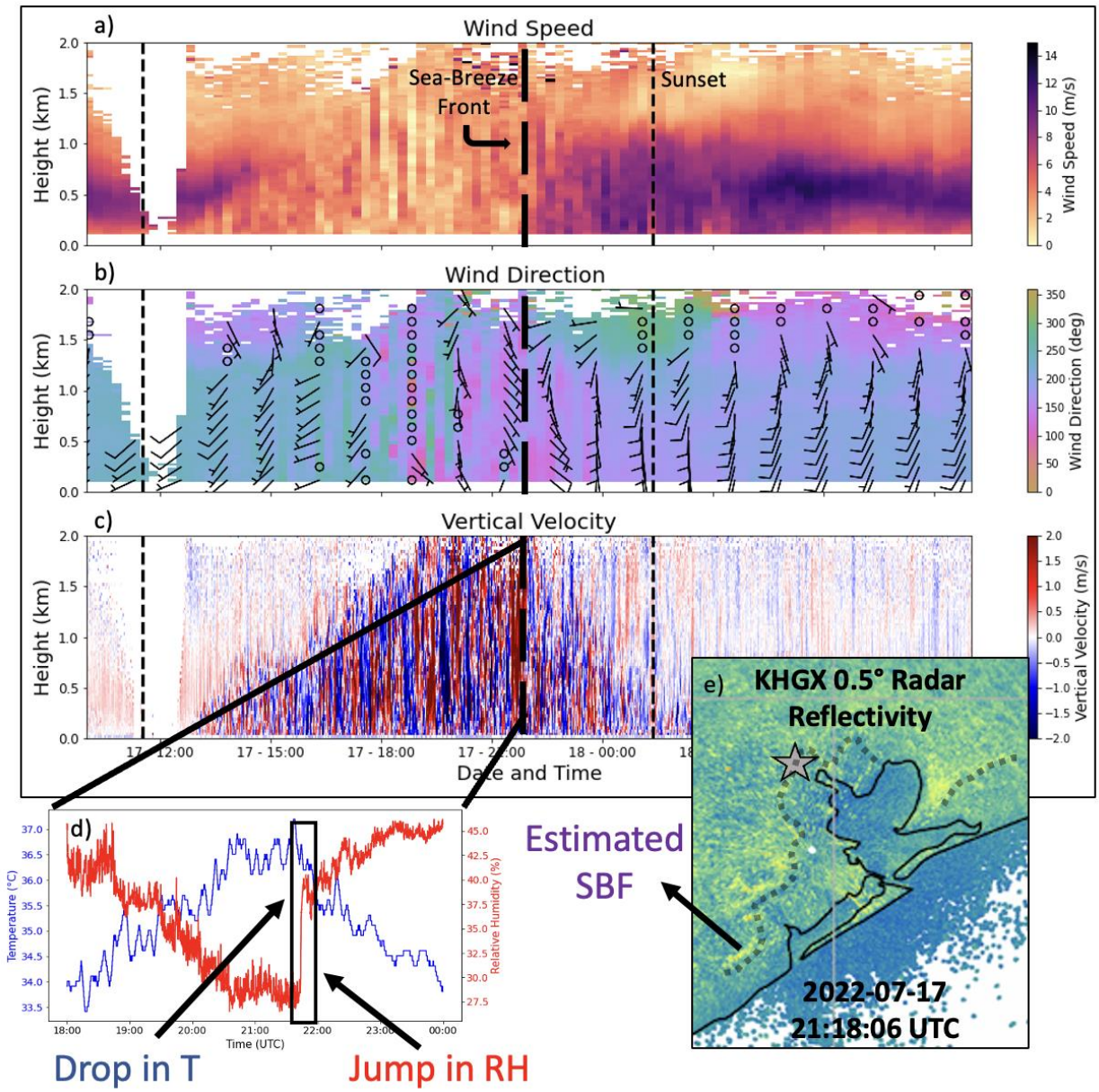


Fig. 2.8: Example of an identified SB case using CUBIC observations and KHGX radar reflectivity data at the urban location on 17 July 2022. Wind speed (a), wind direction and wind barbs (b), and vertical velocity (c) are shown in the main plot, with sunrise/sunset (thin black dashed lines) and SBF (thick black dashed line) times denoted. The smaller subplot shows surface meteorological tower data (d) consisting of temperature (blue), relative humidity (red), and pressure (green) with the SBF denoted by the arrows pointing within the black box. The insert on the lower right, shows the associated radar reflectivity data with the estimated SBF location (black dotted line) and urban site (gray star; e).

2.4 CUBIC Sea Breeze Statistics

To set the stage for future analyses, the CUBIC data are first examined to identify SB cases, noting whether the SB propagates through the city, the timing of the SB passage at each site, and the impacts of regional flow on SB occurrence and timing. This section also addresses question 1 from Sect. 1.3, which is to determine whether a critical land-sea temperature difference is needed for SB development in the Houston region.

After analyzing each day of the CUBIC campaign using the methods outlined in Sect. 2.4, a total of 52 days, or 41% of CUBIC dates, developed a SB in the Houston area. However, the number of days in which quality data are available for the 3 hours before and after SB passage is lower, at 43 cases. Additionally, there were 6 cases in which thermodynamic and kinematic signatures were present in the data that would be consistent with a SB passage, but it was impossible to rule out other factors due to complicated nearby convection. These cases, therefore, are not included in the following SB analyses. It is important to note that not all SB days exhibiting convection led to an inability to detect the SB, there are numerous cases in which convection occurs, but the SB is identified clearly and these cases are still used within the following analyses.

Upon examining the monthly frequency of SB days, there is evidence of a seasonal cycle in the SB occurrence throughout the summer and early fall, with June exhibiting the largest number of SB cases at 15 days (Fig. 2.9). This number decreases in July to 11 cases, has a minimum in August with only 6 cases, and then rises again in September to 11 cases. Statkewicz and Rappenglueck (2023) found the same trend in the quantity of SB days with the potential for rainfall in a 20+ year climatology of SBs in Houston. Their study applied a SB identification criterion consisting of a land-sea temperature change larger than 3°C, the u-component of the geostrophic wind larger than 3 ms^{-1} for onshore flow or less than 6 ms^{-1} for offshore flow, and an onshore wind direction for the time period 9 am to 3 pm local time. Interestingly, when using slightly different criteria (u_g <3 ms^{-1} for onshore or <11 ms^{-1} for offshore) to identify any SB day, they found Houston area SBs increase in frequency through the summer, peaking in August, before a large decrease in September, portraying the importance of selection criteria in SB results.

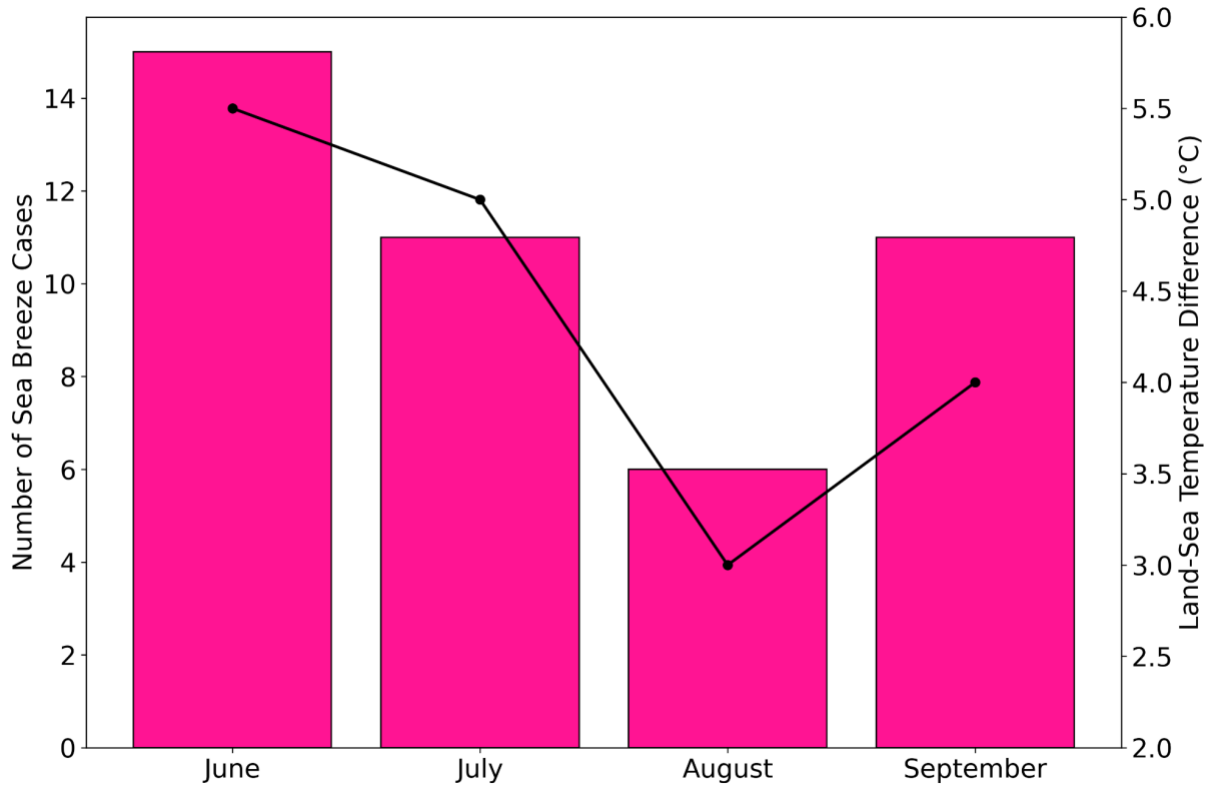


Fig. 2.9: Number of SB cases per month observed during CUBIC. Black line represents 1700-2100 UTC averaged monthly land-sea temperature differences.

In summer 2022, CUBIC SB monthly frequency correlates with the trends of the land-sea temperature differences (ΔT; black dots/line in Fig. 2.9). Daily temperature difference averages from 1700-2100 UTC were calculated between a buoy site off the Gulf coast (29.235°N, -94.410°W) and the urban location (29.9°N, -95.33°W). The relationship between the occurrence of SBs and positive land-sea temperature differences has been well documented in past literature, with a positive ΔT being a necessary prerequisite for SB development. In some locations, like the southern England coast, a ΔT of only 1°C is needed for SB development, whereas a greater ΔT is needed for far inland SB propagation in New England (Watts 1955; Miller and Keim 2003). During CUBIC, the ΔT is greatest in June, exceeding 5°C on average from 17-21 UTC, and at a minimum in August at approximately 3.0°C. Additionally, daily 1800 UTC temperature differences were calculated to investigate whether a critical ΔT is needed for SB development in Houston. The 1800 UTC time is chosen to ensure the PBL is well developed (> 5 hours after sunrise), and 1800 UTC is before the majority of SBs develop. The median ΔT on SB days is just below 6°C, while the

first and third interquartiles are 4.5°C and 7.2°C, respectively (Fig. 2.10). For non-SB days, the median is lower, at 4°C, with 1.5°C and 5.3°C first and third interquartile values. Not only do non-SB days have a greater interquartile range, indicating greater variability in the middle 50% of data, but these days also have longer 'whiskers' (maximum of 1.5 * IQR), which corresponds to a greater spread in values than those experienced in SB days. Nevertheless, in 98.2% of SB days, the ΔT is at least 3°C, which could be used as a threshold for future SB studies in the region, although it would need to be combined with other factors since there is a large overlap of ΔT values between SB and non-SB days (i.e., for 62.7% of non-SB days the ΔT at 1800 UTC was at least 3°C). Additionally, for 57.5% of the SB cases the temperature difference exceeded 5.5°C, while there are only 26.3% of non-SB cases where this threshold was met, indicating a generally larger land-sea temperature difference in SB cases. While past studies have used similar ΔT thresholds in their SB identification methods, it is not always clear why that threshold was chosen. The quantified SB cases exhibiting a ΔT of at least 3°C give important context to future studies applying ΔT thresholds as SB selection criteria in the Houston area.

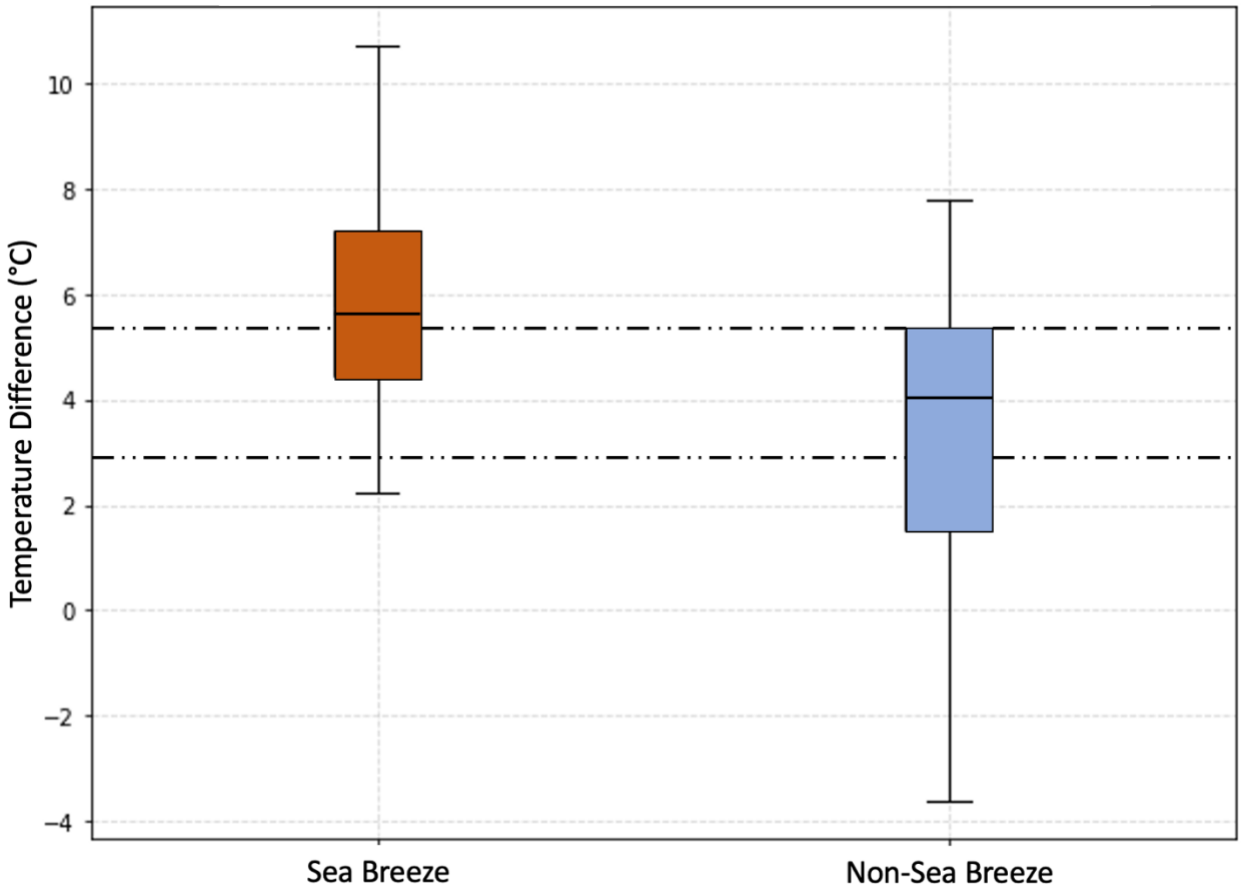


Fig. 2.10: Box and whisker plots comparing 1800 UTC land-sea temperature differences between SB (left) and non-SB (right) cases. Dot-dashed lines represent 3°C and 5.5°C temperature differences.

In addition to monthly SB frequency, the SB cases are further divided into monthly occurrence per regional regime, as defined in Sect. 2.3 above. The onshore regional regime accounts for the greatest number of total SBs, at 16 cases, but with a maximum number in June with 8 cases, then only 2-3 cases from July-September. There appears to be a pattern shift occurring in September, evident via a more uniform distribution of SB cases across regime types (Fig. 2.11). The shift in regional regime for the SB cases is likely related to the equatorward shift of the westerly jet stream and eastward shift of the semi-permanent Bermuda high pressure system as the seasons change (Higgins et al. 1997; Dima and Wallace 2003). Again, daily 1800 UTC ΔT is calculated to investigate the role of the land-sea temperature gradient under differing regional regimes (Fig. 2.12). Despite the differing regional flow, the median ΔT across regimes is similar, varying by only ~1°C from 5.2°C to 6.2°C, however, the distributions are different. The onshore

and southwesterly IQRs are nearly identical, with lower ranges than the offshore and northeasterly regimes (Fig. 2.12). The offshore regime also contains more outliers, evident via the longer whiskers. Contrary to past SB work by Grau et al. (2021) and Statkewicz and Rappenglueck (2023) that show a greater ΔT is necessary for SB development during offshore conditions, the offshore flow regime during CUBIC presents a lower median ΔT than the onshore regime. This could be an indication that the 700 hPa flow does not promote or negate a SB from developing or simply that the flow at this level does not correlate with the ΔT value, since past studies typically use flow closer to the ground.

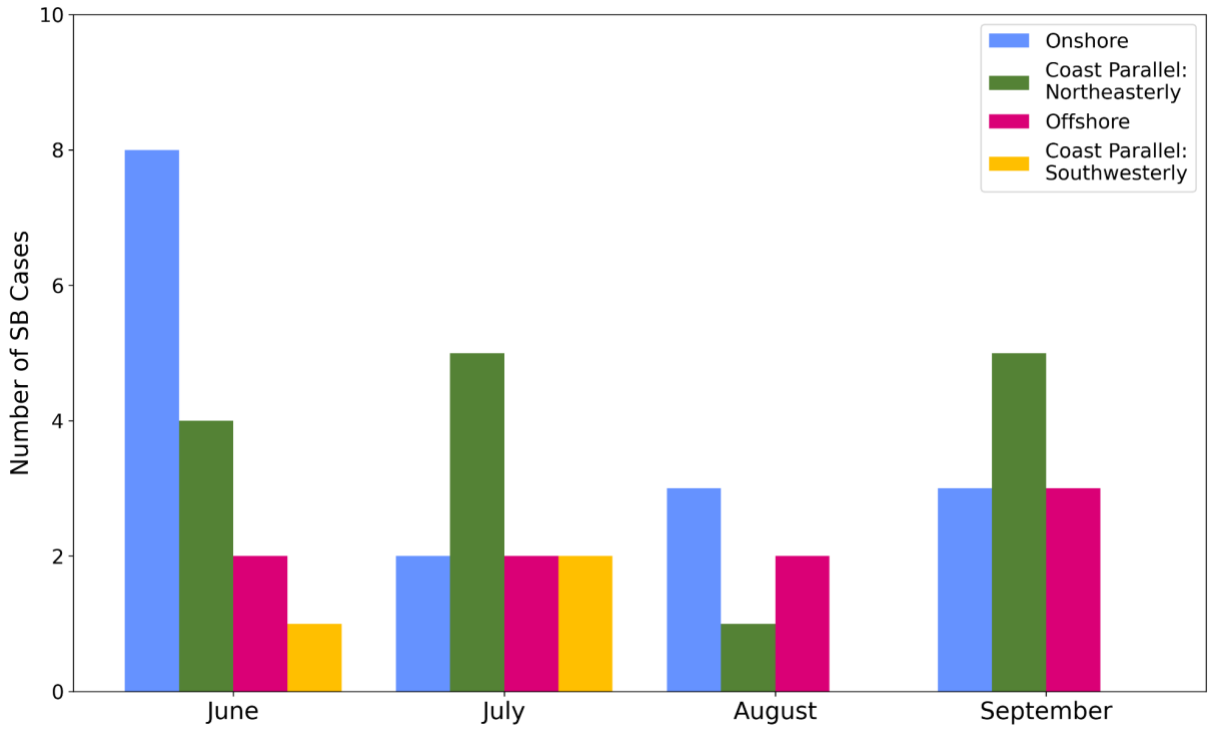


Fig. 2.11: CUBIC observed sea breeze cases divided by regional regime types per month.

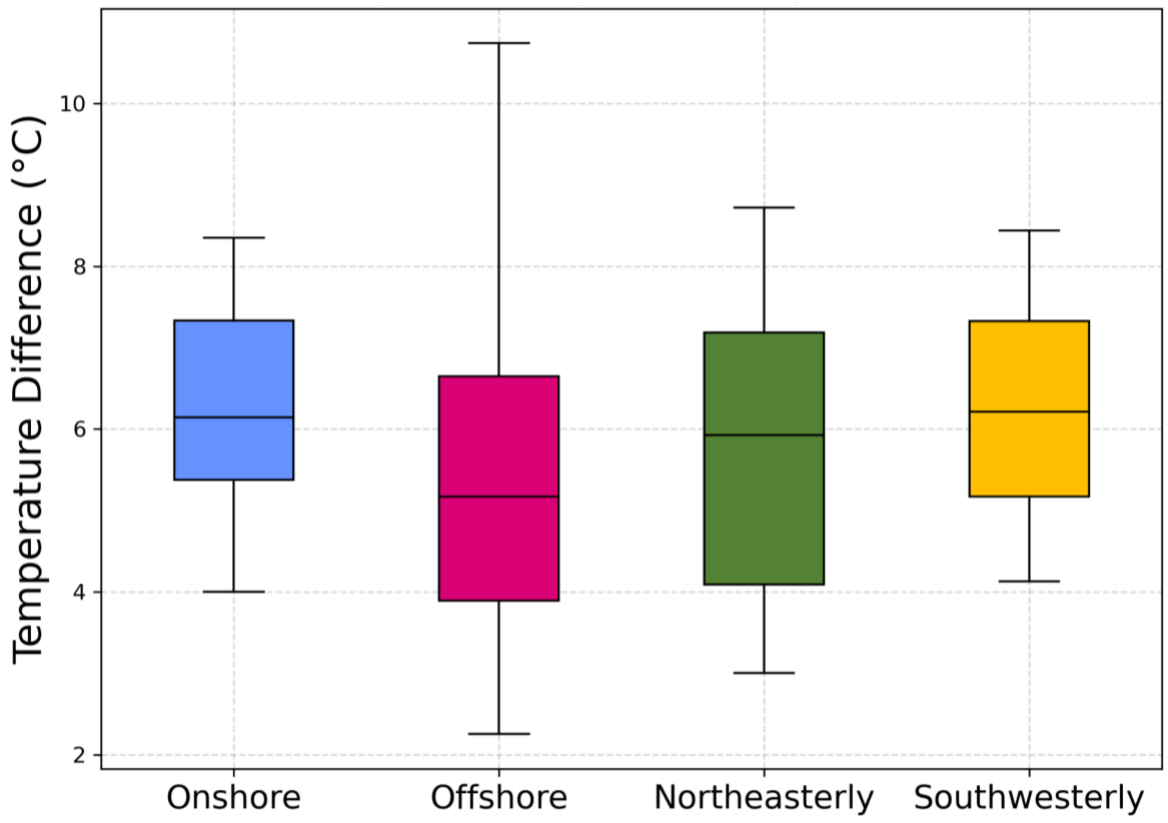


Fig. 2.12: Box and whisker plots comparing land-sea temperature differences on SB days based on regional regime types.

Given the ability to observe the SB from three points across the coastal-urban region, temporal trends of the SB can be examined, which can provide important information about the magnitude of SB modification across the coastal-urban environment. Fig. 2.13 shows the frequency of SB cases at 30-minute binned intervals for each of the three sites. Throughout the CUBIC campaign, the timing of SB onset at the coastal location could span from 1600-2330 UTC, with the majority of SBs taking place between the hours of 1730-1900 UTC. Fig. 2.13 also clearly shows the progression of the SB across the Houston domain, with the exurban site's average SB passage time between 2030-2200 UTC and the urban site experiencing a peak at 2200 UTC and a secondary timing peak at 2330 UTC. In cases where the SB propagates far enough inland to reach the urban location, the average time of propagation is just under 4 hours from the coastal site to the urban site (Fig. 2.14). There is a seasonal change in propagation time going into September, with SB cases propagating from the coastal site to the urban site faster than during the summer

months, although fewer SBs propagate far enough inland to reach the urban location. As a result of the varying SB arrival times, comparisons between SB and non-SB cases are difficult. For this reason, any SB versus non-SB case comparisons are completed using the full diurnal period to investigate general differences, as a SB-relative time axis is not easily achieved for non-SB cases.

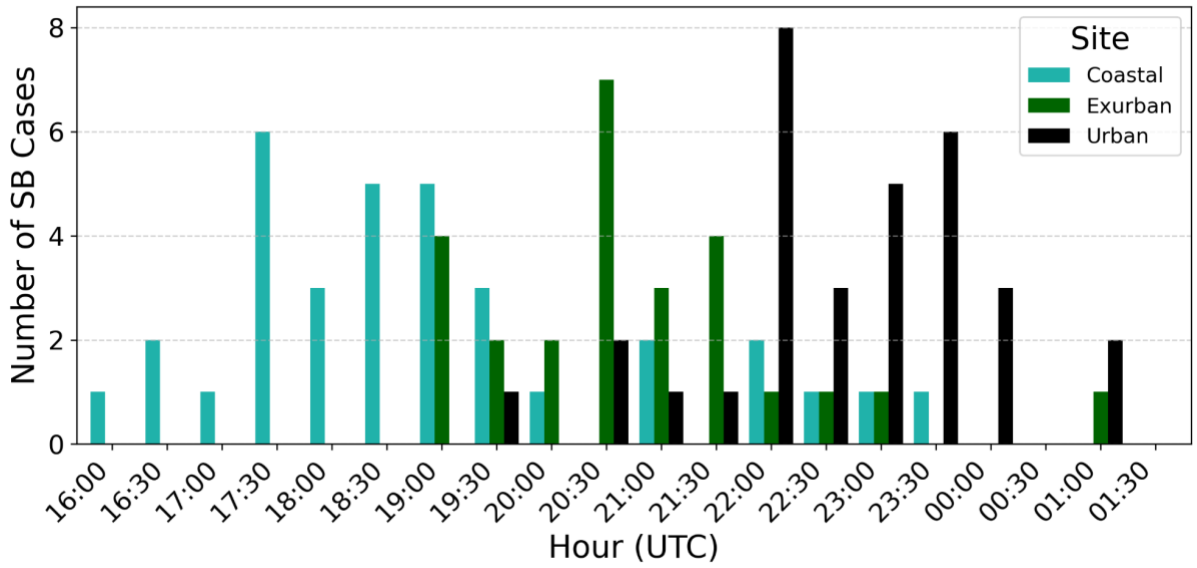


Fig. 2.13: SB passage times binned into 30 min intervals at the coastal (blue), exurban (green), and urban (black) CUBIC observation sites.

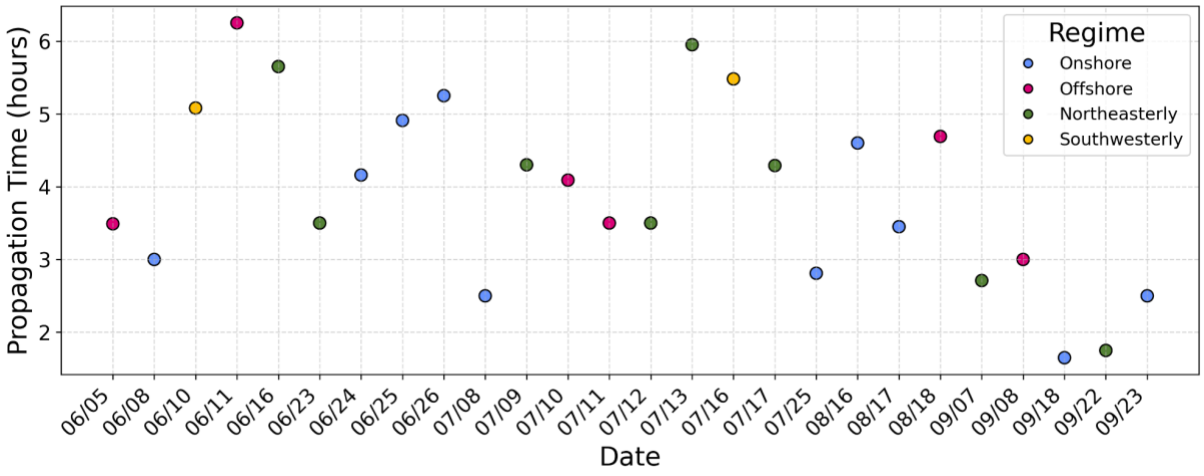


Fig. 2.14: SB propagation time from coastal location to urban site colored by regional flow regime.

To investigate temporal trends in SB timing throughout the campaign, the wide range of SB onset times and the clear seasonal patterns in SB occurrence are further examined by breaking down the timing by month (Fig. 2.15a,c,e). During the summer months (June, July, and August), the SB passage at the coastal location occurs before 2000 UTC, with most SBs passing between 1800-1900 UTC. However, in September, the SB occurs later in the afternoon, with most SBs observed between 2100-2200 UTC. While SB arrival times at the inland sites vary more than at the coastal location, there is a clear shift in SB passage time in September, again, likely related to the changing synoptic flow as the upper-level jet stream propagates southward with the changing seasons. As summer transitions to fall, the Hadley cell begins to shift south, with it the increased potential for increased jet stream undulations (Dima and Wallace 2003). SB onset does not appear to be dependent on regional flow regime, with no clear temporal trends amongst regimes, either at the coast or further inland at the urban site (Fig. 2.15b,d,f). Again, this is inconsistent with past work focused on near-surface synoptic flow, in which the SB onset occurs earlier when synoptic conditions are onshore than those with an offshore flow (Azorin-Molina and Chen 2009; Reddy et al. 2021; Fig. 2.15). Additionally, investigations of land-sea temperature differences and propagation time show no clear relationship when considering all cases together, with a Pearson correlation of r=0.37. However, when considering only the onshore regime cases the correlation is r=0.62, indicating a slight correlation between propagation time and temperature difference for these specific cases. Overall, these results suggest that while land-sea temperature differences are important for SB development, other forcings, such as cloud cover and surface roughness changes, play a role in propagation speed across the coastal-urban interface in cases occurring under offshore, northeasterly, or southwesterly conditions (Fig. 2.16).

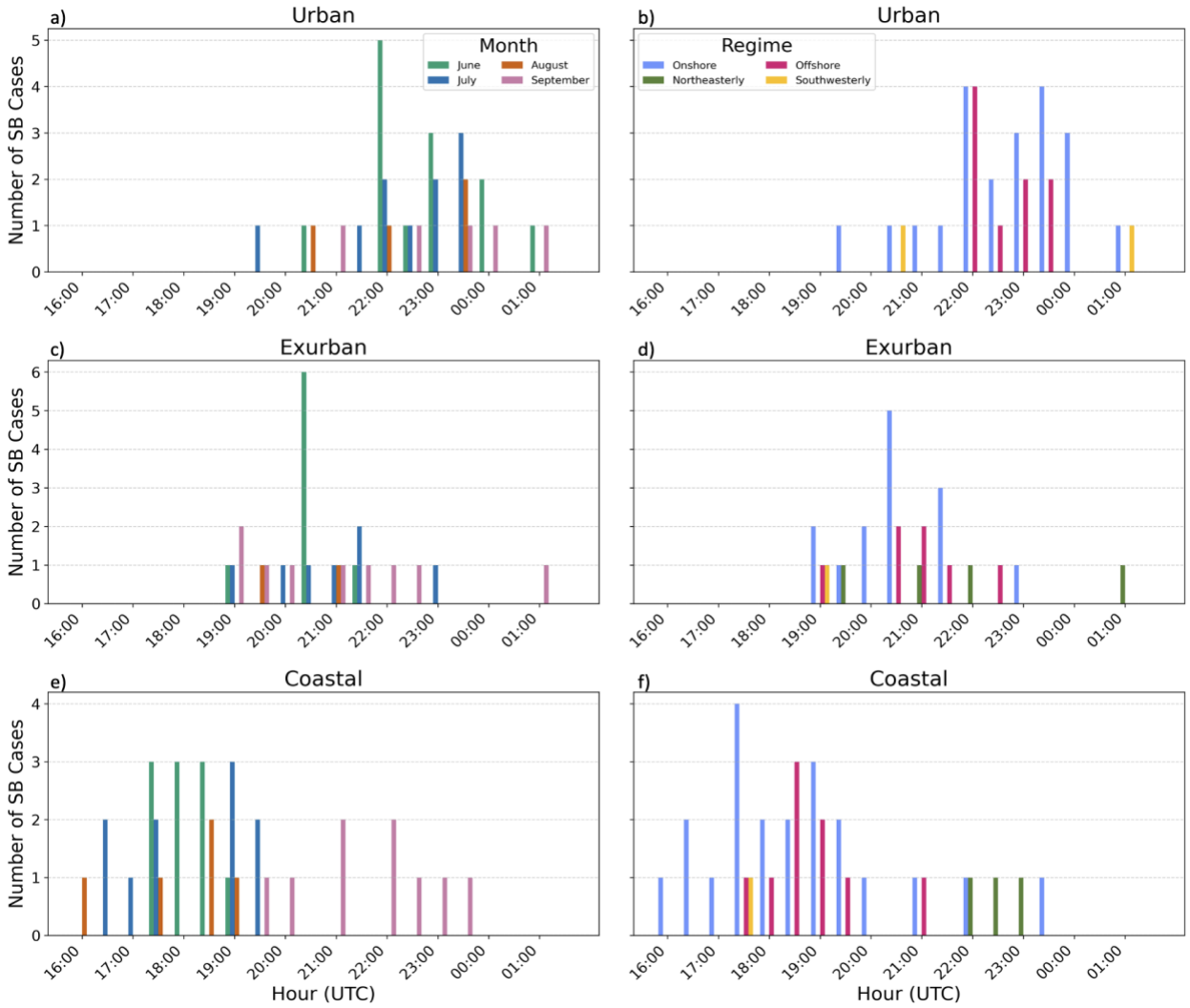


Fig. 2.15: SB passage times in 30 min bins for the Urban site (a, b), Exurban site (c, d), and Coastal site (e, f). Left column (a, c, e) colored by month; June (green), July (blue), August (orange), and September (pink). Right column (b, d, f) colored by regional flow regime; onshore (blue), offshore (pink), northeasterly (green), and southwesterly (gold).

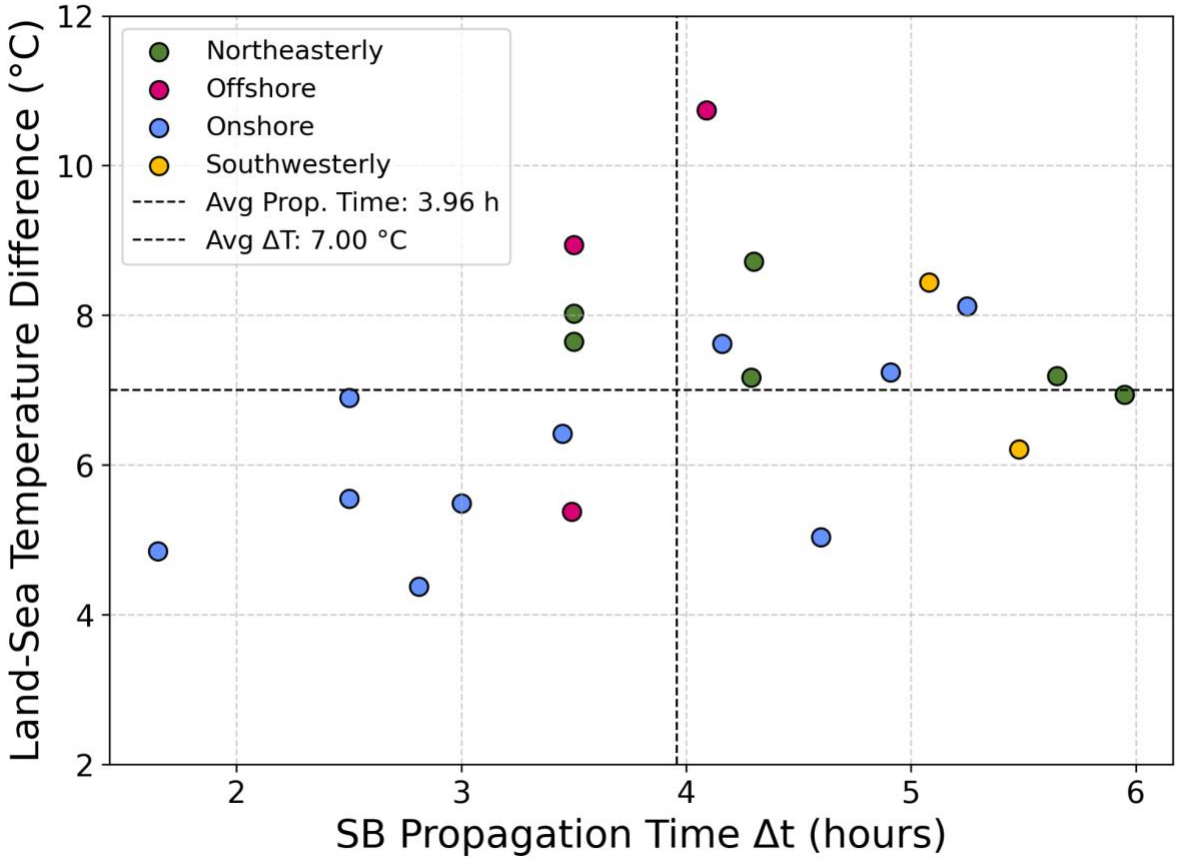


Fig. 2.16: SB propagation time versus land-sea temperature difference scatter plot colored by regional flow regime; onshore (blue), offshore (pink), northeasterly (green), and southwesterly (gold). Dashed lines denote averages.

The analyses and findings above establish the frequency, timing, propagation inland, and regional-scale influences on SB events during the CUBIC campaign, highlighting both seasonal variability and an unexpected minimal role of regional-scale flow in modulating SB onset. A total of 52 SB cases were identified, with 43 cases containing quality data in the several hours before and after SB passage. Of the SB cases, 98.2% occur when land-sea temperature differences are at least 3°C, establishing a threshold for future studies. There are signs of seasonal changes to the SB, with later onset times in September and propagation speeds 1-2 hours faster than the average 4-hour propagation. Investigations into regional flow regime effects on SB timing show no significant differences amongst regimes, suggesting that onset timing and propagation depend on additional mesoscale and seasonal forcings beyond ΔT or regional regime. These results provide

essential context for interpreting the influence of the SB on the lower atmosphere, as SB onset time and resultant PBL modifications can be different depending on which point throughout the diurnal cycle the SB passes over a site. In the chapters that follow, the focus shifts to examining the variability of PBL structures across the coastal-urban region.

Chapter 3

Spatial Variability in Coastal-Urban Planetary Boundary Layer Heights

3.1 Introduction

As mentioned in Ch. 1, the PBLH is an important parameter in boundary layer studies, bounding surface-influenced processes from the free atmosphere. The nocturnal PBL is typically shallow, on the order of tens to hundreds of meters, and distinguished by stable conditions, while the daytime convective boundary layer (CBL) is well-mixed, with turbulence leading to a much deeper PBL, often reaching a PBLH between 1000-3000 m. Spatial differences can occur across heterogeneous surfaces such as land and water interfaces, urban and rural areas, or regions with differing terrain. For example, the urban PBL can be hundreds of meters deeper than the PBL in surrounding rural locations due to increased buoyancy from greater surface temperatures and increased surface roughness (Pal et al. 2012; Fenner et al. 2024). While these synoptic to meso-α scale (200-1000 km) differences in PBLH across differing landscape environments are well documented, less is known about the spatial variability of PBLH within meso-β (20-200 km) to local scale regions, such as across coastal-urban environments. This chapter is motivated by the collection of observations that fill the current gap of available information and provide additional insight into smaller-scale variability within a coastal-urban environment.

Given the importance of PBLH in air quality and convection forecasting, numerous PBLH studies using a range of observational methods have taken place in and around the Houston-Galveston area, enhancing our knowledge of the complicated processes that take place in the region. A ceilometer-based climatology study was conducted to analyze the relationship between PBLH and ground-level ozone and found that peak afternoon PBLH was elevated for longer periods during spring and fall in days with high ozone (Haman et al. 2012). Another study leveraged aircraft-based observations (AMDAR and flight campaign data) and identified spatial variability in PBLH in Houston but highlighted the need for further validation of the AMDAR data in complex coastal-urban regions (Zhang et al. 2020). Nielsen-Gammon et al. (2008) performed a spatiotemporal mixed-layer height case study and found large spatial variations in estimated heights around the Houston area using multiple airborne remote sensing instruments. While these

studies have provided insight into PBLH for specific applications, they were often limited by data availability and instrument limitations, environmental conditions, short deployments, or were only conducted at a single point location. Although comparisons can be made between the different studies, there have been few studies focused on an observation-based investigation of PBLH spatial variability for an extended period, particularly within complex coastal-urban regions, where numerous processes can interact and affect the PBL evolution and local weather patterns in different ways, given the rapid changes to the surface across the domain.

Unfortunately, many past studies have been severely limited by the coarse spatial and temporal resolutions of the operational radiosonde network or targeted field campaign studies, hindering one's ability to understand the spatial heterogeneity of PBLH across a region and/or the full diurnal evolution of PBLH at a location. In many cases, investigators have to choose between a temporally or spatially focused deployment strategy but attempts to mitigate these limitations have been made by utilizing simultaneous observations or using other data sources such as reanalysis data. However, remote sensors are still only a point location measurement, limiting the spatial extent of knowledge unless multiple instruments are deployed throughout a region. These estimates often rely on a single observation parameter to determine the height (e.g., aerosol backscatter for Doppler lidars or derived temperature gradients from radiance observations with interferometers), which can lead to different estimations and therefore uncertainty in the accuracy of the estimated PBLH. Additionally, there are instrument limitations, such as the ability to sense through clouds, that may limit the capabilities of a single-instrument method of estimation (Duncan et. al. 2022). Although, these single-source estimation limitations can be partially mitigated by using collocated instruments whose measurements are then combined via fuzzy logic algorithms, one of which is used within and described in Sect. 3.2.1 (Smith and Carlin 2024).

The CUBIC dataset provides a unique view of the PBLH evolution and variability throughout a coastal-urban environment via three locations in the Houston-Galveston region. The overarching goal of this chapter is to investigate and quantify the spatial and temporal variability of PBLH within a coastal-urban environment by disentangling potential important processes and characteristics (i.e., synoptic flow, SB, temperature, turbulence) responsible for observed differences. Specifically, this chapter investigates how different processes alter the PBLH in terms of depth, timing, and morning/evening transition differences across the area. We hypothesize that substantial spatial heterogeneity in PBLH will exist across the coastal-urban interface, in part due

to urban influences on the PBL and seek to answer the second science question posed in the Chapter 1: What are the primary influences that affect the spatial PBLH diurnal evolution across the coastal-urban interface? The multiple deployment sites and continuous nature of the CUBIC data allow for observations of the full diurnal evolution of PBLH, as well as investigations of mesoscale spatial influences on PBLH variability.

3.2 Data Analysis Methods

3.2.1 Planetary Boundary Layer Height Algorithm

To estimate the PBLH, a fuzzy logic method is applied that combines thermodynamic and kinematic profiling data from each CUBIC platform. Fuzzy logic methods have been applied in a variety of atmospheric science applications, most extensively with radar products (Gourley et al. 2007; Yang et al. 2013; Bonin et al. 2018). In a fuzzy logic approach, input variables are related to an output characteristic via membership functions that range from 0 to 1. The membership functions are defined such that a 'measure of truth' is applied as opposed to a binary yes/no condition. For a set of input variables, membership values are aggregated via a weighted mean. That aggregate field of membership is used to estimate the output characteristics (i.e., PBLH in this instance). The method used here applies the algorithm developed by Smith and Carlin (2023), which uses a two-step approach to estimate PBLH. The first step uses measurements that show mixing is ongoing, which consists of turbulence estimates from the Doppler lidars in the form of calculated vertical velocity variance, σ_w. Additionally, the temperature inversion height is used to enhance the capabilities of the algorithm in the overnight and transition periods when PBL development is dominated by buoyancy-driven processes. The inputs (e.g. σ_w) are regridded onto a 10 m by 10 min grid via interpolation and then evaluated by the membership functions. This results in a 2-dimensional output (time/height) field consisting of values between 0 and 1 that represent the degree of membership within the PBL. The height at which the membership function first reaches 0.5 or below is flagged as the first-generation PBLH estimate. This choice ensures that the height estimate is still connected to the surface and represents the point where half of the inputs indicate that mixing is occurring (Bonin et al. 2018). The second step of the algorithm

includes measurement indicators that mixing has taken place. Specifically, profiles of signal-to-noise (SNR), SNR variance, *u* and *v*-components of wind, potential temperature, and water vapor mixing ratio are used. Each profile is passed through a Haar wavelet transform allowing for the detection of gradients. The membership functions used in the second step on the indicators are dynamic and defined based on the gradients identified, which differs from the static membership functions in the first step. After identification of the gradients, aggregates and the second-generation PBLH estimates are produced following the same procedure as the first-generation but allowing the first-generation estimates to constrain the second-generation estimates (i.e., second-generation PBLH must be within 25% of first-generation estimate). Using a triangle-weighted mean, the PBLH estimates are smoothed, and the smoothed outcome reflects the final estimate. This particular method has been shown to agree well with traditionally used radiosonde-based height estimation methods, with Pearson correlation values > 0.8. For complete details, please see (Smith and Carlin 2023). It is also important to note that this particular algorithm depends on Doppler lidar observations, so if Doppler lidar data is missing (e.g. rainy periods) the PBLH is not calculated for those times and thus continuous results will not be available for the days where these outages are present.

3.2.2 Composite Techniques

Composite analysis techniques have been a long-used method to characterize different meteorological variables of interest (i.e. temperature and wind speed) with long-duration datasets (Bonin et al. 2018; Chen et al. 2021; Zhang et al. 2024). The basis of compositing techniques is to create an averaged final product from data spanning a specific time frame or from within a specific environment. For example, high-temporal-resolution kinematic and thermodynamic profiler observations similar to those deployed in CUBIC have been composited to detect changes within the PBL on the order of minutes in past studies regarding lake breezes, severe convective environments, and bores (Wagner et al. 2008; Loveless et al. 2019; Wagner et al. 2022). Although data from a single summer will not fully encapsulate the range of annual variations, the nearly four-month dataset can serve to supplement our understanding of the PBLH in the Houston region by highlighting features of the PBLH in different land use locations and under different synoptic conditions often experienced during the summer.

Composites of PBLH are created here for each CUBIC site for the duration of the campaign. Days in which little data is available (i.e. excessive rainy periods or instrument issues) are removed from the composite dataset to ensure only quality data is included. Additionally, resulting composites only include data at a specific time if at least 85% of data is available for a given time (e.g. a count is kept for each time stamp and a threshold of 85% is used). Composites are also created for subsets of PBLH cases, including synoptic regimes and SB versus no SB cases. Additional composites are created in the same manner for other atmospheric variables such as potential temperature and vertical velocity variance.

3.3 Campaign-Duration Composites

To gain insight into general summertime heterogeneity of PBLH across the Houston area, Fig. 3.1a depicts the mean composite PBLH at each location encompassing the duration of the CUBIC campaign. While examining a parameter like PBLH, it is important to consider potential differences in data included in the composites. The number of days included in each composite varies across CUBIC sites. Beyond the case numbers, it is also important to consider any patterns in data availability. At the exurban site, data losses occurred during the midday, which is an important time to consider when studying PBLH evolution and trends. To understand how these data outages impact the composites, the analysis is repeated at all three sites, including only the same 44 days where full daytime observations are available at all 3 sites.

To assess how data availability influences the observed PBLH differences, comparison of individual sites using both the reduced (44-day) and full-record composites (urban = 104, exurban = 94, coastal = 64) are conducted. The urban location shows the greatest difference, with differences greater than 75 m from 2000-2300 UTC and maximum differences just over 200 m at 2100 UTC or 4pm local time (local time = UTC - 5; Fig. 3.1b). The exurban site has two peaks where PBLHs differ between the composites by more than 100 m at 1900 and 2130 UTC. These differences between the reduced and full-record PBLH composites are likely due to the limited data in the reduced-record composites that occur during hotter days when deeper PBLs can be expected (i.e. exclusion of hottest days). Still, given the generally small differences between the two composites, the full-record composites will be used throughout the remainder of the analyses to provide a more representative example of summertime PBLH through the Houston region.

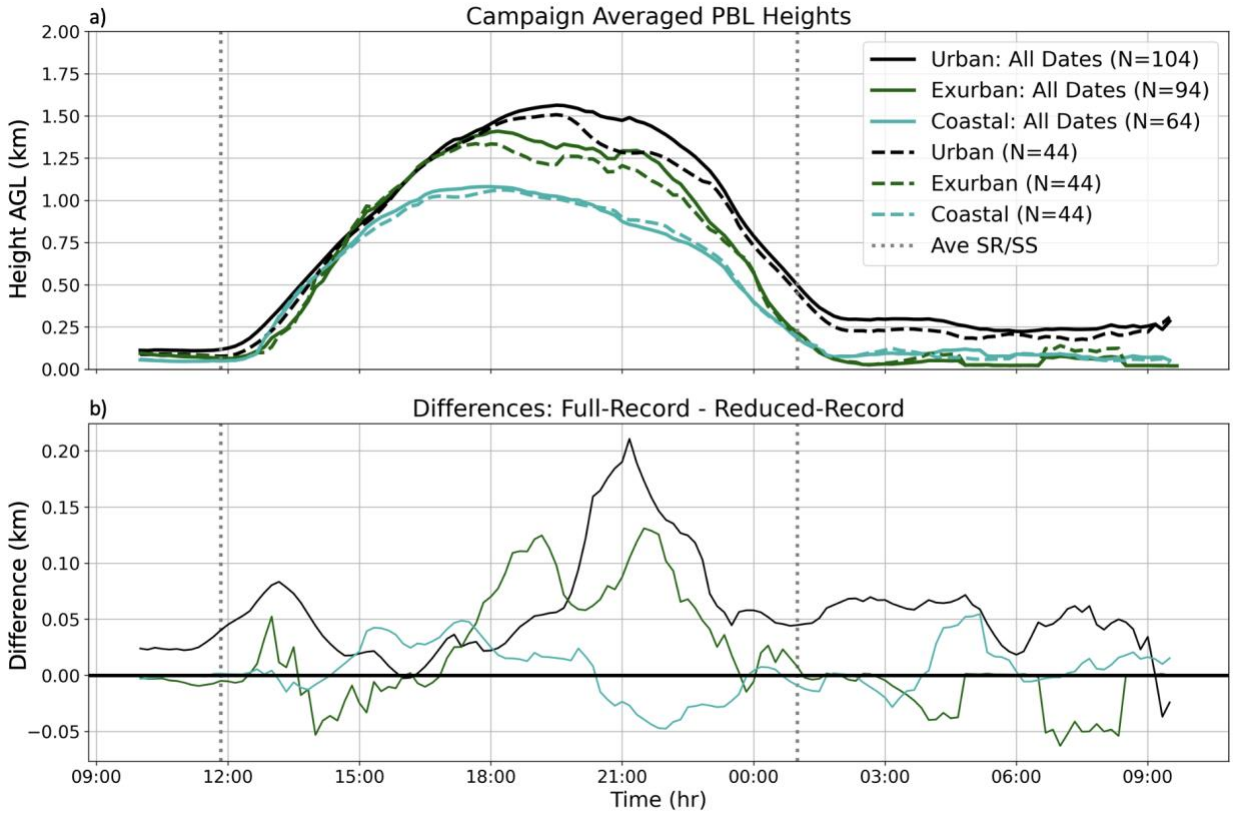


Fig. 3.1: a) Campaign averaged PBLH for the full records at each site (solid lines) and the reduced-record when data were available at all three sites (dashed lines). b) Difference in PBLH estimates between full-record and reduced-record composites. Grey dotted lines indicate campaign average sunrise and sunset times.

Beyond the impact of data availability, Fig. 3.1a also reveals notable spatial and temporal differences in PBLH across the region. For example, the time at which the maximum PBLH is reached varies by 1 hour and 50 minutes between the coastal and urban sites. Furthermore, the height magnitude also varies between sites by ~480 m. The time and height differences are likely influenced by a combination of factors including the UHI and the marine boundary layer. Cities can continue to warm as the day progresses and urban structures and surfaces continue to absorb solar radiation, leading to greater temperatures and resulting in deeper PBLs (Pal et al. 2012). Additionally, the influence of the marine boundary layer with the onshore flow acts to advect a cooler, more stable air mass inland, limiting the depth of the PBL in the region where the TIBL develops. At the urban site, which is located further inland than downtown Houston, enhanced surface warming and roughness over this city has altered the characteristics of TIBL and promoted deeper boundary layers. The CUBIC height differences are greater than a past study investigating PBLH differences in Paris and surrounding suburban and rural areas (Pal et al. 2012). In Paris,

PBLH differences were found to be ~185m between urban and rural areas, and only ~67 m between the city and suburbs. The coastal influences are likely responsible for the greater height differences when compared to the Pal et al. (2012) study, since marine boundary layers are generally shallower than those over land, and Paris does not lie directly on the coast like Houston. In CUBIC, the coastal site is only ~25 km from the coast, meaning the marine boundary layer has little time to be modified by the land surface/continental influences, resulting in a more pure marine impact by the marine boundary layer than further inland, where the marine boundary layer undergoes more modifications to its structure, in part due to the increased influence of the TIBL further from the coast. Near and within the city, additional IBLs form in response to changes of surface roughness and thermal surface properties, acting to further modulate the PBL at the intersection of the marine and continental boundary layers (Mestayer and Anquentin 1995). Potential temperature profiles from the inland sites occasionally show shallow (< 150 m) convectively unstable layers consistent with a TIBL and past works estimating the TIBL depth as a couple of hundred meters. (Arrillaga et al. 2016; Reddy et al. 2020).

To better understand the urban-rural contrasts observed in PBLH, particularly at the urban site, the examination of surface temperature structures associated with the UHI is undertaken. Fig. 3.2 below depicts the average 2 m temperatures for four different hours via the high spatial resolution (2.5 km) Unrestricted Mesoscale Analysis (URMA) data product (NOAA 2025). While surface temperature data is observed at several sites throughout Houston, the URMA product is used to provide a spatially continuous representation of the UHI. The URMA is created using three model analyses (3 km North American Mesoscale, 3 km High-Resolution Rapid Refresh, and 13 km Rapid Refresh), numerous observational data sources, including surface stations, radiosondes, and satellite data, and employs extensive data quality assurance checks. The urban site is within Houston's UHI dome (based on URMA temperature data; Fig. 3.2), despite not being located in the heart of downtown, providing further support for the increased convectively driven mixing and deeper PBLH. The exurban site, located on the outskirts of the city and upwind of the urban-modified air mass in 70.5% of CUBIC days (determined via SOM analyses), follows a similar diurnal PBLH evolution to the coastal site, which further corroborates the hypothesis that urban characteristics are heavily influencing the PBLH at the urban location.

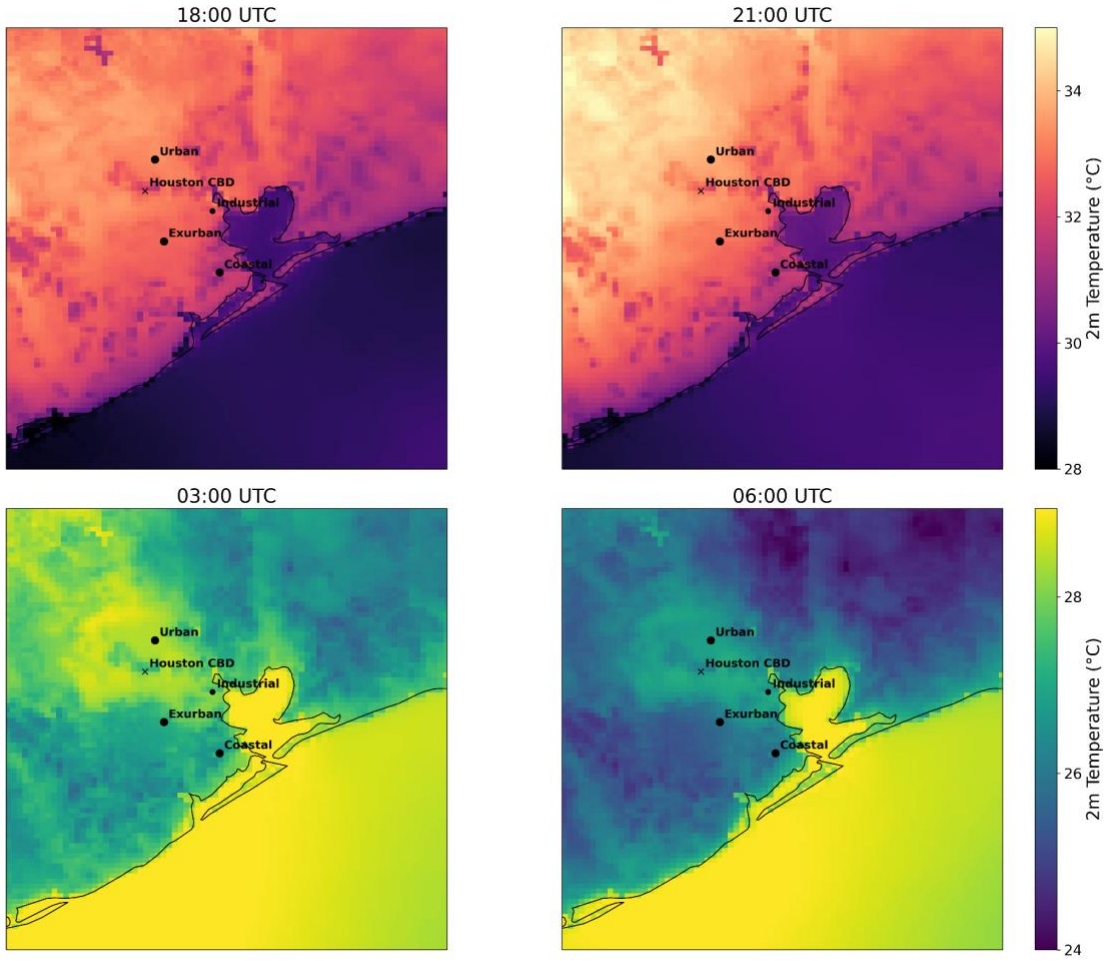


Fig. 3.2: Composites of 2-m surface temperature for the CUBIC campaign duration derived from the URMA reanalysis dataset. Top panels represent daytime temperatures at 1800 and 2100 UTC and bottom panels depict nighttime temperatures at 0300 and 0600 UTC. The observation locations of the three CUBIC sites and the ARM AMF site are shown along with the location of the central business district (CBD) of Houston.

In addition to the daytime influences of the UHI and marine layer, substantial differences in PBLH also emerge during the overnight hours. From 0200-0630 UTC, the urban nocturnal PBLH is approximately 250 m greater than the exurban and coastal locations. Through this time, the PBLH remains consistently elevated at the urban site, suggesting that mixing in the nocturnal boundary layer (NBL) does not collapse at the urban location. This finding is consistent with past evidence of greater PBLH in urban areas during the overnight period due to increased turbulence from warmer surface temperatures (e.g., Pal et al. 2012; Tsiringakis 2021). Overnight, cities can

release stored heat from buildings and pavement, leading to turbulent mixing from buoyancy that results in a deeper NBL than a traditional, purely stable NBL. Additionally, the radiative cooling is lessened in urban areas, leading to more unstable PBLs than the surrounding rural areas. The composite heights alone highlight important local modifications to the PBLH from the UHI and marine boundary layer, but are unable to provide insight into temporal PBLH trends throughout the campaign.

To investigate the temporal trends, violin plots (Fig. 3.3) and the calculated interquartile range (IQR; range between the 25th and 75th percentiles; Fig. 3.4) of PBLH at each site in three-hour intervals. The shape of the violins illustrates the probability of different PBLH estimates, while the lines correspond to the mean (black line) and median (orange line) values. Generally, the greatest variability in PBLH occurs during the late morning and afternoon hours when diurnally driven, buoyant turbulence is at its greatest. The height frequency between the urban and exurban locations are similar from 1500-2100 UTC, with only small increases in frequency around 400 m at 2100 UTC at the urban location (Fig. 3.3). These sites begin to deviate at 0000 UTC, approximately 1 hour prior to average sunset, where the exurban site has greater variability in the lower interquartile range than the urban site. Additionally, the coastal and exurban locations each show a distinct bimodal distribution at 0000 UTC, which is likely related to a combination of factors for the higher and lower PBLH peaks. The lower PBLH bimodal peak could be due to PBL collapse after SB arrival, the occurrence of localized rain showers leading to lower PBLH with limited recovery time prior to sunset, or reflective of faster surface cooling rates at these locations. Contrarily, the secondary PBLH bimodal peak is reflective of days in which clear skies and a more canonical PBL evolution is observed, leading to PBLH decreases after the 0000 UTC hour. After 0000 UTC, the urban PBLH is consistently greater than at the exurban and coastal locations, with greater spread (e.g., height of violins) throughout the overnight period. Given the prominent summertime UHI conditions that the urban site experiences, evident in Fig. 3.2, the greater PBLH and increased IQR in the overnight period (0300-0900 UTC) can be attributed to urban-induced modifications of the PBL. The coastal location exhibits a more uniform distribution of PBLH values at 1500 UTC than the inland locations, indicating a wider range of PBLHs at this time. From 1800-0000 UTC, the shape of the violins at the coastal site are similar to those at the urban and exurban sites, except the range between the lower and upper interquartile is smaller at the coastal location. Overnight, heights are more variable at the coastal location than at the exurban

site, but still confined below 250 m. This could, in part, be due to the difference in the scanning strategies between the coastal and exurban Doppler lidars that was discussed in Sect. 2.1. The sampling frequency was lower at the exurban site (every 20 s instead of every 1 s), meaning smaller-scale turbulence cannot be resolved at the exurban site. Visual comparisons of vertical velocity data from the coastal location shows turbulent motions below 250 m that are not present at the exurban site. The differences may also be driven by the locations themselves, with the coastal site experiencing marine influences that could potentially drive the greater overnight PBLH. The violin plot analyses depict the variability that is included in the campaign PBLH composites in Fig. 3.1 and indicate a large range of PBLHs throughout the campaign, with greater than 1500 m spread during the afternoon hours. Given this variability, further analyses are needed to understand the drivers responsible for the array of PBLH results at each given site.

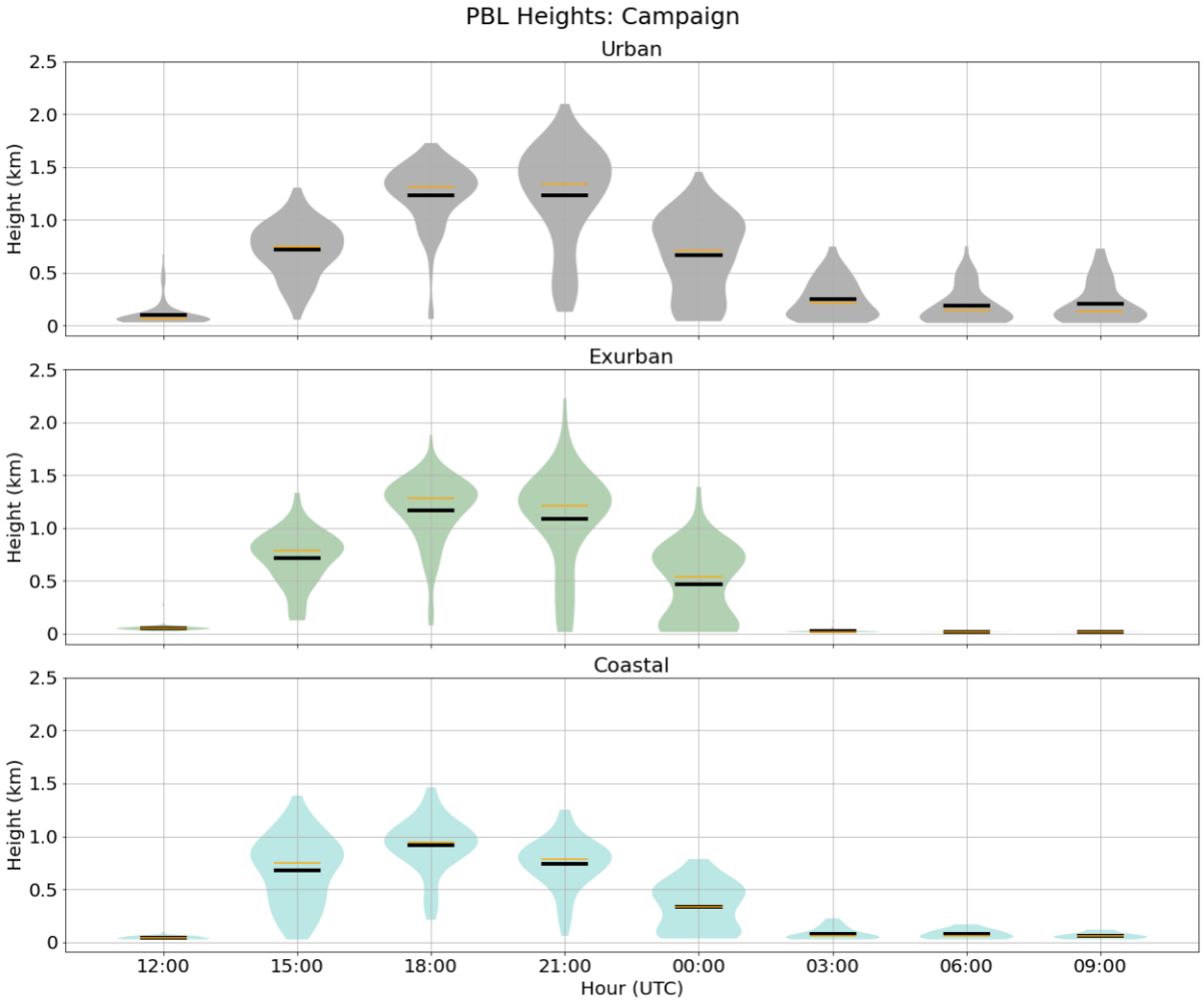


Fig. 3.3: Campaign averaged PBLH violin plots every 3 hours from 1200-0900 UTC. Thick black line indicates value mean, while thin orange line indicates the median.

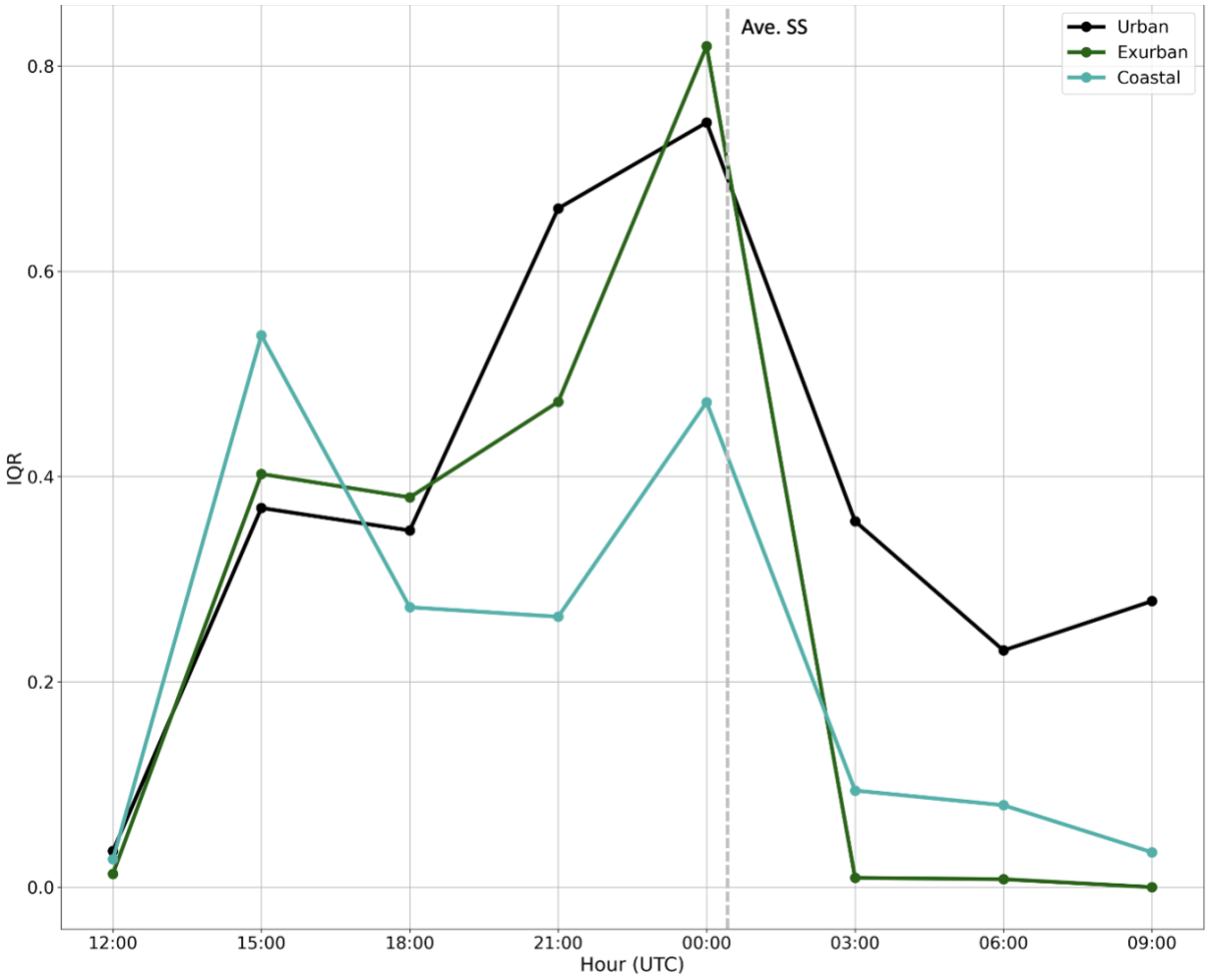


Fig. 3.4: IQR for each site every 3 hours from 1200-0900 UTC. Grey dashed line indicates campaign average sunset time.

3.4 Regional Flow Influences

Past PBLH research has shown diurnal and seasonal variations in the PBLH; however, there is limited research into how the diurnal evolution of PBLH differs under different regional regimes within the same season (Liu and Liang 2010; Seidel et al. 2010; Banks et al. 2015; Jiang et al. 2021). To address this knowledge gap and begin the investigation into important processes responsible for the observed PBLH variability, the CUBIC dates are sorted into four specific regional regimes using the sounding technique described in Sect. 2.3 above. The flow regimes represent differing advected air masses, particularly the onshore and offshore regimes. Given the temperature and moisture differences of the land surfaces between the continental land surface to the northwest and the Gulf to the southeast of Houston, it is hypothesized that the PBL evolution

and any SB events that take place within these contrasting regional flow regimes would be quite different. For example, under offshore regional flow conditions, the advected air mass from over land would be warmer and drier than with onshore regimes, which could result in greater PBLH via buoyant mixing.

The PBLH composites show only a few substantial differences throughout the diurnal evolution (Fig. 3.5). Individual site comparisons show little difference in maximum PBLH between regional regimes. Counterintuitively, the onshore and offshore regimes are similar in maximum height despite their different air mass source regions. There is evidence at the exurban location, via the +/- 1 standard deviation shading, of comparatively larger variability in the PBLH for the northeasterly regime. The exurban location is likely experiencing urban effects under this regime due to the advection of industrial/city air to the north-northeast of the site (Fig. 2.7d). The LCZ classification for the area to the northeast of the exurban site along the Houston ship channel is characterized as heavy industry and is an area with concentrated petrochemical refineries (Fig. 2.1). Given the northeasterly wind flow, the influences of the petrochemical refineries (e.g. increased aerosol content) and urban characteristics (e.g. warmer temperatures) would be advected over the exurban site, corresponding to increased spread just after 2100 UTC. While the average for this regime is not higher than others, the standard deviation does shed light on increased variability, making this an important finding since a higher PBLH leads to a greater volume available for pollutant dispersion in the area and could influence local air pollution forecasts.

Beyond the maximum PBLH values, the regional regime influences the rate at which the PBL develops and decays. Regional flow influences are shown to have the greatest impact during the morning and evening transition periods, when differences in PBL growth and decay rates differ between the regional regimes. The greatest regional influence during the morning transition occurs at the coastal site, where each regime shows a distinct growth pattern, with the southwesterly regime showing the quickest PBL growth, reaching a maximum PBLH just over 1000 m at ~1500 UTC. Meanwhile, the offshore regime's averaged PBLH is only 500 m by 1500 UTC, growing at the slowest rate out of the regimes. Future studies could be conducted to identify the reasons for these differences, including the employment of additional data sources, such as cloud cover or numerical studies. While the exurban site shows little difference in growth rates across regimes, the urban location follows a similar pattern as the coast, with the southwesterly regime growing most rapidly and the offshore the slowest. During the evening transition, the onshore and

northeasterly regimes exhibit similar decay rates at all three sites, evident via their similar slopes. The exurban site exhibits the greatest differences in the evening transition, with the offshore and northeasterly regime showing a faster collapse of the PBL compared to the onshore and southwesterly regime that more gradually decays throughout the evening. Each site reaches a relatively stable nighttime PBLH for each regime at about 0200 UTC (~1 hour after sunset), with exurban and coastal heights between 50-100 m and approximately 250 m at the urban location. It is important to note that the overnight jumps in PBLH shown at the coast and exurban sites are heavily influenced by outflow boundaries from nearby convection that led to increases in vertical velocity variance and resultant deeper PBL.

Taken together, these results suggest that while the general diurnal structure of PBLH remains relatively consistent across regional regimes, important deviations still emerge, particularly during transitional periods of the day. While this analysis only consists of one summer in Houston, the distribution of the regimes across the campaign allows for insight into a wide range of effects from regional regimes on the PBLH. Since the CUBIC regimes aligned with the climatological regime patterns, there is confidence that the results are representative of a typical summertime PBLH in the Houston region. Overall, the differences in PBLH are larger when comparing the three different sites than the differences observed for different regional regimes. Thus, the primary factors for the observed heterogeneity and variability in PBLH are likely due to local and smaller-scale processes occurring across the coastal Houston region.

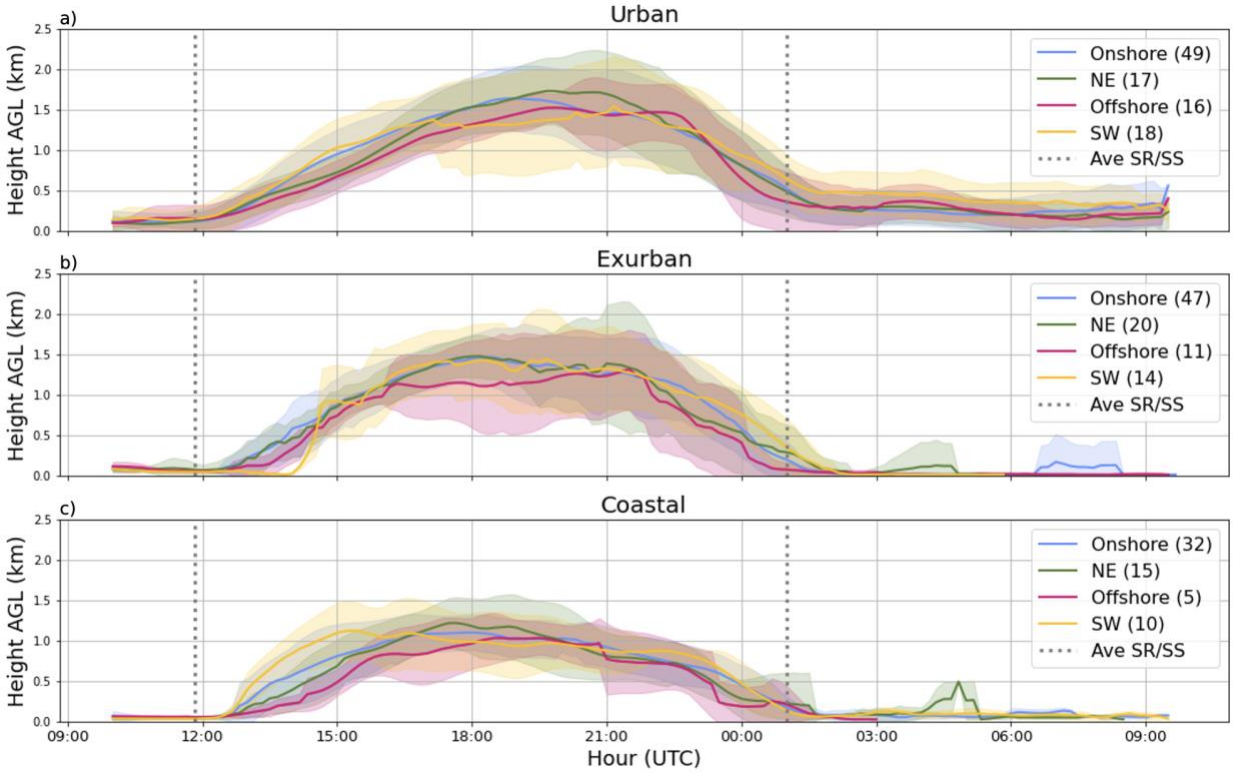


Fig. 3.5: Campaign averaged PBLH at the urban site (a), exurban site (b), and coastal site (c) for onshore (blue), northeasterly (green), offshore (pink), and southwesterly (gold) regional regimes.

3.5 Sea Breeze vs. Non-Sea Breeze Planetary Boundary Layer Heights

Given Houston's proximity to the Gulf, the summertime SB is a common, mesoscale phenomenon that influences PBL dynamics and thermodynamics and thus is hypothesized to account for a large portion of the PBLH variability in the campaign composites from Sect. 3.3. SB PBLH composites are created in which all observed SB cases at a given site are averaged together for the full diurnal period. As was seen in Sect. 2.4, the timing of the SB passage varied throughout the campaign from site to site, but also temporally at each location. The SB onset was earliest at the coastal location, on average ~1830 UTC (1:30 pm LT), but anywhere from 1600-2330 UTC. The SB would then pass the exurban site anytime between 1900-0100 UTC, but typically around ~2100 UTC (4:00 pm LT). Finally, if the SB propagated to the urban location, it would reach the site by ~2300 UTC (6:00 pm LT) or at any time between 1930-0100 UTC. Thus, the pre-SB PBL conditions for each site vary, with the inland locations experiencing no SB effects until the mid to late afternoon, while at the coastal location pre-SB conditions are constrained to morning hours.

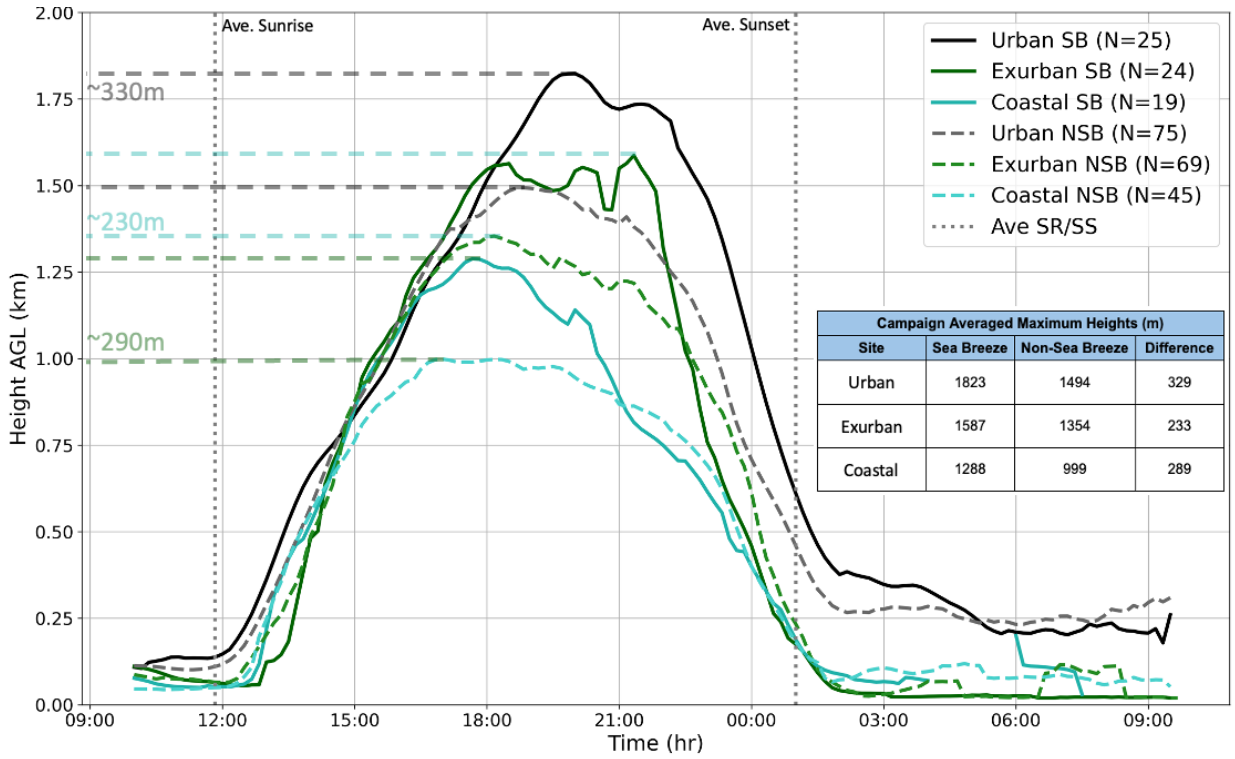
Spatial differences between sites in SB and non-SB cases are consistent with those in the full composites, with deeper PBLs at the urban location and shallower PBLs at the coastal and exurban sites (Fig. 3.6).

Composite PBLHs for SB days are greater than for non-SB days at each of the three sites, with the greatest differences occurring at the urban and coastal locations (Fig. 3.6). SB cases at the urban location result in a maximum PBLH ~330 m greater than days that do not experience a SB. At the coastal location, the difference between SB and non-SB cases is ~290 m, while the exurban site has the smallest increase in maximum heights at ~230 m. However, the afternoon PBLH values at the exurban location may underestimate true maxima due to missing data on the hottest campaign days. While deeper PBLs on SB days may initially seem counterintuitive, as the SB typically results in a stagnation or decrease in PBLH, these results suggest that the SB is more likely to happen on days on which deeper PBLs develop. The SB is more likely to initiate on days with a greater land-sea temperature difference, corresponding to days with stronger surface heating and deeper PBLs. Additionally, the time of the maximum PBLH corresponds well with the average SB onset timing at each site, indicating the pre-SB conditions are typically representative of well-developed PBLs before any SB modifications to the PBLH.

Contrary to the synoptic regime investigation, the morning and evening transition periods indicate minimal differences in growth and decay rates between SB and non-SB cases. The lack of a difference in the morning is not surprising, given that the SB does not form and propagate inland until the early afternoon and therefore would not lead to changes in the morning transition. The evening transitions are slightly different between the two types of cases, with the exurban and coastal locations indicating greater initial PBLH decay rates on SB days. This is likely due to SB effects on the PBL, with the onshore advection of cooler marine air often leading to clearer skies behind the SBF, more radiative loss in the early evening causing decreased heights, and a more abrupt evening transition.

During the overnight period, exurban and coastal PBLH show negligible differences between the two types of cases, but the urban site has some small differences. SB cases result in PBLH ~150-200 m greater in the early overnight period from 0200-0500 UTC. The heights slowly decay after 0200 UTC in SB cases, eventually becoming shallower than non-SB cases by 0530 UTC. In non-SB events, the urban PBLH evolution shows steady heights of ~250 m throughout the entirety of the overnight period. This consistent behavior in non-SB cases could potentially

lead to more accurate air quality forecasts, as a nearly constant PBLH (evident in single case PBLH reviews, not shown) would equate to a consistent volume available for pollutants to be trapped near the surface.



Campaign Averaged Maximum Heights (m)			
Site	Sea Breeze	Non-Sea Breeze	Difference
Urban	1823	1494	329
Exurban	1587	1354	233
Coastal	1288	999	289

Fig. 3.6: PBLH composites for SB (solid lines) and non-SB (dashed) days. The vertical dotted lines correspond to the campaign average sunrise and sunset times. The table insert lists the average maximum heights for each type of case and the corresponding differences. Additional horizontal dashed lines help denote height differences between cases.

3.6 Sea Breeze vs. Non-Sea Breeze Thermodynamic and Kinematic Characteristics

Given the hundreds of meters difference in PBL heights between SB and non-SB cases at each site, this section further investigates the thermodynamic and kinematic characteristics of the PBL to identify what parameters are responsible for the difference in PBLH. While different meteorological factors can influence when the maximum PBLH is reached on any given day (e.g., outflow boundaries, cloud cover), a relative time reference allows comparison between the two types of cases. Analyses here center on the time that the maximum PBLH occurs and show the 3 hours before and after that time. While the majority of SB cases result in stagnated or declining

PBLH after the SB passage, there are a number of cases at the coastal location where the maximum PBLH is not coincident with SB passage. With the earlier SB onset (~1800 UTC or 1pm local time) at the coast the PBL could recover and deepen in the several hours following SB passage and prior to the onset of the evening transition.

Figure 3.7a shows the 100-200 m layer-averaged potential temperature for SB and non-SB cases at each of the three locations. The urban location exhibits temperatures approximately 2.5 K warmer on SB days, while there is less of a difference (< 2 K) in temperatures between the case types at the exurban and coastal locations. At the coastal location, there are slightly higher temperatures (~ 1 K) in the 1-1.5 hours before the maximum PBLH is reached on SB days compared to non-SB days. At the exurban location, the temperature differences leading up to the maximum PBLH are minimal but increase in the 3 hours following the maximum. The greater temperature difference at the urban location relative to the exurban and coastal sites results in a deeper PBL because of increased buoyant mixing due to the warmer temperatures, consistent with observational and numerical modeling findings from Paris, Berlin, and Seoul (Pal et al. 2012; Ryu and Baik 2013; Fenner et al. 2024).

Wind speed differences between SB and non-SB cases also contribute to PBLH variability. Each site exhibits 1-3 ms^{-1} weaker wind speed in SB cases, particularly in the hour leading up to the maximum PBLH (Fig. 3.7b). The combination of warmer temperatures and weaker horizontal winds leads to a greater vertical velocity variance on SB days due to increased buoyancy-driven turbulence (Fig. 3.8). Larger vertical velocity variance within the PBL corresponds to greater turbulent mixing, which leads to deeper PBLs, consistent with our PBLH results. In Figure 3.8 below, the composited vertical velocity variance profiles for 4 hours throughout the middle of the afternoon for SB and non-SB cases are shown. Results indicate greater turbulent mixing on SB days compared to non-SB days, with stronger mixing in the lowest kilometer of the atmosphere in SB cases. The enhanced vertical velocity variance within the lowest kilometer likely corresponds to the depth of the SB, which will be investigated further in the next chapter. Again, the urban location exhibits the greatest difference between the two types of cases, suggesting that urban factors are influencing this location. The combination of warmer temperatures, lower wind speed, and greater vertical velocity variance all coincide with increased PBLH on SB days compared to days that SBs do not form.

These results highlight the mesoscale conditions under which SBs are most prevalent, with distinct differences in pre-SB PBL conditions for SB days that are reflective of different regional forcings that make the formation of a SB more likely. When greater temperatures are present over land, the land-sea temperature difference will be increased, leading to a greater pressure gradient force and density gradient, and raising the likelihood of SB development. Additionally, past research has shown that the SB is more likely to develop under weaker horizontal wind speed conditions (Grau et al. 2021; Wang et al. 2022). Understanding these differing mesoscale conditions is important in understanding how they modulate PBL development and their direct and indirect implications for air quality forecasting and pollution dispersion.

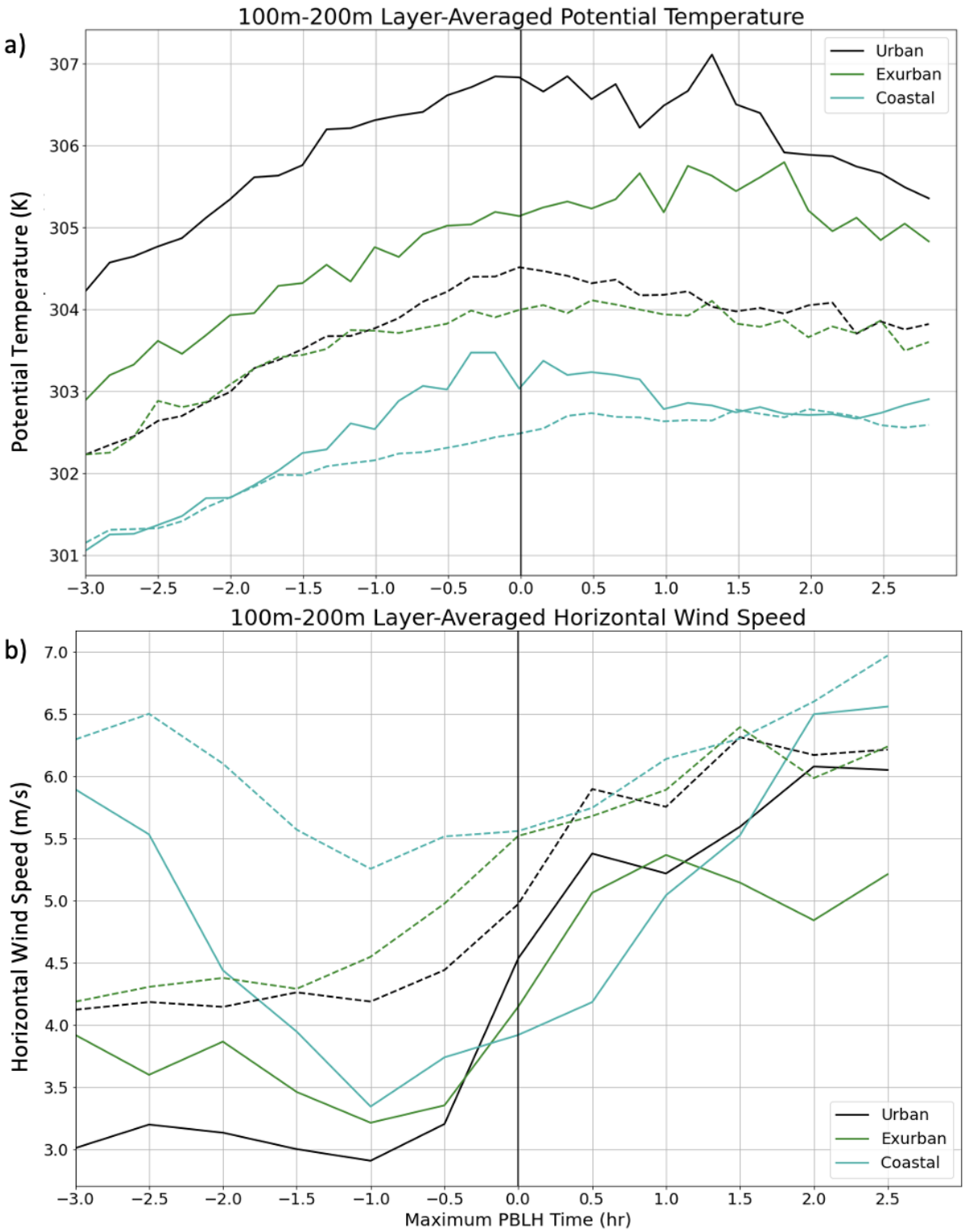


Fig. 3.7: Maximum PBLH time-relative thermodynamic (a) and kinematic (b) 100-200 m layer-averaged time series for 3 hours before and after maximum PBLH time for SB days (Solid lines) and non-SB days (dashed lines). The vertical lines represent the time of maximum PBLH.

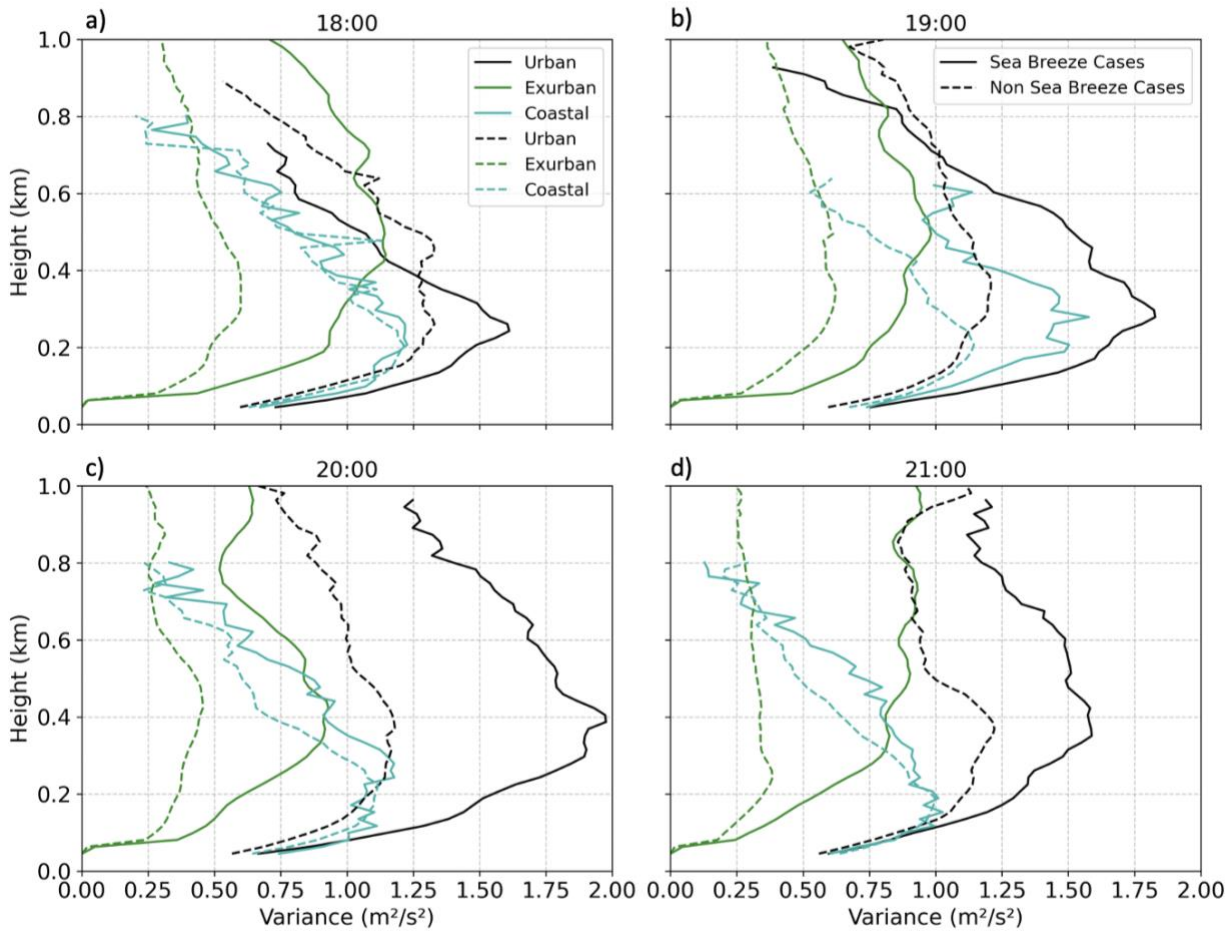


Fig. 3.8: Vertical velocity variance comparisons at a) 1800 UTC, b) 1900 UTC, c) 2000 UTC, and d) 2100 UTC for each location for SB (solid lines) and non-SB (dashed lines) days.

3.7 Summary and Conclusions

This chapter characterizes the spatial heterogeneity and temporal variability of PBLH across a coastal-urban area using high-temporal resolution ground-based remote sensing observations collected during the CUBIC field campaign in the Houston-Galveston region. Three mobile boundary layer profiling units were deployed throughout Houston to sample differing PBL environments, each equipped with thermodynamic and kinematic instruments capable of sampling continuously and through the depth of the PBL. The analyses within this chapter leverage a multi-instrument fuzzy logic PBLH estimation algorithm, enabling a robust evaluation of diurnal and summer-season PBLH evolution across the coastal-exurban-urban domain.

The results demonstrate substantial spatial heterogeneity in PBLH across the coastal-urban interface, driven primarily by mesoscale influences such as the local SB circulation and UHI

effects. During the day, the urban site exhibits PBLH values ~480 m higher than the coastal location, with the timing of maximum PBLH occurring nearly two hours later due to sustained surface heating associated with urban land cover. In the overnight period, the nocturnal PBLH at the urban site remains elevated relative to the coastal and exurban sites by up to 250 m, consistent with persistent turbulent mixing caused by the UHI effect. These findings reinforce the notion that even within a relatively small spatial domain, sharp contrasts in surface characteristics can lead to meaningful differences in boundary layer structure.

Analyses were conducted to determine important processes and characteristics responsible for the observed PBLH spatial heterogeneity. Regional-scale flow regimes revealed limited influence on the maximum PBLH. However, regime-dependent differences in PBL growth and decay rates during the morning and evening transition periods were evident, suggesting regional forcing-dependent interactions with local land-atmosphere coupling processes may be taking place. In contrast, SB events were shown to take place on days with deeper PBLs across all sites when compared to non-SB cases, indicating a more likely SB occurrence when deeper PBLs are present. On average, SB cases were associated with a maximum PBLH ~280 m higher than non-SB cases, with the urban location exhibiting the greatest difference of ~330 m and the exurban location showing the least at ~230 m. Composited thermodynamic and kinematic data indicate that SB days are associated with elevated low-level potential temperatures, suppressed horizontal wind speeds, and enhanced vertical velocity variance, all indicative of increased buoyant and mechanical mixing conducive to deeper PBL development. These findings highlight the importance of the SB and UHI as key modulators of daytime PBL dynamics in coastal-urban regions.

Building on the evidence that the SB forms on days with distinctly different PBL conditions, the next chapter delves deeper into how SB events modify PBL thermodynamics and kinematics across the Houston region. While this chapter established that PBLH varies across the coastal-urban environment and between SB and non-SB days, with the most pronounced effects observed over urban surfaces, important questions remain about how much the SB can impact the PBL and whether intraseasonal variability in regional flow is responsible for distinctive SB modifications.

The results presented in this chapter underscore the critical role of mesoscale processes, particularly the SB and UHI, in shaping PBL structures across the coastal-urban environment. The

observed spatial variability in PBLH, both diurnally and across sites, highlights the sensitivity of PBL dynamics to surface heterogeneity and mesoscale circulations. While synoptic-scale flow regimes exhibited limited influence on daily maximum PBLH, their modulation of morning and even transition patterns suggest a more nuanced role in land-atmosphere interactions. Furthermore, the differing PBL responses across sites point to complex, site-specific interactions between synoptic forcing, surface characteristics, and mesoscale circulations. These findings motivate a deeper investigation into the mechanisms in which SB events modify the thermodynamic and kinematic structures of the PBL, especially under varying synoptic conditions. The next chapter builds on this foundation by isolating the SB impacts on the PBL, with a focus on intraseasonal variability in synoptic flow and associated PBL responses to SB passages.

Chapter 4

Sea Breeze Effects on Planetary Boundary Layer Evolution

4.1 Introduction

As discussed in Sect. 2.2, an important goal of the CUBIC campaign was to improve the understanding of the PBL structure in the Houston region where coastal and urban effects alter the canonical PBL evolution depicted in Fig. 1.1. Specifically, we wanted to explore the hypothesis that SB interactions affect the environment and result in spatially and temporally variable flow. Given that SBs are common in coastal regions, an understanding of their modifications to the PBL is crucial for forecasting purposes and enhancing our knowledge of mesoscale interactions and PBL processes. The previous chapter explored general meteorological conditions and PBL characteristics, with an emphasis on PBLH, throughout the CUBIC campaign. Analyses showed substantial PBL characteristic differences spatially across Houston, the result of mesoscale influences like the SB and UHI. SB days occur more frequently when the pre-SB conditions are warmer and calmer than non-SB days. In this chapter, SB characteristics and modifications to the PBL are explored. The regional flow classification system from just above the PBL (700 hPa or ~3000 m AGL), introduced in Ch. 2, is applied to investigate the possible interconnections between boundary layer processes and mid-level flow. While the SB is a mesoscale, PBL process, this chapter explores the possible impacts lower tropospheric flow can have on the mesoscale SB circulation, hypothesizing that flow above the PBL can impact how the PBL responds to a SB passage.

This science chapter is further motivated by the need to understand the full, well-rounded picture of warm-season SB effects on the PBL throughout the Houston region. In past coastal breeze research, the use of specific thresholds to identify SB cases includes parameters like wind shifts of a certain degree (offshore flow to onshore flow), temperature drops greater than a certain amount, or relative humidity increases. For example, Wagner et al. (2022) classified Lake Michigan lake breeze events requiring a reversal in the *u*-component of the zonal wind from an offshore to onshore flow, an abrupt drop in surface temperature, a decrease in mixed layer height, and no rain within 3 hours of the wind shift. Some work prescribes strict thresholds, like 30° wind

shifts or at least a 3°C positive temperature difference between inland and coastal temperatures in order for a coastal breeze to be identified (Arrillaga et al. 2016; Hughes and Vernon 2018). However, the specific criteria and thresholds have traditionally been tailored to the specific area of the study. While these methods allow for objective SB identification, applying pre-defined thresholds can lead to missed SBs – perhaps many – when non-canonical or weak SB cases occur. Given the predominant wind direction (Fig. 2.1) over the Houston area during the day in the summertime (southerly) and the orientation of the coast (southwest → northeast), initial testing applying traditional, surface parameter-based thresholds to identify SB cases resulted in an inaccurate number of SB cases that do not reflect the true frequency of SB occurrence. Initial testing included 5 cases in which onshore flow before the SB was present and a clear SB radar signature was visible. In the testing, the automated algorithm did not flag these cases, which motivated the development of a holistic identification method for this work. It is expected that SB cases occurring during onshore boundary layer flow condition will result in subtle changes to boundary layer characteristics, making them harder to detect using conventional criteria developed for more canonical SB cases. In particular, this chapter aims to quantify the full range of SB modifications to the PBL and investigate the influence of regional flow regimes on the magnitude of thermodynamic and kinematic changes to the PBL following the passage of the SBF. It is hypothesized that SBs in the Houston area, including non-canonical and weakly forced events, produce measurable modification to the PBL structure that may be dependent on the synoptic environment of passage. Exploring methods that go beyond traditional detection thresholds will enable a comprehensive characterization of the full spectrum of SB events.

The following analyses will first examine two CUBIC SB cases that occur in opposing regional flow regimes to investigate the spatial evolution of the SB and how it modifies the PBL across the coastal-urban environment. The insights gathered from the case study comparisons are then compared with composite analyses to determine whether the PBL responses to the SB are systematically dependent on the regional regime. This chapter, therefore, addresses the third science question outlined in Sect. 1.3: What is the influence of lower tropospheric regional flow in the PBL response to SB passage?

4.2 Sea Breeze Case Comparison: Onshore vs. Offshore

In this section, two SB cases are evaluated: an onshore and offshore SB case which occurred on 17 August and 11 July, respectively. These specific cases were chosen for two main reasons: data availability around SB passage and similar SB passage times at each site, allowing for a comparison between SBs at comparable periods throughout the diurnal cycle. While the kinematic observations at the exurban site are limited around the time of the SB passage due to high temperatures causing the Doppler lidar to shut down (see Sect. 2.1, Fig. 2.2), there are no other significant data gaps at the SB time at any site for either case. The case comparison shows how the cases propagate from the coastal site to the urban site and how the thermodynamic and kinematic responses to the SB differ across the Houston domain. Specific questions are also investigated, such as: are the kinematic responses to the SB different between sites or cases? Is the thermodynamic response consistent between sites or cases? How does the spatial evolution of the SB differ between the cases? In each case, the SB does propagate through the domain to the urban location. The SB propagation time for the onshore case spanned approximately 3 hrs and 50 mins, with SB onset at the coastal location at 1847 UTC (1:47 pm), the exurban location by 2100 UTC (4:00 pm), and reaching the urban site by 2235 UTC (5:35 pm). In the offshore case, the SB propagation time from the coast to the urban site was slightly faster, taking 3 hrs and 30 mins, with passage times at 1930 UTC (2:30 pm), 2130 UTC (4:30 pm), and 2300 UTC (6:00 pm) at the coastal, exurban, and urban sites, respectively. Interestingly, the land-sea temperature difference between the two cases is greater than 2°C despite the similar propagation speeds, with the onshore case at 6.4°C and the offshore case at 8.9°C. Also, the land-sea temperature difference in the offshore case is over 3.5°C greater than the average offshore land-sea temperature difference. Generally, past work has shown that offshore flow leads to a slower propagation speed because of the opposing flow, but the greater temperature difference in the offshore case is likely what drives the 20 minute faster propagation speed, following past literature that uses land-sea temperature differences to determine SB strength (Miller and Keim 2003 ; Igel et al. 2018).

Given the findings from Ch. 3 of distinct pre-SB PBL conditions, the following analyses begin with an examination of the hours prior to SB passage, then move into investigations of the PBL kinematic and thermodynamic responses to the SB, and finally discuss the overall differences between the two regional regime type SB cases. Figs. 4.1-4.3 show the full diurnal period for each case from 1000-1000 UTC (5:00 am-5:00 am) at each of the three observing locations. The SB

passage time is indicated in each figure, as well as distinct breaks in the aerosol layers overnight and indications of elevated wind speeds overnight analogous to nocturnal low-level jets (i.e., low-level wind maximum; Li and Chen, 1998), clearly depicting an array of physical phenomena important to this particular region. During the early morning from 1000-1530 UTC, several hours prior to SB passage, the two cases both indicate southwesterly PBL winds at each site, veering to a more westerly direction within the growing PBL after sunrise (Figs. 4.1-4.3). These near-surface wind directions differ from their upper-level flow, in which the 700 hPa flow is southerly (onshore) and northwesterly (offshore) by 1500 UTC. Despite the contradictory upper-level flow, the early morning PBL wind directions are quite similar, with only a slightly more westerly component to the flow in the onshore case.

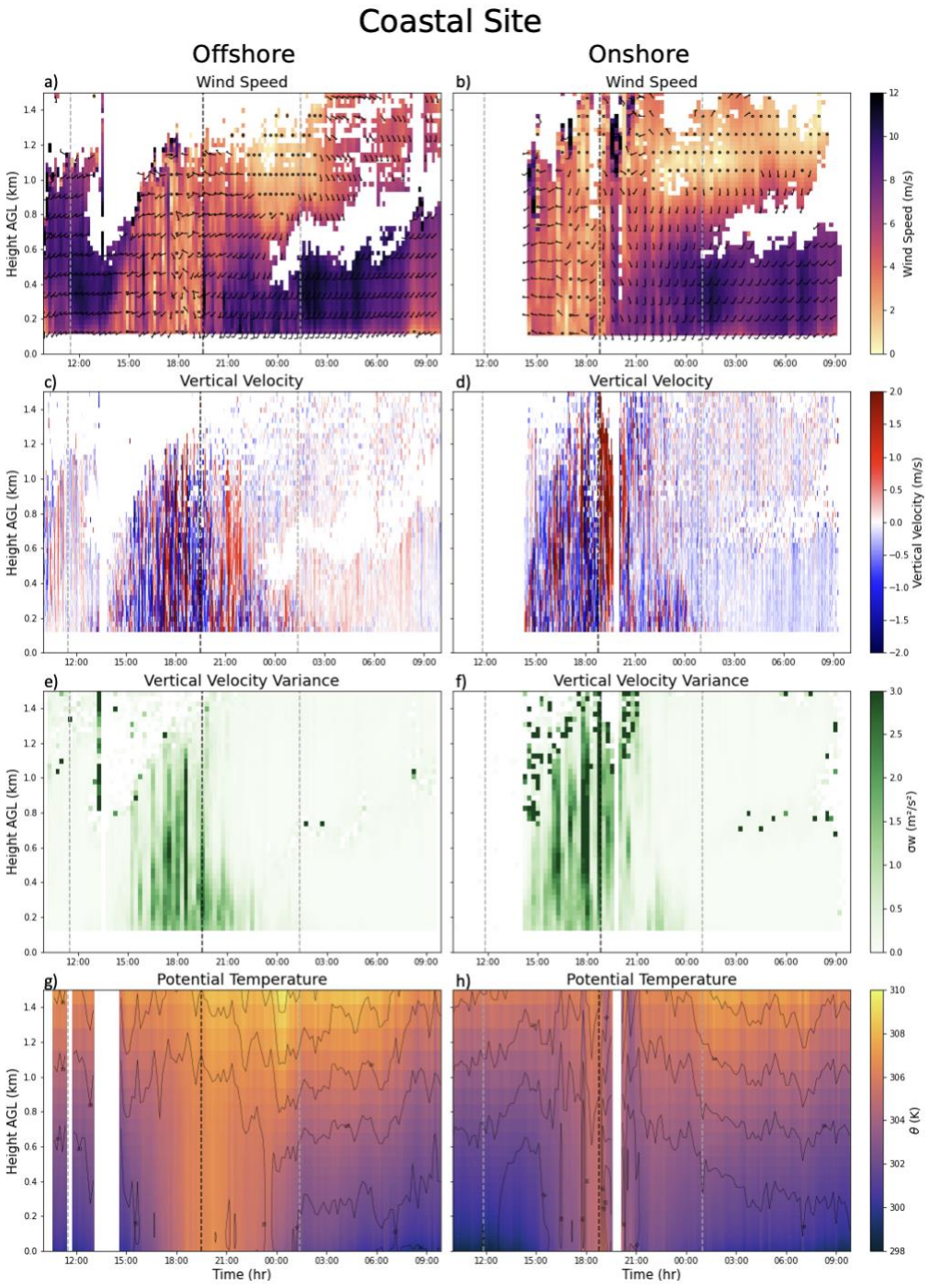


Fig. 4.1: Time-height wind speed and wind barbs (a,b), instantaneous vertical velocity (c,d), vertical velocity variance (e,f), and potential temperature (filled contours) and water vapor mixing ratio (black contours; g,h) at the coastal location from 1000-1000 UTC for the offshore (left) and onshore (right) SB cases. Black dashed lines indicate SB passage times, while grey dashed lines depict sunrise and sunset times.

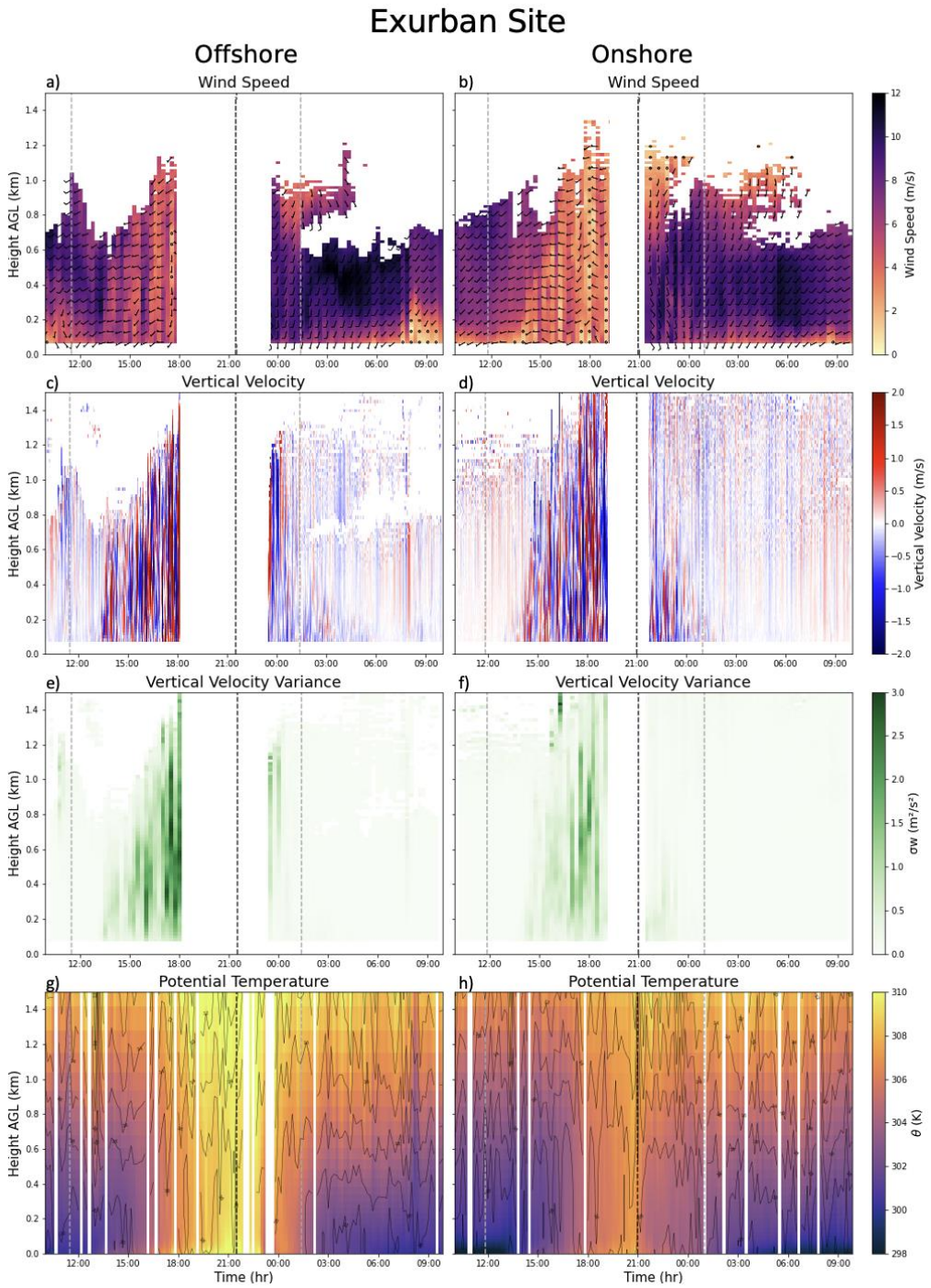


Fig. 4.2: Same as Fig. 4.1, but at the exurban site. Gap in Lidar data due to overheating Lidar.

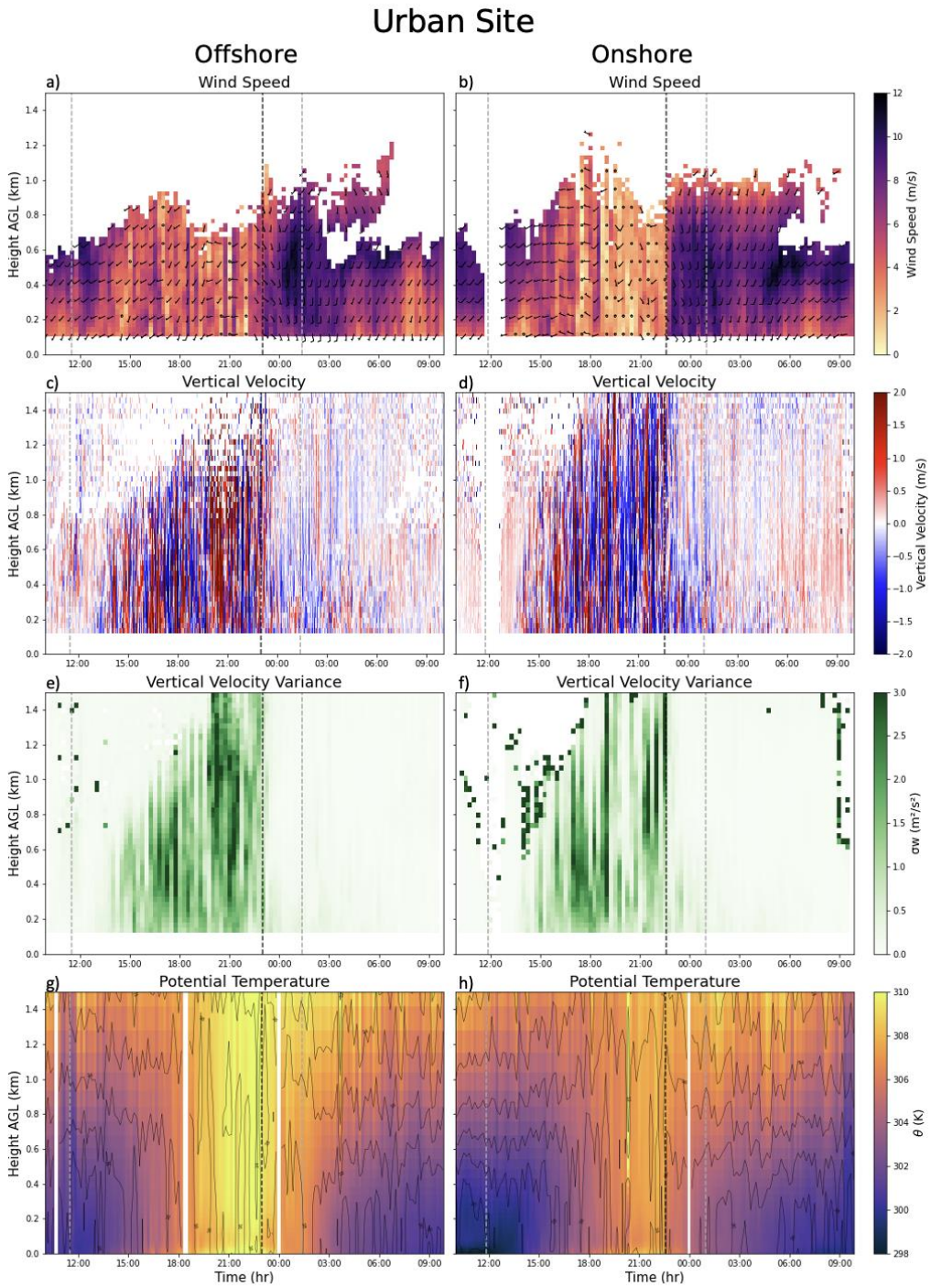


Fig. 4.3: Same as Fig. 4.1, but for the urban location.

While there are some differences between the individual cases, there are also a few spatial differences in the wind speed profiles at 1000 UTC and 1130 UTC (Fig. 4.4). Unfortunately, the early morning lidar wind data is limited from the coastal location, as moisture formed on the lidar

lens, degrading data quality. However, each site shows a clear increase in wind speed with height, reaching a maximum speed between 8-10 ms^{-1}. At 1000 UTC, the onshore case shows stronger winds at the urban site than the exurban location, but the opposite is true for the offshore case. This trend continues through 1300 UTC, but by 1530 UTC, only the onshore case still exhibits spatial differences in the wind profiles, with the urban site showing wind speed ~2 ms^{-1} greater than the coastal and urban sites. The early morning wind conditions across the Houston domain differ only slightly across space, but with opposite trends depending on the specific case.

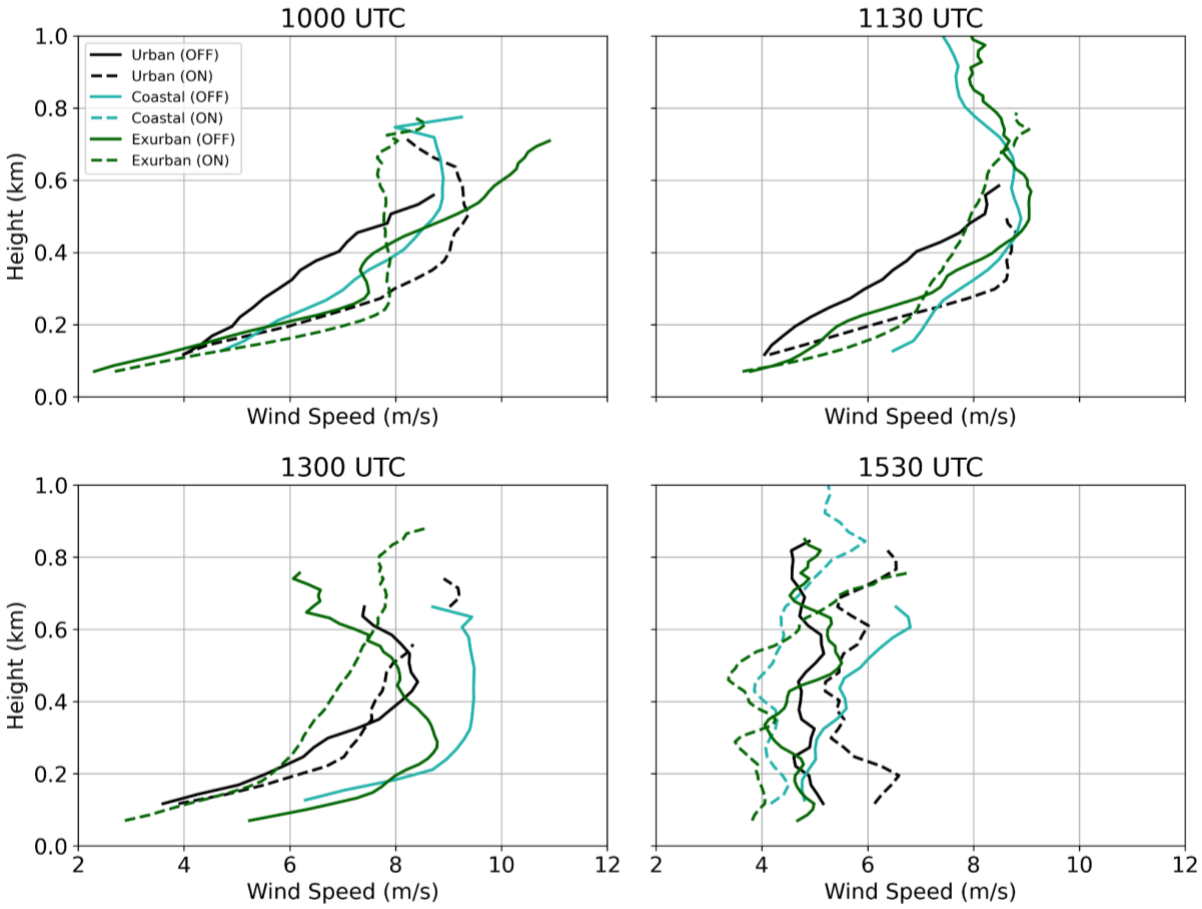


Fig. 4.4: Horizontal wind speed profiles for the onshore (solid) and offshore (dashed) cases for the urban (black), exurban (green), and coastal (blue) sites. Panels show profiles at 1000 UTC, 1130 UTC, 1300 UTC, and 1530 UTC.

Thermodynamically, the near-surface temperatures across sites are very similar through 1300 UTC in both cases (Figs. 4.5 and 4.6). The greatest differences occur above the surface, with

the coastal location showing a gradual increase in potential temperature with height and a relatively constant slow increase through the layer from just above the surface through 2000 m. The inland locations, however, show changing lapse rates with height, evident by the difference in slope of the temperature profiles as height increases. In the onshore case the urban location shows a greater increase in temperatures from the surface to ~100 m below an isothermal layer from 100-250 m at 1000 UTC and 1130 UTC. The exurban site shows a similar greater increase in temperatures near the surface but does not exhibit an isothermal layer. In the offshore case, the urban location shows a smaller increase in potential temperature compared to the exurban and coastal location, consistent with what would be expected with a UHI (i.e., warmer temperatures overnight; Hu and Xue 2016). By 1530 UTC, the inland sites have warmed several degrees more than the coastal location, with each site showing a similar lapse rate above ~500 m. The moisture signatures vary more substantially than the temperatures, with differences in the rate of decreasing moisture with height from the coastal, exurban, and urban sites. The coastal site shows the most consistent rate of decrease, but the inland sites show a clear difference in the stratification of the moisture content. The urban site shows the most pronounced curvature in its profile, indicating that the magnitude of changing rates of moisture decrease with height is greatest at this location. For example, in the onshore case from 1000-1130 UTC, the urban site shows nearly constant moisture content from 100-300 m, while the exurban location shows a sharp decrease within this layer before gradually decreasing. Overall, the greatest spatial differences in the overnight and early morning thermodynamics occur above the surface, with varying lapse rates across the Houston domain for both temperature and moisture. The following analyses will focus specifically on the spatial evolution of SB responses across the CUBIC domain using the two cases.

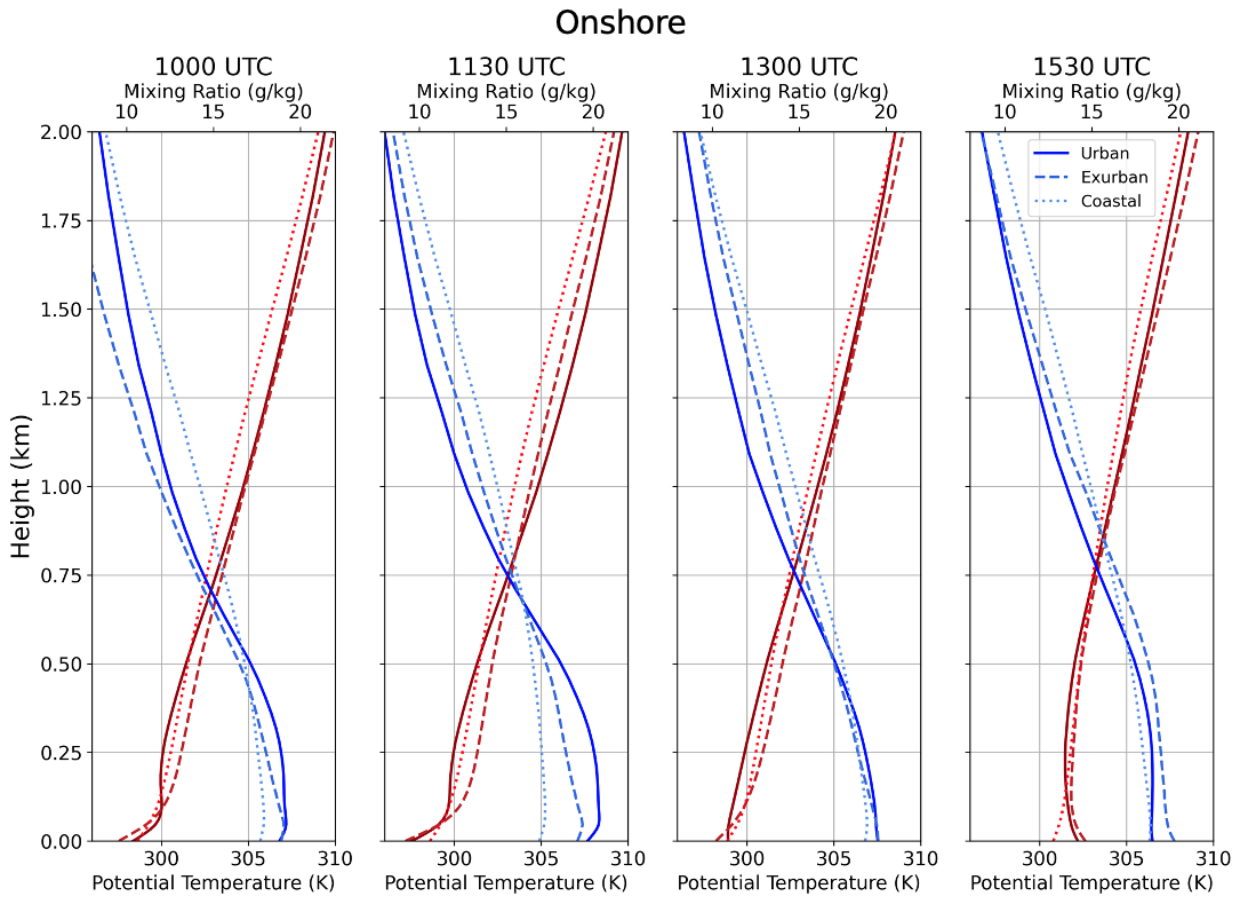


Fig. 4.5: Potential temperature (red) and water vapor mixing ratio (blue) profiles for the onshore case for the urban (solid), exurban (dashed), and coastal (dotted) sites. Profiles are at 1000 UTC, 1130 UTC, 1300 UTC, and 1530 UTC.

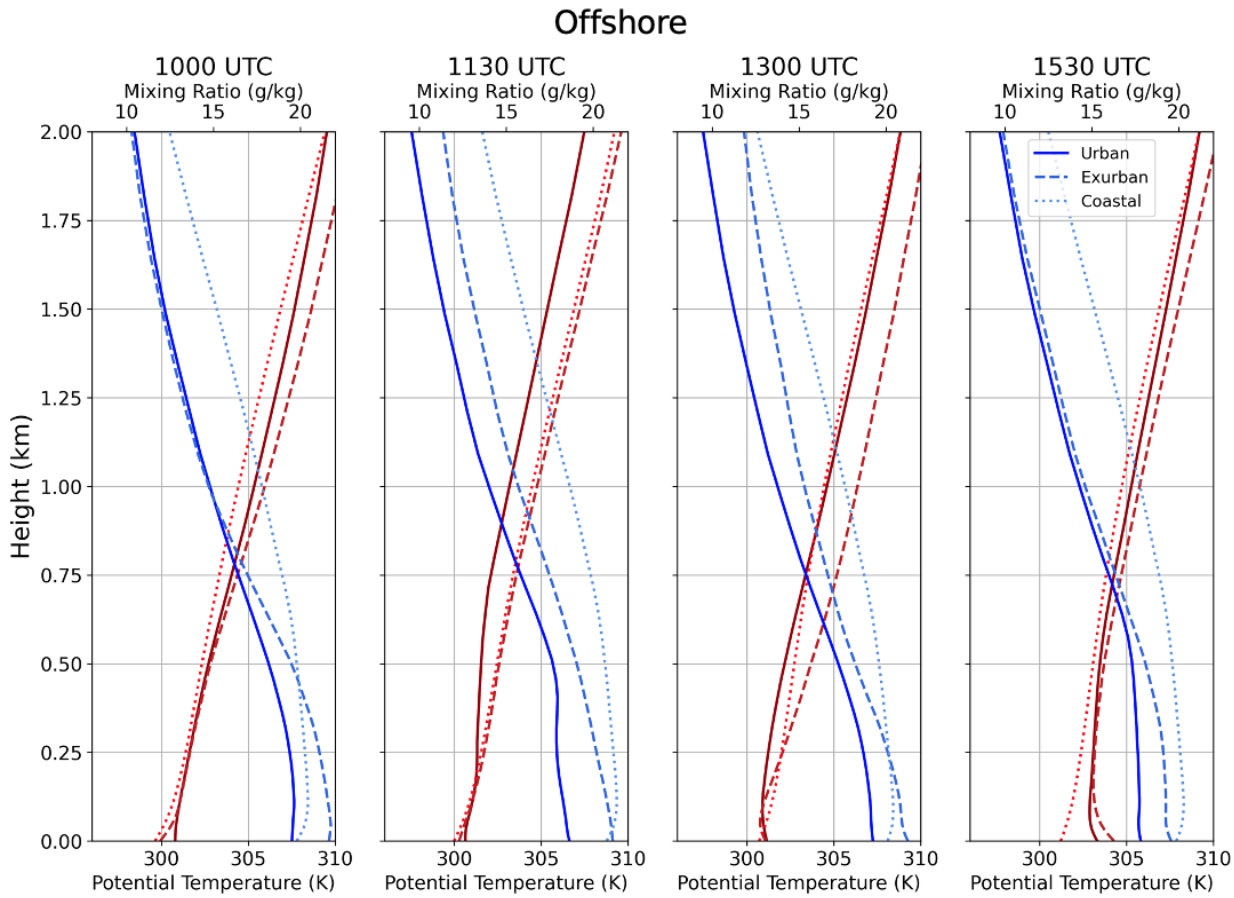


Fig. 4.6: Same as Fig. 4.5, but for the offshore case.

The timing of the SB passage is similar across both cases and sites, occurring within a roughly 45-minute window. This allows the following comparisons to take place during similar times of the day, which can be important since the diurnal evolution of thermodynamic and kinematic properties can vary greatly throughout the diurnal cycle. Before the SB arrives, both cases exhibit well-developed CBLs with strong thermals and positive vertical velocity variance at the urban and coastal sites (Fig. 4.7). The exurban location does not have kinematic data at the SB passage time due to the Lidar overheating, but thermodynamic data exists and will be included. Pre-SB horizontal winds in the onshore case are weak and variable with little difference between sites, while in the offshore case, the coastal site shows weaker and more directionally variable winds compared to the urban location.

After the SB passage, the response in horizontal wind speed varies substantially across the Houston domain. In both cases, the urban site experiences a greater increase in near-surface wind

speed than the coastal site, but the magnitude and profile shape differ between cases (Fig. 4.8). In the onshore case, winds at the urban location were more than 2 ms^{-1} stronger than at the coast, with a small jet-like maximum at ~150 m at the coast, contrasting with a more well-mixed profile inland, indicating a deeper SB response. In the offshore case, wind speed increases by ~4 ms^{-1} up to 300 m at both sites, but above this level, the urban site exhibits stronger winds than the coastal site. The coastal wind maximum occurred between 150-350 m, while the urban maximum was near 500 m, suggesting that the SB kinematic structure deepens as it propagates inland. Not only does the urban location exhibit a greater increase in wind speed post-SB passage, but the offshore case itself shows stronger wind speed across the Houston domain as well.

Vertical motion and turbulence also evolved differently across space (Fig. 4.7). At the coast, a strong (>2 ms^{-1}) updraft at the SBF is observed in the onshore case but not in the offshore case, and neither case exhibits a clear updraft signature at the urban site, suggesting that persistent ascent along the inland propagating SBF is not sustained across the coastal-urban environment. Turbulence within and above the SB layer show contrasting responses at the coast: in the offshore case, the SB layer below 500 m contains short-duration updrafts and downdrafts with increased variance, while in the layer between 500-1250 m, vertical motions appear longer in duration and oscillatory in nature. These signatures are not apparent in the onshore case, where strong upward motions were dominant above the SB inflow layer and enhanced turbulence extends from ~350-1500 m, with variance decreased within the SB layer. At the urban site, both cases show abrupt decreases in vertical velocity variance post-SB, with near-zero values above 500 m and weaker buoyant plumes than pre-SB conditions.

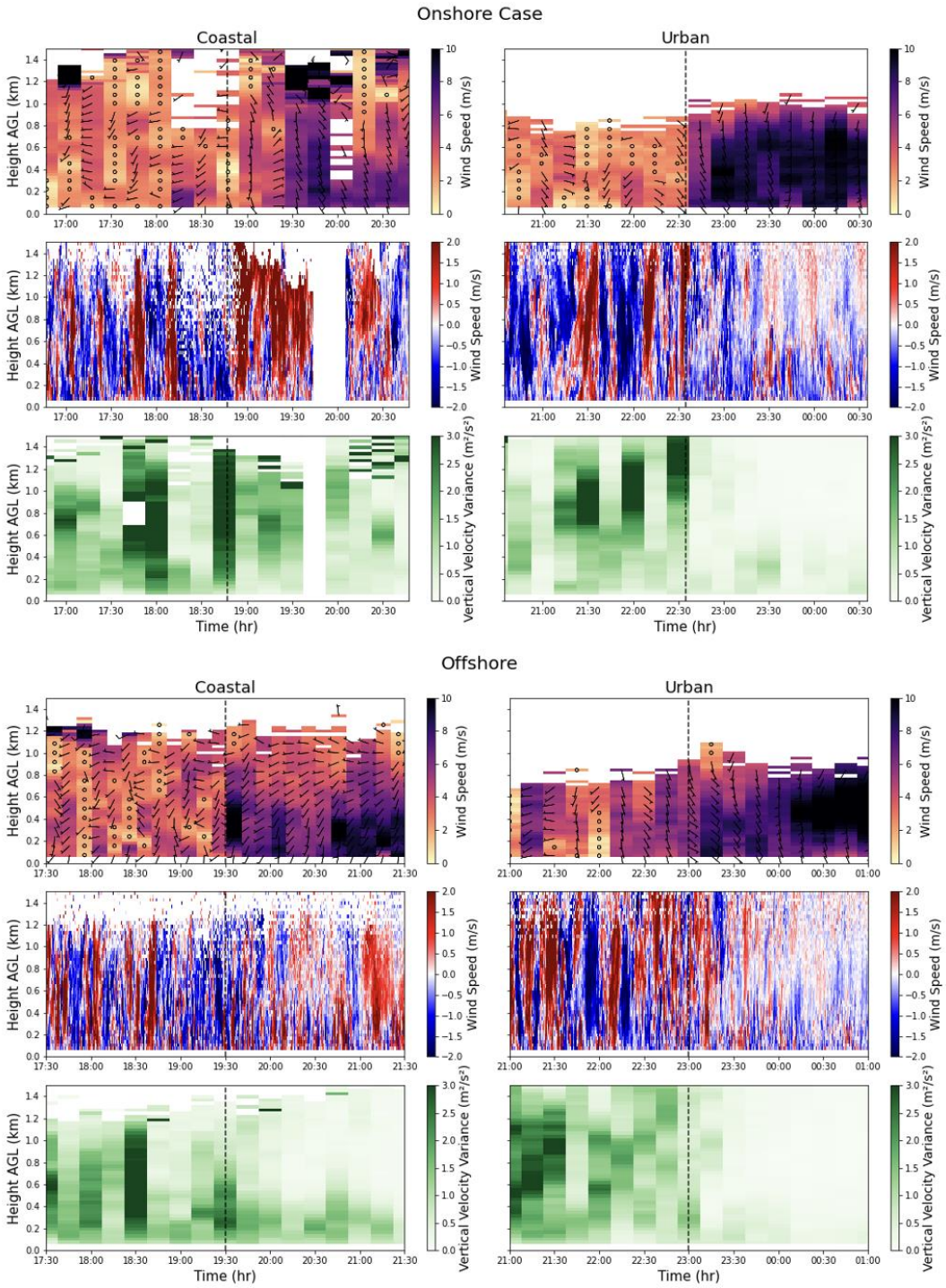


Fig. 4.7: Time-height horizontal wind speed and wind barbs (top), vertical velocity (middle), and vertical velocity variance (bottom) at the coastal (left) and urban (right) sites for the offshore (bottom) and onshore (top) cases. The time axes are centered on SB passage time and span 4 hours total.

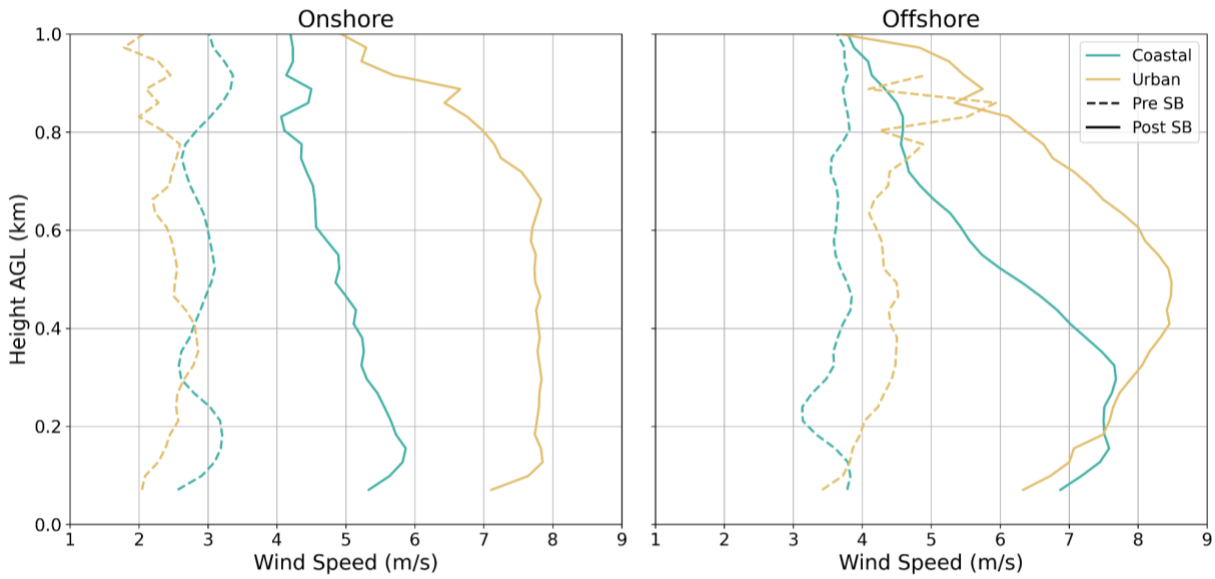


Fig. 4.8: Averaged wind speed two hours before (dashed lines) and two hours after (solid lines) SB passage for the onshore (left) and offshore (right) cases at the coastal (blue) and urban (gold) locations.

Thermodynamic profiles across the three sites reveal notable spatial variability in how the SB modifies the PBL (Fig. 4.9). The individual cases show distinct PBL temperature characteristics throughout the time series, with the onshore case more well-mixed, less stratified, and cooler than the offshore case at all sites. In both cases, inland locations exhibit convectively unstable temperature profiles, with surface temperatures 1-2 K warmer than at 500 m. The spatial differences in temperature responses to the SB in the onshore case are minimal. The SB produces a rapid 1-3 K temperature decrease within 30 minutes at all locations, extending through 1500 m. In the offshore case, the coastal site shows no distinct cooling but instead a stagnation of daytime heating below 1500 m, followed 4-6 hours later (5:50-7:50 pm local time) by a temperature increase aloft, suggesting non-SB related modifications above the SB layer. Inland sites cool more gradually after the SB in the offshore case, with temperature decreases confined to ~500 m at the coastal and exurban locations and ~1000 m at the urban site. Despite many daytime hours left in each case at the coastal location, the consistent southerly flow and advection of the marine air mass inhibit any further heating from taking place near the surface. This is important context, as maximum temperature forecasts and potential health hazards due to heat could be greatly impacted

in the hours after SB passage, even if a drop in temperature associated with the passage of the SBF is negligible.

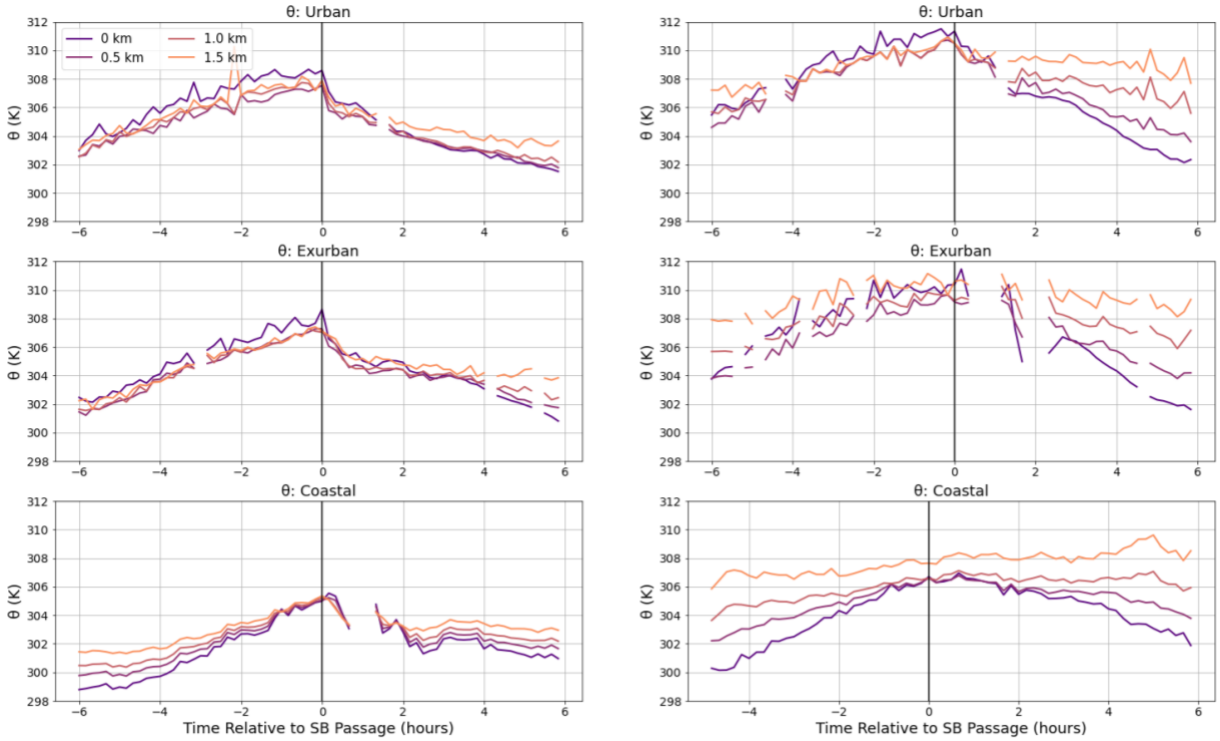


Fig. 4.9: Potential temperature 6-hour time series for the onshore (left) and offshore (right) cases at the urban (top), exurban (middle), and coastal (bottom) sites. Time axes are centered on SB passage time.

Moisture time series show an even larger magnitude and more complex PBL response to the SB (Fig. 4.10). In the onshore case, low-level moisture at the coast rises sharply, by ~10 gkg^{-1} through 1500 m, while inland sites show progressively weaker and shallower increases, only ~3 gkg^{-1} at the exurban location and ~8 gkg^{-1} through 1000 m at the urban site. This decreasing depth with inland distance suggests the top of the SB layer is being mixed and/or eroded by entrainment of the residual PBL as it propagates inland. Given the deepening kinematic signature as the SB propagates inland, the increased wind shear is likely acting to erode the top of the SB layer. In the offshore case, however, the moisture evolution differs. At the coast, only surface moisture increases, while the 500-1500 m layer remains steady before gradually decreasing in moisture content. Further inland, the locations experience ~4 gkg^{-1} increases in moisture concentrated in the

lowest 500 m. Across both cases, the urban site stands out as the only location with consistently large, rapid moisture increases, albeit confined to lower levels.

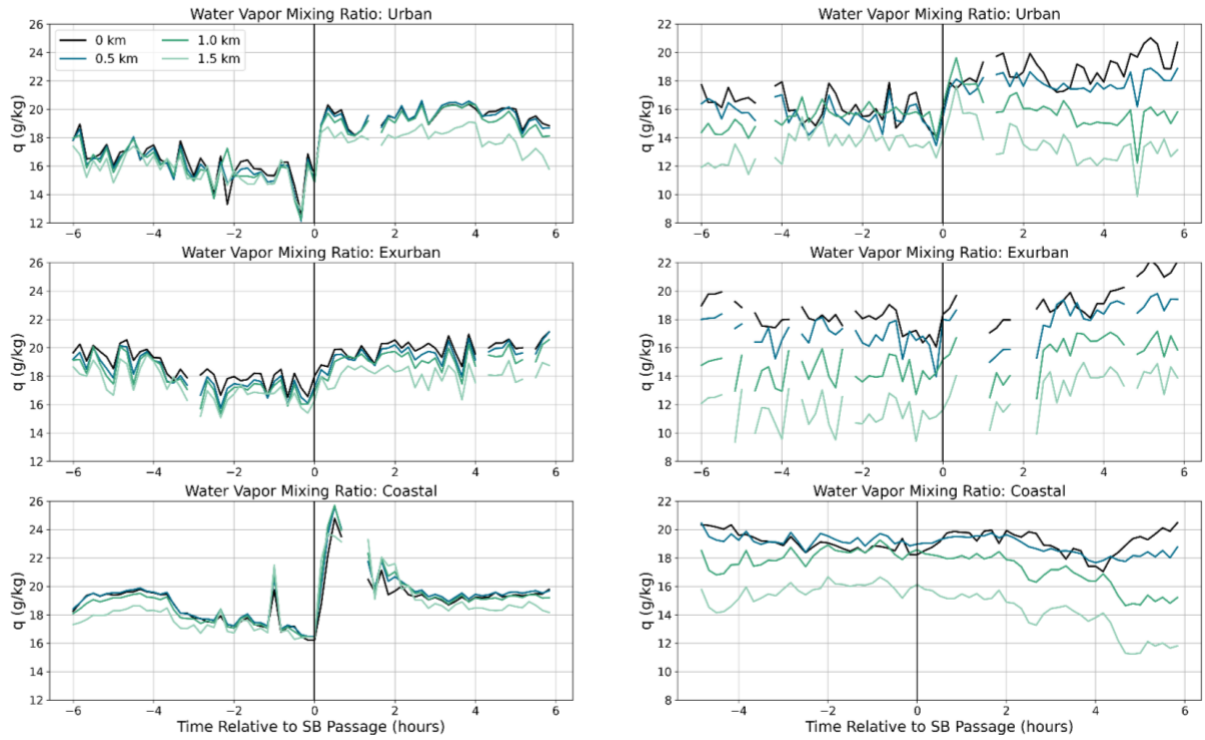


Fig. 4.10: Same as Fig. 4.9 but for water vapor mixing ratio.

Together, these findings highlight that while the SB passage produces broadly similar timing across sites, the depth, structure, and turbulence signatures of the response evolve as the SB moves inland. Stronger and deeper wind profiles at the urban site, contrasting updraft behavior at the coast, and shifts in turbulence regimes above and within the SB layer all point to a complex spatial evolution of SB dynamics across the Houston region. The offshore case exhibits stronger post-SB wind speed across sites, with consistent jet-like wind profile shapes. Thermodynamically, the results indicate that SB-driven thermodynamic changes vary strongly across space: temperature responses become weaker and shallower inland in the onshore case but more gradual in the offshore case, while moisture increases may be strongest at the coast or inland, depending on the case. The spatial patterns also point to mixing processes above the SB layer as a key control on how far inland deep moisture is able to penetrate.

4.3 Kinematic and Thermodynamic Composites

A schematic representation of the PBL and 700 hPa kinematic connections is shown in Fig. 4.11. In the case study analyses, the offshore case indicates greater overall wind speeds compared to the onshore case, with the urban site showing greater relative increases compared to the coast. The 700 hPa flow is generally above the PBL, on average ~3000 m AGL in the midlatitudes, but is hypothesized to be responsible for the enhanced SB response through a feedback-like mechanism. Once a SB has formed, a return flow aloft must also form to close the circulation and satisfy the mass continuity principle. Under the offshore regime, the 700 hPa flow is inherently offshore and oriented in the same direction as the SB return flow, located in the upper portions of the PBL. With both flows in the same direction, the 700 hPa flow could be acting to enhance the return flow portion of the SB circulation. This would, in turn, lead to an enhanced SB flow, again satisfying the necessary mass continuity principle. The opposite holds for the onshore regime (i.e., opposite 700 hPa flow). In the onshore regime, the 700 hPa flow acts against the return flow, which would result in a slower return flow and consequently weaker SB circulation. Given the indications of greater SB flow under offshore regional flow conditions, this explanation and application of interconnections between the PBL and large-scale flow above suggest that while the SB is a PBL mesoscale process, it may be altered by larger-scale flow conditions above the PBL.

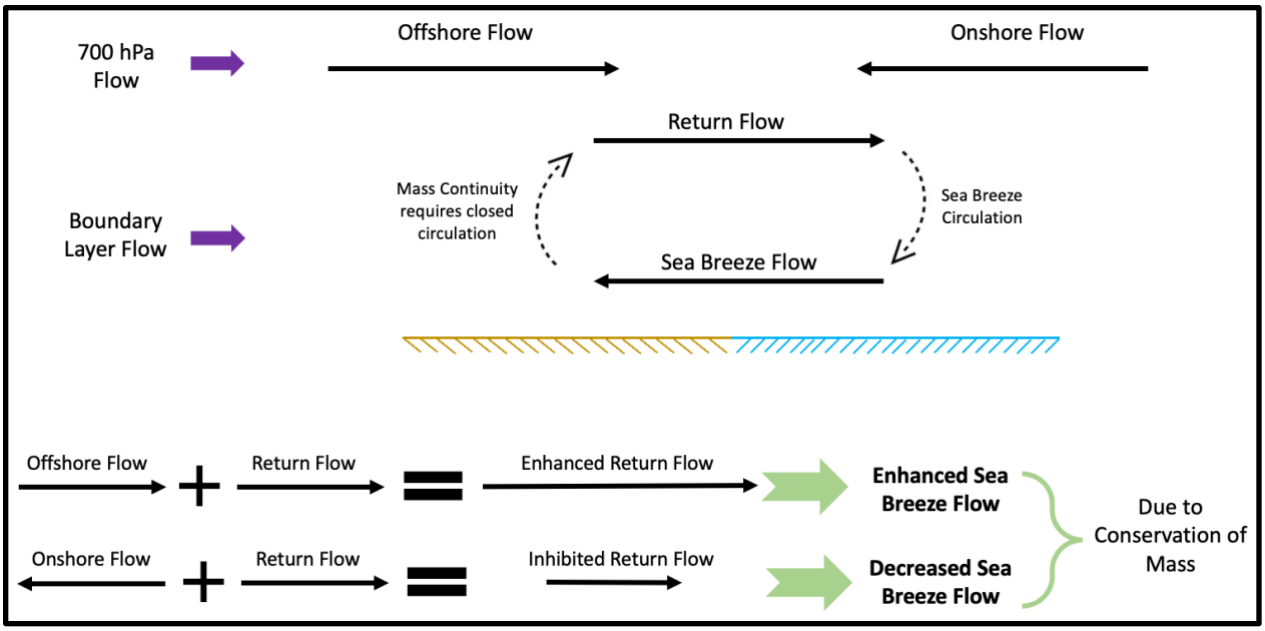


Fig. 4.11: SB circulation schematic depicting physical explanation of PBL and 700 hPa flow interconnections.

While the preceding analyses provide a detailed view of the kinematic and thermodynamic evolution of two differently categorized SB events, the CUBIC campaign observed over 40 SB cases under a range of regional flow regimes. Therefore, investigations into whether the signatures discussed above represent systematic responses tied to the larger-scale environmental flow will now be conducted. To address this, the following section employs composite analyses consisting of all SB cases within each regional flow regime (i.e., onshore, offshore, northeasterly, and southwesterly) to assess how robust the observed patterns are and how they compare to the other two regional regime patterns. The main question examined in the composite analyses is whether the kinematic and thermodynamic impacts of the SB on the PBL outlined above are regime dependent.

With the use of the four-month-long CUBIC dataset and composite analysis techniques, it is possible to examine whether the case differences found in Sect. 4.2 are apparent for the summer of 2022, suggesting a systematic, regime-dependent SB modification to the PBL. Specifically, the following questions will be addressed;

1. Does the offshore flow regime present enhanced flow, following the hypothesized regional flow feedback mechanism from the beginning of Sect. 4.3?

2. Do onshore regime cases result in significantly greater and deeper thermodynamic responses compared to other regime classifications?

The following composites will be centered on the SB passage time to highlight the PBL response specifically due to the SB, despite the array of SB passage times across the regimes (See Sect. 2.4 for SB timing information). To create the composites, the SB passage time for each case is determined, the 4 hours before and after SB passage are used for the composite window, and each case is then averaged together (see Sect 3.2.3 for details on compositing). Each site's composites contain a different number of cases, since data availability and the propagation of the SB through the city were not constant throughout the campaign. As a reminder, given the limited data around the SB passage time from the exurban site, only the coastal and urban locations are used to investigate the kinematic signatures. Table 4.1 below shows the number of cases making up the composites for each given site and regime. It is important to note that only two to three (depending on the site) cases occur in the southwesterly regime, thus the uncertainty would be large. However, it was decided to keep the composites, as the southwesterly regime is still a possible environment in which SBs occur.

Table 4.1: Regional flow composite case numbers at each site.

Regional Flow	**Urban**		**Exurban**		**Coastal**	
	Kinematics	**Thermo**	**Kinematics**	**Thermo**	**Kinematics**	**Thermo**
Onshore	12	13	NA	8	11	13
Offshore	5	5	NA	5	5	7
Northeasterly	8	8	NA	12	8	11
Southwesterly	2	2	NA	0	2	3

Beginning at the coast, under each regional regime, there are increases in wind speed following the SB passage (Fig. 4.12). In the case study results, there was a delayed increase in wind speed in the onshore case; however, that is not present in the composite results. The pre-SB wind profiles are nearly identical in the onshore, offshore, and southwesterly regimes, averaging 3-4 ms^{-1} from the surface to 1000 m (Fig. 4.13). The northeasterly regime is slightly weaker and more evenly mixed from the surface to 500 m before beginning to decrease. In terms of the coastal response to the SB, the onshore and offshore regimes lead to greater sustained winds than the

coast-parallel regimes, with ~1-2 ms^{-1} greater maximum wind speed. The onshore profile shows a very similar shape to that observed in the case study, with it well-mixed below 500 m. While the offshore profile does show a low-level wind maximum at ~150 m, this is considerably less pronounced than in the case study. Given the above-average land-sea temperature difference in the case study, the weaker wind response exhibited by the composites is to be expected, as a larger land-sea temperature difference is what determines the strength of a SB (Miller and Keim 2003). The difference in wind profile shapes between the coast-perpendicular composites suggests a difference in SB depth, with a deeper SB in the onshore cases and a shallower SB under offshore conditions. Additionally, the differences between regime wind speed magnitudes post-SB are quite small, < 1.5 ms^{-1} , suggesting that other, more localized forcings drive the PBL response at this location.

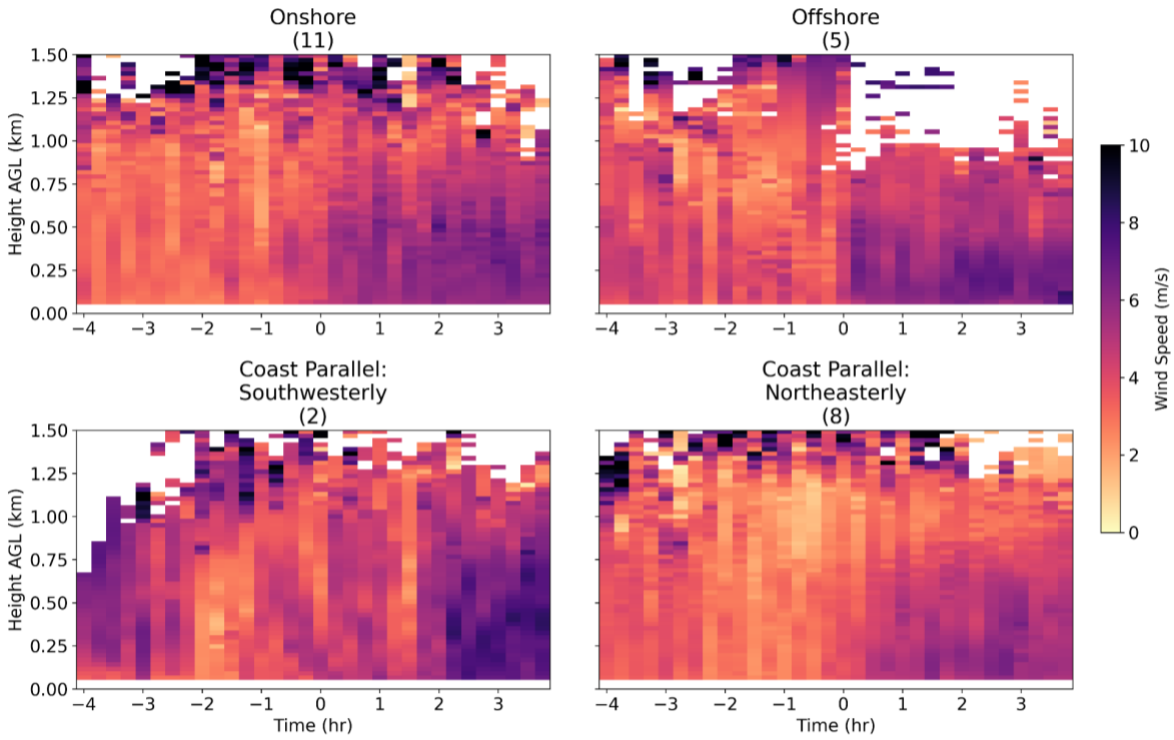


Fig. 4.12: Composite SB passage time-centered wind speed observations at the coastal site for the onshore (a), offshore (b), southwesterly (c), and northeasterly (d) SB cases.

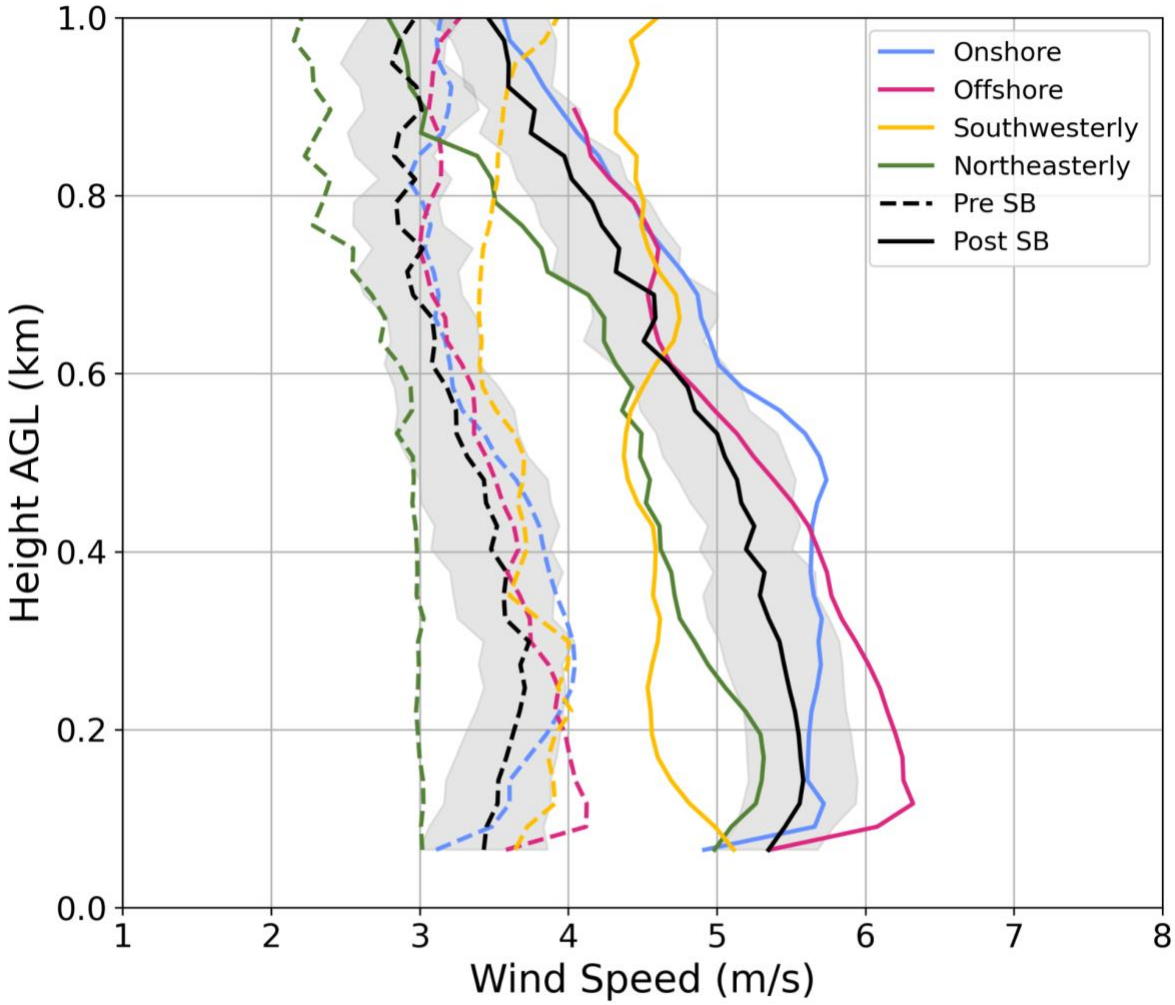


Fig. 4.13: Composites of wind profiles two hours before (dashed lines) and two hours after (solid lines) SB passage at the coastal site for the onshore (blue), offshore (pink), southwesterly (gold), and northeasterly (green) cases. Black profile denotes total average across all cases, with shading representing +/- 1 standard deviation.

At the urban location, the horizontal wind kinematic responses to the SB are more pronounced than those at the coast (Fig. 4.14). Across the regimes, there are greater pre-SB differences in wind speed, with each regime showing immediate increases in the wind speed following the SB passage. Interestingly, there is an initial increase in winds in the northeasterly regime ~3 hours before SB passage, which may be associated with bay breeze instances that also

exhibit increased wind speed (Lappin et al. 2025); however, this has not been confirmed. The post-SB increased winds are generally below 1000 m, with the greatest magnitudes between 150-500 m depending on the regional flow regime (Fig. 4.15). The offshore case exhibits the greatest increase in wind speed and the only discernible difference in profile shape, with a jet-like nose located at ~500 m, indicative of greater shear and associated with a deeper SB layer than the other regimes whose maximum wind occurs at lower heights. The offshore composite analyses are also quite similar to the observed case study from Sect. 4.2 in magnitude and shape. Across the sites, the same findings from the case study hold true, with the offshore case exhibiting a greater kinematic response to the SB and the urban site showing stronger responses compared to the coast. The composite results also support the theory of regional flow enhancing (or inhibiting) the return flow and therefore enhancing (or inhibiting) the SB flow. The difference among regimes, though, is quite minimal. The onshore, northeasterly, and southwesterly regimes show nearly identical post-SB wind profiles and while the offshore regime is different, the overall increased wind speed is no more than 1 ms^{-1} greater than other regimes. As such, the kinematic response to the passage of a SB is more dependent on the spatial characteristics and distance from the Gulf than on lower-tropospheric regional flow.

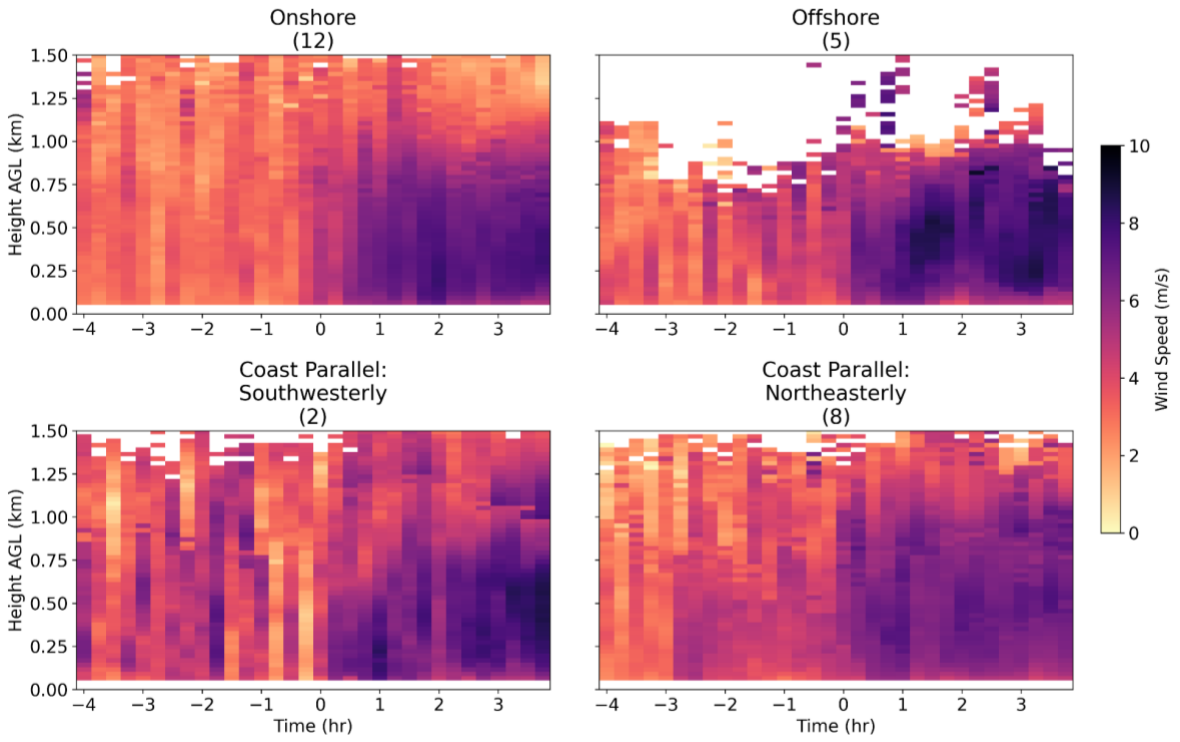


Fig. 4.14: Same as Fig. 4.12 but for the urban location.

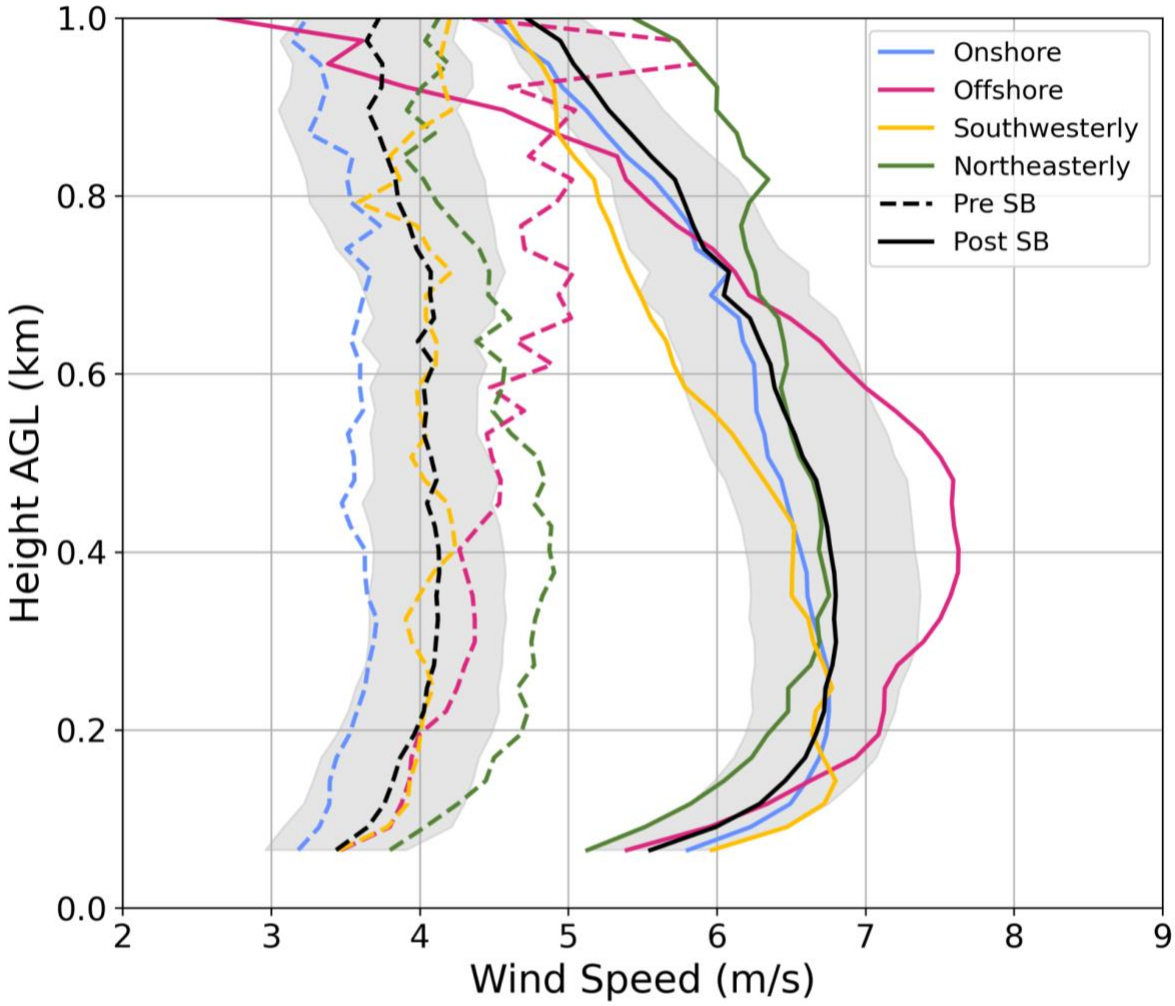


Fig. 4.15: Same as Fig. 4.13 but for the urban location.

The coastal vertical velocity variance (σ_w) composites show distinct differences between the regional regime types, with limited changes to σ_w following the SB passage in the onshore or northeasterly cases, a large decrease in σ_w in the offshore composite, and an increase in σ_w for the southwesterly cases (Fig. 4.16). While the case study results at the coast showed contrasting post-SB σ_w responses, those signatures (i.e., onshore = low σ_w near surface, high above, and offshore = greater σ_w near surface and low above) are not present within the composite results. Instead, there are indications of changing turbulence with height following the SB passage in each regime except the offshore regime that immediately decreases to near zero throughout the PBL. In the 4 hours

following the SB for the other three regimes, σ_w magnitude begins to decrease with height above 500 m.

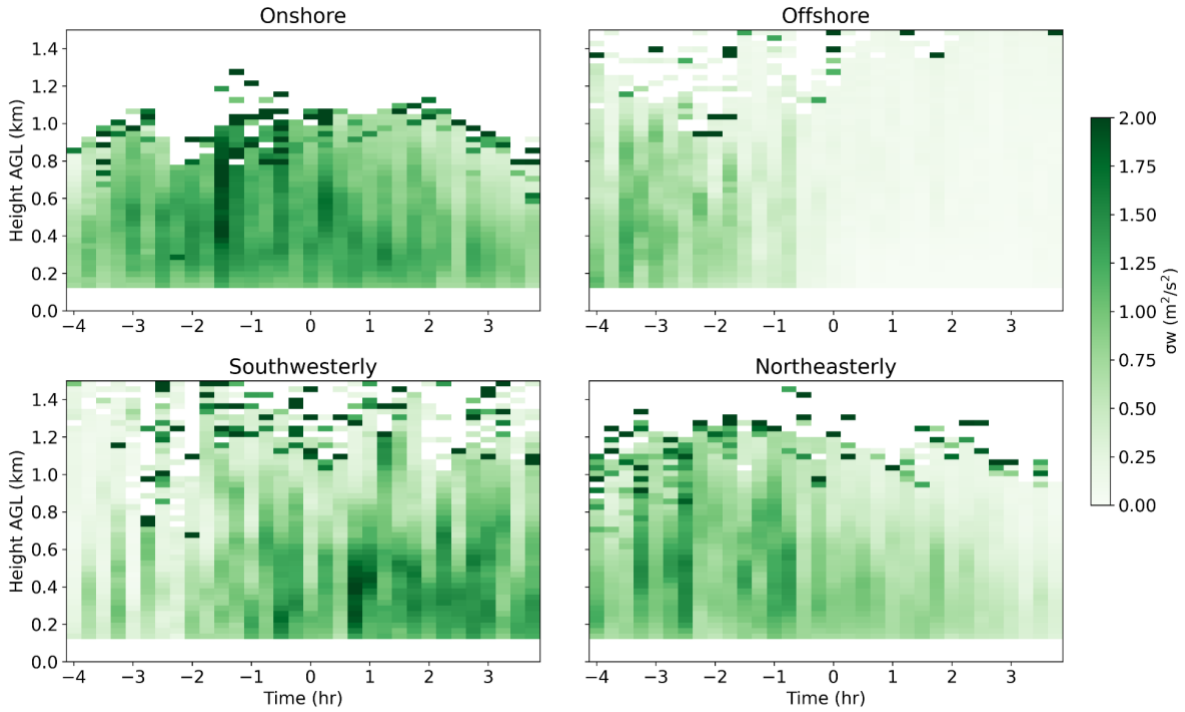


Fig. 4.16: Vertical velocity variance composites at the coastal site for the southerly (top) and northwesterly (bottom) synoptic regime SB cases. Black dashed line depicts differentiation in turbulence regimes post-SB.

One of the biggest spatial differences is shown in the σ_w composites at the urban site. While the coastal location only showed a distinct reduction in σ_w in the offshore regime, at the urban location there is a clear decrease in σ_w post-SB in every regime (Fig. 4.17). There are a few possible explanations for the spatial differences exhibited between sites; the land surface characteristics could be playing a role, the difference in the time of day, or the fact that the coastal site experiences a 'purer' SB (e.g. the SB has not propagated across much land surface yet). At the coastal site, the SB has not yet mixed with a continental air mass, but as it propagates across land, the SB can be modified by entrainment. By the time the SB reaches the urban site, it may have lost much of its initial sharpness, so the forced ascent and associated turbulent updrafts are weaker. Combined with the cooler, more moist air over a rough, previously heated surface could result in the rapid collapse

of the σ_w observed at the urban site. The pre-SB conditions are also notably different between regimes, with enhanced σ_w in the 2-3 hours prior to SB passage in the offshore and northeasterly cases, relatively uniform σ_w in the onshore regime, and more chaotic σ_w behavior in the southwesterly cases, which could also be caused by the limited number of cases (2). Despite these pre-SB conditions, it is clear that regardless of the regional flow over the Houston area, the turbulence is drastically reduced at the urban location with the passage of the SB, consistent with the case study results.

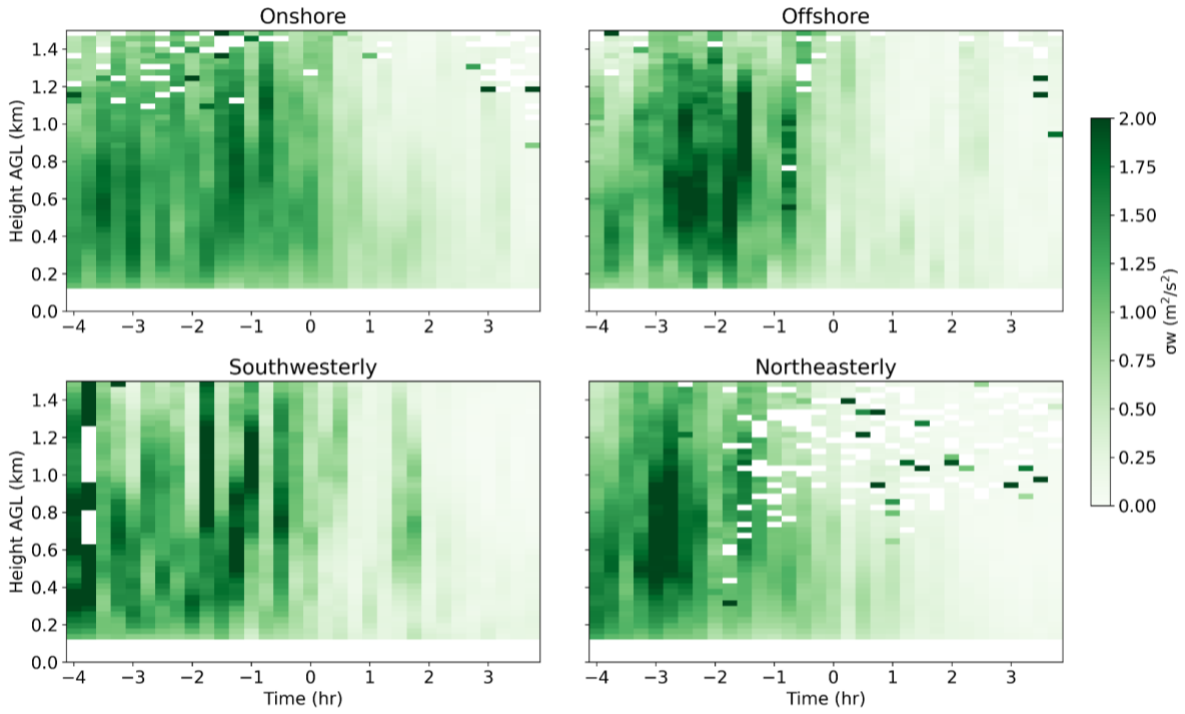


Fig. 4.17: Same as Fig. 4.16 but for the urban location.

The thermodynamic composites show striking similarities in the pre-SB conditions across regimes, with temperatures at the specific sites nearly identical, independent of the regional flow classification (Fig. 4.18). The only exception is in the southwesterly cases, which are notably cooler and more stratified at the coastal site. As with the case study results, the inland sites show surface temperatures greater than the atmosphere above, leading up to the SB passage, indicating convectively unstable conditions. In terms of PBL responses to the SB, the onshore composites show more gradual cooling post-SB than the offshore regime. While the greatest rate of cooling

takes place at the surface, the depth of the cooling differs among sites and regimes. In each regime, the coastal site indicates a warming trend at 1500 m, relatively stagnant conditions at 1000 m, and cooling below, with the offshore cases showing a quicker rate (e.g., steeper slope in time series). The inland sites, however, show no further warming post-SB passage, likely due to the temporal difference in SB passage time, with coastal SB passage typically in the early afternoon, well before peak daytime heating occurs. The main takeaway from the temperature responses is that at the coastal location, differences between regimes are small, but the surface temperature in the offshore cases at the inland sites decreases more rapidly in the first hour post-SB, consistent with the greater wind speed response discussed previously. Additionally, the offshore and northeasterly regimes indicate an initial temperature drop at the SB passage, while the onshore and southwesterly composite drops are negligible. Despite these differences, the temperature trends after 1-hour post-SB passage are nearly identical across regimes, so while the initial response to the SB may vary slightly, that response is short-lived and only observed at the inland sites.

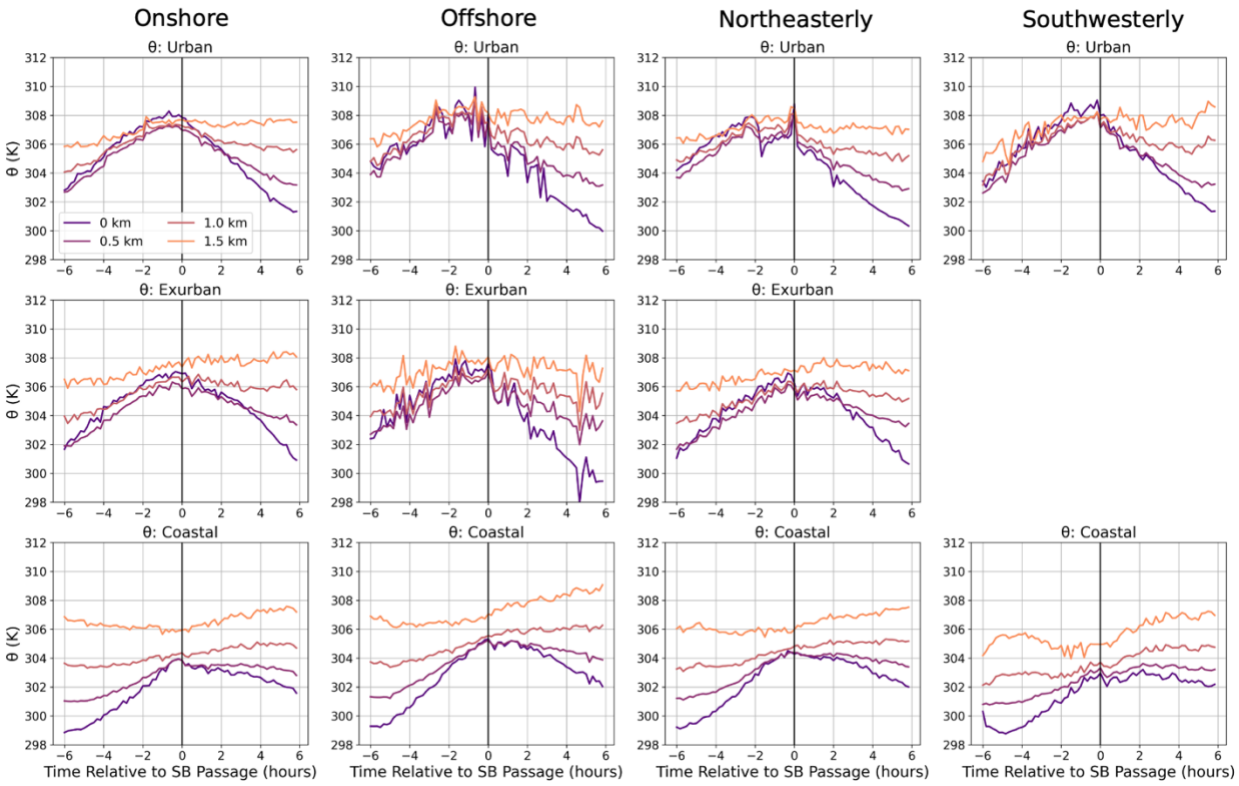


Fig. 4.18: Composite SB passage time-centered temperature observations for the onshore (column 1), offshore (column 2), northeasterly (column 3), and southwesterly (column 4) regional regimes at the urban (top), exurban (middle), and coastal (bottom) sites. Contours correspond to heights from the surface to 2000 m; darker colors = closer to the surface.

One of the biggest differences between the regime types is, again, the moisture response. At the coast, the greatest rise in moisture occurs under onshore conditions and is seen through 1000 m (Fig. 4.19). The increases in the other three regimes are lesser in magnitude (~1 gkg^{-1}) and most prominent only at the surface. The inland sites vary more in their moisture response than the coast, but with similar trends of a more subtle increase at the exurban site and a quicker increase at the urban location. The depth of the SB response at the exurban site does not reach 1000 m in any regime, as evidenced by stagnant or drying trends above 1000 m. While the onshore and northeasterly regimes are moister than the offshore and southwesterly regimes, the relative increases in post-SB moisture are nearly identical, showing that the onshore regional flow cases do not lead to a greater thermodynamic response than other regimes, differing significantly from the case study findings.

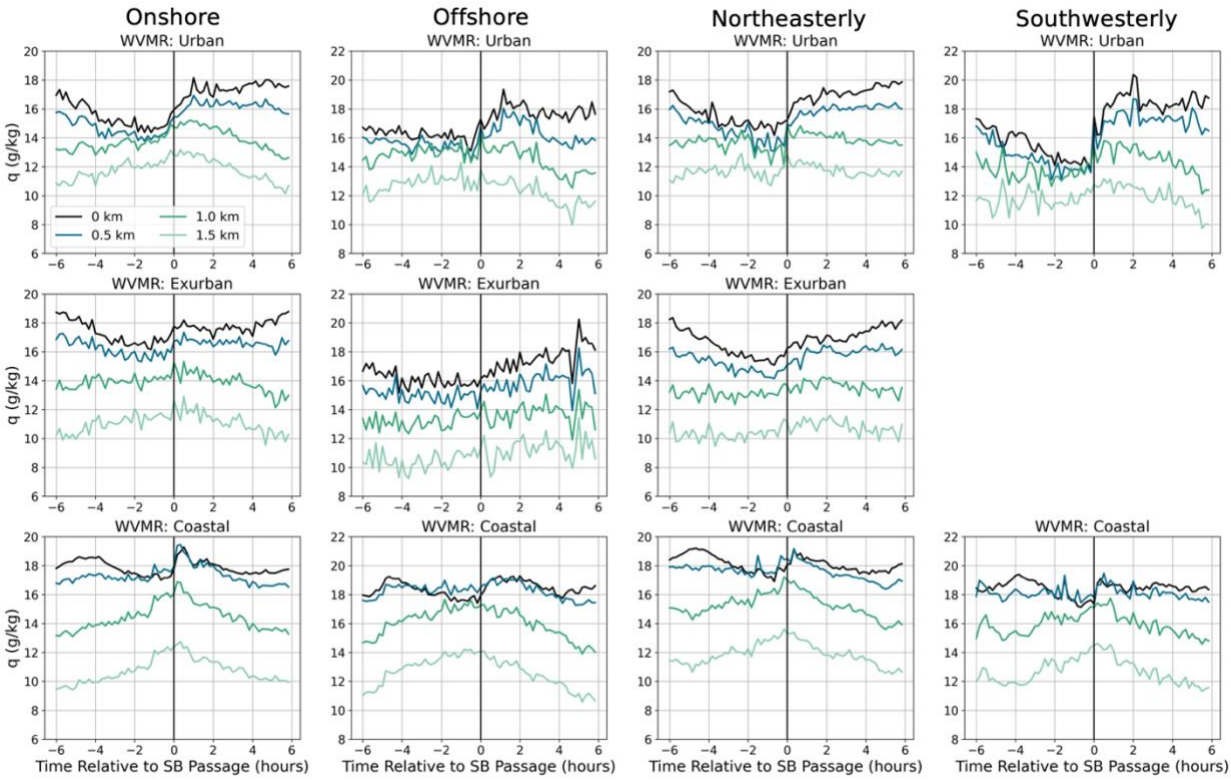


Fig. 4.19: Same as Fig. 4.18, but water vapor mixing ratio.

4.4 Discussion and Conclusions

The case study comparisons and composite analyses highlight the intraseasonal variability of PBL responses to the SB in Houston classified via regional flow regimes. While the horizontal wind speed responses to the SB are weaker at the coast and stronger at the urban location, only in the horizontal wind data are there indications of a regime-dependent response to the SB. The composite results show very similar post-SB wind profiles for the onshore, southwesterly, and northeasterly regimes, but the offshore regime shows a distinct difference at the urban site, with a jet-like structure and a maximum wind speed of ~ 8.5 ms^{-1} at 500 m. Differences exist in the PBL characteristics amongst regimes (e.g., moisture levels, wind speed magnitude), with the greatest differences occurring spatially across Houston. There was no detection of systematic differences in the thermodynamic response to the SB across regional regimes. Instead, the case study analyses suggest that the pre-existing thermodynamic structure is a more important factor in how the SB will modify the PBL. While there are spatial differences across the city with the propagation and

modification of the SB, this chapter shows minimal differences among regional regimes, indicating that larger-scale flow does not lead to *substantial* differences in PBL responses to the SB. There are some indications in the kinematic analyses that the offshore flow regime produces enhanced SB wind speeds, consistent with the schematic in Fig. 4.11; however, these are also small in magnitude, suggesting not a substantial impact from the regional flow. The thermodynamic findings, along with the kinematic analyses, indicate that local-scale and surface processes are more important in driving the observed variability in PBL responses to the SB than the regional flow. The case study analyses showed distinct post-SB responses, proving that the response to the SB is not consistent.

The work shown and described above has highlighted important spatial differences within PBL characteristics and the intraseasonal variability of PBL responses to the SB, both of which are important factors in understanding the evolution of the PBL in the coastal-urban environment. An additional and important aspect that adds complexity to the Houston region's summertime weather is the occurrence of daytime thunderstorms. In the onshore case investigated within this chapter, CI occurs along the inland propagating SBF. Observations at the coast show that within 3 minutes of the SB passage, strong (> 2 ms^{-1}) upward motions occur from the surface through 1500 m above the ground, particularly above the SB inflow layer. This response to the SB is coupled with a rapid rise in moisture of > 10 gkg^{-1} and a drop in temperature of ~3 K. While similar magnitude thermodynamic responses are observed at the urban site, the persistent upward motions are not. Thus, it appears that forced ascent is prevalent near the coast but dissipates with the inland propagation of the SBF. This raises the question of what processes are necessary for successful CI, especially if forced ascent along the SBF diminishes inland. Is the influx of a high equivalent potential temperature air mass enough to destabilize the atmosphere behind the SB, allowing parcels to more easily reach the lifted condensation level? The CUBIC dataset offers rich, high-resolution profiling observations from multiple points along the SB path, but further tools are needed to understand which mesoscale processes may be responsible for the observed CI, to further investigate the observed signals, and to capture the continuous evolution of the SB as it propagates inland.

Chapter 5

Sea Breeze Forced Convection Initiation: A Case Study on Observations and Ensemble Forecasts from 17 August 2022

5.1 Introduction

The high-temporal resolution observations continuously collected during the CUBIC campaign capture a detailed look at the diurnal evolution of the PBL and SB propagation and related PBL modifications at multiple strategically chosen locations. The results presented in the previous chapters provided new insights about the complex interactions of PBL and mesoscale processes in a coastal urban environment, but open questions remain about how the SB characteristics evolve as it propagates inland and the role of the SB in CI. Using the site-specific measurements in combination with NWP simulations extends the spatial context and allows for in-depth examinations of processes across the coastal-urban environment. While accurately simulating the physical processes that are important to atmospheric phenomena within the PBL continues to be an area of active research for NWP models, using NWP simulations alongside observations can be a useful tool to both better understand observed phenomena and to evaluate model performance (Smith et al. 2019; Reddy et al. 2022; Kim et al. 2023).

Prior research on SB-related CI has focused on the prevalence of CI near the SBF, with many studies relying on idealized NWP simulations to further our understanding of the mesoscale processes most important to CI in these environments (Azorin-Molina et al. 2015; Fu et al. 2021; Boyer et al. 2025). These studies have found differing results in terms of the most preferred areas for SB-forced CI to occur, whether it be ahead or along/behind the SBF (Rao and Fuelberg 2000; Fovell 2005; Boyer et al. 2025). In cases where CI occurs ahead of the SBF, work has shown two particular pathways for CI. First, the area is primed for CI by the SB through persistent ascent and vertical moisture advection ahead of the SB, which establishes an elevated tongue of moist air (Fovell 2005). Second, that CI can occur ahead of the front due to the development of enhanced convergence ahead of the SB (Fankauser et al. 1995). When CI exists behind the SBF, recent works have attributed this to the advection of a mesoscale air mass with high θ_e (MAHTE; Boyer et al. 2025; James et al. 2025). MAHTEs are found on the cool side of a frontal boundary and lead to

destabilization of the atmosphere behind the SBF. Not only can a MAHTE be advected inland, but the return flow (i.e., upper portion of SBC) advects relatively drier (lower theta-e) air aloft, acting to increase lapse rates and further destabilize the atmosphere. While the SBF can act as a forcing mechanism to trigger convection, providing the dynamic lift of an updraft to carry parcels from the surface through the PBL, predicting the location and timing of SB-forced CI remains a challenge, especially in regions characterized by considerable surface heterogeneity that can lead to substantially different thermodynamic structures across a region, such as coastal-urban regions like Houston.

The analyses in Ch. 4 revealed that onshore cases have generally weaker kinematic responses to the SB than offshore cases and that the responses are weaker at the coast compared to further inland at the urban site, regardless of regime. Additionally, the onshore composites exhibited a generally deeper thermodynamic response to the SB than in other regimes. In the case study of the 17 August 2022 case, the magnitude of the kinematic and thermodynamic responses was exceptionally strong. This case also exhibited clear CI near the SBF as it propagates inland, while many other onshore cases do not produce CI, suggesting that the kinematic and thermodynamic signatures present in this case are important to successfully initiate convection. The past literature has shown forced ascent and convergence along the SBF are needed as a triggering and lifting mechanism for CI, but observations from this case show ascent at the SBF only at the coastal location, far removed from where the CI occurs. However, the observations do support a deep, moist air mass behind the SBF that persists inland, which falls in line with the theory of CI occurring due to destabilization on the cool side of the frontal boundary.

In this final chapter, CUBIC observations from the onshore case examined in Ch. 4, which exhibits apparent SB-forced CI, are analyzed alongside an ensemble of forecasts produced by the National Severe Storms Laboratory Warn-on Forecast System (WoFS; Stensrud et al. 2009; Heinselman et al. 2024). The observational data can only provide insight into what happened at a single point, but adding in model data provides the opportunity to examine the spatial evolution of the SB and driven responses continuously through time. The 17 August 2022 case is characterized by strong responses following SB passage, with strong upward motions at the coastal site (though not at the urban site) and rapid, large moisture increases across the Houston region. Past SB CI literature shows a consensus that moisture is a necessary component for successful CI to occur, independent of where the CI originates with respect to the SBF (Fovell 2005; Sharma et al. 2024;

Boyer et al. 2025). Based on the case results from Ch. 4 and previous SB-CI studies, we hypothesize that the CI in this case depends on two mechanisms:

1. The forced ascent *at the coast* to establish a moist air mass and advect moisture vertically (Fankauser et al. 1995; Fovell 2005) and
2. The moist air mass advects inland, even though the forced ascent is less prevalent inland. This air mass can destabilize (increased CAPE, decreased CIN) enough that forced ascent *inland* is not a *required* condition for CI (Boyer et al. 2025; James et al. 2025).

5.2 Warn-on Forecast System Overview

The WoFS is a convection-allowing ensemble (CAE) NWP modeling system that creates an ensemble of 36 forecasts. The model has high spatial resolution, with a horizontal 750 X 750 grid at 3-km spacing and 51 terrain following vertical levels. The WoFS uses the 36-member High Resolution Rapid Refresh (HRRR) Data Assimilation System (HRRR-DAS; Doswell et al. 2022) to initialize the forecast and a combination of operational HRRR forecasts and perturbations from the Global Ensemble Forecast System (GEFS) provides the boundary conditions (Zhou et al. 2022). The WoFS is a mixed-physics ensemble-based system with a combination of 6 unique physics parameterizations (Table 5.1). The WoFS also has a rapid data assimilation cycle, assimilating conventional observations, multi-radar/multi-sensor (MRMS) radar reflectivity, MRMS radial velocity, GOES-16 cloud water path data, and GOES-16 clear sky radiances every 15 mins, allowing for the latest observations to help guide the model forecasts.

The WoFS was created at NSSL and designed specifically to provide probabilistic guidance for hazards that are associated with individual convective storms (Skinner et al. 2022). The WoFS is different from traditional CAEs that operate in a ‘next-day’ capacity and provide guidance for regional convective threats. The WoFS goal is to provide ‘now-casting’, 0-6 hour forecasts issued every 30 minutes, which aligns with lead times consistent with the National Weather Service’s watch-to-warning products and can act as the bridge between observations and the next day model simulations from traditional CAEs. A single 6-hour forecast is used herein, initialized at 1700 UTC and running to 2300 UTC. To date, the WoFS has been most commonly applied in severe and impactful weather situations such as potential severe weather outbreak days,

fire weather, or cases in which high flood risks are in place (Jones et al. 2022; Britt et al. 2024; Burke et al. 2024). The WoFS was run post-mortem for this project, with only the first 18 members included in the WoFS-like ensemble due to computational expense. The application of the WoFS to simulate the SB is outside of its typical use case; however, while it is not the scope of this chapter, this experiment can be used as a proof of concept, to confirm whether this modeling configuration holds the ability to accurately forecast more weakly forced mesoscale boundaries and the associated CI.

Table 5.1: WoFS model specifications, including ensemble member specific physics combinations.

Warn-on Forecast System Specifications		**Ensemble Member**	**PBL Scheme**	**SW Radiation Scheme**	**LW Radiation Scheme**
Model Version	WRF-ARW v3.9+	1, 7, 13	YSU	Dudhia	RRTM
Grid Dimension	300x300x50	2, 8, 14	YSU	RRTMG	RRTMG
Domain Size	750 km x 750 km	3, 9, 15	MYJ	Dudhia	RRTM
Horizontal Grid Resolution	3 km	4, 10, 16	MYJ	RRTMG	RRTMG
PBL	YSU, MYJ, MYNN	5, 11, 17	MYNN	Dudhia	RRTM
Radiation SW/LW	Dudhia/RRTM, RRTMG/RRTMG	6, 12, 18	MYNN	RRTMG	RRTMG
Microphysics	NSSL double-moment				
Land Surface Model	RUC (smirnova)				

5.3 PBL Parameterizations

The use of NWP within the meteorological field is far-reaching and extremely important to our fundamental understanding of atmospheric processes. However, there are still challenges that make accurately simulating the many scales of motions present in the atmosphere difficult. While technology and computing sources have greatly improved within the last several decades, turbulence and other sub-mesoscale processes occur at scales that are still too small for operational numerical models to simulate explicitly, requiring the use of parameterizations (i.e., inherent assumptions of atmospheric processes; Stensrud 2007). Of particular interest to this work, a mix

of PBL parameterizations is used within the WoFS to handle the vertical transport of heat and momentum as well as turbulence. PBL schemes differ in their treatment of the turbulence closure problem that arises from Reynolds averaging. Reynolds averaging results in unknown moments of turbulence, which can be handled by PBL parameterizations in a number of different ways, with the two main choices being either local or nonlocal mixing. Local mixing schemes refer to parameterizations where each model level interacts only with the adjacent level, producing smaller turbulent eddies and a slower vertical transfer of momentum, heat, and moisture. Conversely, nonlocal mixing schemes allow for vertical mixing across model levels, leading to larger eddies and a more physically reasonable portrayal of real atmospheric eddies that vary in size. Many previous studies focused on PBL parameterization behavior have found that non-local schemes generally have a warm, dry bias while local mixing schemes exhibit cool and moist biases (Zhong et al. 2007; Coniglio et al. 2013; Gomez et al. 2016; Potvin et al. 2020).

In the WoFS, three different PBL parameterization schemes are used: the Yonsei University (YSU), Mellor-Yamada-Janjic (MYJ), and Mellor-Yamada_Nakanishi-Niino Level 2.5 (MYNN) schemes (Janjic 2002; Hong et al. 2006; Nakanishi and Niino 2006). The YSU scheme is a non-local, first-order turbulence closure scheme, while the MYJ and MYNN are 1.5-order closure schemes, both with local mixing. The YSU scheme utilizes a turbulence diffusion equation, based on an eddy diffusivity coefficient and counter gradient correction term, to derive the prognostic flux variables located within the mixed layer. The MYJ scheme uses a one-dimensional prognostic equation for turbulent kinetic energy (TKE), while the MYNN predicts sub-grid TKE terms, the differences of which lead to changes in how the model simulation handles vertical mixing.

5.4 Forecast Evaluation and Coastal Sea Breeze Modifications to the PBL

Prior to process-specific investigations using the NWP output, a comparison to the observed conditions is necessary to ensure the simulation captures a representative environment. On 17 August 2022, under onshore 700 hPa synoptic regime conditions, a SB forms along the coast in the early afternoon, propagates inland through the city of Houston, and results in apparent SB-forced CI, evident via radar reflectivity imagery from the operational KHGX WSR-88D radar (Fig. 5.1). The SB propagation through the city was 10 minutes faster than the CUBIC campaign-

average propagation time, taking approximately 3 hours and 45 minutes to propagate from the coastal location to the urban site. It was observed at the coast at ~1850 UTC, the exurban site by ~2100 UTC, and reached the urban location by ~2235 UTC. Comparing the observed reflectivity with WoFS ensemble simulated composite reflectivity shows some ensemble members overproducing convection, but also evidence of CI in the same general region as what was observed, lending confidence in the ensemble's ability to reliably represent this case (Fig. 5.2).

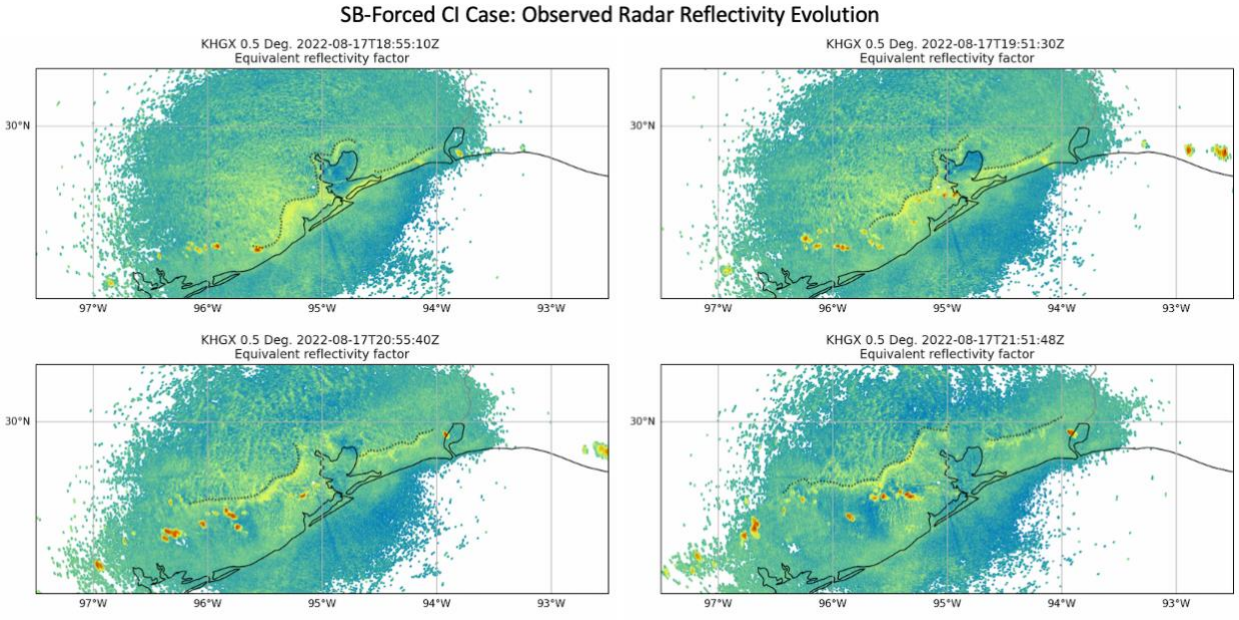


Fig. 5.1: Observed radar reflectivity on 17 August 2022 at KHGX. Dotted lines indicate the leading edge of the SBF.

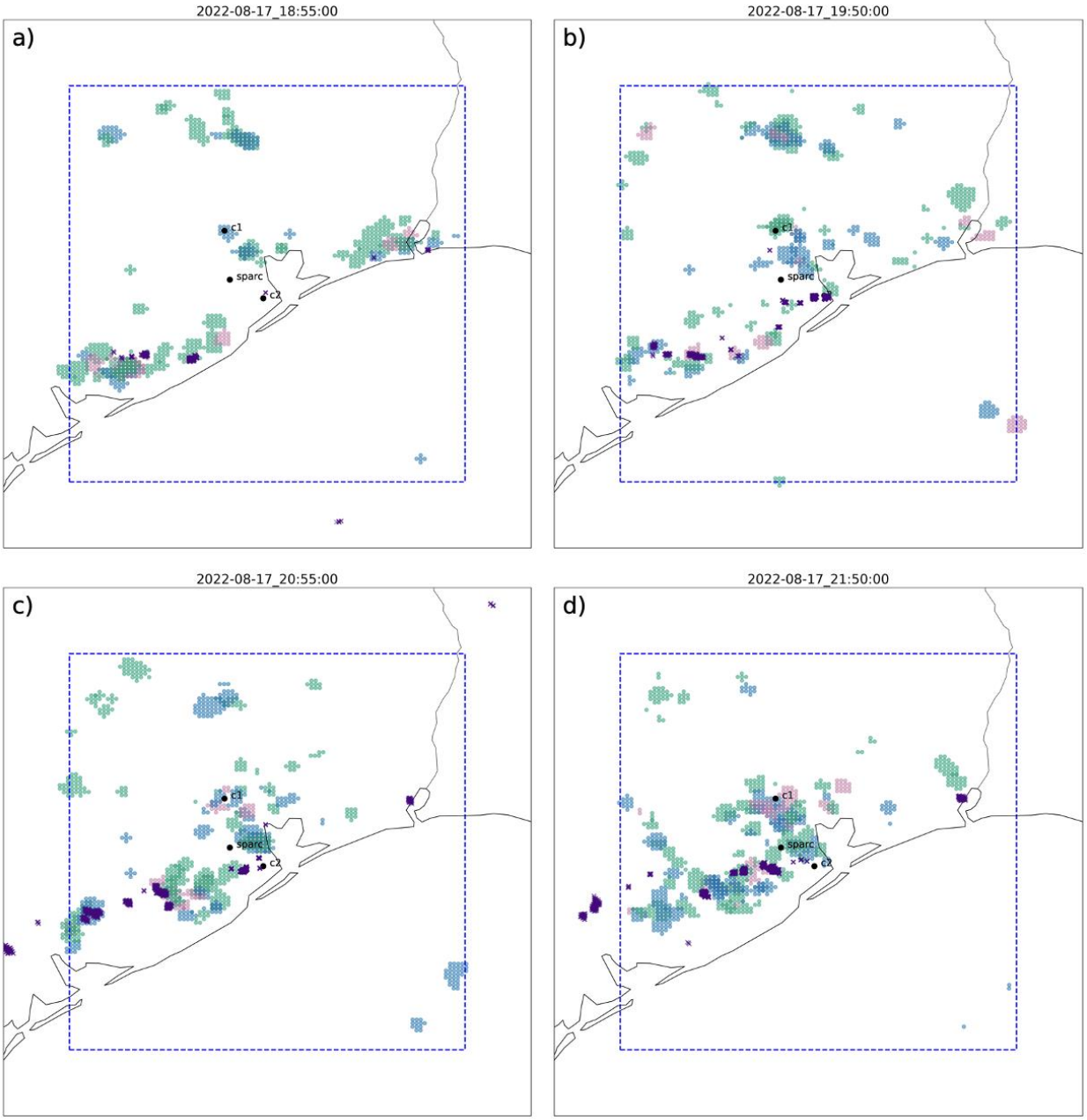


Fig. 5.2: Observed (purple x-markers) and simulated radar reflectivity >= 35 dBz. Ensemble members colored by PBL scheme: YSU (pink), MYJ (green), and MYNN (blue).

The following point analysis comparisons are completed by finding the 4 nearest model grid cells to each observation site's latitude and longitude, averaging those profiles together, and then using the averaged model profile to compare against observed profiles. This method mitigates possible translation errors and potential spurious individual grid cells from contaminating the

results. Fig. 5.3 depicts the AMF radiosonde observed and modeled temperature profiles at 1730 UTC, thirty minutes after model initialization. From the surface to ~850 hPa, the ensemble members are consistently warm-biased compared to the observations by ~1-3°C. In the observed profile, there are two lower-tropospheric temperature inversions, one at ~850 hPa and another at ~800 hPa. Each ensemble member indicates a change in lapse rates around these heights, with most members showing isothermal layers.

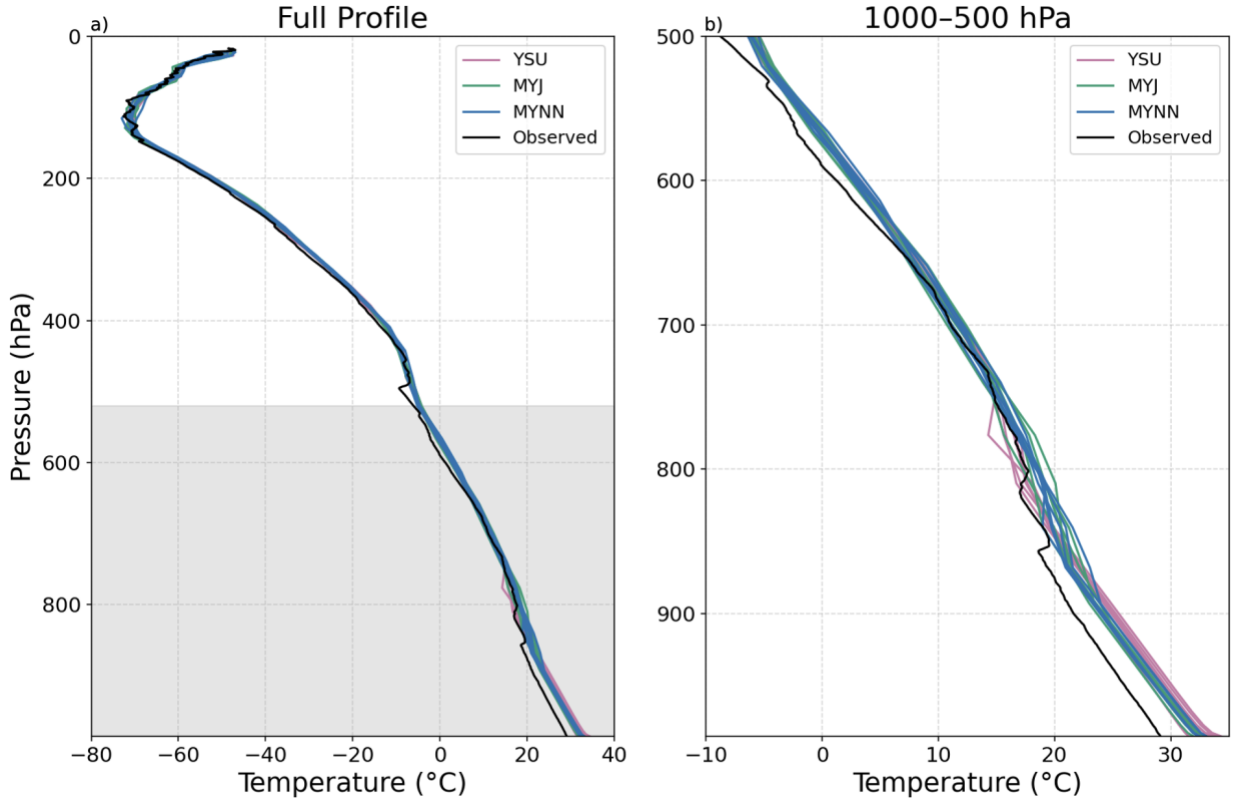


Fig. 5.3: Observed (black) versus modeled (colored) temperature profiles at 1730 UTC radiosonde. The observed temperature profile was collected with a radiosonde released at the AMF site. Ensemble members colored via PBL scheme; YSU (pink), MYJ (green), and MYNN (blue), and shading in (a) corresponds to profiles shown in (b).

Given the low spread amongst common PBL scheme members in Fig. 5.3, the ensemble mean for each PBL scheme can be used for a more concise exploration of ensemble model behavior. Comparing the surface temperatures from the coastal and urban locations for the duration of the WoFS run, the warm bias found in the AMF profile comparison is shown throughout nearly the

full simulation run for each PBL scheme-specific ensemble mean at the coastal location (Fig. 5.4). At the urban site, the observed temperatures become greater than the modeled surface temperatures beginning just after 1900 UTC and continue to warm until 2230 UTC, leading to a change in the bias later in the simulation period. This is partially due to rain-cooled temperatures within the different ensemble members, evident via rapid reductions in temperature in the ensemble means, while the urban site did not receive rain to lead to cooling temperatures.

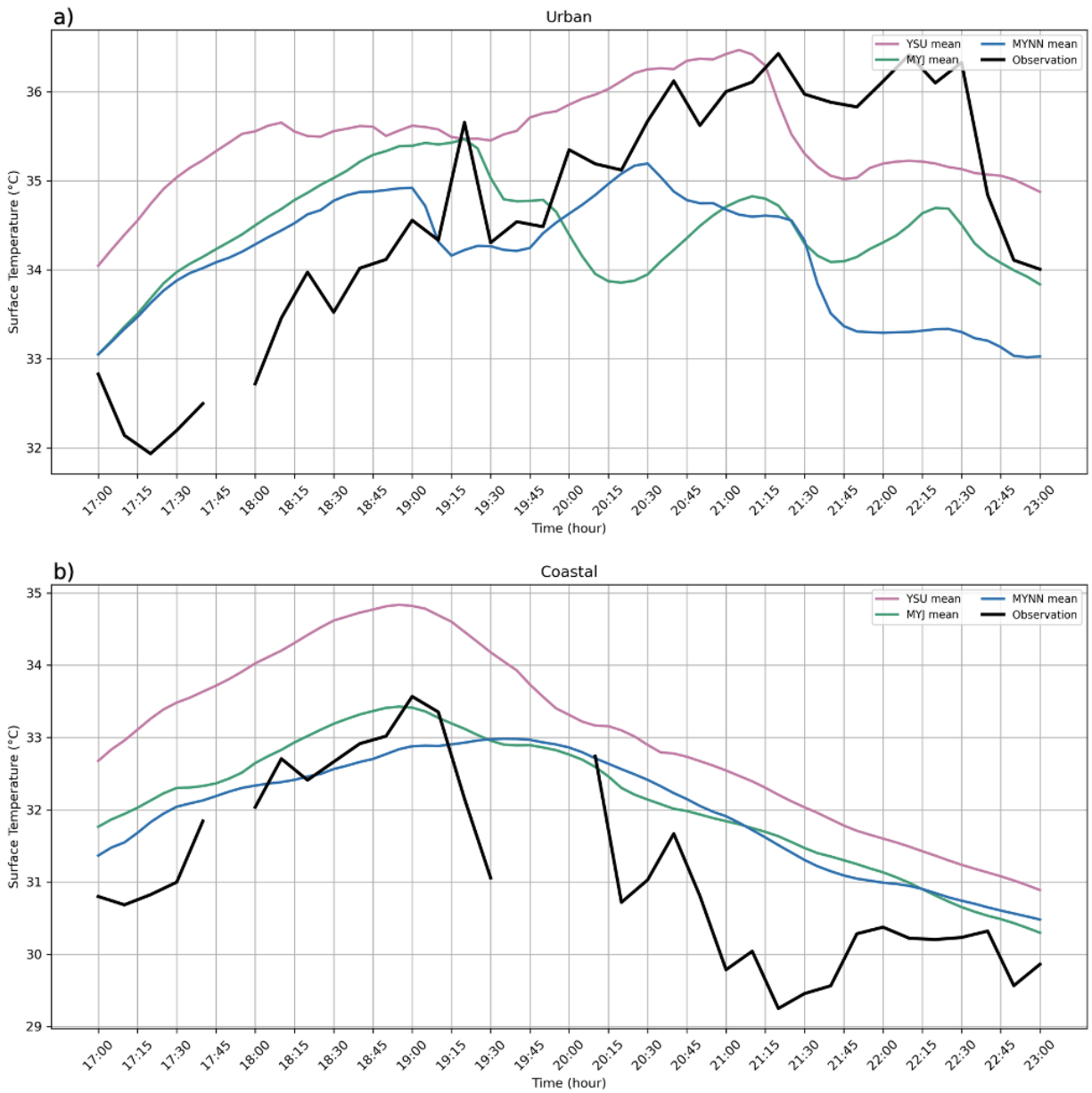


Fig. 5.4: Comparison of observed and WoFS PBL-scheme averaged surface temperatures for the duration of the simulation at the urban (a) and coastal (b) sites.

To further confirm the representative nature of the simulation run, identifying modeled SB occurrence in each ensemble member is necessary, as the SB is the key component of this case's observed PBL evolution and CI. The same multi-step approach to identify the SB that is described in Sect. 2.4 for the observational data is used to determine SB occurrence and passage times in the ensemble data, with the exception of radar reflectivity data. The numerical simulation is not of a

high enough resolution to resolve the low dBZ fine-line radar SB signature associated with the SBF. For the selected case, every ensemble member successfully depicts a SB, however, not all members show clear propagation of the SB through the entirety of the Houston region. Given the prevalence of convection throughout the Houston domain, tracking of the SB through the city is difficult to discern from potential thunderstorm and/or outflow influences in many members. Despite this, the SB passage is clear at the coastal location in all members, the exurban site in 13/18 members, but only discernible at the urban location in 2/18 members. Given that the SB passage is discernible at the coastal site for each member, site specific comparisons of observed and modeled SB modifications to the PBL will focus on this location. While some members do initiate convection along the coast, this occurs outside of the CUBIC domain (southwest and northeast), with most members producing CI further inland from the coastal site.

Within the ensemble, the timing of modeled SB arrival at the coastal location spans a 2-hour window, with an average arrival time of 1915 UTC and a bimodal peak in timing at 1900 UTC and 1945 UTC when binned into 15 minute periods (Fig 5.5). The observed SB passage occurs at 1847 UTC, so each of the ensemble members was within ~1 hr of the observed passage. The YSU scheme leads to earlier SB passage times than the more spread SB passage times of the MYNN and MYJ schemes (Fig. 5.5).

The earlier passage times for YSU members are coincident with greater surface and land-sea temperatures (Fig. 5.6). The ΔT is calculated at 1800 UTC, prior to SB passage, between a point in the Gulf and the urban location, consistent with the analyses in Sect. 2.3. The members in which the YSU PBL parameterization is used have an average ΔT of 1°C warmer (~8°C) than the other parameterizations (~7°C), showing that the earlier SB passage times are correlated with greater land-sea temperature differences. This finding is in line with the CUBIC onshore SB cases, in which a weak correlation ($r = 0.62$) between SB onset and land-sea temperature differences was found (see Sect. 2.4). The observed ΔT was 6.4°C at 1800 UTC, with 5/18 ensemble members simulating the observed ΔT within 0.5°C. Overall, one member's ΔT is too small, 5 members are within 0.5°C, and the remaining 12/18 members are too large; all YSU members are in this group.

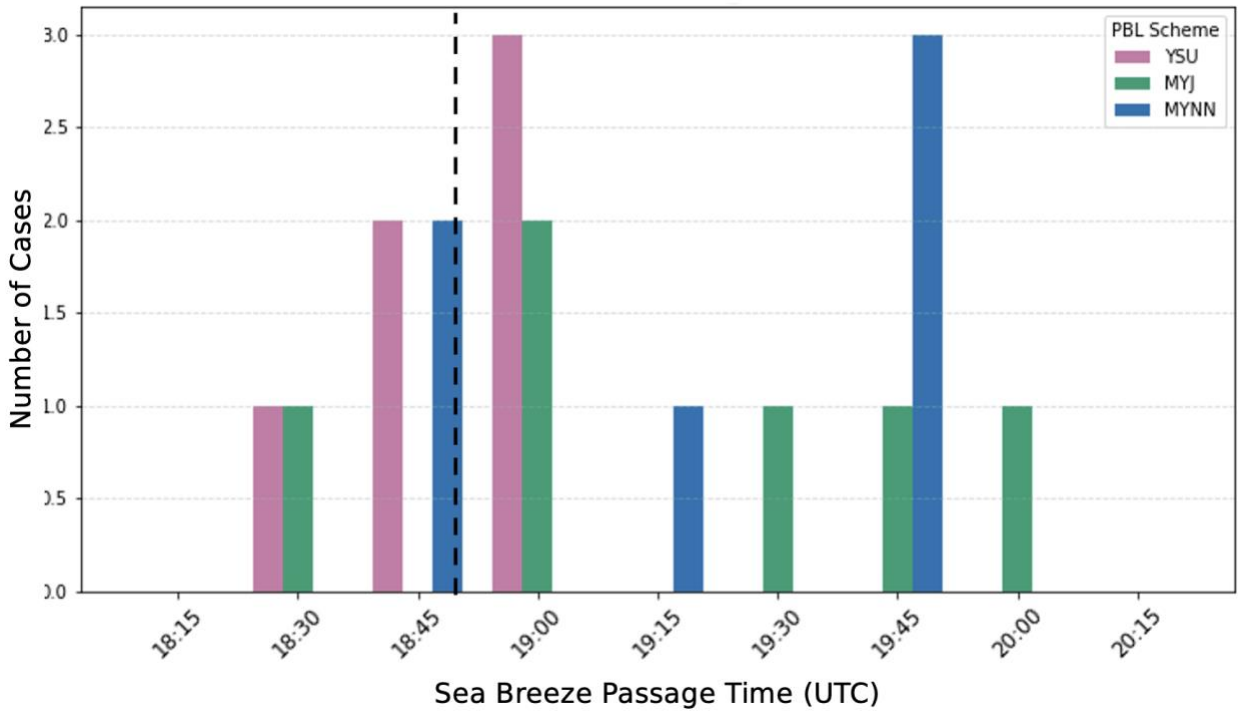


Fig. 5.5: Sea breeze passage times for each ensemble member at the coastal location. Colors correspond to the three different PBL schemes: YSU (pink), MYJ (green), and MYNN (blue). The black dashed line represents the observed SB time.

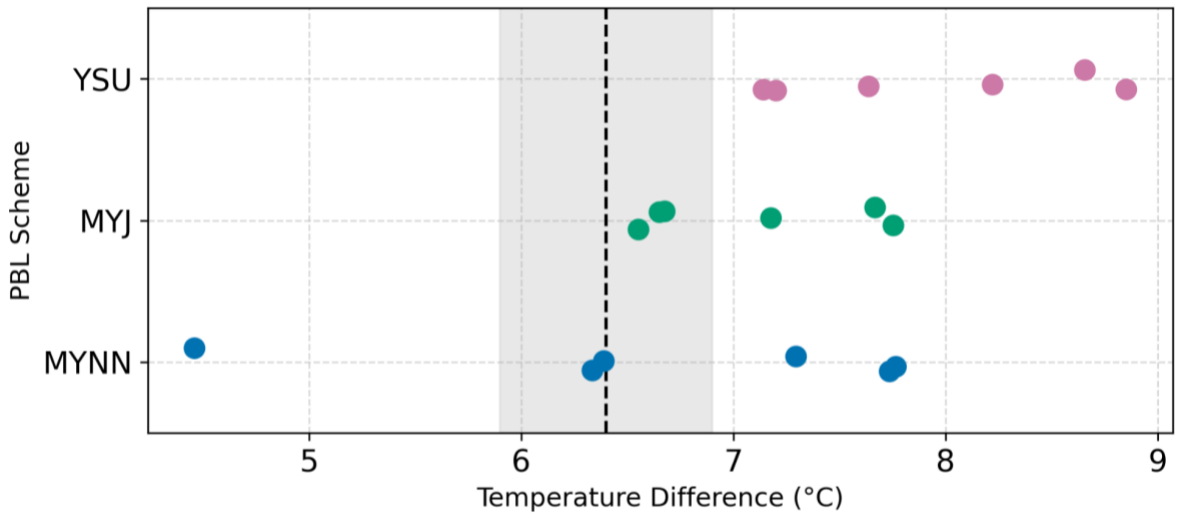


Fig. 5.6: Land-sea temperature differences for each ensemble member, separated by PBL schemes. The horizontal line indicates the observed value, while the light grey area corresponds to +/- 0.5°C of the observed value, and vertical displacement is done to mitigate overlapping points.

In Ch. 4, the case study analyses at the coast for 17 August 2022 showed several distinct PBL responses to the SB that were considerably stronger than those in the onshore composite analyses. This included an increase in horizontal wind speeds by > 2.5 ms^{-1}, rapid increase in water vapor mixing ratio greater than 8 gkg^{-1} throughout the lowest 1500 m, and a multi-degree drop in temperature also in the layer below 1500 m. To investigate the model's ability to simulate the SB well and capture the exceptional responses observed in this case, the modeled kinematic and thermodynamic responses to the SB are compared with the coastal observations. Comparing the modeled horizontal wind speed responses to the lidar observations show good agreement. While the observed wind speeds prior to the SB were lower than the majority of the ensemble predictions and differences can be noted when grouping simulation results based on PBL-scheme, the observed wind speed response to the SB falls within the middle of the ensemble envelope in the lowest 500 m (Fig. 5.7). Overall, the horizontal wind speed response across the model ensemble captures the shape and magnitude of the observed response.

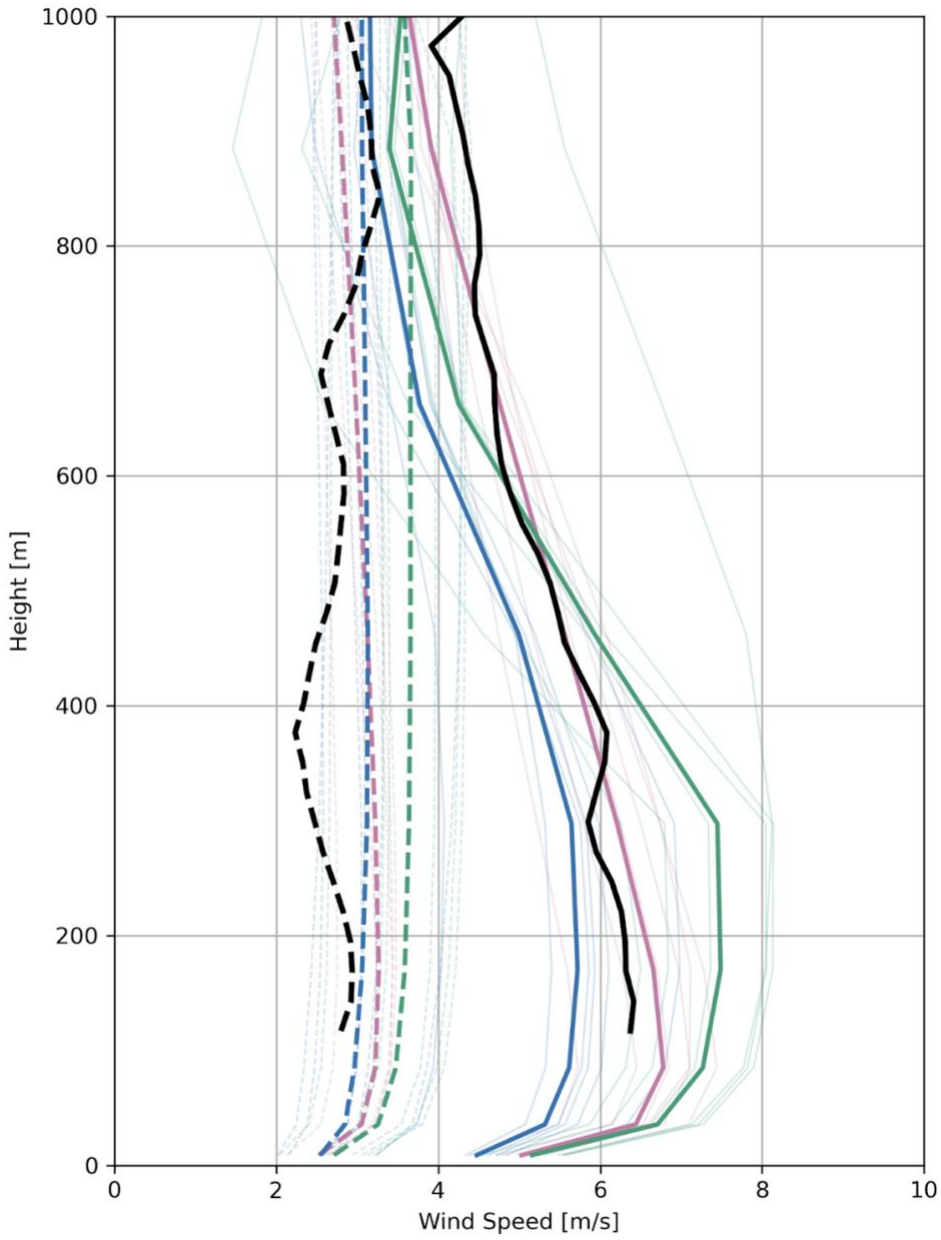


Fig. 5.7: Doppler lidar observed (black) and simulated (colored) wind profiles two hours before (dashed lines) and two hours after (solid lines) SB passage at the coastal site. Thick colored lines denote PBL-scheme averaged profiles and skinny lines represent each individual ensemble member. Colors represent different PBL schemes: YSU (pink), MYJ (green), and MYNN (blue).

The simulated thermodynamic responses show less agreement with observations and an increase in ensemble spread (Fig. 5.8). Given the simulated timing difference in the ensemble members, Figs. 5.8 and 5.9 show the time-height thermodynamic data, with observed and

simulated SB passage times indicated in each panel, so that one can examine the timing and magnitude difference in thermodynamic responses to the SB between the simulated and observed data. The observed temperatures cool by multiple degrees within the first 30 minutes post-SB passage in the layer from the surface up to ~1750 m. Additionally, by 2100 UTC (~2 hours after SB arrival), enhanced cooling occurs below 500 m, with surface temperatures dropping down to or below 302 K. The depth of the initial thermodynamic response to the SB in the model ensemble is generally underestimated, with many members only showing cooling up to 1000-1500 m, as opposed to the observed 1750 m. This difference in depth response can be attributed to the modeled SB depth, evident via the wind barbs shown in Fig. 5.8. Many members show the winds begin to veer to a west-northwesterly direction with height between 1250-1500 m, thus cooling from the SB would not extend beyond this depth. Again, there are some PBL scheme-specific differences amongst the ensemble members, with MYNN showing the least SB cooling. Each MYJ member depicts the enhanced cooling below 500 m, although the timing of the cooling relative to the SB passage time varies. While the ensemble members differ in their responses to the SB, in general, most members capture the more subtle initial drop in temperature and delayed enhanced cooling in the hours post SB passage.

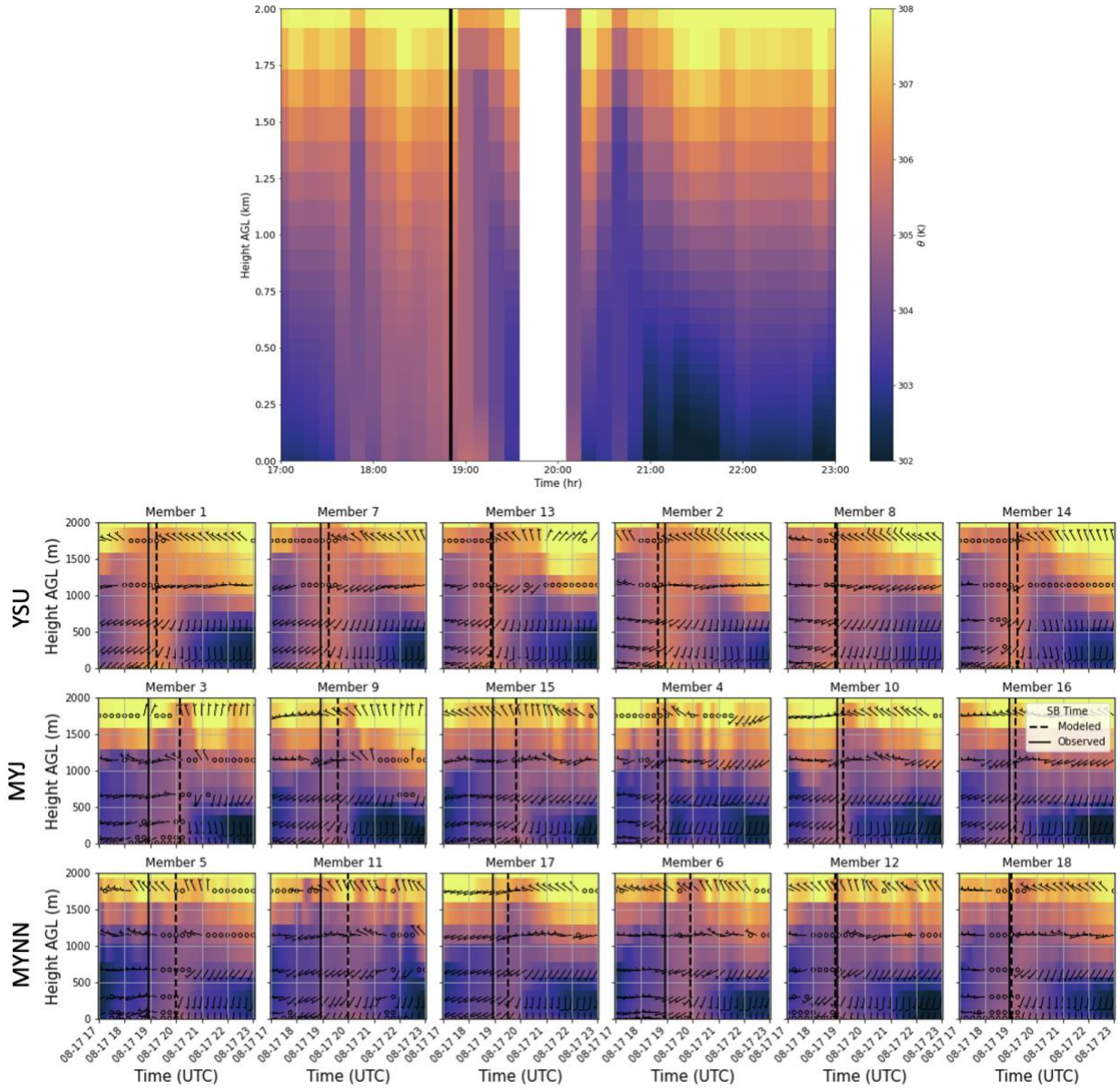


Fig. 5.8: Observed (top) and simulated (bottom) potential temperature for the duration of the simulation period (1700-2300 UTC). Solid black lines denote observed SB passage, dashed black lines depict modeled SB passage, and wind barbs are included on simulated subplots. The top row in the bottom half corresponds to YSU ensemble members, the middle row denotes MYJ ensemble members, and the bottom row shows MYNN ensemble members.

The greatest deviation from observations occurs with the modeled moisture, both with the pre-SB moisture content in the PBL and the underestimated SB moisture response (Fig. 5.9). In the observations, there is a rapid increase in moisture in the layer from the surface through 2000

m (strongest in the lowest 1000 m), increasing from ~16 gkg^{-1} to ~23-26 gkg^{-1}. Prior to the SB, most of the MYJ and MYNN members are too moist, some members by > 2 gkg^{-1} below 1500 m. Contrarily, the YSU members are closer to the observed pre-SB conditions, despite the previously established warm bias. Regardless of capturing the pre-SB moisture well, the YSU members show minimal and delayed increases in water vapor mixing ratio upon SB passage, with each member underestimating the increase in moisture. The MYJ ensemble members handle the moisture response the best, with five out of six members indicating a rapid increase in moisture content, particularly in the lowest 500-1000 m. The MYNN members have mixed results, with some members indicating no discernible moisture increase and some having delayed increases in moisture. Collectively, the ensemble spread for moisture responses to the SB is large, with no member able to capture the magnitude and timing of the observed moisture response in this case, but many members showing smaller increases.

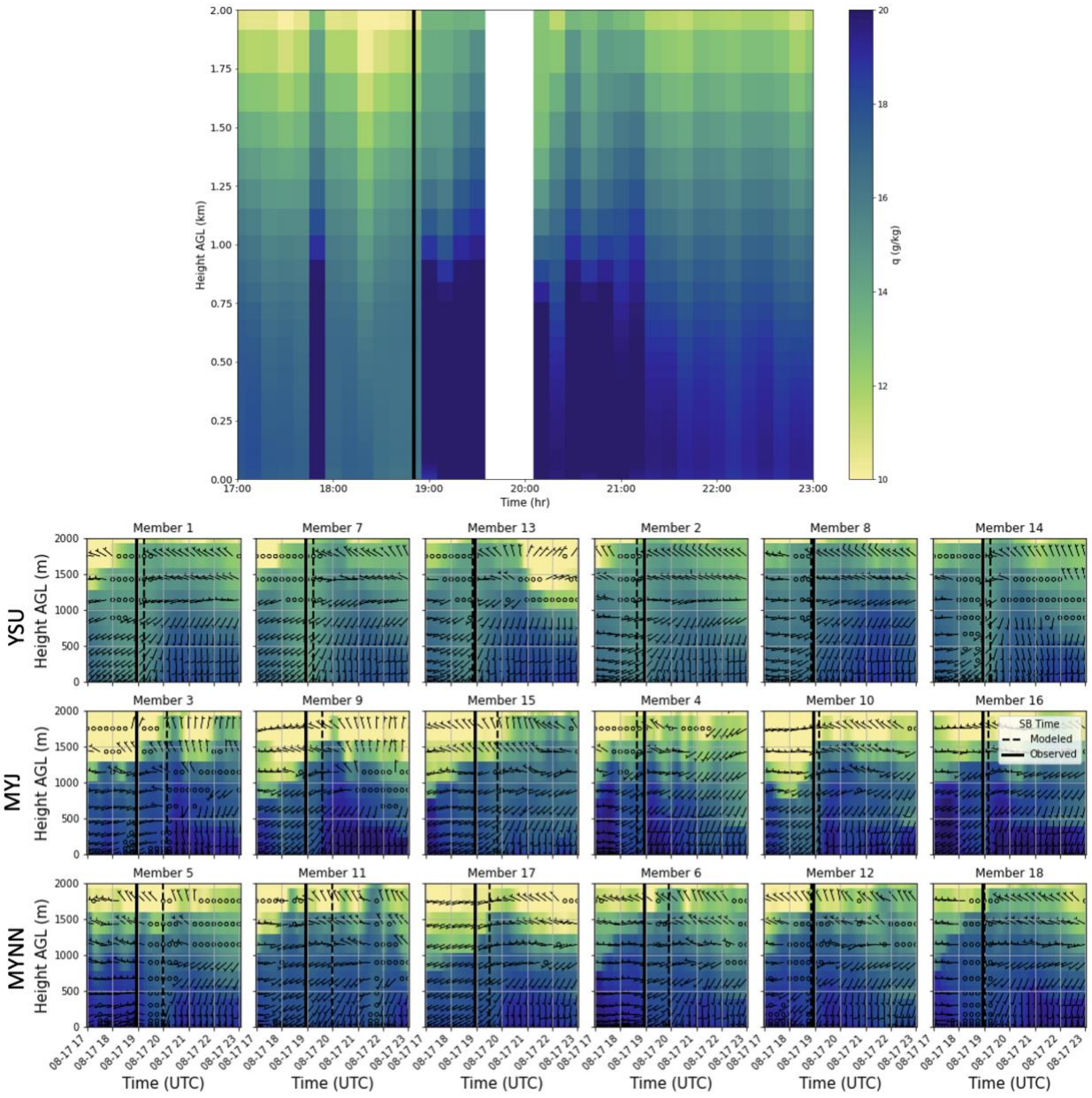


Fig. 5.9: Same as Fig. 5.8, but for water vapor mixing ratio.

Comparisons of the PBL responses to SB passage highlight that while the kinematic signatures are well represented, the thermodynamic responses are not captured as well. The ensemble simulations broadly succeed in capturing the occurrence and timing of the SB, though with notable variability across PBL schemes and some discrepancies relative to observations. All members depict the SB passage at the coastal site, with propagation inland becoming increasingly ambiguous due to simulated convection and outflow interactions. Simulated cooling is limited to

a shallower layer than observed and all members underestimate the observed rapid moistening. These results show that the ensemble can reliably reproduce the dynamical structure of the SB, but may struggle with the thermodynamic impacts, particularly moisture transport, which has significant implications for CI. However, the model spread in thermodynamic responses does allow for the further examination of CI success or failure, given the slightly differing environments and progression of the SB, which will be explored in the next section. Building from this foundation, the next section explores the hypothesis introduced in section 5.1 that CI depends on two mechanisms: (i) forced ascent at the coast acting to establish a moist air mass and (ii) advection of the air mass inland destabilizing the environment such that persistent forced ascent inland is not required for CI.

5.5 Mesoscale Process Investigations - Sea Breeze Spatial Evolution and Convection Initiation

As discussed in Sect. 5.1, past work focused on SB-CI has shown that increased low-level moisture and ascent can both be important factors for successful SB-CI to occur. The 17 August 2022 case observations showed rapid increases in moisture upon SB passage, which several ensemble members were able to simulate, although not of the correct magnitude. Additionally, the simulated wind speed response at the coast was comparable to the observed response at the coast, indicating that the model is able to capture the SB and thus can be used for further investigations into the convection evolution. The 4-D model data allows for investigations across space, enhancing our knowledge of the SB processes and their evolution as the SB propagates inland and further allows for investigations of post-SB destabilization in the region. These investigations provide a critical link between the simulated (and observed) SB-forced PBL modifications and the convective outcomes.

The following analyses will use a variety of methods, including nearest point profiles, spatial plots, and vertical cross sections that are drawn perpendicular to the coast between points corresponding to locations urban site (30.13°N, -95.44°W) and southeast of the coastal site (29.07°N, -94.79°W, Fig. 5.10). To simplify the analysis, the first 6 ensemble members corresponding to one of each of the physics combinations available in WoFS are shown (the

remaining 12 members repeat these configurations with perturbations added). This method is used instead of PBL parameter-specific ensemble means to mitigate possible dilution of signal caused by different SB passage times. Recalling from table 5.1, the first six ensemble members used the following physics parameterizations: three PBL schemes (YSU, MYJ, and MYNN) and two shortwave and longwave radiation schemes (Dudhia/RRTM or RRTMG/RRTMG). Moving forward, a shorthand nomenclature will be used for brevity when referring to these ensemble members: YSU-D/R, YSU-R/R, MYJ-D/R, MYJ-R/R, MYNN-D/R, and MYNN-R/R.

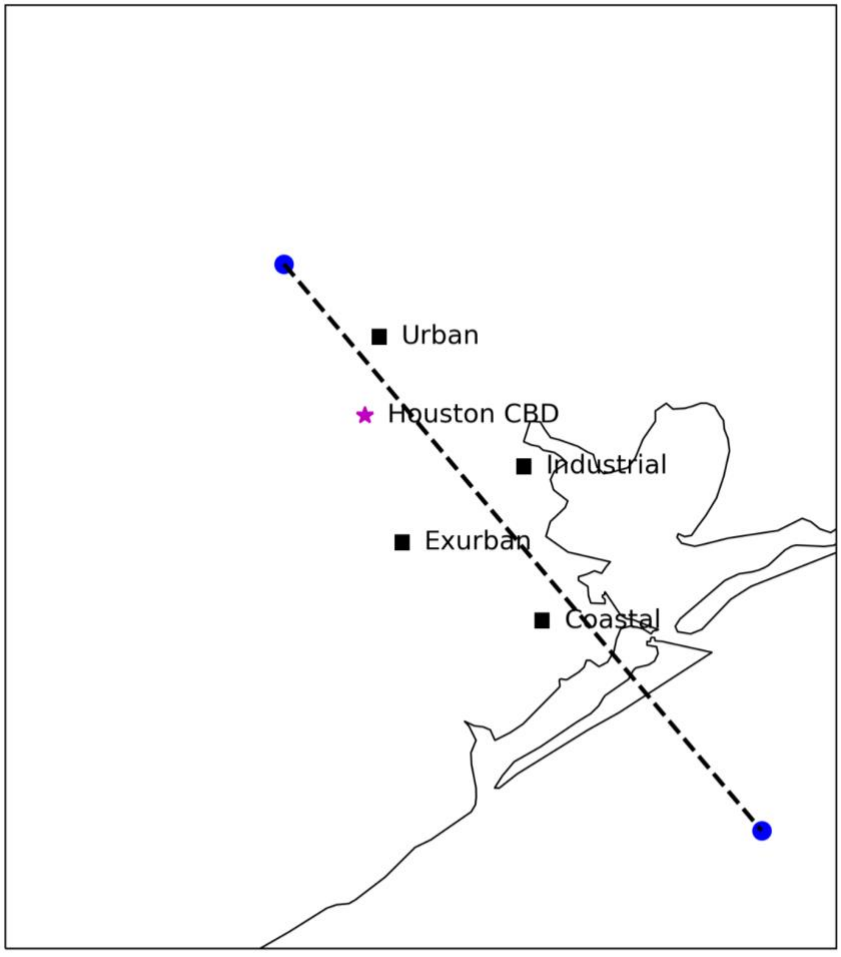


Fig. 5.10: Depiction of vertical cross section path (dashed line) across Houston CBD showing the start and end points (blue dots) to the southeast of the coastal site and northwest of the urban site, respectively.

Given the hypothesis that forced ascent along the SBF plays a key role in priming a moist air mass conducive to CI, it is essential to first compare the observed ascent at the coast to the modeled ascent then move to examinations of the spatial evolution of the ascent as the SBF propagates inland. In comparing the ascent at the coastal site, the observations indicate strong and persistent upward motions at and behind the SBF that are > 2 ms^{-1} (Fig. 5.11). A similar signature is apparent in four out of the six ensemble members: YSU-D/R, YSU-R/R, MYJ-D/R, and MYNN-R/R. However, none of these members indicate the correct magnitude of the upward motions, maximizing at 1.5 ms^{-1}or lower. The YSU-D/R is particularly weak, < 0.5 ms^{-1}, but the duration of the upward motion signature is similar to the observations, indicating persistent ascent as the SBF passes over the site. The MYNN-D/R member shows a shallow and weak updraft signature shortly after the SB passage, but overall does not indicate persistent ascent along the SBF. While the MYJ-R/R member indicates ascent at the SBF, it is of the same magnitude and duration as updrafts well after the SB passage, which suggests the updraft may not be solely tied to the SBF alone.

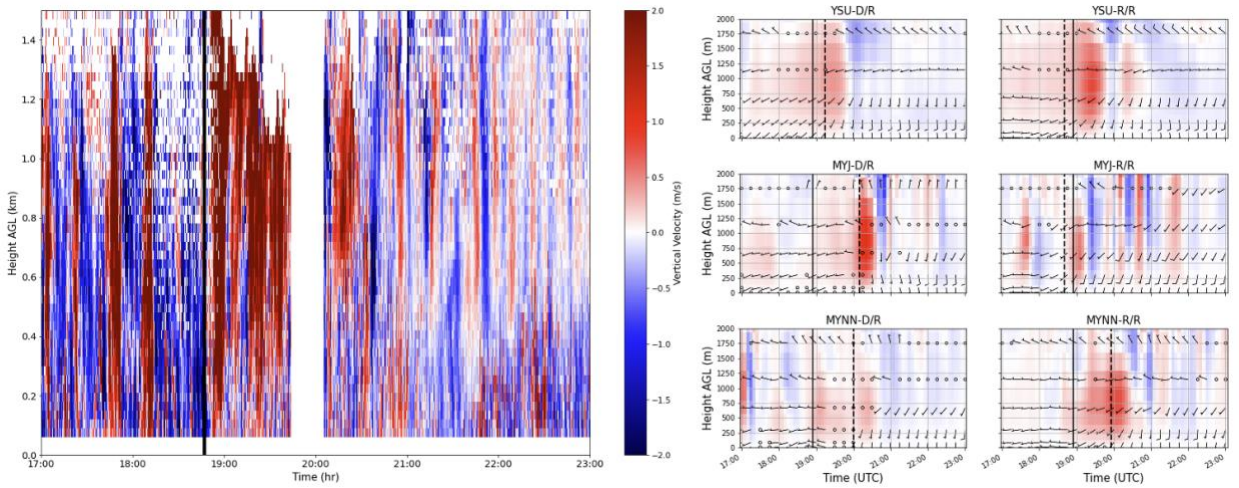


Fig. 5.11: Observed (left) and simulated (right) vertical velocity through duration of simulation period (1700-2300 UTC). Solid black lines denote observed SB passage, dashed black lines depict modeled SB passage, and wind barbs are included on simulated subplots.

Examining the ascent signals across space, at 1910 UTC, the SB has begun to propagate inland and is near the coastal site in the following members: YSU-D/R, YSU-R/R, and MYJ-R/R. The YSU-R/R member shows a clear updraft signature along the well-formed SBF, with updrafts

through 2000 m (Fig. 5.12; black boxes). While the YSU-D/R member shows weak upward motions further inland, there are no indications of forced ascent along the SBF at this particular time. In the MYJ-R/R member, there is an indication of a weak (~0.5 ms^{-1}) updraft along the leading edge of the SBF, although this member's environment has likely already been modified by nearby convection. An hour later, the SBF has reached the coast in each member, with updraft signatures > 0.5 ms^{-1} reaching over 2000 m in three of the six members (YSU-D/R, YSU-R/R, and MYJ-D/R; Fig. 5.13). The MYNN members do not show strong signals of SB frontal ascent, only shallow and weak signals that are not persistent at the leading edge of the SB along the coastal region. Therefore, four of the six ensemble members (YSU-D/R, YSU-R/R, MYJ-D/R, and MYJ-R/R) clearly indicate strong SBF ascent at the coast, prior to the inland propagation of the SB. Of note, the MYNN-R/R member showed clear, persistent ascent in Fig. 5.11 but not in Figs. 5.12 and 5.13. The vertical cross section path is slightly displaced from the exact coastal observation location, which suggests that the frontal ascent may not be consistent along the entirety of the SBF. Additionally, by 2010 UTC there has been CI in both the MYJ-R/R and MYNN-R/R members, modifying their nearby environments and potentially affecting the inland propagation of the SBF and any associated ascent signature.

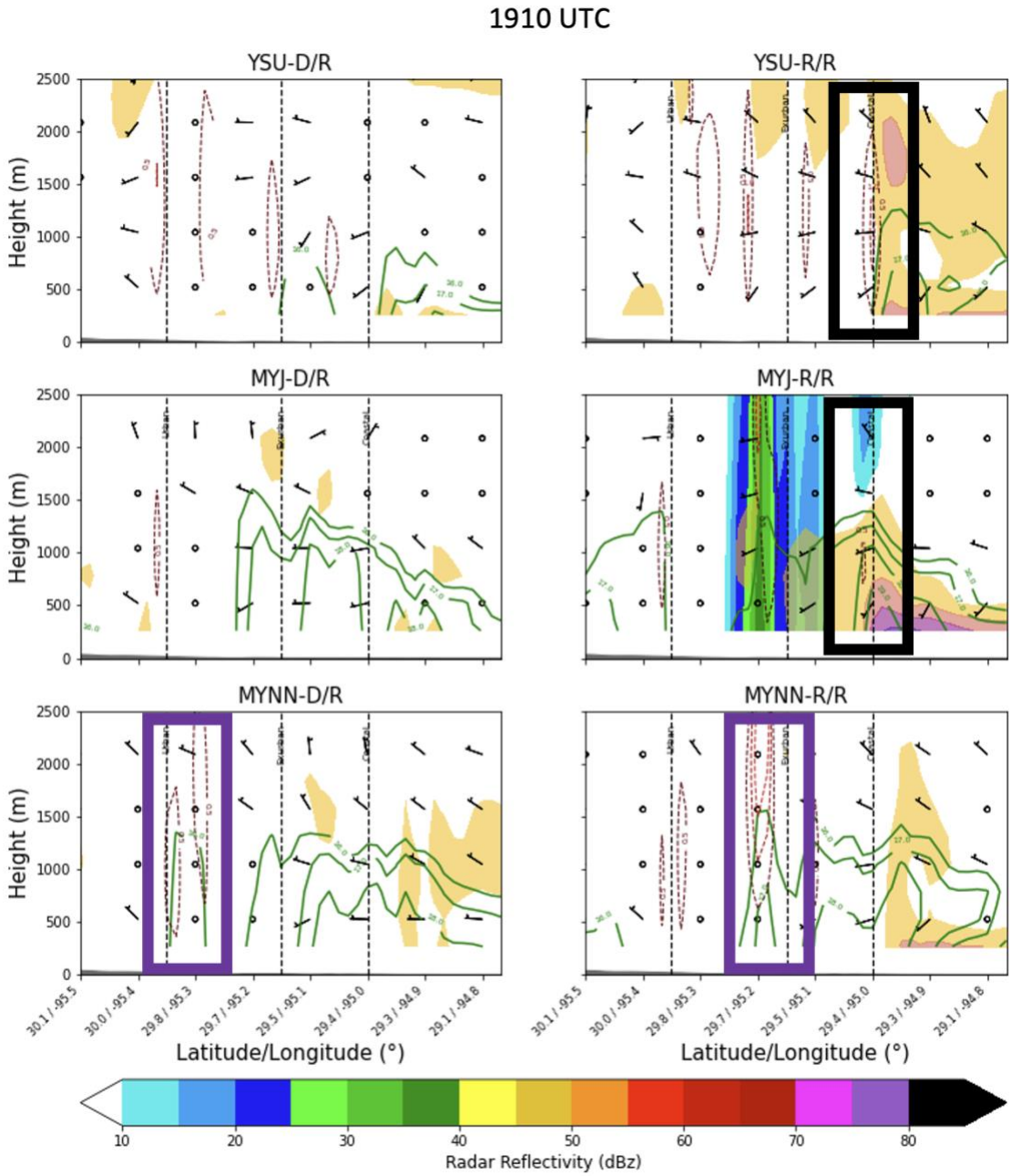


Fig. 5.12: Vertical cross section at 1910 UTC depicting wind barbs, updrafts > 0.5 ms^{-1} (red dashed contours), water vapor mixing ratio > 16.0 gkg^{-1} (green contours), horizontal wind speed > 4 ms^{-1} (warm colored filled contours), and radar reflectivity > 10 dBz (filled contours). Black boxes denote updrafts along SBF while purple boxes show updrafts ahead of SBF but associated with the leading edge of moist airmass.

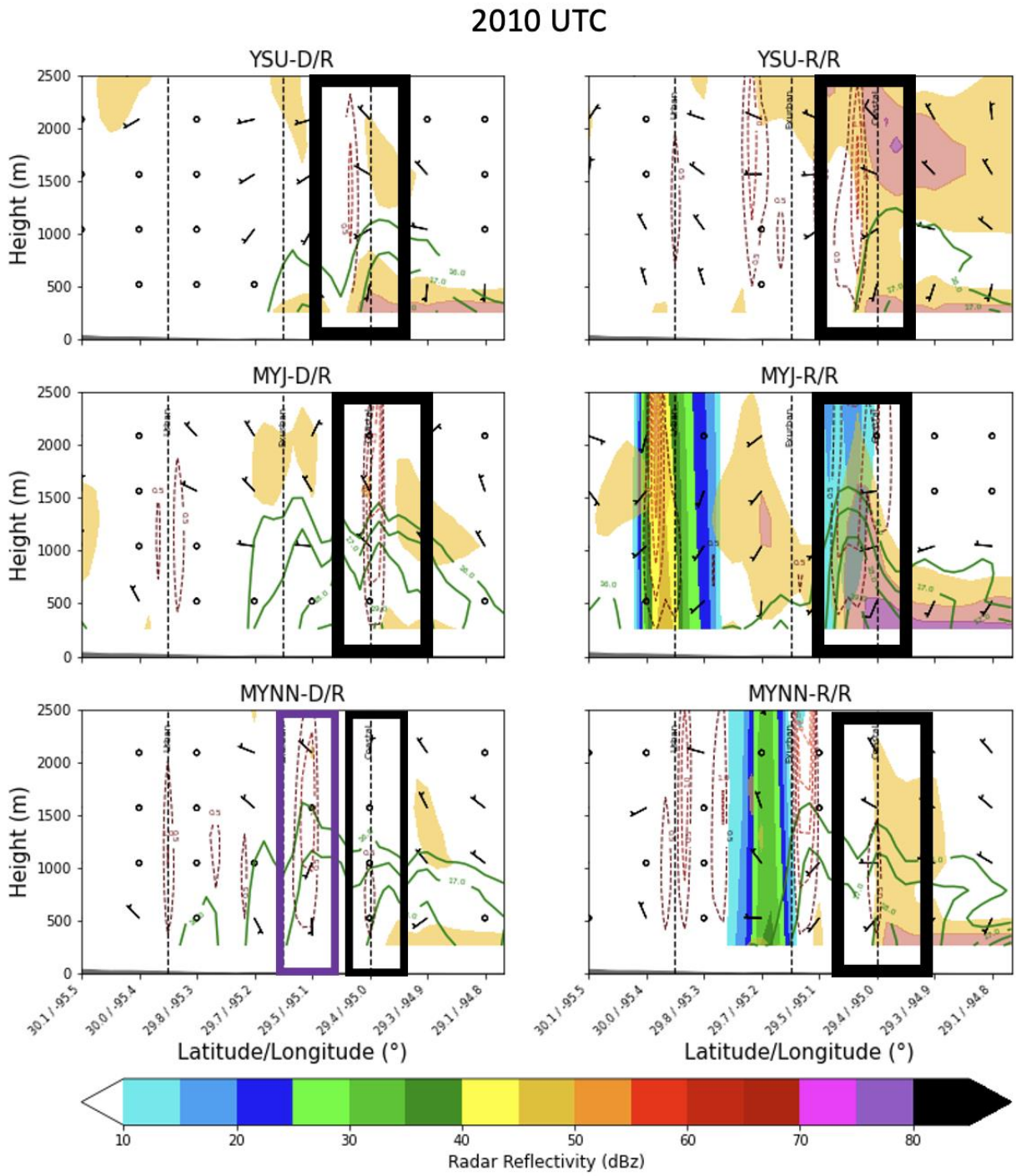


Fig. 5.13: Same as Fig. 5.12, but at 2010 UTC.

As the SBF propagates inland, there is no persistently forced updraft present in the YSU ensemble members (Figs. 5.14 and 5.15). These members also do not initiate convection within the CUBIC domain. However, the MYJ-D/R and both MYNN members do show evidence of

updrafts through time as the SBF moves inland, though these updrafts tend to modulate and are sometimes displaced slightly ahead of the front (Figs. 5.12 and 5.13; purple boxes). Regardless, these three members show persistent ascent that propagates inland with the SB, which differs from the point observations that show no discernible updraft inland at the urban location. By 2230 UTC, both the MYJ-D/R and MYNN-D/R members have CI that has occurred along the cross-sectional path and in association with the SB. These cross-section analyses show that the ensemble members that initiate convection show more persistent updrafts associated with the inland propagating SBF, while the members that lack persistent updraft signatures fail to produce CI even if they showed clear ascent at the coast. These findings suggest that persistent ascent along (or ahead of) the SBF as it propagates inland is an important process for CI to occur and disproves our hypothesis that ascent at the coast to establish a moist air mass and vertically advect the moisture is more important than sustained ascent. In future studies, it should also be investigated to what extent the UHI plays a role in modifying the vertical distribution of moisture with the inland propagating SB.

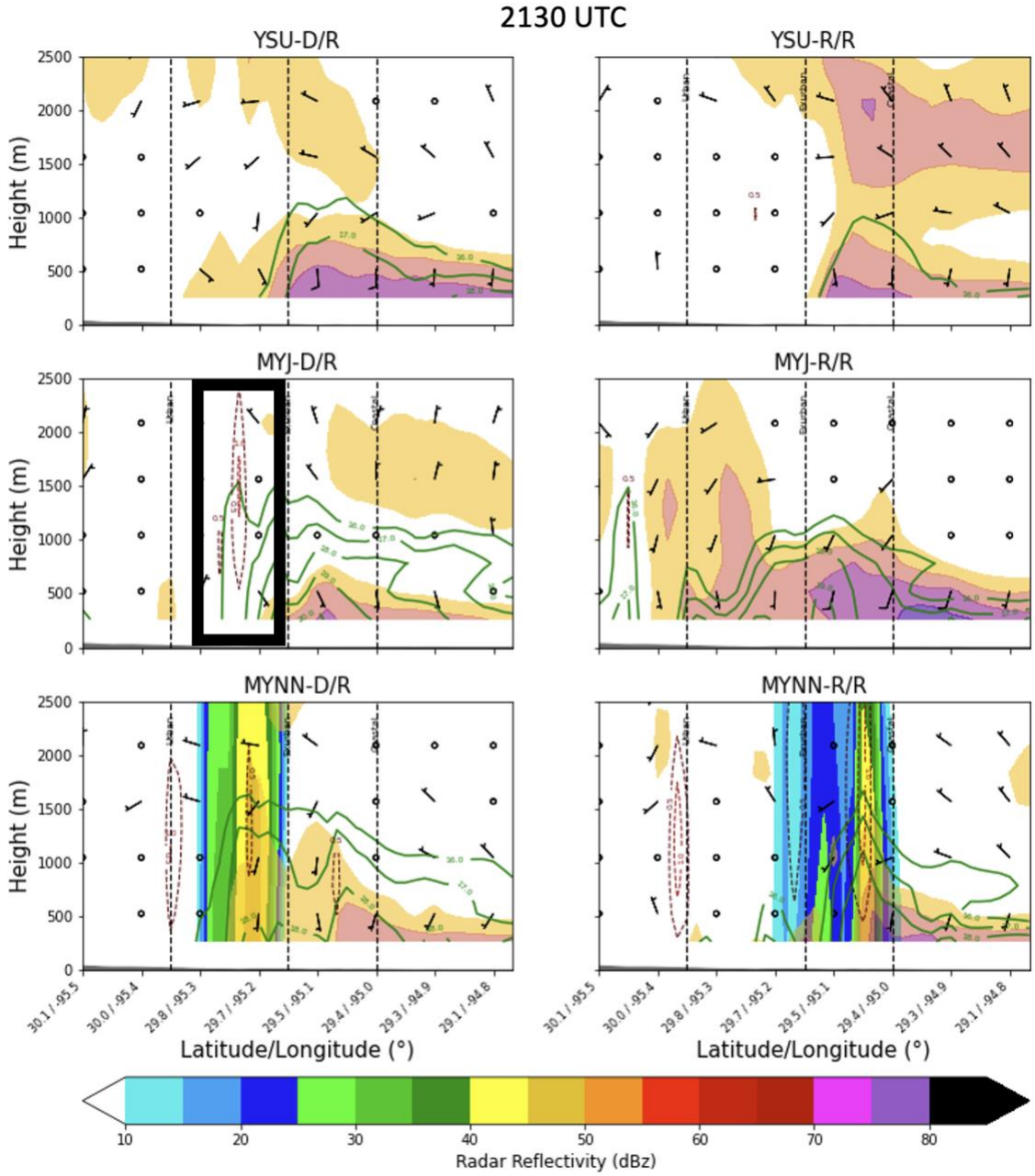


Fig. 5.14: Same as Fig. 5.12, but at 2130 UTC.

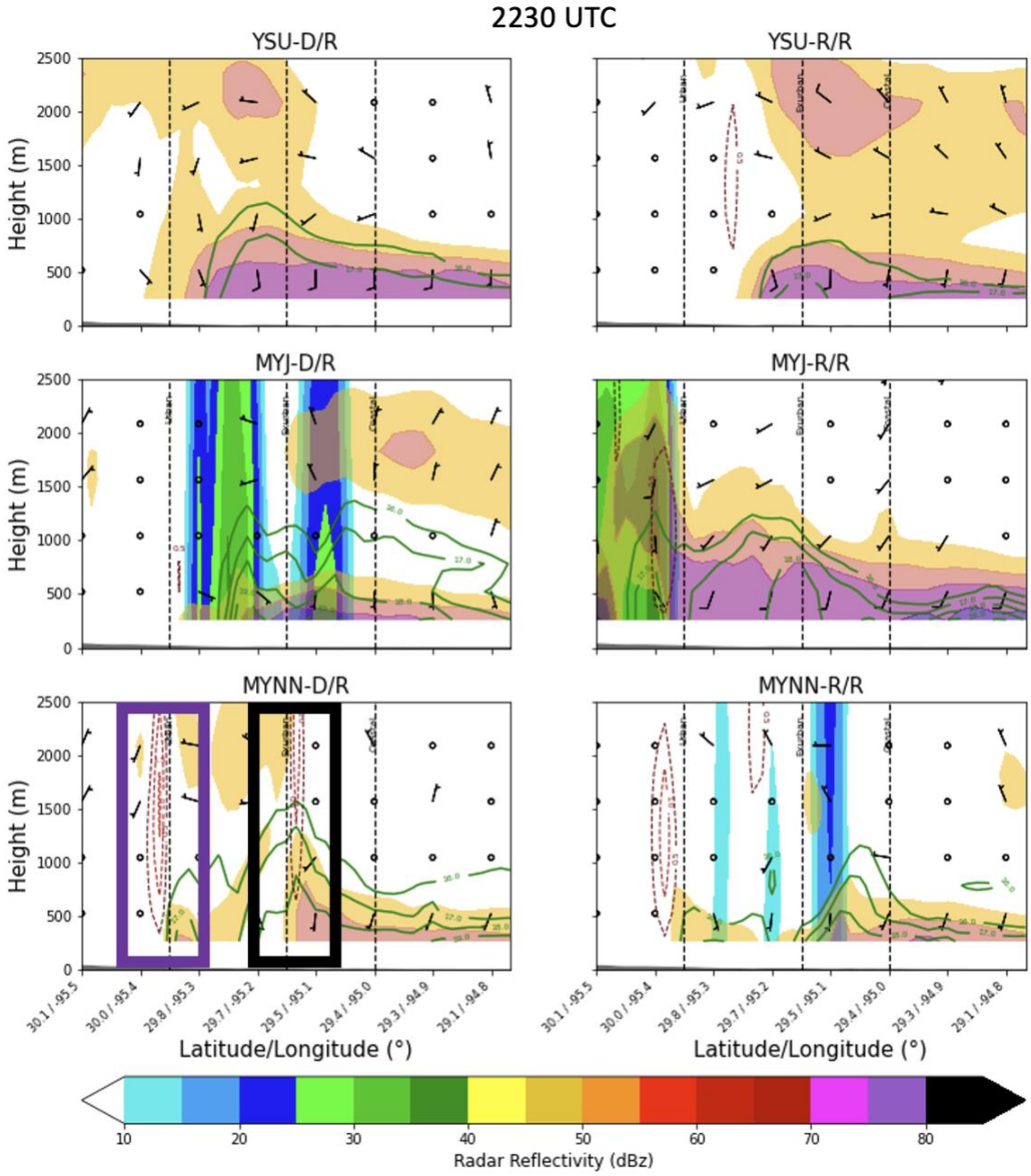


Fig. 5.15: Same as Fig. 5.12, but at 2230 UTC.

While the previous analyses showed that the forced ascent at the coast is not what establishes the elevated moist air mass, the coastal water vapor mixing ratio analyses from Sect. 5.4 indicates moistening of the environment post-SB; thus the expectation for a moist air mass is still prevalent. Furthermore, the observations of the moisture from the coastal and urban sites in Ch. 4 indicate that the thermodynamic response to the SB may weaken inland, but it does become

more concentrated within a shallower layer as the SB propagates inland. This finding is attributed to the continuous mixing of the continental and SB air masses as the SB propagates inland, modifying the SB inflow layer. The second mechanism hypothesized to be important to the CI in this case is the advection of the elevated moist air mass inland which is able to then destabilize enough that the forced ascent inland is not necessary for successful CI. Again, while the ascent at the coast is not responsible for priming the air mass, there is still evidence of a moist air mass; thus, the advection of this moist air is still expected. In the following analyses, the evolution of water vapor mixing ratio is examined across space to examine whether evidence of a concentrated layer of moisture forms as the SB propagates inland.

The advection of the moisture inland as the SB propagates shows differing evolutions across the ensemble members (Figs. 5.16-5.19). Among the YSU members, there are indications of a more concentrated air mass as the SB propagates inland. The MYJ and MYNN members show no discernible weakening or development of a more concentrated moist layer, although the progression of the moist layer across the domain is limited due to CI along the path of the cross-section. In these members, each shows a relatively consistent moisture gradient through space up until convection occurs, suggesting that as the moist air mass advects across the domain, no perceptible weakening is taking place. These members also exhibit more moisture in place throughout the simulation period, which suggests that the spatial moisture distribution prior to the SB is important. As unveiled in the previous analyses, the ensemble members that produce convection also exhibited more prominent ascent, which can deepen the pre-existing moisture. In this case, the pre-existing environment is important for the SB to successfully prime the environment enough for CI to occur (i.e., moisten and destabilize), which is also aided by more vigorous ascent. Thus, while priming the moist air mass by the SB is critical and aided by persistent ascent, there must be pre-existing, supportive moisture ahead of the SB for CI to successfully occur, which partially disproves the original hypothesis.

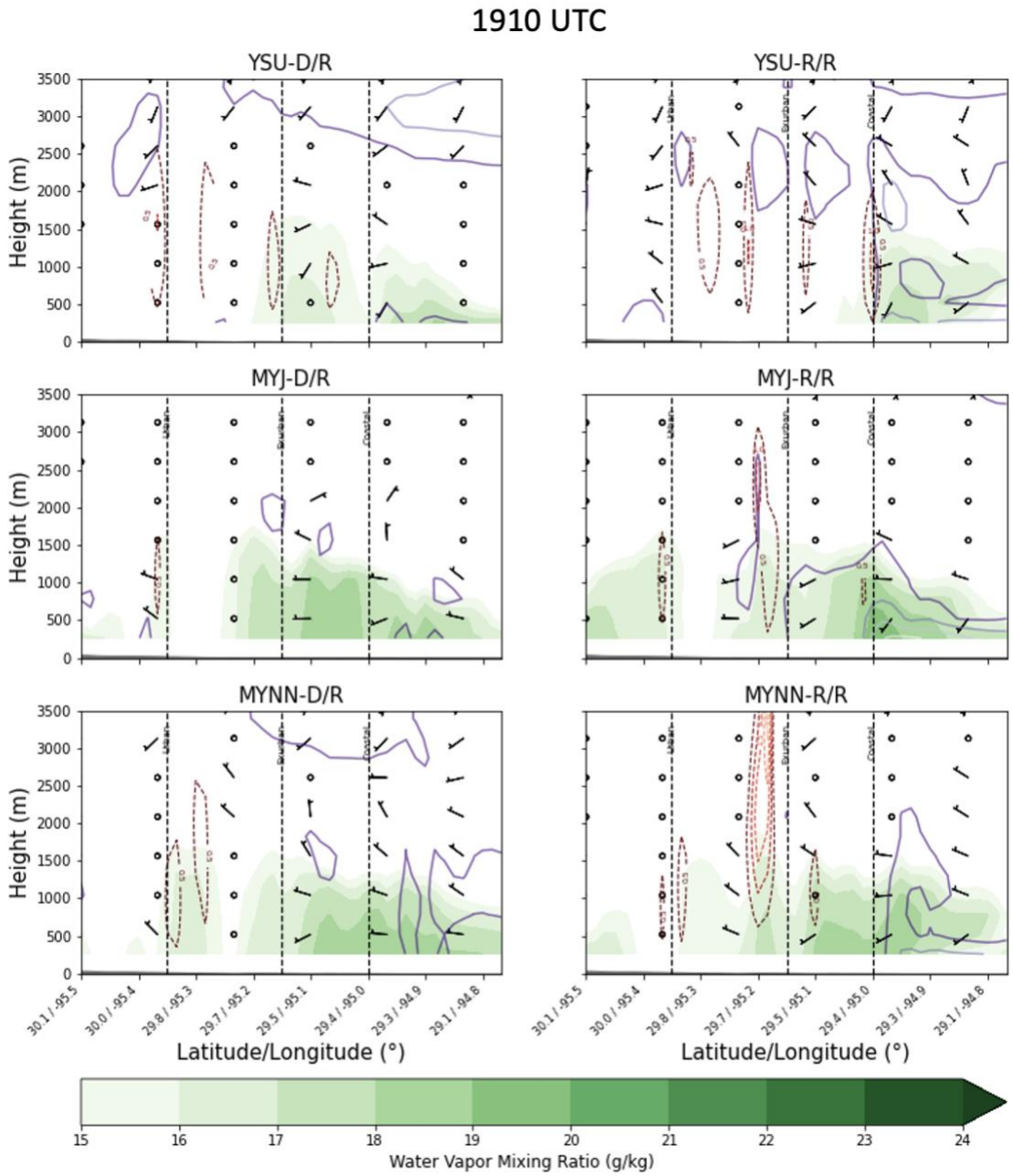


Fig. 5.16: Vertical cross section at 1910 UTC depicting wind barbs, updrafts > 0.5 ms^{-1} (red dashed contours), horizontal wind speed > 4 ms^{-1} (purple contours), and water vapor mixing ratio > 15 gkg^{-1} (green filled contours).

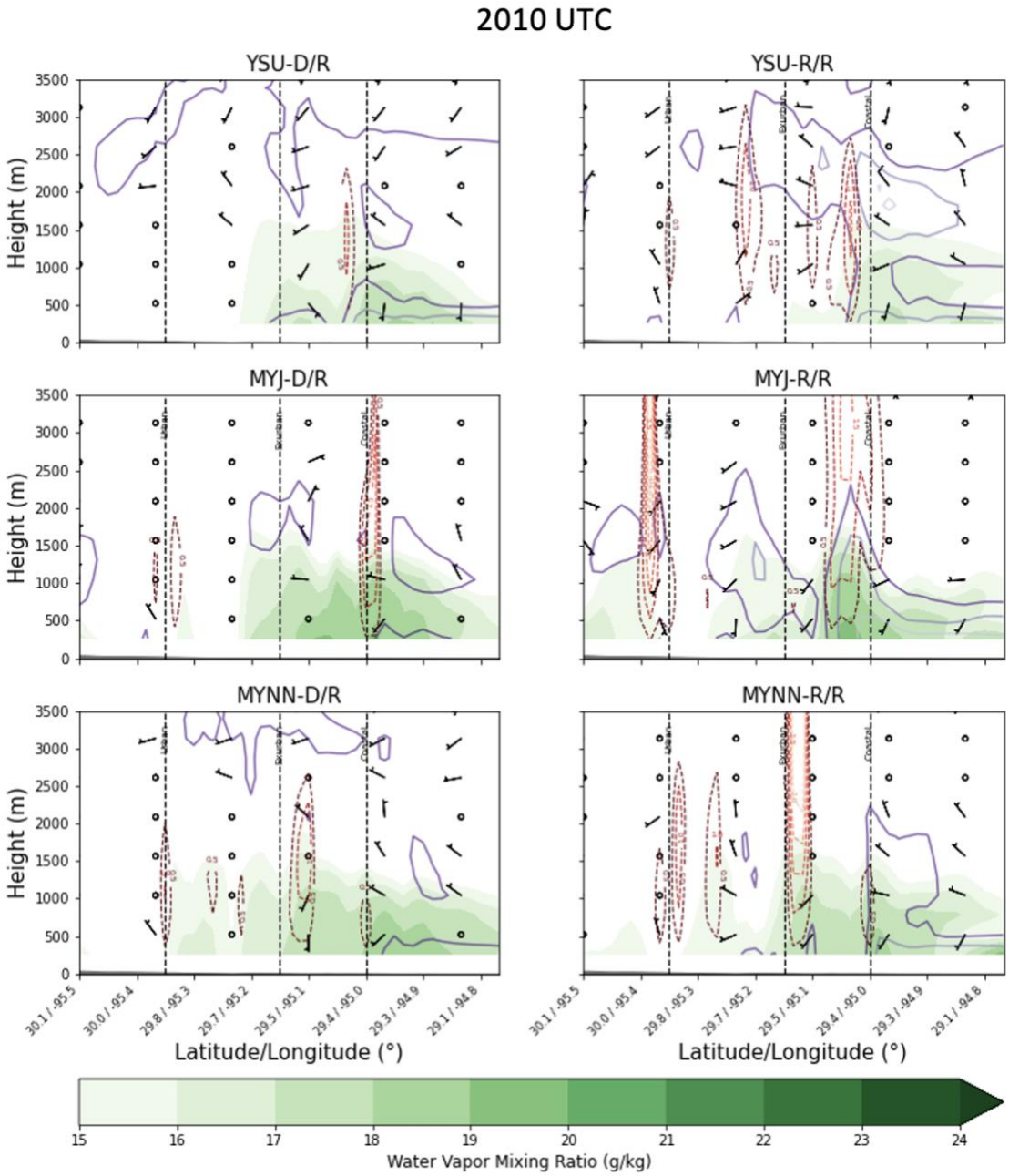


Fig. 5.17: Same as Fig. 5.16, but at 2010 UTC.

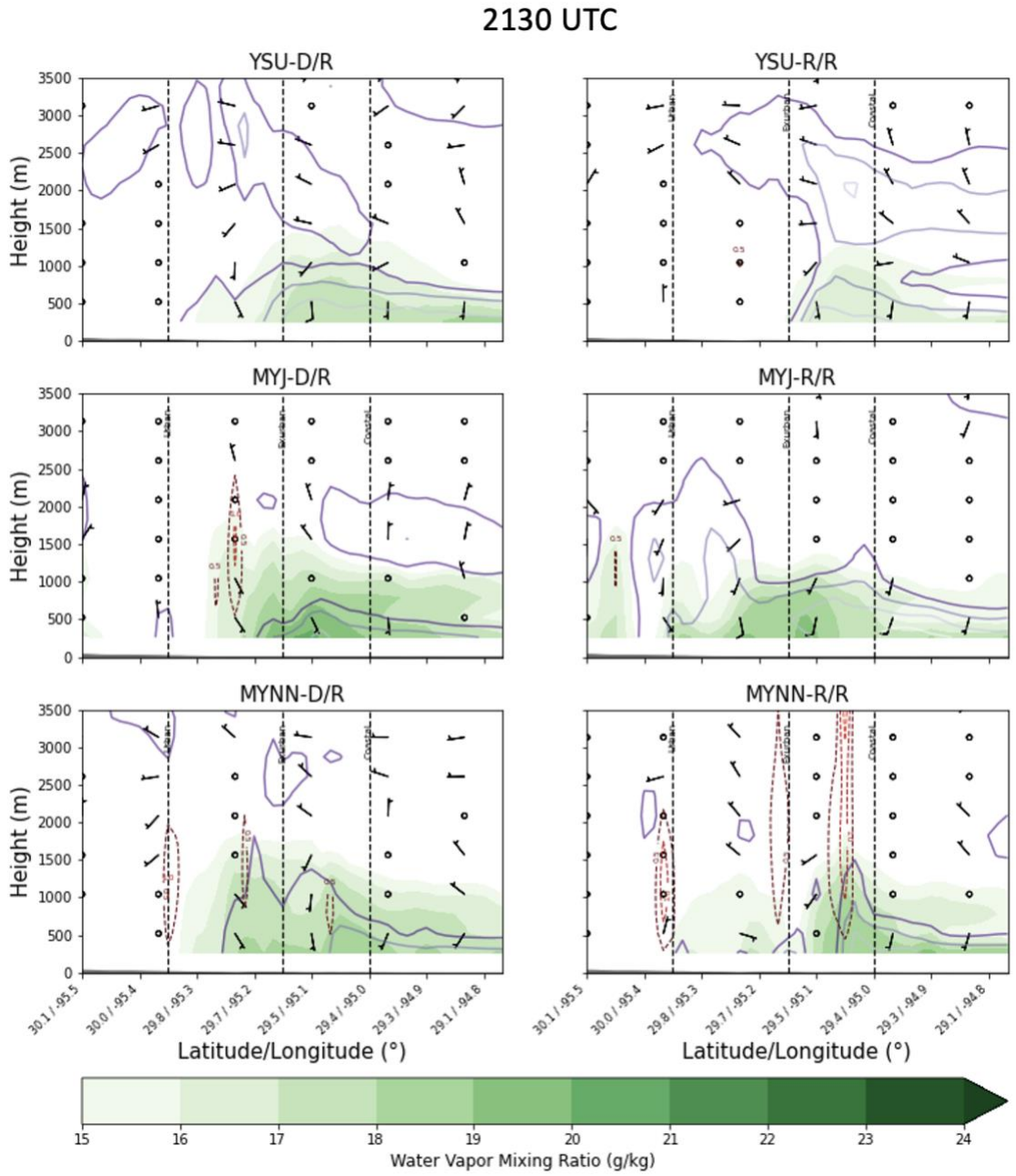


Fig. 5.18: Same as Fig. 5.16, but at 2130 UTC.

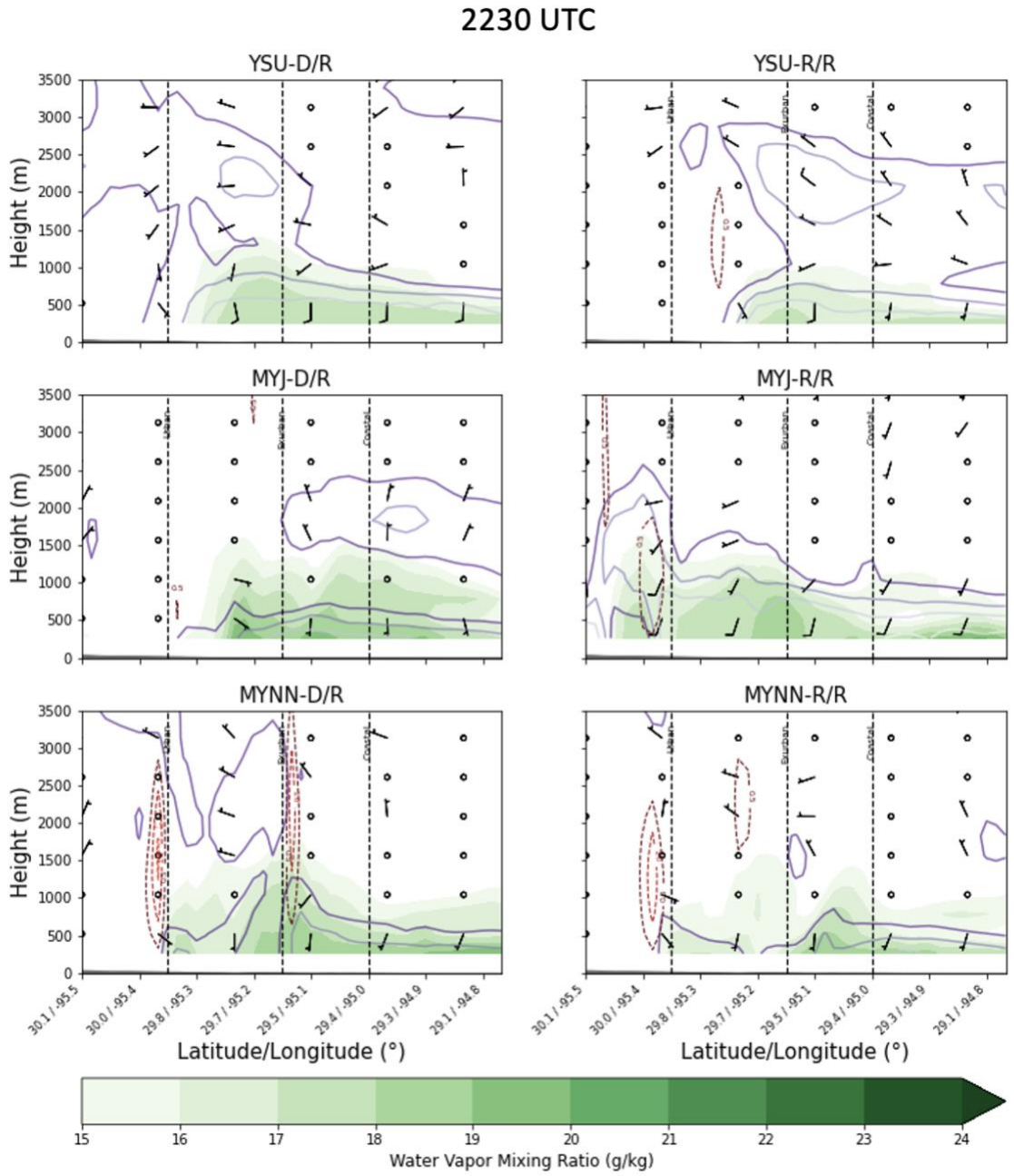


Fig. 5.19: Same as Fig. 5.16, but at 2230 UTC.

The final process of the hypothesis that has not been explicitly examined yet is the destabilization behind the SBF in connection with both the inland propagation of a MAHTE within the SB layer and the advected drier air mass by the return flow aloft. Based on our hypothesis and the expectation of the closed SB circulation shown in Ch. 4, it is anticipated that the moisture advection, and therefore priming, is further enhanced by the return flow. Equivalent potential

temperature (θ_e), which is a conserved quantity that reflects the effects of both temperature and moisture, is a useful diagnostic tool for identifying air masses with enhanced convective potential (i.e., destabilization; Hanft and Houston 2018). In the following analyses, the evolution of θ_e is examined across space to examine whether evidence of a destabilized air mass is present behind the SBF. Tracking θ_e as the SB moved inland also highlights regions where marine inflow and SBF ascent have combined to moisten and destabilize the environment for successful CI.

The propagation of the SBF across the Houston domain does show a MAHTE of varying strength behind the SB within each ensemble member (Figs. 5.20-5.23). Similar to the moisture evolution shown above, the MAHTE in the YSU members is much weaker than in the MYJ and MYNN members. However, there is clear evidence of the advection of drier air with the return flow, apparent via the quick decrease in θ_e just behind the SBF and above the MAHTE. Meanwhile, the MYJ and MYNN members show a stronger MAHTE behind the SB that propagates inland and is further modified through time by the local CI that occurs. These members show varying effects from the return flow, with MYJ-D/R and MYNN-D/R members indicating possible return flow enhanced destabilization prior to CI, but the MYJ-R/R and MYNN-R/R members not showing a clear signature. Thus, while each ensemble member shows a MAHTE behind the SBF, indicating some destabilization behind the front, the advection of the return flow aloft is not always present to enhance the destabilization.

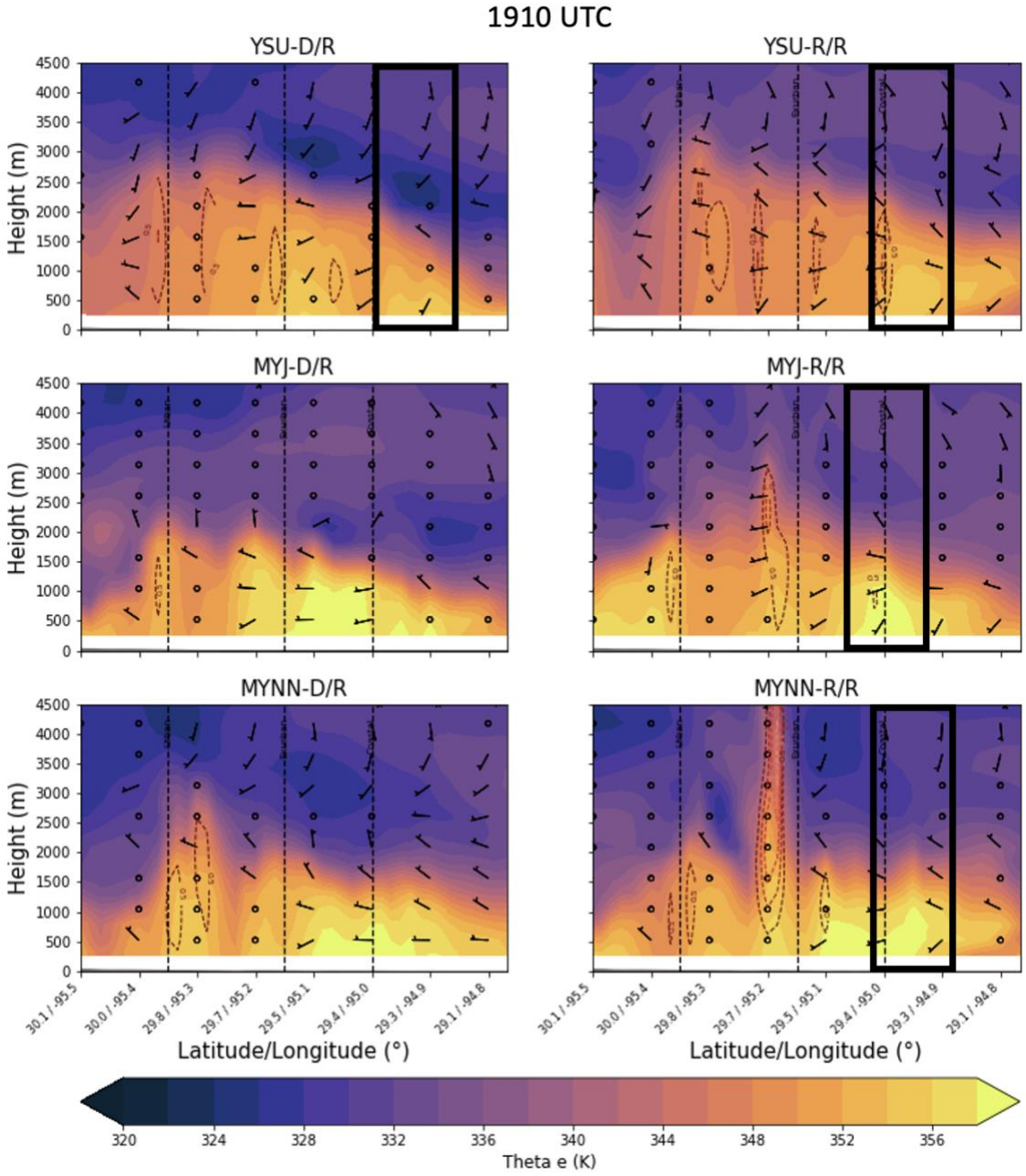


Fig. 5.20: Vertical cross section at 1910 UTC depicting wind barbs, updrafts > 0.5 ms^{-1} (red dashed contours), and equivalent potential temperature (filled contours). Black boxes denote location of MAHTE behind the SBF.

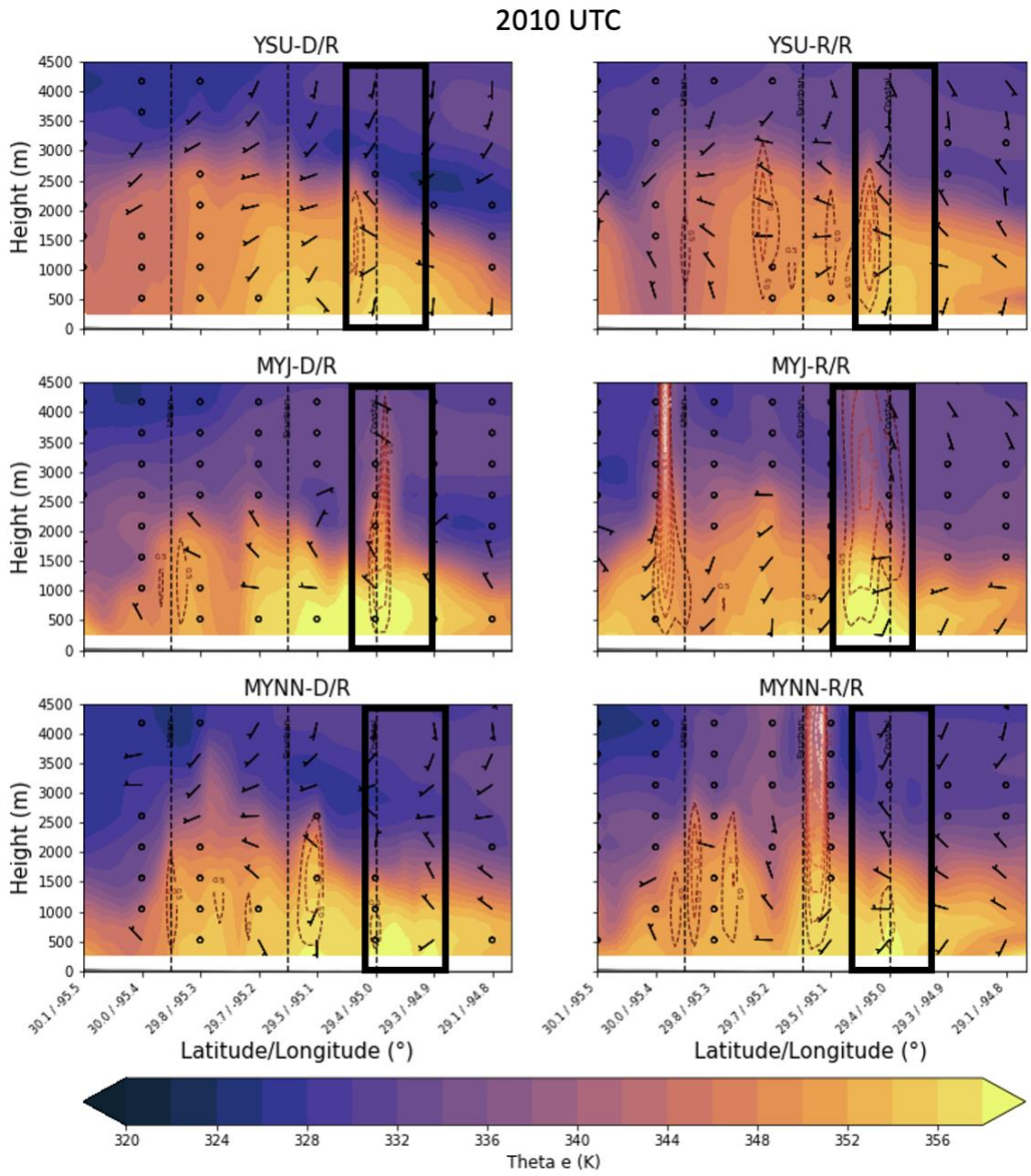


Fig. 5.21: Same as Fig. 5.20, but at 2010 UTC.

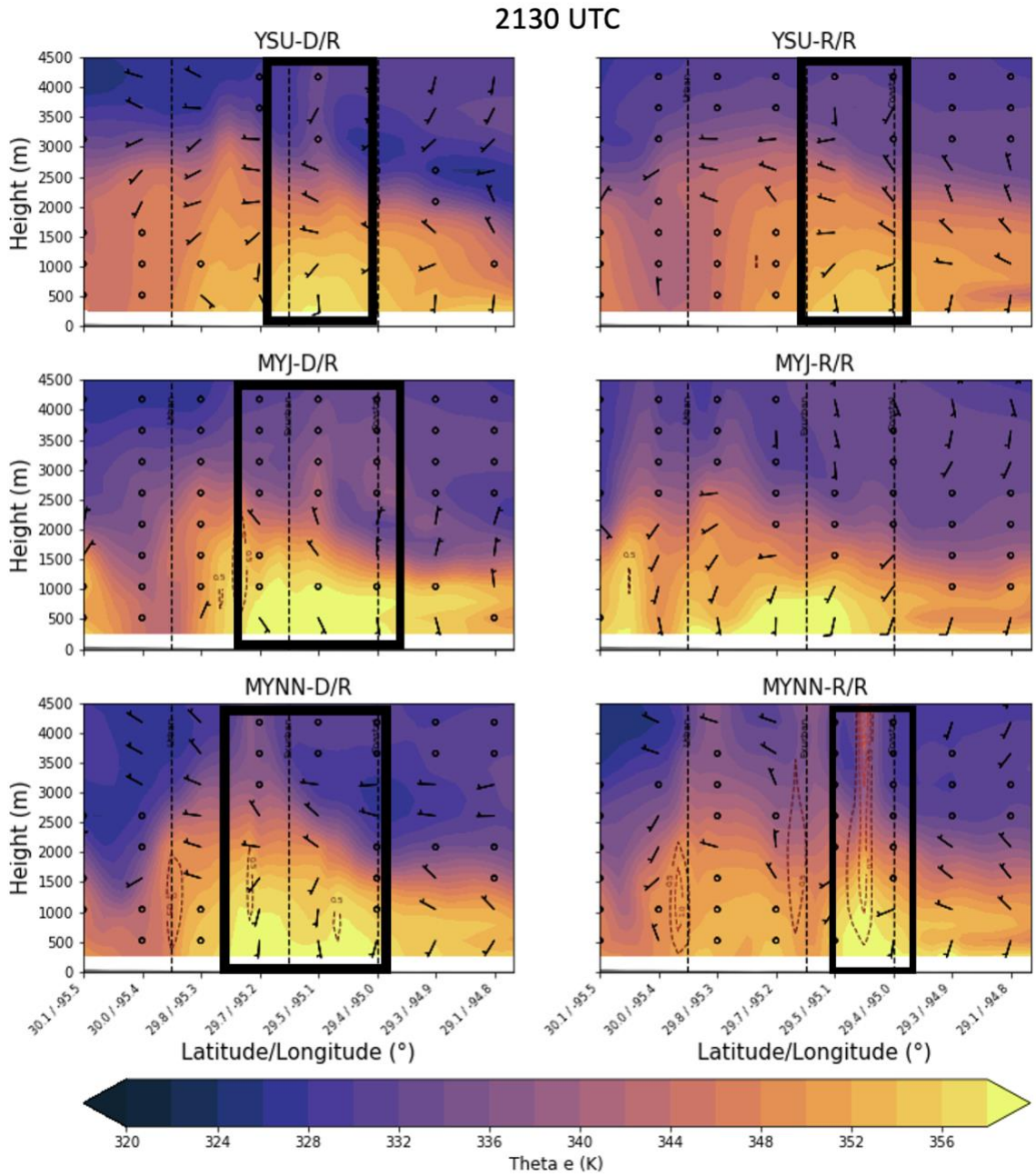


Fig. 5.22: Same as Fig. 5.20, but at 2130 UTC.

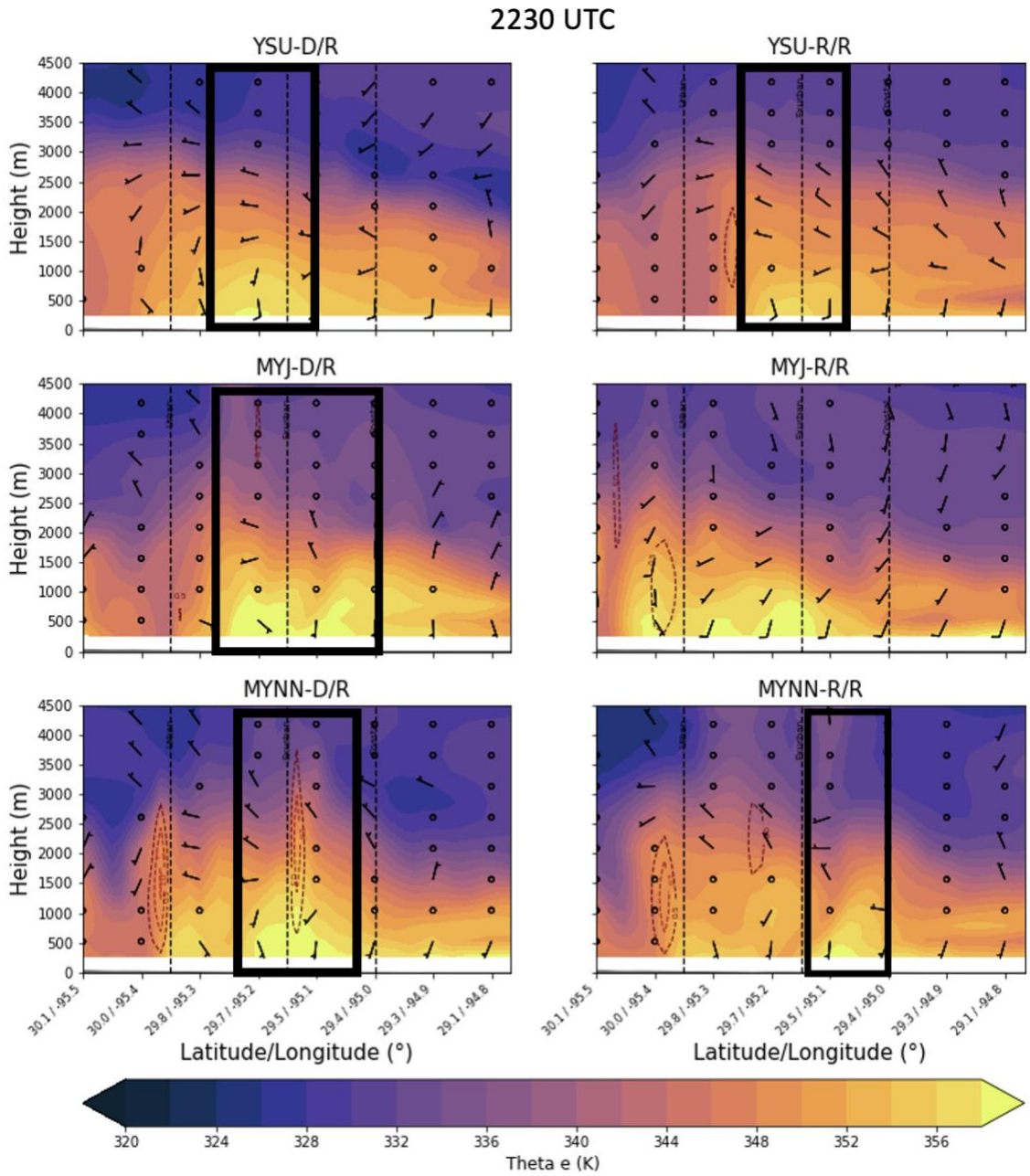


Fig. 5.23: Same as Fig. 5.20, but at 2230 UTC.

5.6 Discussion and Conclusions

High temporal resolution observations from the CUBIC campaign, combined with spatially continuous WoFS ensemble forecasts, provide an extensive view of the SB structure, its evolution across space and time, and its relationship to CI across the Houston region. The analyses in Ch. 4 showed that onshore cases have weaker kinematic responses to the SB, but generally deeper

thermodynamic responses. In the case of 17 August 2022, the magnitude of kinematic and thermodynamic responses were exceptionally strong and the case presented CI along the SBF as it propagated inland, suggesting that the strong SB responses may play a role in CI potential. This chapter explores the hypothesis, formed based off Ch. 4 results and prior SB-CI studies, that the CI in this case depends on two main mechanisms; forced ascent at the coast to establish a moist air mass and that the elevated moist air mass advects inland, destabilizing enough that ascent inland is not necessary for CI to occur.

The analyses within this chapter only partially support the hypothesis posed. Each ensemble member shows evidence of a moist, unstable air mass following the SBF, but not all members have forced ascent *at the coast*. Forced ascent along the coast is not critical for destabilizing the air mass in this case. Instead, persistent ascent along the inland propagating SBF appears important, as this ascent is prevalent in ensemble members that successfully produce CI. Additionally, pre-existing moisture can be further deepened by the persistent upward motion. While the ensemble shows evidence of a MAHTE behind the leading edge of the SBF, proof of the return flow advecting a cooler, drier air mass above the SB inflow layer was inconsistent among ensemble members, particularly those with CI. The presence of a MAHTE alone suggests a destabilized atmosphere behind the front, but the destabilization is not *further enhanced* by the return flow in all members. However, this work only explored a single case, thus further work is necessary to determine whether these results remain true in other CUBIC cases before any generalization can be made.

The combined analysis of observations and WoFS results allowed us to gain new insights and showed that specific processes do appear necessary and important for successful CI to occur. Persistent ascent ahead of and along the inland propagating SBF was prevalent in members exhibiting convection, thus it may be a key differentiating factor for CI. Although our observations do not show the forced ascent, the modeling data suggest that ascent is occurring in the gaps between our observations. Additionally, the observed radar reflectivity and ensemble members show initiated convection prior to reaching the urban location, leaving gaps in the observational data in which ascent, important to CI, could be occurring. The results herein also point to moisture content as being an important factor for CI, regardless of whether the air mass is established by coastal ascent. The members that did not initiate convection (YSU members) showed less pre-SB moisture and weaker MAHTEs than those that successfully achieved CI.

The ensemble members that do initiate convection do so in differing regions with respect to the location of the SBF. The MYJ-R/R member is overzealous with its handling of the convection, producing cells ahead, along, and behind the SBF. This member, therefore, is not considered a reasonable representative member for what was observed. The MYJ-D/R and MYNN members, though, initiate convection either displaced slightly ahead of the SBF or along/behind the front. The MYNN-R/R member initiates convection ahead of the SBF, with this member exhibiting strong ascent and deep moisture ahead of the main SBF. This evolution is consistent with the findings by Fovell (2005), that showed persistent forced ascent ahead of the leading edge of the front elevates moisture and, with the persistent ascent, can trigger convection. The MYNN-D/R member, on the other hand, has CI along the SBF in line with the MAHTE and forced ascent, suggesting the combined factors of a destabilized atmosphere and forced ascent at the SBF work together to successfully produce CI. The MYJ-D/R member has CI slightly away from the cross-sectional path, but shows evidence of SBF enhancement of the convective cells, suggesting that even CI triggered ahead of the SBF can be further intensified by the arrival of the SB. The ensemble of forecasts and their differing handling of CI suggest that the collocated deep moist air mass and forced ascent are the important factors to where CI will occur. Without the forced ascent, a moist air mass alone is not enough to produce CI (e.g., YSU members). Thus, while different perturbations within the ensemble may lead to CI occurring in a different region with respect to the SBF location, the same physical mechanisms are essentially at play for CI.

Altogether, while the original hypothesis was only partially supported, this analysis provides insight into the mechanisms that control CI in association with the Houston SB. The findings highlight that a moist, high θ_e air mass alone is insufficient for CI without persistent ascent, and that the collocation of a deep moist air mass and ascent along or ahead of the SBF is a key discriminator between ensemble members that produce CI and those that do not. Although this study focuses on a single case, its high-resolution observations and ensemble context offer a valuable framework for diagnosing SB-CI interactions. Future work expanding this analysis to multiple events can help determine the robustness of these relationships.

Chapter 6

Summary and Conclusions

The PBL is a dynamic layer of the atmosphere, pivotal in driving meteorological processes that influence weather patterns, climate behavior, and air pollution dispersion. Furthermore, coastal-urban environments are a complex region comprised of many compounding PBL processes. As an estimated 40% of the United States population resides within coastal-urban areas, it is increasingly important to further our understanding of the mesoscale processes that take place and that continue to be a source of forecasting errors that can have potential impacts on the health and safety of residents (Ha et al. 2015; NOAA 2024; Joe et al. 2025). One of the most prevalent and influential mesoscale circulations that affects coastal-urban regions is the SB. Driven by daytime land-sea thermal contrasts, the SB modifies the exchange of heat, moisture, and momentum in the PBL as it propagates inland. The accurate representation of SBs is important, as the SB can affect local air pollution, convection and precipitation outlooks, offshore wind energy production, and heat stress forecasting. Past literature has shown a large spread in the effects of the SB on the PBL, which necessitates continued exploration of the SB. Many past studies focus specifically on air quality effects, convection, or seasonal changes, but there have been limited observational studies focused on intraseasonal variability of the PBL through the evolution of a SB passage. The overarching goal of this dissertation aimed to further our understanding of the complex coastal-urban environment and interactions between mesoscale processes, with a particular focus on SB effects on the PBL. This dissertation used an array of high temporal resolution observations at strategically chosen sites across Houston's coastal-urban region to highlight the spatial evolution and intraseasonal variability of the PBL and SB modifications to the PBL. Additional tools, such as fuzzy logic algorithms and NWP simulations, were used alongside the observations for detailed insights to the diurnal evolution of PBLH and the needed factors for successful SB-forced CI to occur.

The CUBIC field campaign consisted of a four-month-long deployment using collocated ground-based remote sensing instruments at three distinct sites across the coastal-urban environment of Houston, Texas. Each site collected continuous, high-resolution kinematic and thermodynamic data to culminate in a rich dataset suitable for spatial and temporal analyses of the PBL. A classification method for handling the large number of CUBIC cases was developed.

Initially, a SOM technique was applied to objectively sort each CUBIC day into one of four synoptic regimes based on 700 hPa geopotential heights following the techniques applied by Wang et al. (2022). However, verification of the SOM's ability to represent the regional flow over the Houston area showed an inability for the SOM to capture the local conditions. Thus, a regional flow classification method based on sounding analyses (700 hPa flow) over the Houston area was adapted to ensure any connections between the upper-level flow and PBL responses to the SB were local. SB cases were identified using a multistep approach utilizing the CUBIC datasets and operational NEXRAD radar data, with a total of 52 days developing a SB and 43 cases in which continuous data in the 4-6 hours surrounding the SB passage was collected. While a purely objective SB identification method was not employed in this work, the applied approach ensured weak and non-canonical SB cases that occurred were captured, mitigating the potential loss of cases if traditional objective methods were to be applied. A seasonal trend in SB occurrence was documented, consistent with land-sea temperature trends, in which June produces the greatest number of SBs, decreasing numbers through the summer, and then an increase with a shift into fall in September. This trend is consistent with the monthly averaged land-sea temperature difference trend. Additionally, in 98.2% of SB cases, the land-sea temperature difference exceeded 3°C, indicating this value could be applicable for thresholding in objective SB identification methods with minimal case omission. However, given the vast array of environments around the world where SBs occur, this 3°C threshold is likely only useful in the Houston region. Similar analysis could be explored if studying the SB in a different location, but this 3°C value may be quite useful for future work in the Southeast Texas region.

An important goal of the CUBIC campaign was to characterize the PBL within the Houston region. To address this, the implementation of a fuzzy logic algorithm for PBLH estimation utilizing the CUBIC observations was employed and results were analyzed to gain insight about the diurnal evolution of the PBL. Composites of PBLH from each site showed substantial spatial heterogeneity across the coastal-urban domain, driven primarily by the mesoscale influences of the SB and UHI. The urban location showed a ~480 m higher maximum PBLH than at the coast, as well as elevated PBLH in the overnight period when the UHI effects are greatest. There was also a temporal difference across space, with the urban site reaching a maximum PBLH two hours after the coastal location. While the effects of the regional flow on the diurnal evolution of PBLH showed no significant difference in maximum heights reached, there is variability in the growth

and decay rates during the morning and evening transitions across regimes. Ultimately, given the minimal regime-specific differences, the primary factors for observed heterogeneity and variability in PBLH are due to local and small-scale processes. SB cases occur in deeper PBL environments and UHI effects result in deeper PBLs both during the day and in the overnight period. Thus, the primary influences that affect the spatial PBLH diurnal evolution across the coastal-urban interface are SBs and the UHI.

To better understand the array of PBL responses to the SB and possible effects from regional flow, an in-depth case study analysis was conducted for two cases, with the results compared against composite analyses. The case studies showed that the depth, structure, and turbulence signatures of the PBL response to the SB evolve as the SB propagates inland. The urban location exhibited stronger and deeper wind profiles, with the offshore case resulting in greater post-SB wind speed magnitudes. The thermodynamic responses vary strongly across space between the two cases, with some indications that point to mixing processes acting to suppress the depth of the moisture response as the SB propagates inland. Composites showed only in the horizontal wind data indications of a regime-dependent response to the SB. Compared to the onshore regime, post-SB wind profiles reached a greater maximum wind speed and a more pronounced jet-like structure in the offshore regime. This kinematic response was hypothesized to be related to the enhanced return flow by the 700 hPa flow, which in turn enhanced the SB flow via the conservation of mass and the understanding of the SB as a closed circulation process. There was no indication of a systematic difference in the thermodynamic response to the SB for the different regional regimes. Instead, the composite analyses, alongside the case study results, show that the pre-existing thermodynamic structure is a more important factor in how the SB will modify the PBL than the regional flow. Thus, the regional regime does not result in substantial differences in how the PBL responds to the SB, indicating that local-scale and surface processes are more important drivers of observed variability. The effects of surface fluxes, cloud cover, and spatial heterogeneity in land cover could all be playing a role in how the PBL responds to a SB passage.

The onshore case studied in Ch. 4 showed exceptionally strong thermodynamic and kinematic responses to the SB, exhibited CI along the SBF, and presented an ideal case to combine the high temporal resolution data with an NWP ensemble simulation to investigate the spatial evolution of the SB and determine the important factors that contribute to SB-forced CI. Given the signal for strong SB-forced ascent at the coast, but no updraft at the urban site, it was hypothesized

that two mechanisms were important for CI to occur: forced ascent at the coast establishes and deepens a moist airmass, and the moist airmass advects inland, destabilizing enough that forced ascent inland is not required for CI. However, the results only partially support this hypothesis. All members exhibit a MAHTE behind the SBF, but not all members show strong ascent at the coastal location, suggesting that the forcing near the coast is not what establishes and deepens a moist airmass. Instead, persistent ascent along the inland propagating SBF acts to both deepen the layer of moist air and increase the moisture content in the SB inflow region. Contrary to the original hypothesis, both persistent ascent ahead of and/or along the SBF and pre-existing moisture content are important for successful CI to occur and are key differentiating factors amongst the ensemble members that do and do not produce CI. The added benefit of spatially continuous data provided by the model simulation allowed for evaluation of the SB evolution across the coastal-urban domain. While the CUBIC observations showed no forced ascent at the urban site, the simulations were able to fill in the gaps between the coastal and urban sites and exhibited forced ascent across much of the domain prior to CI occurring.

This work has expanded our knowledge of PBL dynamics across the coastal-urban interface and the role highly spatially heterogeneous land characteristics can play in mesoscale processes. While this study included four months of data collection and numerous SB cases to explore, there are still important unanswered questions regarding the SB and how it affects the PBL. The role of surface forcings, such as latent and sensible heat fluxes, is one area that this work does not consider. Additionally, how these surface forcings change across the coastal-urban region is not fully understood and likely plays a significant role in how the PBL responds to the SB. The findings from this work suggest that flow above the PBL leads to negligible differences in PBL responses to the SB, so future work focusing on the interconnections and interactions between the surface layer and atmosphere above (e.g., land-atmosphere interactions/feedbacks) would likely advance our understanding of how the SB evolves through time. While the case study analyses showed that pre-existing moisture is important for successful CI to occur, an expanded analysis of more cases would be able to provide more robust answers to the key factors for SB-CI. Future work should explore longer-term climatologies, assess the impact of additional mesoscale features such as outflow boundaries or low-level jets, and evaluate model performance in capturing the observed SB response patterns. A continued hindrance to expanding our knowledge of how the PBL and SB evolve through the coastal-urban region is the lack of spatially dense observations

through the depth of the PBL. The expansive high-resolution dataset collected during CUBIC provides a robust basis for these next steps and underscores the value of targeted, synergistic observational campaigns in complex regions.

Reference List

Arrillaga, J. A., C. Yagüe, M. Sastre, and C. Román-Cascón, 2016: A characterisation of sea-breeze events in the eastern Cantabrian coast (Spain) from observational data and WRF simulations. *Atmospheric Research*, **181**, 265–280, https://doi.org/10.1016/j.atmosres.2016.06.021.

Arrillaga, J. V. De Arellano, F. Bosveld, H. K. Baltink, C. Yagüe, M. Sastre, and C. Román-Cascón, 2018: Impacts of afternoon and evening sea-breeze fronts on local turbulence, and on CO_2 and radon-222 transport. *Quart J Royal Meteoro Soc*, **144**, 990–1011, https://doi.org/10.1002/qj.3252.

Arya, P. S., 2001: *Introduction to Micrometeorology.* Vol. 79 2nd ed., Elsevier, North Carolina State University, https://shop.elsevier.com/books/introduction-to-micrometeorology/arya/978-0-12-059354-5.

Aryee, J. N. A., L. K. Amekudzi, K. Preko, W. A. Atiah, and S. K. Danuor, 2020: Estimation of planetary boundary layer height from radiosonde profiles over West Africa during the AMMA field campaign: Intercomparison of different methods. *Scientific African*, **7**, e00228, https://doi.org/10.1016/j.sciaf.2019.e00228.

Atkins, N. T., and R. M. Wakimoto, 1997: Influence of the Synoptic-Scale Flow on Sea Breezes Observed during CaPE. *Monthly Weather Review*, **125**, 2112–2130, https://doi.org/10.1175/1520-0493(1997)125%253C2112:IOTSSF%253E2.0.CO;2.

Azorin-Molina, C., and D. Chen, 2009: A climatological study of the influence of synoptic-scale flows on sea breeze evolution in the Bay of Alicante (Spain). *Theor Appl Climatol*, **96**, 249–260, https://doi.org/10.1007/s00704-008-0028-2.

Azorin-Molina, C., S. Tijm, E. E. Ebert, S.-M. Vicente-Serrano, and M.-J. Estrela, 2015: High Resolution HIRLAM Simulations of the Role of Low-Level Sea-Breeze Convergence in Initiating Deep Moist Convection in the Eastern Iberian Peninsula. *Boundary-Layer Meteorology*, **154**, 81–100, https://doi.org/10.1007/s10546-014-9961-z.

Baker, R. D., B. H. Lynn, A. Boone, W.-K. Tao, and J. Simpson, 2001: The Influence of Soil Moisture, Coastline Curvature, and Land-Breeze Circulations on Sea-Breeze-Initiated Precipitation. *Journal of Hydrometeorology*, **2**, 193–211, https://doi.org/10.1175/1525-7541(2001)002%253C0193:TIOSMC%253E2.0.CO;2.

Banks, R. F., J. Tiana-Alsina, J. M. Baldasano, F. Rocadenbosch, A. Papayannis, S. Solomos, and C. G. Tzanis, 2016a: Sensitivity of boundary-layer variables to PBL schemes in the WRF model based on surface meteorological observations, lidar, and radiosondes during the HygrA-CD campaign. *Atmospheric Research*, **176–177**, 185–201, https://doi.org/10.1016/j.atmosres.2016.02.024.

Banta, R. M., and Coauthors, 2005: A Bad Air Day in Houston. *Bulletin of the American Meteorological Society*, **86**, 657–670, https://doi.org/10.1175/BAMS-86-5-657.

Banta, R. M., and Coauthors, 2011: Dependence of daily peak O3 concentrations near Houston, Texas on environmental factors: Wind speed, temperature, and boundary-layer depth. *Atmospheric Environment*, **45**, 162–173, https://doi.org/10.1016/j.atmosenv.2010.09.030.

Batchvarova, E., and S.-E. Gryning, 1998: Wind climatology, atmospheric turbulence and internal boundary-layer development in Athens during the MEDCAPHOT-TRACE experiment. *Atmospheric Environment*, **32**, 2055–2069, https://doi.org/10.1016/S1352-2310(97)00422-6.

Bonin, T. A., B. J. Carroll, R. M. Hardesty, W. A. Brewer, K. Hajny, O. E. Salmon, and P. B. Shepson, 2018: Doppler Lidar Observations of the Mixing Height in Indianapolis Using an Automated Composite Fuzzy Logic Approach. *Journal of Atmospheric and Oceanic Technology*, **35**, 473–490, https://doi.org/10.1175/JTECH-D-17-0159.1.

Bornstein, R. D., and W. T. Thompson, 1981: Effects of Frictionally Retarded Sea Breeze and Synoptic Frontal Passages on Sulfur Dioxide Concentrations in New York City. *Journal of Applied Meteorology and Climatology*, **20**, 843–858, https://doi.org/10.1175/1520-0450(1981)020%253C0843:EOFRSB%253E2.0.CO;2.

Boyer, C. H., and J. M. Keeler, 2025: An Idealized Parameter Study of Destabilization and Convection Initiation in Coastal Regions. Part II: Onshore Synoptic-Scale Flow. *Journal of the Atmospheric Sciences*, **82**, 541–557, https://doi.org/10.1175/JAS-D-23-0179.1.

Britt, K. C., P. S. Skinner, P. L. Heinselman, C. K. Potvin, M. L. Flora, B. Matilla, K. H. Knopfmeier, and A. E. Reinhart, 2024: Verification of Quasi-Linear Convective Systems Predicted by the Warn-on-Forecast System (WoFS). *Weather and Forecasting*, **39**, 155–176, https://doi.org/10.1175/WAF-D-23-0106.1.

Browning, K. A., and R. Wexler, 1968: The Determination of Kinematic Properties of a Wind Field Using Doppler Radar. *Journal of Applied Meteorology and Climatology*, **7**, 105–113, https://doi.org/10.1175/1520-0450(1968)007%253C0105:TDOKPO%253E2.0.CO;2.

Burke, P. C., J. Barnwell, M. Reagan, M. A. Rose, T. J. Galarneau, R. Otto, and A. Orrison, 2024: The 21 August 2021 Catastrophic Flash Flood at Waverly, Tennessee: Harnessing the Warn-on-Forecast System for Confident Prewarning Messaging of Extreme Rainfall. *Bulletin of the American Meteorological Society*, **105**, E1800–E1821, https://doi.org/10.1175/BAMS-D-23-0205.1.

Caicedo, V., and Coauthors, 2019: Bay Breeze and Sea Breeze Circulation Impacts on the Planetary Boundary Layer and Air Quality From an Observed and Modeled DISCOVER-AQ Texas Case Study. *J. Geophys. Res. Atmos.*, 2019JD030523, https://doi.org/10.1029/2019JD030523.

Calmet, I., and P. Mestayer, 2016: Study of the thermal internal boundary layer during sea-breeze events in the complex coastal area of Marseille. *Theoretical and Applied Climatology*, **123**, 801–826, https://doi.org/10.1007/s00704-015-1394-1.

Carpenter, A., 2024: Rural 'buffer ring' can reduce urban heat island effect by more than 0.5 °C. *Carbon Brief*, August 1, 2024, https://www.carbonbrief.org/rural-buffer-ring-can-reduce-urban-heat-island-effect-by-more-than-0-5c.

Chen, C.-C., J. H. Richter, C. Liu, M. W. Moncrieff, Q. Tang, W. Lin, S. Xie, and P. J. Rasch, 2021: Effects of Organized Convection Parameterization on the MJO and Precipitation in E3SMv1. Part I: Mesoscale Heating. *Journal of Advances in Modeling Earth Systems*, **13**, e2020MS002401, https://doi.org/10.1029/2020MS002401.

Chen, F., and Coauthors, 2011: The integrated WRF/urban modelling system: development, evaluation, and applications to urban environmental problems. *International Journal of Climatology*, **31**, 273–288, https://doi.org/10.1002/joc.2158.

Coniglio, M. C., J. Correia, P. T. Marsh, and F. Kong, 2013: Verification of Convection-Allowing WRF Model Forecasts of the Planetary Boundary Layer Using Sounding Observations. *Weather and Forecasting*, **28**, 842–862, https://doi.org/10.1175/WAF-D-12-00103.1.

Crosman, E. T., and J. D. Horel, 2010: Sea and Lake Breezes: A Review of Numerical Studies. *Boundary-Layer Meteorol*, **137**, 1–29, https://doi.org/10.1007/s10546-010-9517-9.

Daum, P. H., L. I. Kleinman, S. R. Springston, L. J. Nunnermacker, Y.-N. Lee, J. Weinstein-Lloyd, J. Zheng, and C. M. Berkowitz, 2003: A comparative study of O3 formation in the Houston urban and industrial plumes during the 2000 Texas Air Quality Study. *Journal of Geophysical Research: Atmospheres*, **108**, https://doi.org/10.1029/2003JD003552.

Demuzere, M., J. Kittner, and B. Bechtel, 2021: LCZ Generator: A Web Application to Create Local Climate Zone Maps. *Front. Environ. Sci.*, **9**, 637455, https://doi.org/10.3389/fenvs.2021.637455.

Dima, I. M., and J. M. Wallace, 2003: On the Seasonality of the Hadley Cell. *J. Atmos. Sci.*, **60**, 1522–1527, https://doi.org/10.1175/1520-0469(2003)060%253C1522:OTSOTH%253E2.0.CO;2.

Dowell, D. C., and Coauthors, 2022: The High-Resolution Rapid Refresh (HRRR): An Hourly Updating Convection-Allowing Forecast Model. Part I: Motivation and System Description. *Weather and Forecasting*, **37**, 1371–1395, https://doi.org/10.1175/WAF-D-21-0151.1.

Duncan Jr., J. B., and Coauthors, 2022: Evaluating convective planetary boundary layer height estimations resolved by both active and passive remote sensing instruments during the CHEESEHEAD19 field campaign. *Atmos. Meas. Tech.*, **15**, 2479–2502, https://doi.org/10.5194/amt-15-2479-2022.

Everett, L., 2018: The future of atmospheric boundary layer observing, understanding, and modeling: Proceedings of a workshop. *Natl. Acad. Press*.

Fankhauser, J. C., N. A. Crook, J. Tuttle, L. J. Miller, and C. G. Wade, 1995: Initiation of Deep Convection along Boundary Layer Convergence Lines in a Semitropical Environment. *Monthly Weather Review*, **123**, 291–314, https://doi.org/10.1175/1520-0493(1995)123%253C0291:IODCAB%253E2.0.CO;2.

Fenner, D., and Coauthors, 2024: urbisphere-Berlin Campaign: Investigating Multiscale Urban Impacts on the Atmospheric Boundary Layer. *Bulletin of the American Meteorological Society*, **105**, E1929–E1961, https://doi.org/10.1175/BAMS-D-23-0030.1.

Ferdiansyah, M. R., A. Inagaki, and M. Kanda, 2020: Detection of sea-breeze inland penetration in the coastal-urban region using geostationary satellite images. *Urban Climate*, **31**, 100586, https://doi.org/10.1016/j.uclim.2020.100586.

Ford, T. W., S. M. Quiring, O. W. Frauenfeld, and A. D. Rapp, 2015: Synoptic conditions related to soil moisture-atmosphere interactions and unorganized convection in Oklahoma. *Journal of Geophysical Research: Atmospheres*, **120**, 11,519-11,535, https://doi.org/10.1002/2015JD023975.

Fovell, R. G., 2005: Convective Initiation ahead of the Sea-Breeze Front. *Monthly Weather Review*, **133**, 264–278, https://doi.org/10.1175/MWR-2852.1.

Fu, S., R. Rotunno, J. Chen, X. Deng, and H. Xue, 2021: A large-eddy simulation study of deep-convection initiation through the collision of two sea-breeze fronts. *Atmospheric Chemistry and Physics*, **21**, 9289–9308, https://doi.org/10.5194/acp-21-9289-2021.

Garratt, J. R., 1994: Review: the atmospheric boundary layer. *Earth-Science Reviews*, **37**, 89–134, https://doi.org/10.1016/0012-8252(94)90026-4.

Geerts, B., and Coauthors, 2018: Recommendations for In Situ and Remote Sensing Capabilities in Atmospheric Convection and Turbulence. *Bulletin of the American Meteorological Society*, **99**, 2463–2470, https://doi.org/10.1175/BAMS-D-17-0310.1.

Gilliam, R. C., S. Raman, and D. D. S. Niyogi, 2004: Observational and Numerical Study on the Influence of Large-Scale Flow Direction and Coastline Shape on Sea-Breeze Evolution. *Boundary-Layer Meteorology*, **111**, 275–300, https://doi.org/10.1023/B:BOUN.0000016494.99539.5a.

Gómez, I., R. J. Ronda, V. Caselles, and M. J. Estrela, 2016: Implementation of non-local boundary layer schemes in the Regional Atmospheric Modeling System and its impact on simulated mesoscale circulations. *Atmospheric Research*, **180**, 24–41, https://doi.org/10.1016/j.atmosres.2016.04.020.

Gourley, J. J., P. Tabary, and J. P. du Chatelet, 2007: A Fuzzy Logic Algorithm for the Separation of Precipitating from Nonprecipitating Echoes Using Polarimetric Radar Observations. *Journal of Atmospheric and Oceanic Technology*, **24**, 1439–1451, https://doi.org/10.1175/JTECH2035.1.

Grau, A., M. A. Jimenez, and J. Cuxart,: Statistical characterization of the sea-breeze physical mechanisms through in-situ and satellite observations.

Gu, J., Y. Zhang, N. Yang, R. Wang, School of Hydrology and Water Resources, Nanjing University of Information Science and Technology, Nanjing 210044, China, and State Oceanic Administration Key Laboratory for Polar Science, Polar Research Institute of China, Shanghai 200136, China, 2020: Diurnal variability of the planetary boundary layer height estimated from radiosonde data. *Earth and Planetary Physics*, **4**, 1–14, https://doi.org/10.26464/epp2020042.

Ha, S., J. Berner, and C. Snyder, 2015: A Comparison of Model Error Representations in Mesoscale Ensemble Data Assimilation. *Monthly Weather Review*, **143**, 3893–3911, https://doi.org/10.1175/MWR-D-14-00395.1.

Haman, C. L., B. Lefer, and G. A. Morris, 2012: Seasonal Variability in the Diurnal Evolution of the Boundary Layer in a Near-Coastal Urban Environment. *Journal of Atmospheric and Oceanic Technology*, **29**, 697–710, https://doi.org/10.1175/JTECH-D-11-00114.1.

Haman, C. L., E. Couzo, J. H. Flynn, W. Vizuete, B. Heffron, and B. L. Lefer, 2014: Relationship between boundary layer heights and growth rates with ground-level ozone in Houston, Texas. *JGR Atmospheres*, **119**, 6230–6245, https://doi.org/10.1002/2013JD020473.

Hanft, W., and A. L. Houston, 2018: An Observational and Modeling Study of Mesoscale Air Masses with High Theta-E. *Monthly Weather Review*, **146**, 2503–2524, https://doi.org/10.1175/MWR-D-17-0389.1.

Heaviside, C., X.-M. Cai, and S. Vardoulakis, 2015: The effects of horizontal advection on the urban heat island in Birmingham and the West Midlands, United Kingdom during a heatwave. *Quarterly Journal of the Royal Meteorological Society*, **141**, 1429–1441, https://doi.org/10.1002/qj.2452.

Heinselman, P. L., and Coauthors, 2024: Warn-on-Forecast System: From Vision to Reality. *Weather and Forecasting*, **39**, 75–95, https://doi.org/10.1175/WAF-D-23-0147.1.

Hersbach, H., and Coauthors, 2023: ERA5 hourly data on single levels from 1940 to present. *Copernicus Climate Change Service (C3S) Climate Data Store (CDS)*, https://doi.org/10.24381/cds.adbb2d47.

Hewitson, B., and R. Crane, 2002: Self-organizing maps: applications to synoptic climatology. *Clim Res*, **22**, 13–26.

Hidalgo, J., V. Masson, and L. Gimeno, 2010: Scaling the Daytime Urban Heat Island and Urban-Breeze Circulation. *Journal of Applied Meteorology and Climatology*, **49**, 889–901, https://doi.org/10.1175/2009JAMC2195.1.

Higgins, R. W., Y. Yao, E. S. Yarosh, J. E. Janowiak, and K. C. Mo, 1997: Influence of the Great Plains Low-Level Jet on Summertime Precipitation and Moisture Transport over the Central United States. *Journal of Climate*, **10**, 481–507, https://doi.org/10.1175/1520-0442(1997)010%253C0481:IOTGPL%253E2.0.CO;2.

Hong, S.-Y., Y. Noh, and J. Dudhia, 2006: A New Vertical Diffusion Package with an Explicit Treatment of Entrainment Processes. *Monthly Weather Review*, **134**, 2318–2341, https://doi.org/10.1175/MWR3199.1.

Hu, X.-M., and M. Xue, 2016: Influence of Synoptic Sea-Breeze Fronts on the Urban Heat Island Intensity in Dallas–Fort Worth, Texas. *Monthly Weather Review*, **144**, 1487–1507, https://doi.org/10.1175/MWR-D-15-0201.1.

Hughes, C. P., and D. E. Veron, 2018: A Characterization of the Delaware Sea Breeze Using Observations and Modeling. *Journal of Applied Meteorology and Climatology*, **57**, 1405–1421, https://doi.org/10.1175/JAMC-D-17-0186.1.

Igel, A. L., S. C. van den Heever, and J. S. Johnson, 2018: Meteorological and Land Surface Properties Impacting Sea Breeze Extent and Aerosol Distribution in a Dry Environment. *Journal of Geophysical Research: Atmospheres*, **123**, 22–37, https://doi.org/10.1002/2017JD027339.

James, A., and A. Houston, 2025: Advancing understanding of mesoscale airmasses with high theta-E through airmass boundary classification. Undergraduate Honors Thesis, University of Nebraska–Lincoln.

Janjić, Z. I., 2022: Nonsingular implementation of the Mellor-Yamada level 2.5 scheme in the NCEP Meso model.

Jensen, M. P., 2019: *Tracking Aerosol Convection Interactions ExpeRiment (TRACER) Science Plan*, accessed 10 July 2024, https://doi.org/10.2172/1561242.

Jensen, M. P., and Coauthors, 2023: Tracking aerosol convection interactions experiment (TRACER) field campaign report (No. DOE/SC-ARM-23-038). https://doi.org/10.2172/2202672.

Jensen, M. P., and Coauthors, 2025: Studying Aerosol, Clouds, and Air Quality in the Coastal Urban Environment of Southeastern Texas. *Bulletin of the American Meteorological Society*, BAMS-D-23-0331.1, https://doi.org/10.1175/BAMS-D-23-0331.1.

Jiang, Y., and Coauthors, 2021: The thermodynamic structures of the planetary boundary layer dominated by synoptic circulations and the regular effect on air pollution in Beijing. *Atmospheric Chemistry and Physics*, **21**, 6111–6128, https://doi.org/10.5194/acp-21-6111-2021.

Joe, P., and Coauthors, 2025: Insights from Nowcasting and Mesoscale Research Working Group Projects of the World Weather Research Programme. *Bulletin of the American Meteorological Society*, **106**, E1221–E1245, https://doi.org/10.1175/BAMS-D-24-0046.1.

Jones, T., R. Ahmadov, E. James, G. Pereira, S. Freitas, and G. Grell, 2022: Prototype of a Warn-on-Forecast System for Smoke (WoFS-Smoke). *Weather and Forecasting*, **37**, 1191–1209, https://doi.org/10.1175/WAF-D-21-0143.1.

Kim, E., and Coauthors, 2023: Turbulent characteristics in complex coastal areas assessed using BSWO observations and WRF-LES simulation results. *Atmospheric Research*, **289**, 106756, https://doi.org/10.1016/j.atmosres.2023.106756.

Klein, P.., E. Smith, T. Wagner, J. Gibbs, T. Bell, J. Gebauer, M. Spencer, and M. Carney, 2023: TRACER-Coastal Urban Boundary-Layer Interactions with Convection (TRACER-CUBIC) field campaign report (No. DOE/SC-ARM-23-027). https://doi.org/10.2172/1984939.

Kohonen, T., 2012: Self-organizing maps. Springer Science & Business Media, https://doi.org/10.1007/978-3-642-56927-2.

Kotthaus, S., and Coauthors, 2023: Atmospheric boundary layer height from ground-based remote sensing: a review of capabilities and limitations. *Atmos. Meas. Tech.*, **16**, 433–479, https://doi.org/10.5194/amt-16-433-2023.

Kristovich, D. A. R., E. Takle, G. S. Young, and A. Sharma, 2019: 100 Years of Progress in Mesoscale Planetary Boundary Layer Meteorological Research. *Meteorological Monographs*, **59**, 19.1-19.41, https://doi.org/10.1175/AMSMONOGRAPHS-D-18-0023.1.

Kusaka, H., F. Kimura, H. Hirakuchi, and M. Mizutori, 2000: The effects of land-use alteration on the sea breeze and daytime heat island in the Tokyo metropolitan area. *Journal of Meteorological Society of Japan*, **78**, 405-420, https://doi.org/10.2151/jmsj1965.78.4_405.

Kustas, W. P., J. H. Prueger, J. I. MacPherson, M. Wolde, and F. Li, 2005: Effects of Land Use and Meteorological Conditions on Local and Regional Momentum Transport and Roughness for Midwestern Cropping Systems. *Journal of Hydrometeorology*, **6**, 825–839, https://doi.org/10.1175/JHM460.1.

Lappin, F., T. Bell, P. Klein, and G. de Boer, 2025: Quantifying the Thermodynamic Impacts on the Atmospheric Boundary Layer due to the Sea Breeze in the Coastal Houston Region. *Journal of Applied Meteorology and Climatology*, **64**, 607–623, https://doi.org/10.1175/JAMC-D-24-0203.1.

Li, J., and Y.-L. Chen, 1998: Barrier Jets during TAMEX. *Monthly Weather Review*, **126**, 959–971, https://doi.org/10.1175/1520-0493(1998)126%253C0959:BJDT%253E2.0.CO;2.

Liu, S., and X.-Z. Liang, 2010: Observed Diurnal Cycle Climatology of Planetary Boundary Layer Height. *Journal of Climate*, **23**, 5790–5809, https://doi.org/10.1175/2010JCLI3552.1.

Liu, Y., and R. H. Weisberg, 2011: A review of self-organizing map applications in meteorology and oceanography. *Self-organizing maps: Applications and novel algorithm design*, **1**, 253-272, https://doi.org/10.1175/2010JCLI3552.1.

Liu, Z., Y. Sun, L. Li, and Y. Wang, 2011: Particle mass concentrations and size distribution during and after the Beijing Olympic Games. *Huan Jing Ke Xue*, **32**, 913-923, https://doi.org/10.1175/2010JCLI3552.1.

Loveless, D. M., T. J. Wagner, D. D. Turner, S. A. Ackerman, and W. F. Feltz, 2019: A Composite Perspective on Bore Passages during the PECAN Campaign. *Monthly Weather Review*, **147**, 1395–1413, https://doi.org/10.1175/MWR-D-18-0291.1.

Maahn, M., D. D. Turner, U. Löhnert, D. J. Posselt, K. Ebell, G. G. Mace, and J. M. Comstock, 2020: Optimal Estimation Retrievals and Their Uncertainties: What Every Atmospheric Scientist Should Know. *Bulletin of the American Meteorological Society*, **101**, E1512–E1523, https://doi.org/10.1175/BAMS-D-19-0027.1.

Marshall, C. H., R. A. Pielke, L. T. Steyaert, and D. A. Willard, 2004: The Impact of Anthropogenic Land-Cover Change on the Florida Peninsula Sea Breezes and Warm Season Sensible Weather. *Monthly Weather Review*, **132**, 28–52, https://doi.org/10.1175/1520-0493(2004)132%253C0028:TIOALC%253E2.0.CO;2.

Mechem, D. B., C. S. Wittman, M. A. Miller, S. E. Yuter, and S. P. de Szoeke, 2018: Joint Synoptic and Cloud Variability over the Northeast Atlantic near the Azores. *Journal of Applied Meteorology and Climatology*, **57**, 1273–1290, https://doi.org/10.1175/JAMC-D-17-0211.1.

Meir, T., P. M. Orton, J. Pullen, T. Holt, W. T. Thompson, and M. F. Arend, 2013: Forecasting the New York City Urban Heat Island and Sea Breeze during Extreme Heat Events. *Weather and Forecasting*, **28**, 1460–1477, https://doi.org/10.1175/WAF-D-13-00012.1.

Mestayer, P. G., and S. Anquetin, 1995: Climatology of Cities. *Diffusion and Transport of Pollutants in Atmospheric Mesoscale Flow Fields*, A. Gyr and F.-S. Rys, Eds, Springer Netherlands, 165–189, https://doi.org/10.1007/978-94-015-8547-7_7.

Miao, S., F. Chen, Q. Li, and S. Fan, 2011: Impacts of Urban Processes and Urbanization on Summer Precipitation: A Case Study of Heavy Rainfall in Beijing on 1 August 2006. *Journal of Applied Meteorology and Climatology*, **50**, 806–825, https://doi.org/10.1175/2010JAMC2513.1.

Miao, Y., S. Liu, Y. Zheng, and S. Wang, 2016: Modeling the feedback between aerosol and boundary layer processes: a case study in Beijing, China. *Environmental Science and Pollution Research*, **23**, 3342–3357, https://doi.org/10.1007/s11356-015-5562-8.

Miller, D. J., and Coauthors, 2020: Characterizing Elevated Urban Air Pollutant Spatial Patterns with Mobile Monitoring in Houston, Texas. *Environ. Sci. Technol.*, **54**, 2133–2142, https://doi.org/10.1021/acs.est.9b05523.

Miller, S. T. K., and B. D. Keim, 2003: Synoptic-Scale Controls on the Sea Breeze of the Central New England Coast. *Weather and Forecasting*, **18**, 236–248, https://doi.org/10.1175/1520-0434(2003)018%253C0236:SCOTSB%253E2.0.CO;2.

Miller, S. T. K., B. D. Keim, R. W. Talbot, and H. Mao, 2003: Sea breeze: Structure, forecasting, and impacts. *Reviews of Geophysics*, **41**, https://doi.org/10.1029/2003RG000124.

Nakanishi, M., and H. Niino, 2006: An Improved Mellor–Yamada Level-3 Model: Its Numerical Stability and Application to a Regional Prediction of Advection Fog. *Boundary-Layer Meteorology*, **119**, 397–407, https://doi.org/10.1007/s10546-005-9030-8.

National Research Council, 2009: Observing weather and climate from the ground up: a nationwide network of networks. *The National Academies Press*, https://doi.org/10.17226/12540.

Nielsen-Gammon, J. W., and Coauthors, 2008: Multisensor Estimation of Mixing Heights over a Coastal City. *Journal of Applied Meteorology and Climatology*, **47**, 27–43, https://doi.org/10.1175/2007JAMC1503.1.

NOAA, 2024: What percentage of the American population lives near the coast? National Ocean Service website, https://oceanservice.noaa.gov/facts/population.html, accessed 16 June 2024.

Noble, S., B. Viner, and J. Wermter, 2024: Summary of atmospheric characteristics of days with inland penetrating sea breezes from 2015 to 2021. *Atmospheric Science Letters*, **25**, e1192, https://doi.org/10.1002/asl.1192.

Ohashi, Y., and H. Kida, 2002: Local Circulations Developed in the Vicinity of Both Coastal and Inland Urban Areas: A Numerical Study with a Mesoscale Atmospheric Model. *Journal of Applied Meteorology*, **41**, 30–45, https://doi.org/10.1175/1520-0450(2002)041%253C0030:LCDITV%253E2.0.CO;2.

Oke, T. R., 1995: The Heat Island of the Urban Boundary Layer: Characteristics, Causes and Effects. *Wind Climate in Cities*, J.E. Cermak, A.G. Davenport, E.J. Plate, and D.X. Viegas, Eds, Springer Netherlands, 81–107, https://doi.org/10.1007/978-94-017-3686-2_5.

Oke, T. R., 2006: Towards better scientific communication in urban climate. *Theoretical and Applied Climatology*, **84**, 179–190, https://doi.org/10.1007/s00704-005-0153-0.

O'Lenick, C. R., and Coauthors, 2020: A Case-Crossover Analysis of Indoor Heat Exposure on Mortality and Hospitalizations among the Elderly in Houston, Texas. *Environ Health Perspect*, **128**, 127007, https://doi.org/10.1289/EHP6340.

Pal, S., and Coauthors, 2012: Spatio-temporal variability of the atmospheric boundary layer depth over the Paris agglomeration: An assessment of the impact of the urban heat island intensity. *Atmospheric Environment*, **63**, 261–275, https://doi.org/10.1016/j.atmosenv.2012.09.046.

Papanastasiou, D. K., D. Melas, and I. Lissaridis, 2010: Study of wind field under sea breeze conditions; an application of WRF model. *Atmospheric Research*, **98**, 102–117, https://doi.org/10.1016/j.atmosres.2010.06.005.

Päschke, E., R. Leinweber, and V. Lehmann, 2015: An assessment of the performance of a 1.5 mm Doppler lidar for operational vertical wind profiling based on a 1-year trial. *Atmospheric Measurement Techniques*, **8**, 2251–2266, https://doi.org/10.5194/amt-8-2251-2015.

Pinto, J. O., D. B. Parsons, W. O. J. Brown, S. Cohn, N. Chamberlain, and B. Morley, 2006: Coevolution of Down-Valley Flow and the Nocturnal Boundary Layer in Complex Terrain. *Journal of Applied Meteorology and Climatology*, **45**, 1429–1449, https://doi.org/10.1175/JAM2412.1.

Pinto, J. O., and Coauthors, 2021: The Status and Future of Small Uncrewed Aircraft Systems (UAS) in Operational Meteorology. *Bulletin of the American Meteorological Society*, **102**, E2121–E2136, https://doi.org/10.1175/BAMS-D-20-0138.1.

Potvin, C. K., and Coauthors, 2020: Assessing Systematic Impacts of PBL Schemes on Storm Evolution in the NOAA Warn-on-Forecast System. *Monthly Weather Review*, **148**, 2567–2590, https://doi.org/10.1175/MWR-D-19-0389.1.

Rao, P. A., and H. E. Fuelberg, 2000: An Investigation of Convection behind the Cape Canaveral Sea-Breeze Front. *Monthly Weather Review*, **128**, 3437–3458, https://doi.org/10.1175/1520-0493(2000)128%253C3437:AIOCBT%253E2.0.CO;2.

Rappenglück, B., R. Perna, S. Zhong, and G. A. Morris, 2008: An analysis of the vertical structure of the atmosphere and the upper-level meteorology and their impact on surface ozone levels in Houston, Texas. *J. Geophys. Res.*, **113**, 2007JD009745, https://doi.org/10.1029/2007JD009745.

Reddy, T. V. R., S. K. Mehta, A. Ananthavel, S. Ali, V. Annamalai, and D. N. Rao, 2021: Seasonal characteristics of sea breeze and thermal internal boundary layer over Indian east coast region. *Meteorology and Atmospheric Physics*, **133**, 217–232, https://doi.org/10.1007/s00703-020-00746-1.

Reddy, B. R., C. V. Srinivas, and B. Venkatraman, 2022: Observational analysis and numerical simulation of sea breeze using WRF model over the Indian southeast coastal region. *Meteorology and Atmospheric Physics*, **134**, 57, https://doi.org/10.1007/s00703-022-00891-9.

Reusch, D. B., R. B. Alley, and B. C. Hewitson, 2005: Relative Performance of Self-Organizing Maps and Principal Component Analysis in Pattern Extraction from Synthetic Climatological Data. *Polar Geography*, **29**, 188–212, https://doi.org/10.1080/789610199.

Rogers, R. R., W. L. Ecklund, D. A. Carter, K. S. Gage, and S. A. Ethier, 1993: Research Applications of a Boundary-Layer Wind Profiler. *Bulletin of the American Meteorological Society*, **74**, 567–580, https://doi.org/10.1175/1520-0477(1993)074%253C0567:RAOABL%253E2.0.CO;2.

Rogers, C. D., 2000: Inverse methods for atmospheric sounding: theory and practice. Vol. 2, World Scientific.

Ryu, Y.-H., and J.-J. Baik, 2013: Daytime Local Circulations and Their Interactions in the Seoul Metropolitan Area. *Journal of Applied Meteorology and Climatology*, **52**, 784–801, https://doi.org/10.1175/JAMC-D-12-0157.1.

Sarkar, A., R. S. Saraswat, and A. Chandrasekar, 1998: Numerical study of the effects of urban heat island on the characteristic features of the sea breeze circulation. *Proceedings of the Indian Academy of Sciences - Earth and Planetary Sciences*, **107**, 127–137, https://doi.org/10.1007/BF02840463.

Seibert, P., 2000: Review and intercomparison of operational methods for the determination of the mixing height. *Atmospheric Environment*, **34**, 1001–1027, https://doi.org/10.1016/S1352-2310(99)00349-0.

Seidel, D. J., C. O. Ao, and K. Li, 2010: Estimating climatological planetary boundary layer heights from radiosonde observations: Comparison of methods and uncertainty analysis. *J. Geophys. Res.*, **115**, 2009JD013680, https://doi.org/10.1029/2009JD013680.

Sharma, M., A. D. Rapp, C. J. Nowotarski, and S. D. Brooks, 2024: Observed Variability in Convective Cell Characteristics and Near-Storm Environments across the Sea- and Bay-Breeze Fronts in Southeast Texas. *Monthly Weather Review*, **152**, 2419–2441, https://doi.org/10.1175/MWR-D-23-0243.1.

Sheridan, S. C., and C. C. Lee, 2011: The self-organizing map in synoptic climatological research. *Progress in Physical Geography: Earth and Environment*, **35**, 109–119, https://doi.org/10.1177/0309133310397582.

Skinner, P. S., and Coauthors, 2023: Interpreting Warn-on-Forecast System Guidance, Part I: Review of Probabilistic Guidance Concepts, Product Design, and Best Practices. *J. Operational Meteor.*, 110–131, https://doi.org/10.15191/nwajom.2023.1109.

Smiley, K. T., I. Noy, M. F. Wehner, D. Frame, C. C. Sampson, and O. E. J. Wing, 2022: Social inequalities in climate change-attributed impacts of Hurricane Harvey. *Nat Commun*, **13**, 3418, https://doi.org/10.1038/s41467-022-31056-2.

Smith, C. L., A. Webb, G. J. Levermore, S. J. Lindley, and K. Beswick, 2011: Fine-scale spatial temperature patterns across a UK conurbation. *Climatic Change*, **109**, 269–286, https://doi.org/10.1007/s10584-011-0021-0.

Smith, E. N., and J. T. Carlin, 2024: A multi-instrument fuzzy logic boundary-layer-top detection algorithm. *Atmospheric Measurement Techniques*, **17**, 4087–4107, https://doi.org/10.5194/amt-17-4087-2024.

Smith, E. N., J. G. Gebauer, P. M. Klein, E. Fedorovich, and J. A. Gibbs, 2019: The Great Plains Low-Level Jet during PECAN: Observed and Simulated Characteristics. *Monthly Weather Review*, **147**, 1845–1869, https://doi.org/10.1175/MWR-D-18-0293.1.

Sohrabi, S., J. Zietsman, and H. Khreis, 2020: Burden of Disease Assessment of Ambient Air Pollution and Premature Mortality in Urban Areas: The Role of Socioeconomic Status and Transportation. *International Journal of Environmental Research and Public Health*, **17**, https://doi.org/10.3390/ijerph17041166.

Spassiani, A. C., and M. S. Mason, 2021: Application of Self-organizing Maps to classify the meteorological origin of wind gusts in Australia. *Journal of Wind Engineering and Industrial Aerodynamics*, **210**, 104529, https://doi.org/10.1016/j.jweia.2021.104529.

Spicer, E., 2024: LCZ Factsheet: United States of America - Houston.

Spuler, S. M., M. Hayman, R. A. Stillwell, J. Carnes, T. Bernatsky, and K. S. Repasky, 2021: MicroPulse DIAL (MPD) – a diode-laser-based lidar architecture for quantitative atmospheric profiling. *Atmospheric Measurement Techniques*, **14**, 4593–4616, https://doi.org/10.5194/amt-14-4593-2021.

Statkewicz, M. D., and B. Rappenglueck, 2023: A comparative analysis of the sea breeze on the Texas Gulf Coast and its impact on precipitation. *Urban Climate*, **49**, 101568, https://doi.org/10.1016/j.uclim.2023.101568.

Steele, C. J., S. R. Dorling, R. von Glasow, and J. Bacon, 2013: Idealized WRF model sensitivity simulations of sea breeze types and their effects on offshore windfields. *Atmospheric Chemistry and Physics*, **13**, 443–461, https://doi.org/10.5194/acp-13-443-2013.

Stensrud, D. J., 2007: Parameterization schemes: keys to understanding numerical weather prediction models. Cambridge University Press.

Stensrud, D. J., and Coauthors, 2009: Convective-Scale Warn-on-Forecast System: A Vision for 2020. *Bulletin of the American Meteorological Society*, **90**, 1487–1500, https://doi.org/10.1175/2009BAMS2795.1.

Stewart, I. D., and T. R. Oke, 2012: Local Climate Zones for Urban Temperature Studies. *Bulletin of the American Meteorological Society*, **93**, 1879–1900, https://doi.org/10.1175/BAMS-D-11-00019.1.

Strader, S. M., W. S. Ashley, A. M. Haberlie, and K. Kaminski, 2022: Revisiting U.S. Nocturnal Tornado Vulnerability and Its Influence on Tornado Impacts. *Weather, Climate, and Society*, **14**, 1147–1163, https://doi.org/10.1175/WCAS-D-22-0020.1.

Stull, R. B., 2012: *An Introduction to Boundary Layer Meteorology*. Springer Science & Business Media, google-Books-ID: 2PjrCAAAQBAJ.

Teixeira, J., and Coauthors, 2021: Toward a global planetary boundary layer observing system: The NASA PBL incubation study team report.

Tsiringakis, A., 2021: Understanding physical processes and feedback mechanisms between the urban surface and the overlying atmosphere. Wageningen University and Research.

Turner, D. D., and U. Löhnert, 2014: Information Content and Uncertainties in Thermodynamic Profiles and Liquid Cloud Properties Retrieved from the Ground-Based Atmospheric Emitted Radiance Interferometer (AERI). *Journal of Applied Meteorology and Climatology*, **53**, 752–771, https://doi.org/10.1175/JAMC-D-13-0126.1.

Turner, D. D., and W. G. Blumberg, 2019: Improvements to the AERIoe Thermodynamic Profile Retrieval Algorithm. *IEEE J. Sel. Top. Appl. Earth Observations Remote Sensing*, **12**, 1339–1354, https://doi.org/10.1109/JSTARS.2018.2874968.

U.S. Environmental Protection Agency, 2025: Air Data – ozone exceedances. https://www.epa.gov/outdoor-air-quality-data/air-data-ozone-exceedances.

Varquez, A. C. G., M. Nakayoshi, and M. Kanda, 2015: The Effects of Highly Detailed Urban Roughness Parameters on a Sea-Breeze Numerical Simulation. *Boundary-Layer Meteorology*, **154**, 449–469, https://doi.org/10.1007/s10546-014-9985-4.

Viana, M., P. Hammingh, A. Colette, X. Querol, B. Degraeuwe, I. de Vlieger, and J. van Aardenne, 2014: Impact of maritime transport emissions on coastal air quality in Europe. *Atmospheric Environment*, **90**, 96–105, https://doi.org/10.1016/j.atmosenv.2014.03.046.

Voogt, J. A., and T. R. Oke, 2003: Thermal remote sensing of urban climates. *Remote Sensing of Environment*, **86**, 370–384, https://doi.org/10.1016/S0034-4257(03)00079-8.

Wagner, T. J., W. F. Feltz, and S. A. Ackerman, 2008: The Temporal Evolution of Convective Indices in Storm-Producing Environments. *Weather and Forecasting*, **23**, 786–794, https://doi.org/10.1175/2008WAF2007046.1.

Wagner, T. J., P. M. Klein, and D. D. Turner, 2019: A New Generation of Ground-Based Mobile Platforms for Active and Passive Profiling of the Boundary Layer. *Bulletin of the American Meteorological Society*, **100**, 137–153, https://doi.org/10.1175/BAMS-D-17-0165.1.

Wagner, T. J., A. C. Czarnetzki, M. Christiansen, R. B. Pierce, C. O. Stanier, A. F. Dickens, and E. W. Eloranta, 2022: Observations of the Development and Vertical Structure of the Lake-

Breeze Circulation during the 2017 Lake Michigan Ozone Study. *Journal of the Atmospheric Sciences*, **79**, 1005–1020, https://doi.org/10.1175/JAS-D-20-0297.1.

Wang, D., and Coauthors, 2022: Linking Synoptic Patterns to Cloud Properties and Local Circulations Over Southeastern Texas. *JGR Atmospheres*, **127**, https://doi.org/10.1029/2021JD035920.

Wang, X., X. Liu, Y. Liu, N. Zhang, and Q. Wu, 2025: Characteristics of sea-land breeze circulation in coastal-urban regions of China. *Frontiers of Earth Science*, https://doi.org/10.1007/s11707-025-1147-0.

Watkins, L. E., M. K. Wright, L. C. Kurtz, P. M. Chakalian, E. S. Mallen, S. L. Harlan, and D. M. Hondula, 2021: Extreme heat vulnerability in Phoenix, Arizona: A comparison of all-hazard and hazard-specific indices with household experiences. *Applied Geography*, **131**, 102430, https://doi.org/10.1016/j.apgeog.2021.102430.

Watts, A. J., 1955. Sea breeze at Thorney Island. *Meteorol. Mag,* **84**, 42-48,

Weckwerth, T. M., J. Hanesiak, J. W. Wilson, S. B. Trier, S. K. Degelia, W. A. Gallus, R. D. Roberts, and X. Wang, 2019: Nocturnal Convection Initiation during PECAN 2015. *Bulletin of the American Meteorological Society*, **100**, 2223–2239, https://doi.org/10.1175/BAMS-D-18-0299.1.

Williams, E. J., B. M. Lerner, P. C. Murphy, S. C. Herndon, and M. S. Zahniser, 2009: Emissions of NOx, SO2, CO, and HCHO from commercial marine shipping during Texas Air Quality Study (TexAQS) 2006. *Journal of Geophysical Research: Atmospheres*, **114**, https://doi.org/10.1029/2009JD012094.

Wu, Y., and Coauthors, 2024: Ozone pollution episodes and PBL height variation in the NYC urban and coastal areas during LISTOS 2019. *Atmospheric Environment*, **320**, 120317, https://doi.org/10.1016/j.atmosenv.2023.120317.

Xu, X., Y. Tang, Y. Wang, H. Zhang, R. Liu, and M. Zhou, 2023: Triggering effects of large topography and boundary layer turbulence on convection over the Tibetan Plateau. *Atmos. Chem. Phys.*, **23**, 3299–3309, https://doi.org/10.5194/acp-23-3299-2023.

Yang, M., C. Ren, H. Wang, J. Wang, Z. Feng, P. Kumar, F. Haghighat, and S.-J. Cao, 2024: Mitigating urban heat island through neighboring rural land cover. *Nature Cities*, **1**, 522–532, https://doi.org/10.1038/s44284-024-00091-z.

Yang, Y., X. Chen, and Y. Qi, 2013: Classification of convective/stratiform echoes in radar reflectivity observations using a fuzzy logic algorithm. *Journal of Geophysical Research: Atmospheres*, **118**, 1896–1905, https://doi.org/10.1002/jgrd.50214.

Yoshikado, H., 1994: Interaction of the sea breeze with urban heat islands of different sizes and locations. *Journal of the Meteorological Society of Japan. Ser. II*, **72**, 139–143, https://doi.org/10.2151/jmsj1965.72.1_139.

Yuan, J., A. Venkatram, and V. Isakov, 2006: Dispersion from ground-level sources in a shoreline urban area. *Atmospheric Environment*, **40**, 1361–1372, https://doi.org/10.1016/j.atmosenv.2005.10.024.

Zhang, Y., K. Sun, Z. Gao, Z. Pan, M. A. Shook, and D. Li, 2020: Diurnal Climatology of Planetary Boundary Layer Height Over the Contiguous United States Derived From AMDAR and Reanalysis Data. *JGR Atmospheres*, **125**, e2020JD032803, https://doi.org/10.1029/2020JD032803.

Zhang, Y., W. Zhou, X. Yu, Y. Tian, and R. Zhang, 2024: Long-term coupled variability of temperature and precipitation in eastern China and the underlying mechanisms. *Climate Dynamics*, **62**, 1447–1465, https://doi.org/10.1007/s00382-023-06963-9.

Zhong, S., H. In, and C. Clements, 2007: Impact of turbulence, land surface, and radiation parameterizations on simulated boundary layer properties in a coastal environment. *Journal of Geophysical Research: Atmospheres*, **112**, https://doi.org/10.1029/2006JD008274.

Zhou, X., and Coauthors, 2022: The Development of the NCEP Global Ensemble Forecast System Version 12. *Weather and Forecasting*, **37**, 1069–1084, https://doi.org/10.1175/WAF-D-21-0112.1.